



Title	Synthesis and Properties of Calix[3]pyrrole and Its Derivatives
Author(s)	稲葉, 佑哉
Citation	北海道大学. 博士(工学) 甲第15872号
Issue Date	2024-03-25
DOI	10.14943/doctoral.k15872
Doc URL	http://hdl.handle.net/2115/92123
Type	theses (doctoral)
File Information	INABA_Yuya.pdf



[Instructions for use](#)

Ph.D. Thesis

Synthesis and Properties of Calix[3]pyrrole and Its Derivatives

(Calix[3]pyrrole とその類縁体の合成および物性)

Graduate School of Chemical Sciences and Engineering,

Hokkaido University

Yuya Inaba

Contents

Chapter 1. General Introduction

- 1.1. Oligopyrrole Macrocycles
- 1.2. Synthetic Methods for Oligopyrrole Macrocycles
- 1.3. Elusive Tripyrrolic Macrocycle, Calix[3]pyrrole
- 1.4. Overview of This Thesis
- 1.5. References

Chapter 2. Synthesis, Structure, and Ring Expansion Reaction of Calix[3]pyrrole

- 2.1. Introduction
- 2.2. Synthesis of Calix[3]pyrrole
- 2.3. Strained Structure of Calix[3]pyrrole
- 2.4. Ring Expansion Reaction of Calix[3]pyrrole
- 2.5. Anion Binding Study of Calix[3]pyrrole
- 2.6. Conclusion
- 2.7. Experimental Section
- 2.8. References

Chapter 3. Scope and Mechanistic Analysis of Ring Expansion Reaction of Calix[3]pyrrole and Analogues

- 3.1. Introduction
- 3.2. Synthesis of Furan Embedded Analogues of Calix[3]pyrrole
- 3.3. Comparison of Strain and Reactivity in Ring Expansion Reaction
- 3.4. Strain Increase by *N*-methylation and Isolation of Reaction Intermediate
- 3.5. Reaction Mechanism Analysis
- 3.6. Conclusion
- 3.7. Experimental Section
- 3.8. References

Chapter 4. Construction of Chiral System by Controlling Aromatic Ring Inversion in Calix[3]pyrrole

- 4.1. Introduction
- 4.2. Preparation of Chiral Calix[1]furan[1]pyrrole[1]thiophene
- 4.3. Suppression of Racemization by *N*-methylation
- 4.4. Ring Expansion Reaction of Calix[1]furan[1]pyrrole[1]thiophene
- 4.5. Conclusion
- 4.6. Experimental Section
- 4.7. References

Chapter 5. Acid Stability of B(III)-Calix[3]pyrrole and Application to the Design of Highly Acid Stable BODIPY

- 5.1. Introduction
- 5.2. Acid-stability of B(III)-calix[3]pyrrole
- 5.3. Design and Synthesis of Acid-Stable Cyclic BODIPY
- 5.4. Acid Resistance of Cyclic BODIPY
- 5.5. Application of Cyclic BODIPY to Stain Strongly Acidic Materials
- 5.6. Conclusion
- 5.7. Experimental Section
- 5.8. References

Chapter 6. Conclusion and Outlook

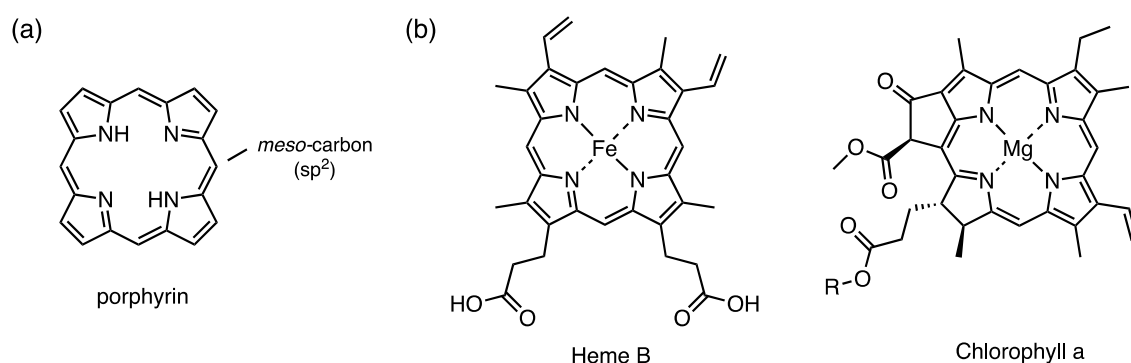
- 6.1. Conclusion
- 6.2. Future Perspectives
- 6.3. References

Chapter 1

General Introduction

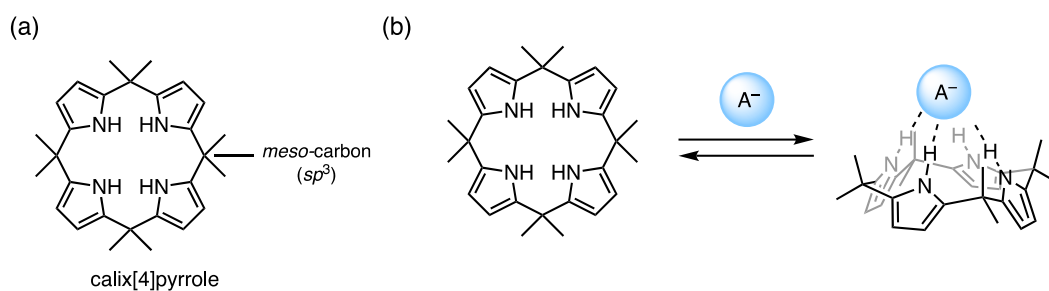
1.1. Oligopyrrolic Macrocycles

Oligopyrrolic compounds represent a diverse property and have been utilized in a growing number of applications¹⁻⁵. Among them, oligopyrrolic macrocycles such as porphyrins⁶, expanded porphyrins⁷, and calixpyrroles⁸, have attracted much attention for several decades due to their unique properties. Porphyrins are composed of four pyrrole subunits linked at α -carbons by sp^2 carbons, called *meso*-carbons, (**Scheme 1-1a**), and have a planar structure with 18π aromaticity.⁹ This structure can be found in nature. For example, heme in blood heme proteins has a porphyrin structure with an iron ion at the center of the macrocycle¹⁰, and chlorophyll in plant cells also has a porphyrin skeleton with a magnesium ion at the center¹¹ (**Scheme 1-1b**). Because these naturally occurring porphyrin-containing compounds are vital to living species, porphyrin is often referred to as the “pigment of life”. After the discovery of the porphyrin structure, a large number of porphyrins have been synthesized, and these artificial porphyrins have been investigated for their properties as chemosensors^{12, 13}, optoelectronic materials^{14,15}, and photosensitizers^{16,17}.



Scheme 1-1. (a) The general structure of porphyrin and (b) examples of naturally occurring porphyrin-related compounds.

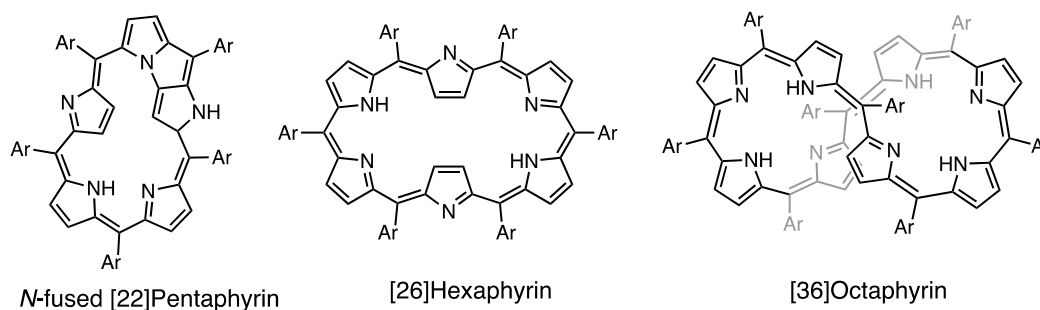
Along with porphyrins, calix[n]pyrroles, which consist of pyrroles linked at the α -position by sp^3 *meso*-carbons (**Scheme 1-2a**), have also attracted attention. Calix[4]pyrrole was found as a condensation product of acetone and pyrrole and was initially named acetonepyrrole¹⁸. After the discovery that calix[4]pyrrole is a good anion receptor¹⁹, calixpyrroles have been widely investigated for their synthesis and application as host materials in supramolecular chemistry^{20,21} (**Scheme 1-2b**).



Scheme 1-2. (a) The chemical structure of calix[4]pyrrole and (b) its anion binding ability.

After the discovery of porphyrins and calix[4]pyrroles, analogues of different sizes were also of interest. In the case of porphyrins, the larger macrocycles with increasing number of pyrrole subunits were expected to have a larger π -conjugation system and different conformational flexibility. Indeed, expanded porphyrins (**Scheme 1-3**) are reported to have characteristic optical properties, conformational features, and reactivity depending on the size of macrocycles⁷. For calix[n]pyrroles, it has been reported that increasing the number of repeating units and ring size leads to different anion binding affinities.^{19,22,23}

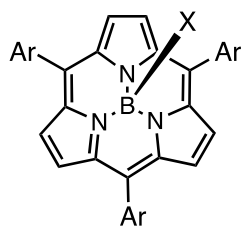
Expanded porphyrin



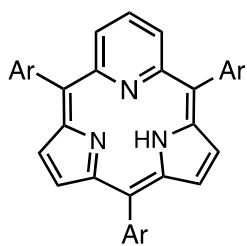
1.2. Synthetic Methods for Oligopyrrolic Macrocycles

Porphyrins and calixpyrroles are synthesized by linking pyrroles. As mentioned in the previous section, calix[4]pyrrole was first prepared by the acid-catalyzed condensation reaction of acetone and pyrrole by A. Baeyer²⁴. Porphyrins are also prepared by acid-catalyzed condensation reaction of pyrrole and aldehydes, followed by oxidation^{25,26}. In these reactions, the repeated Friedel-Crafts type reaction of pyrrole and carbonyl compound results in the formation of α -*meso*- α linkage of the pyrroles. Interestingly, this condensation reaction tends to yield tetrapyrrolic macrocycles selectively. Macrocycles with more than four pyrrole units were also found in the acid-catalyzed condensation reaction under varying conditions. For example, the condensation reaction of pyrrole and aldehyde under 10 times higher concentrations than in conventional porphyrin synthesis gave various sizes of expanded porphyrins²⁷. It was also reported that calix[5]pyrrole, or calix[8]pyrrole could be obtained by the condensation reaction of 3,4-difluoropyrrole and acetone under acidic conditions at high concentration²⁸. The entropically unfavorable construction of large porphyrinoid macrocycles is even possible. However, ring-contracted tripyrrolic macrocycles have never been found in the process of condensation reaction. The reason why tetrapyrrolic macrocycles rather than tripyrrolic macrocycles are preferred has not been elucidated.

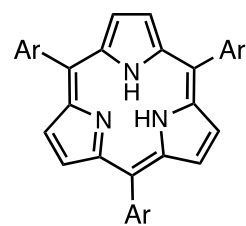
Although tripyrrolic macrocycles have not been found in traditional porphyrin synthesis, many researchers have been interested in tripyrrolic systems as ring-contracted analogues of porphyrin or calix[4]pyrrole. To date, several tripyrrolic macrocycles and analogues have been reported (**Scheme 1-4**). Inokuma and Osuka *et al.* and Kobayashi *et al.* reported the synthesis of subporphyrin, a ring-contracted analogue of porphyrin, as a boron complex by condensation reaction of tripyrrolylborane and aldehydes^{29,30}. R. Myśliborski *et al.* reported the synthesis of subpyrriporphyrin as a core-modified analogue³¹, and Yamada and Kobayashi *et al.* synthesized triphyrin(2.1.1) as a *meso*-expanded analogue.³² Similarly, B. S. Kumar *et al.* recently reported the synthesis of *meso*-expanded calix[3]pyrrole³³. Although various tripyrrolic macrocycles have been reported, tripyrrolic macrocycles bridged by single *meso*-carbons as porphyrins or calixpyrroles without any metal at the center had never been achieved until Song and Osuka *et al.* very recently (2022) reported the synthesis of boron-free subporphyrin via Suzuki-Miyaura cross-coupling reaction strategy³⁴.



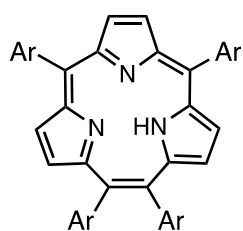
B(III)-subporphyrin
Osuka *et al.* (2007)
Kobayashi *et al.* (2007)



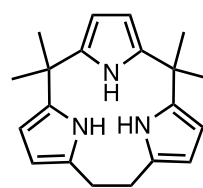
subpyriporphyrin
L.-Grazynski *et al.* (2006)



subporphyrin
Song *et al.* (2022)



Triphyrin(2.1.1)
Yamada, Kobayashi, *et al.* (2007)



meso-expanded
calix[3]pyrrole
Panda *et al.* (2020)

Scheme 1-4. Structure of known tripyrrolic macrocycles.

1.3. Elusive Tripyrrolic Macrocycle, Calix[3]pyrrole

While several examples of ring-contracted porphyrin analogues with three pyrrole subunits are known, it is still unknown why tripyrrolic macrocycles have not been found in the condensation reactions of pyrrole and carbonyl compounds. In the synthesis of porphyrins or calixpyrroles, continuous condensation reactions of pyrrole and carbonyl compounds initially yield linearly linked oligopyrrolic compounds, then their intramolecular cyclization affords macrocyclic compounds³⁵ (Scheme 1-5). In the case of porphyrin synthesis, an *sp*³ *meso*-carbon bridged tetrapyrrolic macrocycle called “porphyrinogen” is formed and subsequently oxidized to furnish porphyrin. Therefore, the ring size of porphyrin is determined at the point where the porphyrinogen-like oligopyrrolic macrocycle is formed.

Given that, the author noticed calix[3]pyrrole, ring-contracted macrocycle of calix[4]pyrrole with three pyrrole subunits linked by *sp*³ carbons. The synthesis of calix[3]pyrrole requires overcoming the fact that linear tripyrrole never cyclizes and that the tetrapyrrolic macrocycle is selectively constructed. However, if calix[3]pyrrole were to be synthesized, investigation of the structure and properties of calix[3]pyrrole might provide a clue to solve the long-standing question.

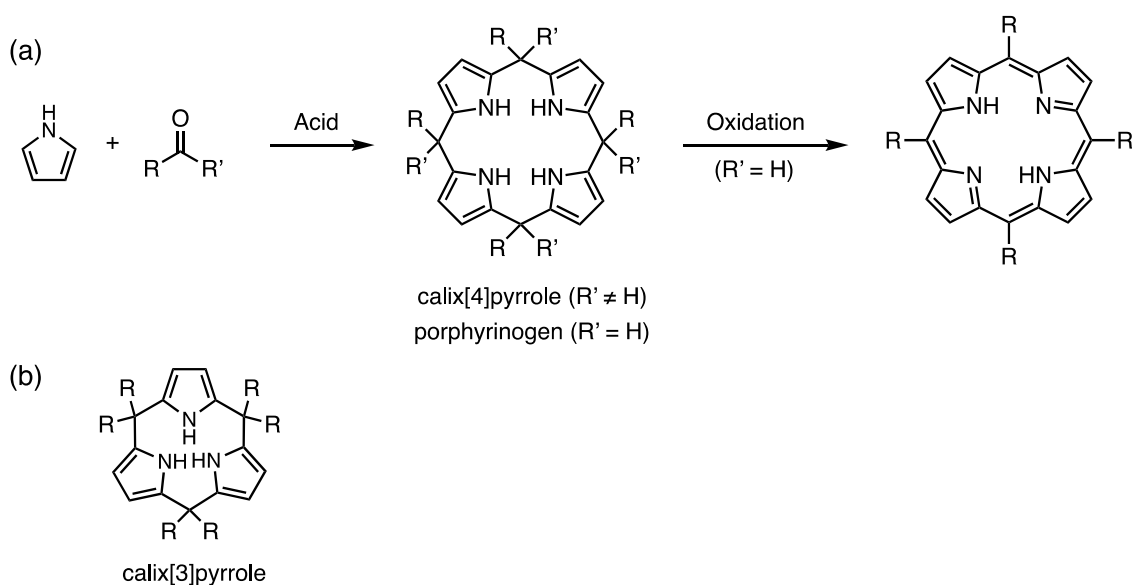


Figure 1-6. (a) General reaction mechanism of porphyrin synthesis and (b) chemical structure of calix[3]pyrrole.

1.4. Overview of This Thesis

The objective of this thesis is to prepare calix[3]pyrrole to answer the question why tripyrrolic macrocycles were not found in traditional porphyrin synthesis conditions, and to develop the discoveries of calix[3]pyrrole into new chemistry. Therefore, the author first attempted to synthesize calix[3]pyrrole and explore its properties, which could be an answer to the long-standing question in porphyrin-related chemistry. Secondly, based on the findings obtained from calix[3]pyrrole, especially the properties derived from the contracted ring system, the new chemistry of calix[3]pyrrole and related compounds were explored.

In Chapter 2, the synthesis, structural analysis, and characteristic reactivity of calix[3]pyrrole are described. As a synthetic route for calix[3]pyrrole, a process starting from an aliphatic hexaketone compound via cyclization and Paal-Knorr pyrrole formation reaction was chosen. Although direct cyclization of the aliphatic hexaketone was not effective, cyclization after protection of the 1,4-diketone part by furan ring formation successfully afforded a cyclic hexaketone that could be converted to the desired calix[3]pyrrole via the Paal-Knorr pyrrole formation reaction. Single crystal X-ray diffraction analysis and computational analysis revealed that calix[3]pyrrole has a much more strained structure compared to the larger calix[*n*]pyrroles. It was also found that calix[3]pyrrole underwent a ring expansion reaction under acidic conditions to form calix[6]pyrrole, which was gradually converted to calix[4]pyrrole over time. The highly strained structure and ring expansion reaction of calix[3]pyrrole were considered to be the reason for the absence of tripyrrolic macrocycles in traditional porphyrin synthesis.

In Chapter 3, a detailed analysis of the ring expansion reaction of furan-embedded calix[3]pyrrole analogues with various strains is mentioned. The furan-embedded analogues of calix[3]pyrrole were prepared in a similar manner to calix[3]pyrrole. The strain of these analogues was found to decrease as the number of pyrroles decreased, and the reactivity in the ring expansion reaction also decreased, indicating that the strain is the trigger to induce the ring expansion reaction. Furthermore, methylation of the pyrrole nitrogen also increased the strain of a calix[3]pyrrole analogue to activate the macrocycle for the ring expansion reaction. *N*-methylation also allowed the author to isolate the intermediate of the ring expansion reaction. Finally, the mechanism of the ring expansion reaction was proposed to consist of two steps, ring cleavage of the calix[3]-type macrocycle driven by strain release and cyclization after dimerization of reaction intermediates. Since ring cleavage was site-selective, the ring-expanded product of the furan-pyrrole mixed compound had a defined sequence of pyrrole and furan.

In Chapter 4, the chirality and racemization behavior of asymmetric calix[3]pyrrole analogues are expressed. By introducing three different heteroaromatic rings, pyrrole, furan and thiophene, the calix[3]pyrrole core became chiral, reflecting its non-planar structure, and showed the existence of a pair of enantiomers separable by chiral HPLC. The resulting chiral calix[1]furan[1]pyrrole[1]thiophene was found to undergo racemization via aromatic ring inversion, which could be suppressed by methylation of the pyrrole nitrogen. The absolute configuration was determined by single crystal X-ray diffraction analysis. Since the racemization behavior changed drastically before and after *N*-methylation, kinetic resolution upon *N*-methylation was attempted in the presence of chiral ammonium salt, resulting in moderate enantiomeric excess. The ring expansion reaction of calix[1]furan[1]pyrrole[1]thiophene was also carried out, and not only double-sized macrocycle but also triple- and quadruple-sized rings were isolated. The resulting ring-expanded products were not resolved into the pair of enantiomers, suggesting that the chirality of calix[1]furan[1]pyrrole[1]thiophene is due to its small macrocycle size.

In Chapter 5, stabilization of calix[3]pyrrole by boron complexation and its application to the design of acid-stable boron dipyrromethene (BODIPY) are described. While the most characteristic feature of calix[3]pyrrole appeared to be the strain-induced ring expansion reaction, this reaction is also recognized as the decomposition of calix[3]pyrrole. Following the fact that subporphyrin was obtained using boron as a template, a boron complex of calix[3]pyrrole was synthesized and its stability to acid was investigated. It was found that boron-calix[3]pyrrole does not undergo deboronation or ring cleavage under acidic conditions, but instead forms an adduct with acid by protonation of the pyrrole and coordination of the conjugate base to the boron center. This acid tolerance of boron-calix[3]pyrrole was then applied to the design of acid-stable BODIPY dye. The prepared cyclic BODIPY, which was designed based on the structure of boron-calix[3]pyrrole, not only showed high acid tolerance but also fluorescence switching upon protonation under acidic conditions.

In Chapter 6, the thesis is summarized, and future perspectives described.

1.5. References

1. H. Maeda, Y. Bando, Recent progress in research on anion-responsive pyrrole-based π -conjugated acyclic molecules, *Chem. Commun.*, **2013**, 49, 4100–4113.
2. Y. Ding, Y. Tang, W. Zhu, Y. Xie, Fluorescent and colorimetric ion probes based on conjugated oligopyrroles, *Chem. Soc. Rev.*, **2014**, 44, 1101–1112.
3. J. L. Sessler, S. Camiolo, P. A. Gale, Pyrrolic and polypyrrolic anion binding agents, *Coord. Chem. Rev.*, **2003**, 240, 17–55.
4. M. Jurow, A. E. Schuckman, J. D. Batteas, C. M. Drain, Porphyrins as molecular electronic components of functional devices, *Coord. Chem. Rev.*, **2010**, 254, 2297–2310.
5. F. Wang, C. Bucher, Q. He, A. Jana, J. L. Sessler, Oligopyrrolic Cages: From Classic Molecular Constructs to Chemically Responsive Polytopic Receptors, *Acc. Chem. Res.*, **2022**, 55, 1646–1658.
6. Y. Shi, F. Zhang, R. J. Linhardt, Porphyrin-based compounds and their applications in materials and medicine, *Dyes Pigm.*, **2021**, 188, 109136.
7. T. Tanaka, A. Osuka, Chemistry of meso-Aryl-Substituted Expanded Porphyrins: Aromaticity and Molecular Twist, *Chem. Rev.*, **2017**, 117, 2584–2640.
8. I. A. Rather, S. A. Wagay, M. S. Hasnain, R. Ali, New dimensions in calix[4]pyrrole: the land of opportunity in supramolecular chemistry, *RSC Adv.*, **2019**, 9, 38309–38344.
9. J. I. Wu, I. Fernández, P. v. R. Schleyer, Description of Aromaticity in Porphyrinoids, *J. Am. Chem. Soc.*, 2013, 135, 315–321.
10. J. G. Riess, Oxygen Carriers (“Blood Substitutes”) – Raison d'Être, Chemistry, and Some Physiology *Blut ist ein ganz besonderer Saft*, *Chem. Rev.*, **2014**, 114, 3919–3962.
11. Horton, P.; Ruban, V. A.; Walters, G. R. Regulation of light harvesting in green plants, *Annu. Rev. Plant. Physiol. Plant. Mol. Biol.*, **1996**, 47, 655–684.
12. S. Ishihara, J. Labuta, W. V. Rosson, D. Ishikawa, K. Minami, J. P. Hill, K. Ariga, Porphyrin-based sensor nanoarchitectonics in diverse physical detection modes, *Phys. Chem. Chem. Phys.*, **2014**, 16, 9173–9746.
13. M. Farinone, K. Urbanska, M. Pawlicki, BODIPY- and Porphyrin-Based Sensors for Recognition of Amino Acids and Their Derivatives, *Molecules*, **2020**, 25, 4523.
14. O. Ostroverkhova, Organic Optoelectronic Materials: Mechanisms and Applications, *Chem. Rev.*, **2016**, 116, 13279–13412.

15. L.-L. Li, E. W.-G. Diau, Porphyrin-sensitized solar cells, *Chem. Soc. Rev.*, **2013**, *42*, 291–304.
16. R. Bonnet. Photosensitizers of the porphyrin and phthalocyanine series for photodynamic therapy, *Chem. Soc. Rev.*, **1995**, *24*, 19–33.
17. M. Ethirajan, Y. Chen, P. Joshi, K. R. Pandey, The role of porphyrin chemistry in tumor imaging and photodynamic therapy, *Chem. Soc. Rev.*, **2011**, *40*, 340–362.
18. P. Rothemund, C. L. Gage, Concerning the Structure of “Acetonepyrrole”, *J. Am. Chem. Soc.*, **1955**, *12*, 3340–3342.
19. P. A. Gale, J. L. Sessler, V. Král, V. Lynch, Calix[4]pyrrole: Old Yet New Anion-Binding Agents, *J. Am. Chem. Soc.*, **1996**, *118*, 5140–5141.
20. D. S. Kim, J. L. Sessler, Calix[4]pyrroles: versatile molecular containers with ion transport, recognition, and molecular switching functions, *Chem. Soc. Rev.*, **2015**, *44*, 532–546.
21. F. H. Kohnke, Calixpyrroles: from Anion Ligands to Potential Anticancer Drugs, *Eur. J. Org. Chem.*, **2020**, *28*, 4261–4272.
22. G. Cafeo, F. H. Kohnke, M. F. Parisi, R. P. Nascone, G. L. La Torre, D. J. Williams, The Elusive β -Unsubstituted Calix[5]pyrrole Finally Captured, *Org. Lett.*, **2002**, *4*, 2695–2697.
23. G. Cafeo, F. H. Kohnke, G. L. La Torre, A. J. P. White, D. J. Williams, The complexation of halide ions by a calix[6]pyrrole, *Chem. Commun.*, **2000**, *36*, 1207–1208.
24. A. Baeyer, Uber ein Condensationsproduct von Pyrrol mit Aceton, *Ber. Dtsch. Chem. Ges.*, **1886**, *19*, 2184–2185.
25. P. Rothemund, Formation of Porphyrins from Pyrrole and Aldehydes, *J. Am. Chem. Soc.*, **1935**, *57*, 2010–2011.
26. A. D. Alder, F. R. Longo, J. D. Finarelli, J. Goldmacher, J. Assour, L. Korsakoff, A simplified synthesis for *meso*-tetraphenylporphyrine, *J. Org. Chem.*, **1967**, *32*, 476.
27. J.-Y. Shin, H. Furuta, K. Yoza, S. Igarashi, A. Osuka, *meso*-Aryl-Substituted Expanded Porphyrins, *J. Am. Chem. Soc.*, **2001**, *123*, 7190–7191.
28. J. L. Sessler, J. A. Shriver, K. Jursíková, V. M. Lynch, M. Marquez, Direct Synthesis of Expanded Fluorinated Calix[*n*]pyrroles: Decafluorocalix[5]pyrrole and Hexadecafluorocalix[8]pyrrole, *J. Am. Chem. Soc.*, **2000**, *122*, 12061–12062.
29. Y. Inokuma, Z. S. Yoon, D. Kim, A. Osuka, *meso*-Aryl-Substituted Subporphyrins: Synthesis, Structures, and Large Substituent Effects on Their Electronic Properties, *J. Am. Chem. Soc.*, **2007**, *129*, 4747–4761.

30. N. Kobayashi, Y. Takeuchi, A. Matsuda, *meso*-Aryl Subporphyrins, *Angew. Chem. Int. Ed.*, **2007**, *46*, 758–760.
31. R. Myśluborski, L. L.-Grażyński, L. Szterenber, T. Lis, Subpyriporphyrin–A [14]Triphyrin(1.1.1) Homologue with an Embedded Pyridine Moiety, *Angew. Chem. Int. Ed.*, **2006**, *45*, 3670–3674.
32. Z.-Li. Xue, Z. Shen, J. Mack, D. Kuzuhara, H. Yamada, T. Okujima, N. Ono, X.-Z. You, N. Kobayashi, A Facile One-Pot Synthesis of *meso*-Aryl-Substituted [14]Triphyrin(2.1.1), *J. Am. Chem. Soc.*, **2008**, *130*, 16478–16479.
33. B. S. Kumar, N. N. Pati, K. V. J. Jose, P. K. Panda, Synthetic access to calix[3]pyrroles *via meso*-expansion: hosts with diverse guest chemistry, *Chem. Commun.*, **2020**, *56*, 5637–5640.
34. L. Liu, J. Kim, L. Xu, Y. Rao, M. Zhou, B. Yin, J. Oh, D. Kim, A. Osuka, J. Song, Synthesis of Subporphyrin Free Bases, *Angew. Chem. Int. Ed.*, **2022**, *61*, e202214342.
35. A. D. Adler, F. R. Longo, W. Shergalis, Mechanistic Investigations of Porphyrin Synthesis. I. Preliminary Studies on *ms*-Tetraphenylporphyrin, *J. Am. Chem. Soc.*, **1964**, *86*, 3145–3149.

Chapter 2

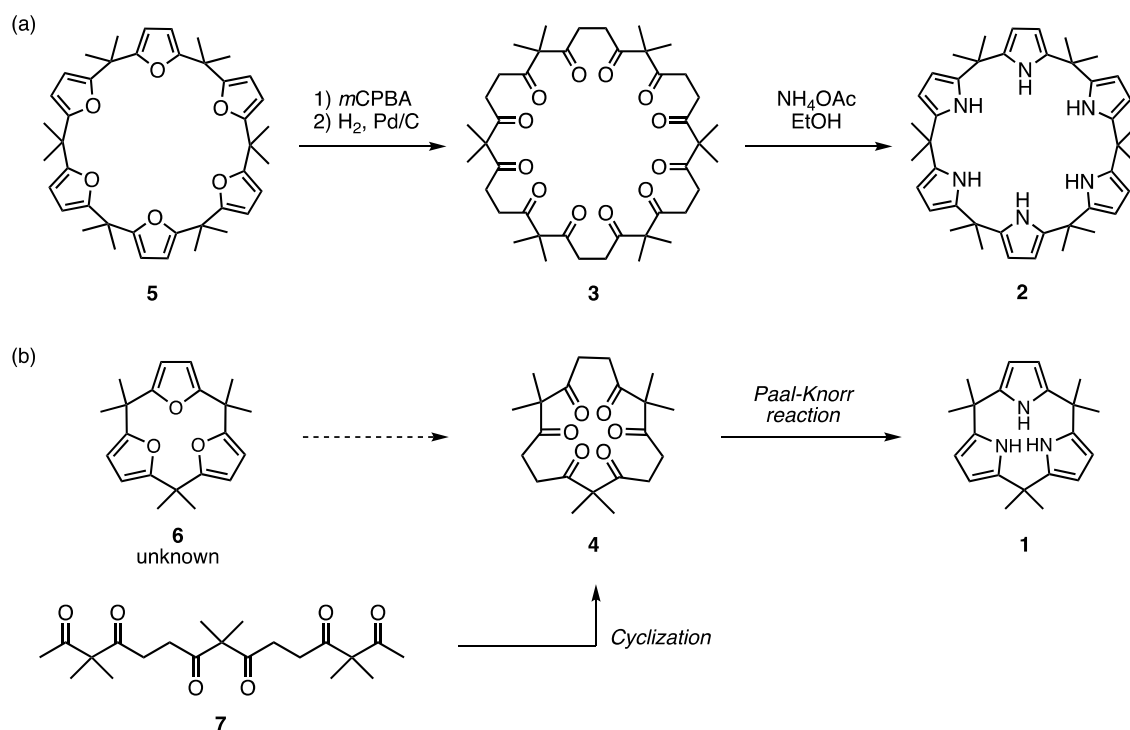
Synthesis, Structure, and Properties of Calix[3]pyrrole

Abstract

The synthesis, structural analysis, and reactivity study of calix[3]pyrrole were carried out. The synthesis of calix[3]pyrrole was achieved by Paal-Knorr pyrrole formation reaction of cyclic hexaketone precursor, which was prepared from aliphatic hexaketone compound via furan formation and cyclization reaction. Crystal structure analysis and computational analysis revealed a highly strained structure of calix[3]pyrrole compared to larger analogues. Due to the large macrocyclic strain, calix[3]pyrrole underwent a very rapid ring expansion reaction under acidic conditions to give calix[6]pyrrole, and then slowly converted to calix[4]pyrrole. This reactivity may be one of the reasons why tripyrrolic macrocycles have never been found in the acid-catalyzed condensation reaction of pyrrole and carbonyl compounds.

2.1. Introduction

As introduced in Chapter 1, the absence of tripyrrolic macrocycles and the selective formation of tetrapyrrolic macrocycles have been a question in the synthesis of oligopyrrolic macrocycles. Not only would calix[3]pyrrole **1** be a key to answering this question, but also unique properties derived from its contracted macrocycle size could be expected. Since it is easy to imagine that the synthesis of calix[3]pyrrole **1** could not be achieved by conventional acid-catalyzed condensation reaction, a completely different approach was required. In this sense, the author focused on the Paal-Knorr pyrrole formation reaction-based synthesis using cyclic oligoketone precursors. In 2000, Cafeo *et al.* reported the synthesis of calix[6]pyrrole **2** from cyclic dodecaketone **3** via Paal-Knorr pyrrole formation reaction¹ (**Scheme 2-1**). Following this approach, the author envisioned that calix[3]pyrrole **1** might also be accessible from the cyclic hexaketone precursor **4**. Although cyclic dodecaketone **2** was prepared from calix[6]furan **5** obtained from furan and acetone², a parent compound calix[3]furan **6**, is unknown in the case of cyclic hexaketone **4**. Thus, the synthesis of calix[3]pyrrole **1** had to start from the cyclization of the linear hexaketone **7** that is reported by Y. Manabe *et al.*³.



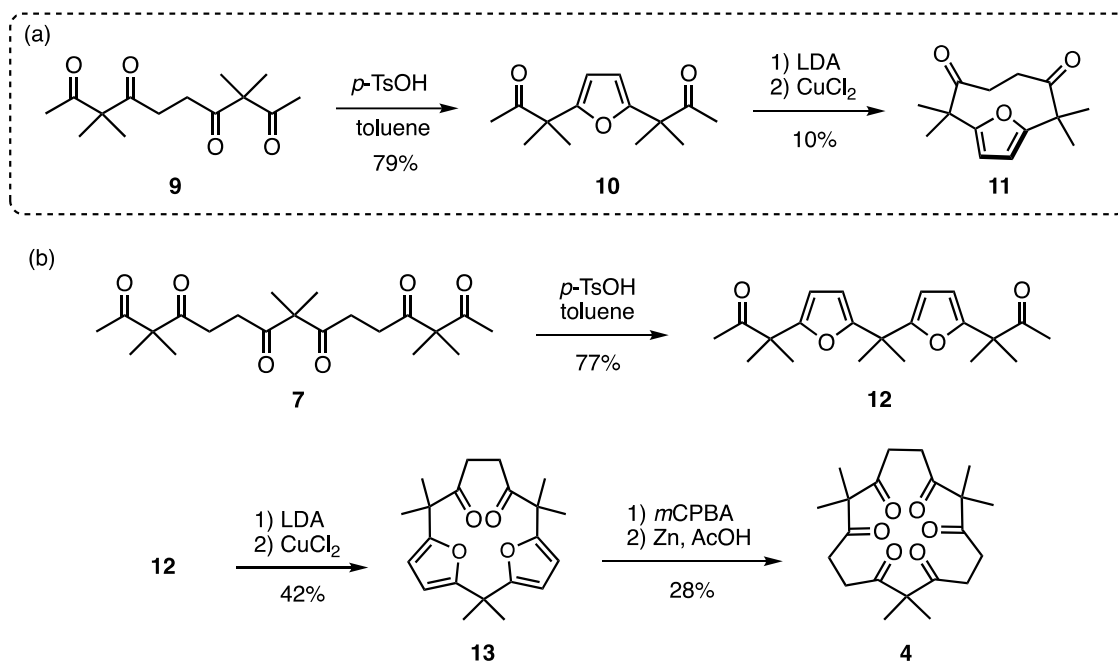
Scheme 2-1. (a) Synthesis of calix[6]pyrrole **2** from calix[6]furan **5** via cyclic dodecaketone **3** and (b) possible synthetic pathway for calix[3]pyrrole **1**.

In this chapter, the synthesis of calix[3]pyrrole **1** from linear hexaketone **7** via cyclization and Paal-Knorr pyrrole formation reaction, and the structural analysis of calix[3]pyrrole **1** were performed. Due to the small macrocycle size, calix[3]pyrrole **1** was found to have large strain compared with calix[4]-, calix[5]-, and calix[6]pyrroles based on single crystal structure and computational analysis. Furthermore, calix[3]pyrrole **1** underwent ring expansion reaction under conventional acid-catalyzed condensation reaction conditions to give first calix[6]pyrrole **2** and then calix[4]pyrrole, demonstrating its high reactivity under acidic conditions.

2.2. Synthesis of Calix[3]pyrrole

Linear hexaketone **7** was prepared according to the reported procedure from 3,3-dimethyl-2,4-pentanedione (**8**) via mono- and bis-silylation and silver(I) oxide mediated coupling reaction. Compound **7** was then subjected to the oxidative coupling reaction conditions to give the cyclic hexaketone **4**. Although copper(II) mediated coupling condition using lithium enolate⁴ and silver(I), cerium(IV) or hypervalent iodine mediated condition using enol silyl ether^{5,6,7} were tried, none of them gave cyclic hexaketone **4**. During the cyclization reaction attempts, it was found that furan compound **10** obtained from linear tetraketone **9**⁸ underwent cyclization reaction upon treatment with LDA followed by oxidation with copper(II) chloride to give **11**. This finding that an even smaller cycle can be formed from shorter oligoketone chain motivated the author to attempt cyclization of **7** via furan formation. Paal-Knorr type furan formation reaction of **7** using *p*-toluenesulfonic acid in refluxing toluene furnished linear difuran compound **12** in 77% yield (**Scheme 2-2**). Linear difuran **12** was then subjected to the oxidative coupling reaction, deprotonation by lithium diisopropylamide (LDA), followed by the addition of copper(II) chloride. After quenching the reaction and chromatographic separation, the cyclized product **13** was obtained in 42%. Furan was then converted back to 1,4-diketone using *m*-chloroperbenzoic acid and zinc powder to give cyclic hexaketone **4** in 28% yield.

The resulting cyclic hexaketone **4** was subjected to a Paal-Knorr pyrrole formation reaction using ammonium acetate in refluxing ethanol. After work-up and chromatographic separation, the desired calix[3]pyrrole **1** was isolated in 41% yield (**Figure 2-1a**). In the ¹H NMR spectrum, **1** showed three peaks at $\delta = 6.91$, 5.83, and 1.59 ppm, which were assigned to the pyrrole NH proton, pyrrole CH proton, and methyl groups, respectively. In the high-resolution electron spray ionization (HR-ESI) mass spectrum, **1** was observed as $[M-H]^+$ at $m/z = 320.2131$ (calculated for $[M-H]^+$, C₂₁H₂₆N₃: $m/z = 320.2131$). Single crystal X-ray diffraction analysis of **1** clearly revealed the structure of **1** with three pyrroles connected at α -position via dimethylmethylene bridge (**Figure 2-1b**). It was also found that **1** was adopted in partial-cone conformation where two pyrroles are up, and one pyrrole is down. Furthermore, two pyrrole NHs facing the same direction were hydrogen-bonded to a water molecule, promising its anion-binding ability.



Scheme 2-2. (a) Model reaction for cyclization of oligoketone via furan formation, and (b) the synthesis of cyclic hexaketone **4**.

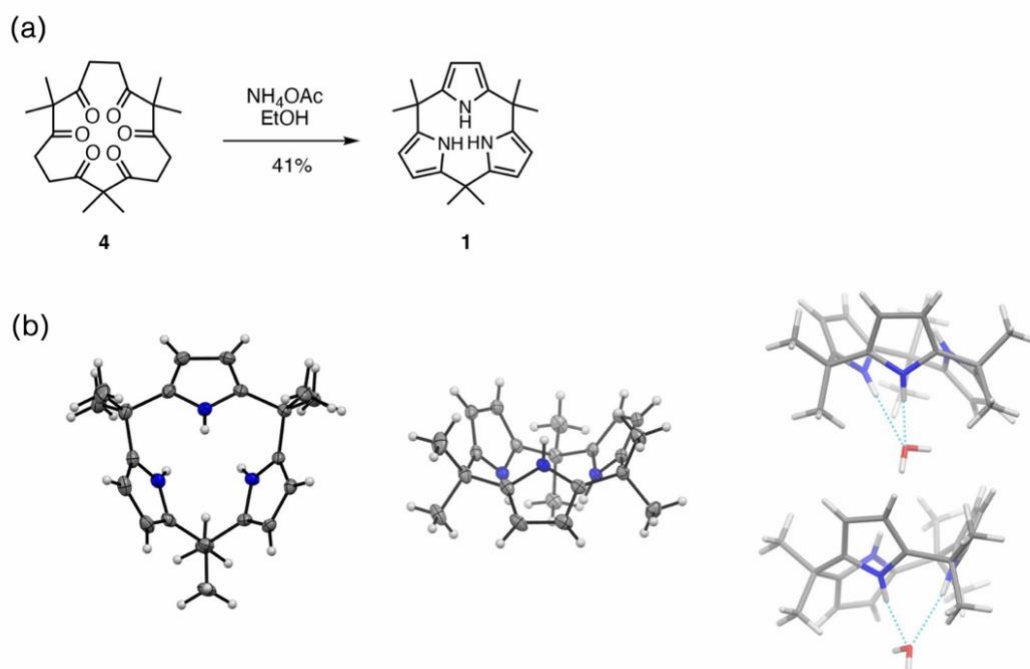


Figure 2-1. (a) Paal-Knorr pyrrole formation reaction of **4** to access calix[3]pyrrole **1**, (b) single crystal structure of **1** viewed from top (left) and side (middle), and asymmetric structure showing hydrogen bonding with water (right) (C: gray, H: white, N: blue, O: red).

2.3. Strained Structure of Calix[3]pyrrole

Detailed analysis of the crystal structure of calix[3]pyrrole **1** revealed that pyrroles in **1** is not planar, indicating that **1** has macrocyclic strain. In order to determine the degree of pyrrole deformation in **1**, deformation angles α and β were introduced, which are used to evaluate deformations in cyclophanes⁹. α represents the angle between the N–C2–C3 plane and the N–C3–C4 plane, and β represents the angle between the N–C2–C3 plane and the C_{meso} –C2 bond (Figure 2-4b). In calix[3]pyrrole **1**, the deformation angles α and β were determined to be 2.52° and 9.20°, respectively. Compared to the deformation angles of calix[4]pyrrole **14**, calix[5]pyrrole **15**, and calix[6]pyrrole **2**, those of calix[3]pyrrole **1** were significantly larger, representing that **1** is much more strained than the larger analogues **14**, **15**, and **2** (Figure 2-4c).

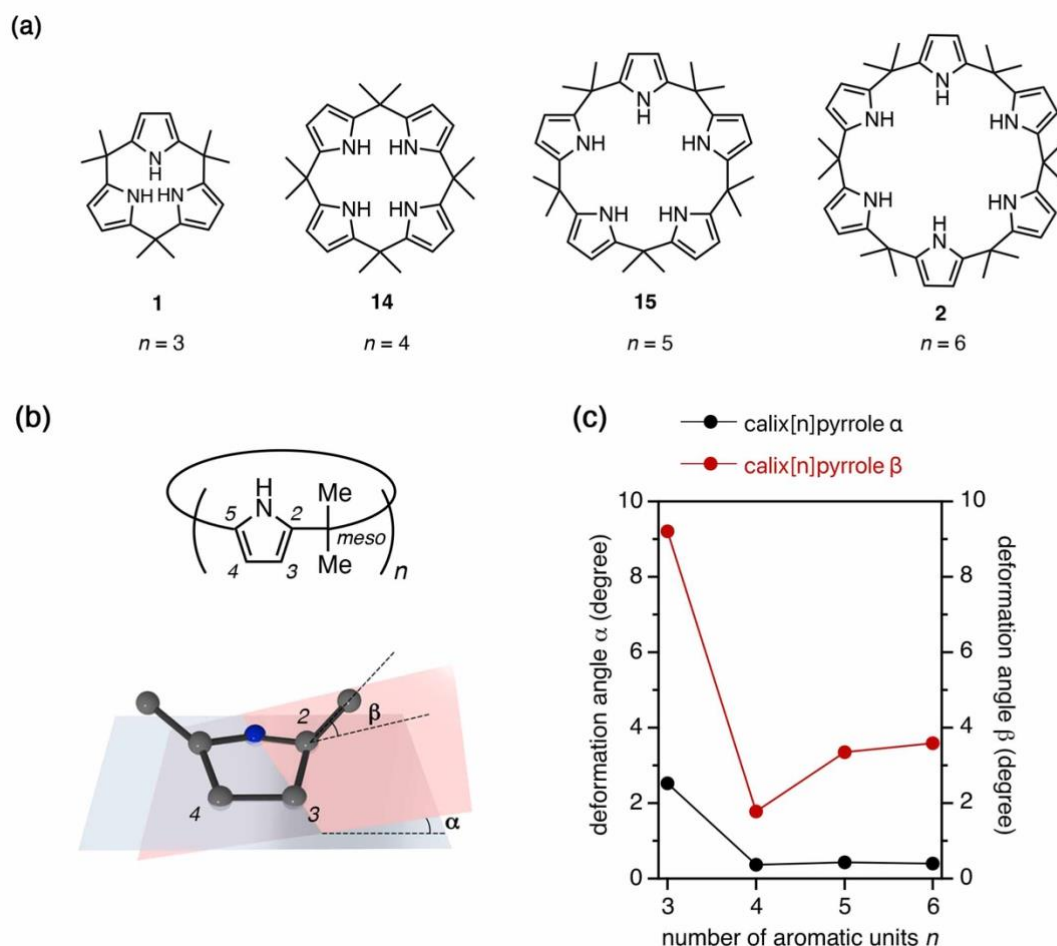


Figure 2-2. (a) Chemical structures of **1**, **14**, **15**, and **2**, (b) definition of deformation angles α and β , and (c) plot of deformation angles against the number of repeating units.

To support this observation, a computational analysis was also performed. The strain energies of **1**, **14**, **15**, and **2** were calculated as energy per repeating unit (total energy/number of repeating units) using energies obtained by DFT calculation (**Figure 2-3a**). The obtained energy per repeating unit of **1** was 23.04 kJ/mol greater than that of **7**, which had the lowest energy per repeating unit. Relative energy per repeating unit of **15** and **2** were only 0.91 and 3.80 kJ/mol higher than that of **14**, respectively, indicating a similar tendency for deformation angle difference (**Figure 2-3b**).

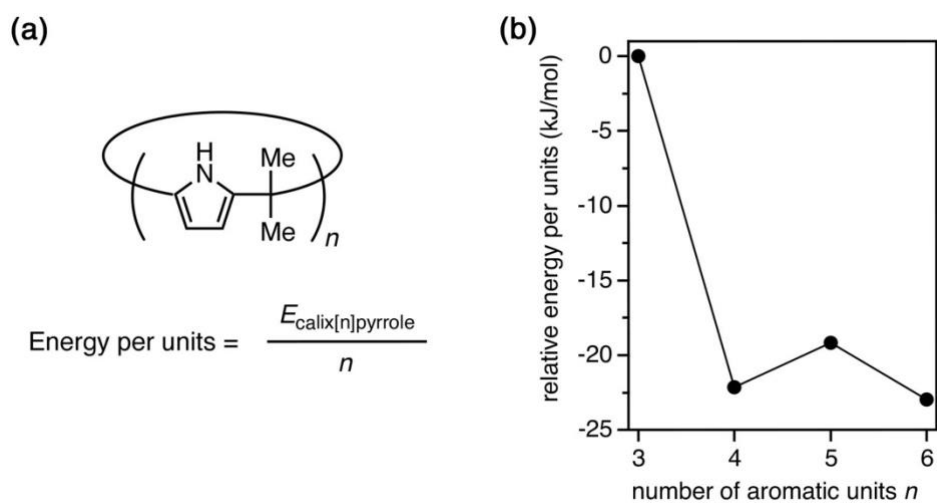
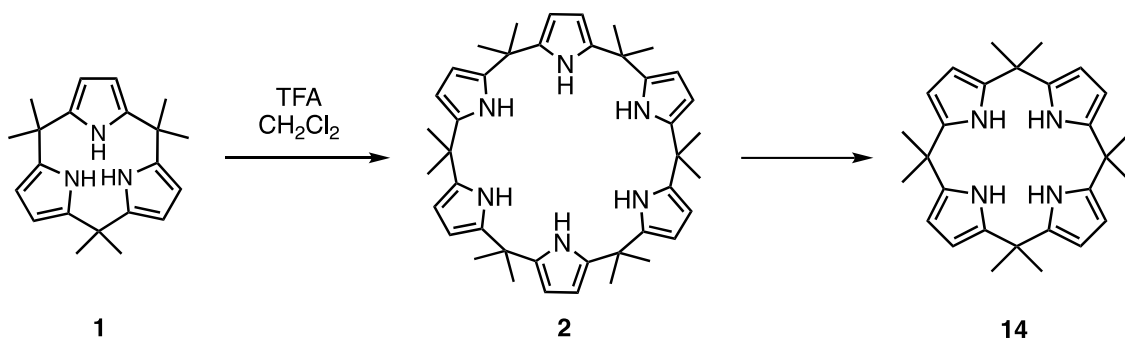


Figure 2-3. (a) Definition of calculated energy per repeating units and (b) plot of energy per repeating units against the number of repeating units.

2.4. Ring Expansion Reaction of Calix[3]pyrrole

Having achieved the synthesis of calix[3]pyrrole **1**, it was next investigated what happens when **1** is subjected to the conditions that is used for the condensation reaction of pyrrole and carbonyl compound. **1** was dissolved in dichloromethane and trifluoroacetic acid was added (traditional porphyrin synthesis conditions¹⁰) and monitored by HPLC and ¹H NMR spectroscopy. Surprisingly, **1** disappeared 10 seconds after the addition of trifluoroacetic acid, and the quantitative formation of another compound was observed. Analysis of the HPLC chromatogram and ¹H NMR spectrum revealed that the newly observed compound was calix[6]pyrrole **2** (Figure 2-4, 2-5). Continuous monitoring of the reaction revealed further conversion of **2** to another different compound. Again the HPLC chromatogram and ¹H NMR spectrum were measured to show that the final product was calix[4]pyrrole **14**. As a result, it was found that when calix[3]pyrrole **1** was placed under acidic conditions, a rapid ring expansion reaction proceeded to give double-sized macrocycle, calix[6]pyrrole **2**, as the kinetic product, and then **2** underwent scrambling reaction to give calix[4]pyrrole **14** (Scheme 2-3) as the thermodynamically favored product.



Scheme 2-3. Ring expansion reaction of **1**.

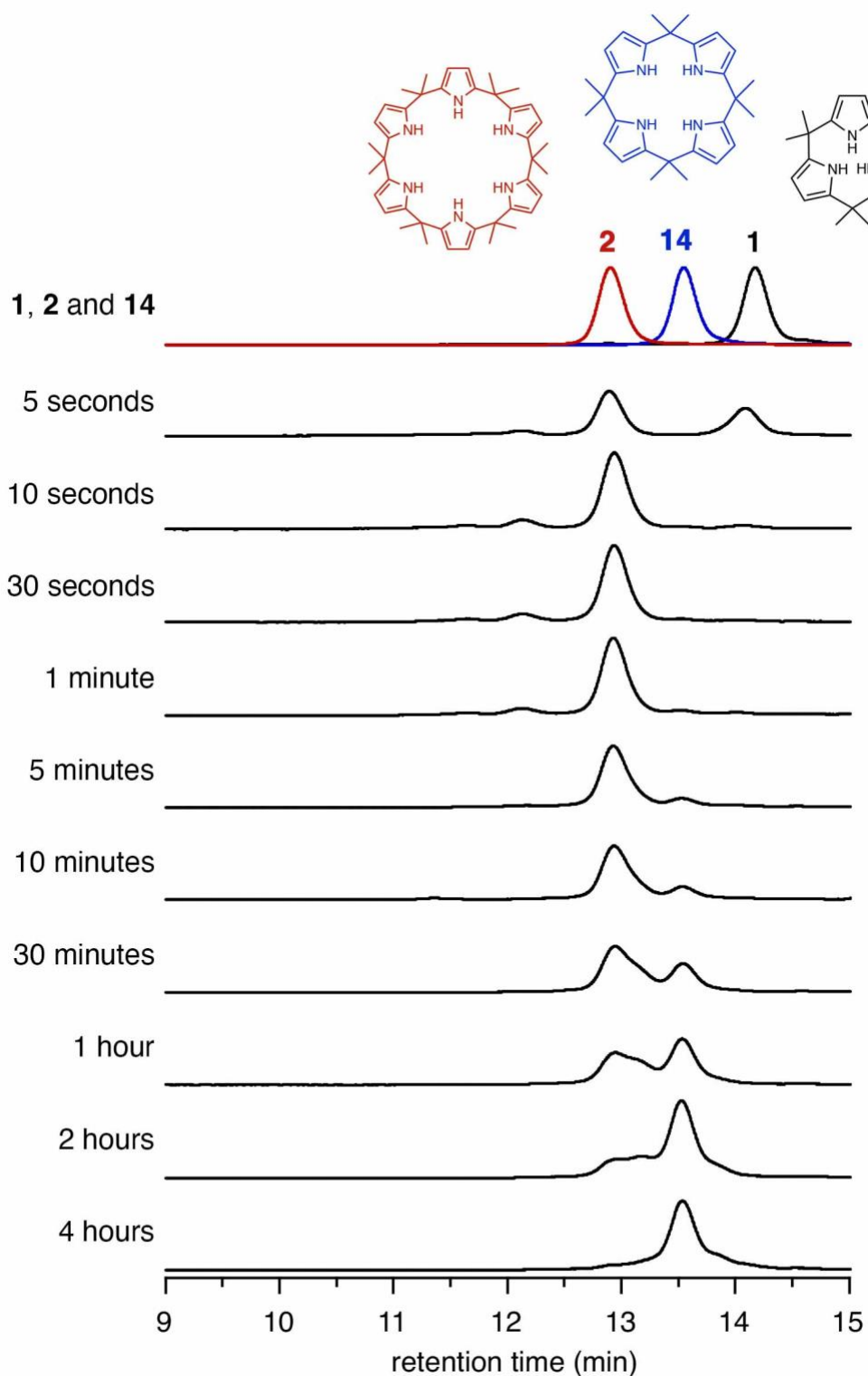


Figure 2-4. HPLC chromatograms corresponding to the ring expansion reaction of **1** by TFA in dichloromethane (Column: TOSOH TSKgel G2000HXL×2, mobile phase: chloroform, detection: absorption at 245 nm, flow rate: 1.0 mL/min).

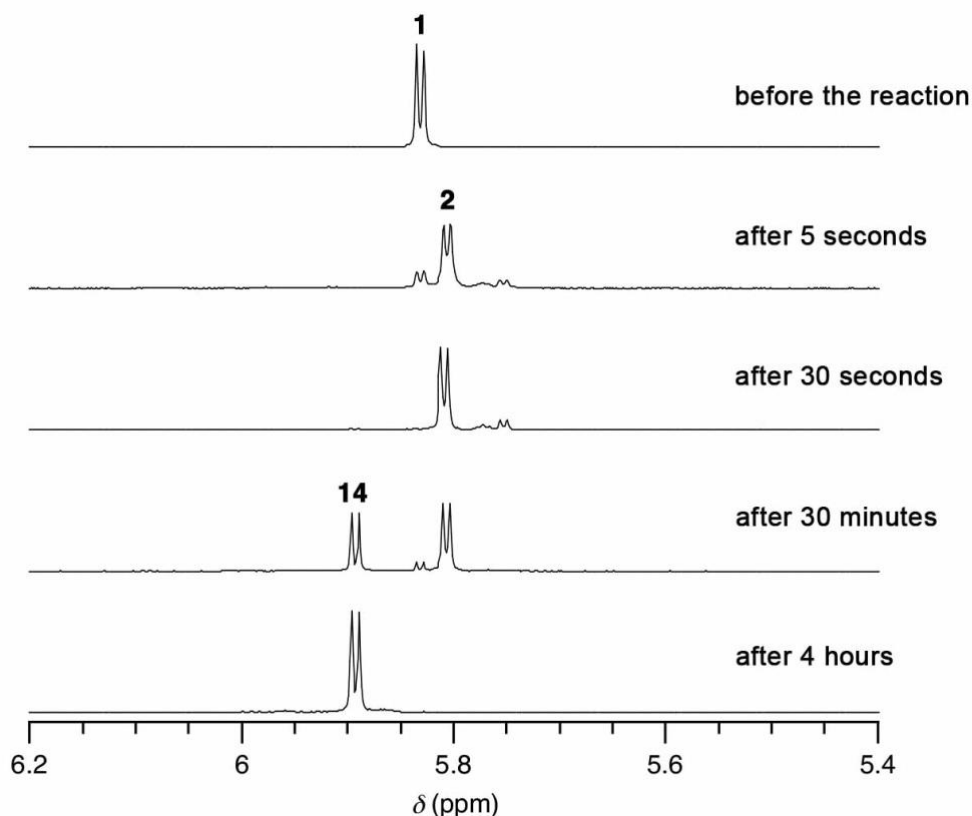


Figure 2-5. ^1H NMR spectra corresponding to the ring expansion reaction of **1** by TFA in dichloromethane (chloroform-*d*, 400 MHz, 298 K).

The same reaction was observed when **1** was exposed to hydrochloric acid in ethanol, a conventional calix[4]pyrrole synthesis conditions¹¹. Reaction monitoring confirmed that calix[3]pyrrole **1** underwent a rapid ring expansion reaction to give **2**, and further transformation to give **14** (**Figure 2-6**). To this end, calix[3]pyrrole **1** was found to undergo a rapid ring expansion reaction under acidic conditions to give calix[6]pyrrole **2**, which was then transformed to calix[4]pyrrole **14**. This reactivity, as well as the large macrocyclic strain, may be the reason why the tripyrrolic macrocycle has never been found under traditional acid-catalyzed condensation reaction conditions. Calix[3]pyrrole **1** is unfavorable to be formed due to its strain, and it will immediately undergo a ring expansion reaction even if it is formed.

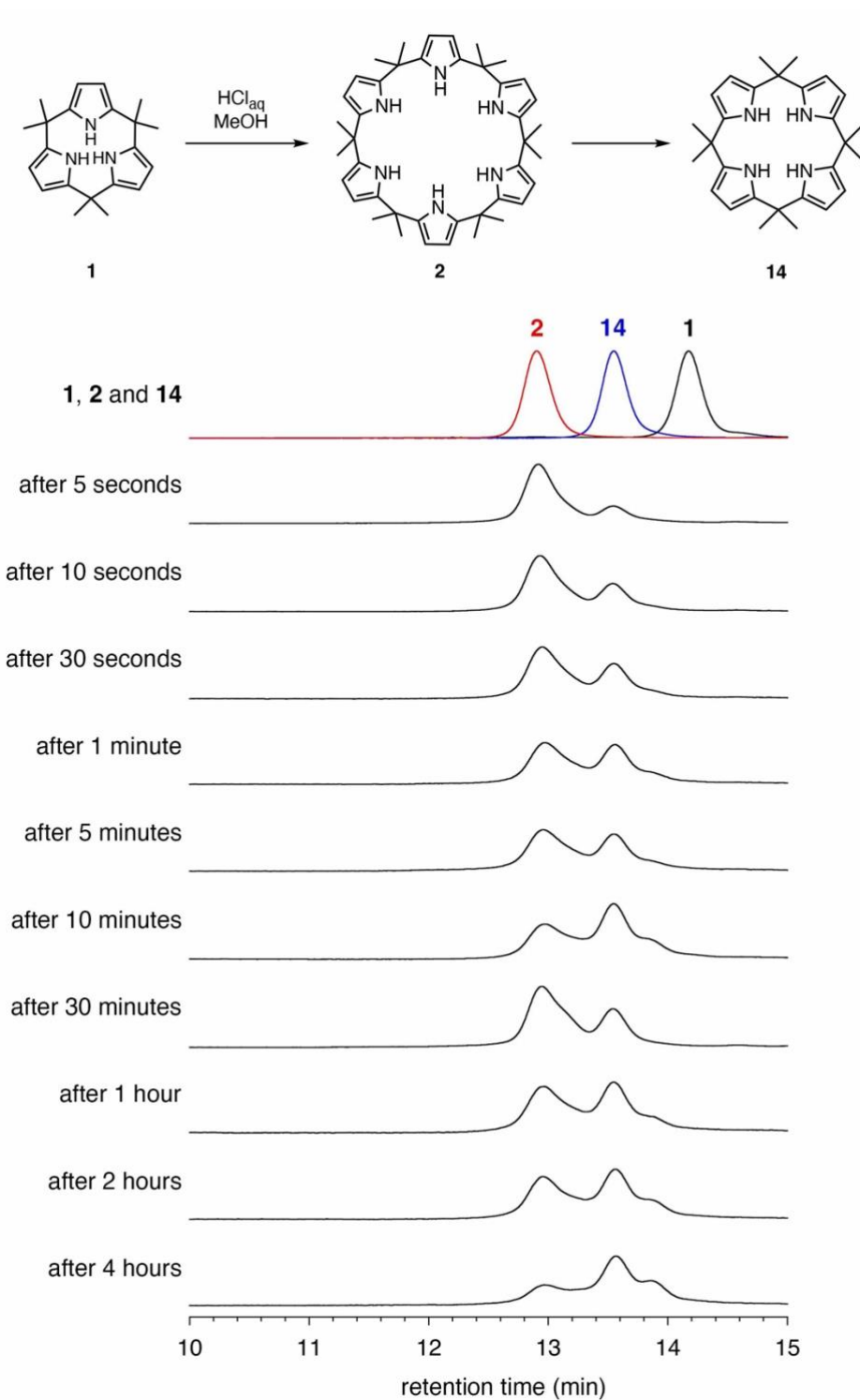


Figure 2-6. HPLC chromatograms corresponding to the ring expansion reaction of **1** by hydrochloric acid in ethanol (Column: TOSOH TSKgel G2000HXL \times 2, mobile phase: chloroform, detection: absorption at 245 nm, flow rate: 1.0 mL/min).

2.5. Anion Binding Ability of Calix[3]pyrrole

Next, the anion binding ability of calix[3]pyrrole **1** was investigated because calix[*n*]pyrroles ($n = 4 - 6$) have been reported to bind anions^{2,12,13}. Ring size is an important factor for macrocyclic supramolecular hosts. When tetra-*n*-butylammonium fluoride (TBAF) was added to the dichloromethane solution of **1**, a peak shift was observed in the ¹H NMR spectrum (**Figure 2-7a**). Further addition of TBAF resulted in a further shift of the peaks, indicating that **1** and TBAF interact in fast equilibrium. In Job's plot analysis^{14,15}, the shift of the NH proton signal was maximal when **1**: TBAF = 1:1, suggesting 1:1 complexation (**Figure 2-7b**). The association constant was calculated to be $230 \pm 20 \text{ M}^{-1}$ from titration experiment using increasing amounts of TBAF in dichloromethane-*d*₂ and non-linear curve fitting with the 1:1 association model^{14,15} (**Figure 2-7c**). Single crystal of **1**-TBAF complex was obtained by slow evaporation of dichloromethane solution of **1** in the presence of excess amount of TBAF. Single crystal X-ray diffraction analysis of **1**-TBAF revealed that **1** interacts with the fluoride anion using all three pyrrole NHs by adopting a cone conformation in which all pyrrole nitrogens are directed toward the one fluoride anion (**Figure 2-8**).

Association constants with chloride, bromide, and iodide were also determined using tetra-*n*-butylammonium (TBA) salts (**Table 2-1**). The association constant with TBACl was calculated to be $9.2 \pm 0.2 \text{ M}^{-1}$, much smaller than that with TBAF. The association constants became smaller with increasing anion size, $1.9 \pm 0.4 \text{ M}^{-1}$ with TBABr and $< 1 \text{ M}^{-1}$ with TBAI. Since the coordination site of calix[3]pyrrole is very small, the radius of chloride, bromide, and iodide anions may be too large to coordinate effectively.

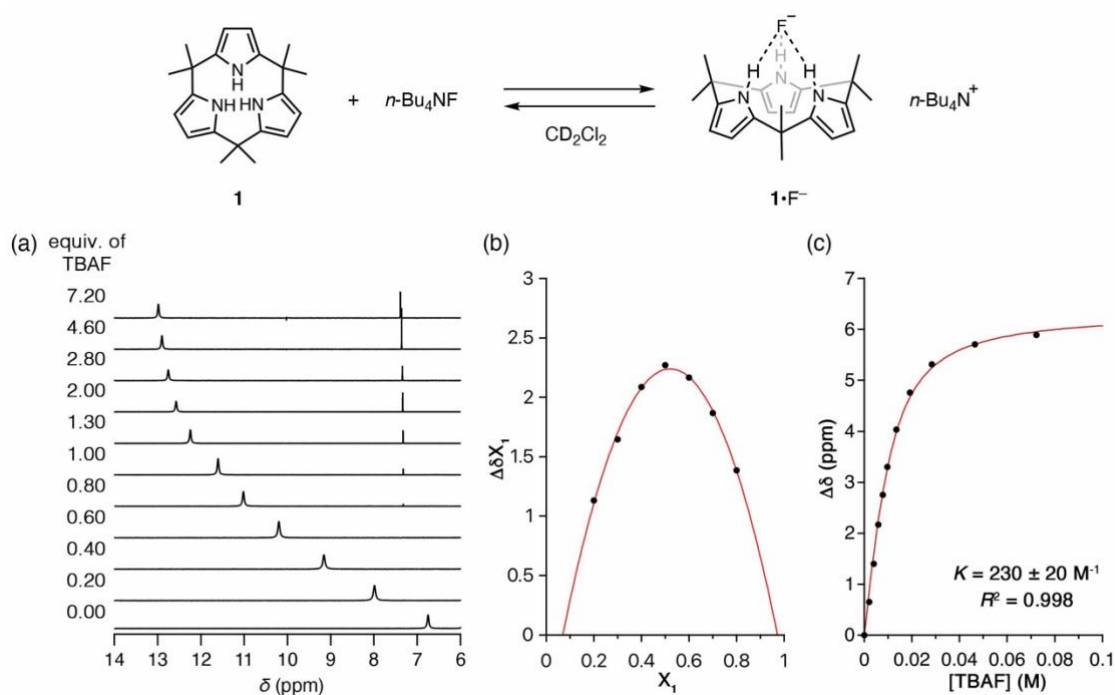


Figure 2-7. Fluoride anion binding by calix[3]pyrrole **1**. (a) ^1H NMR spectra of **1** in 6.0 mM dichloromethane- d_2 solution titrated with TBAF (from 0.0 to 7.2 equivalent), (b) Job's plot analysis between **1** and TBAF, where $[\mathbf{1}] + [\text{TBAF}] = 10.0 \text{ mM}$ and $X_1 = [\mathbf{1}]/([\mathbf{1}] + [\text{TBAF}])$, and (c) non-linear curve fitting analysis of the chemical shift changes for the NH protons of **1** with the addition of TBAF.

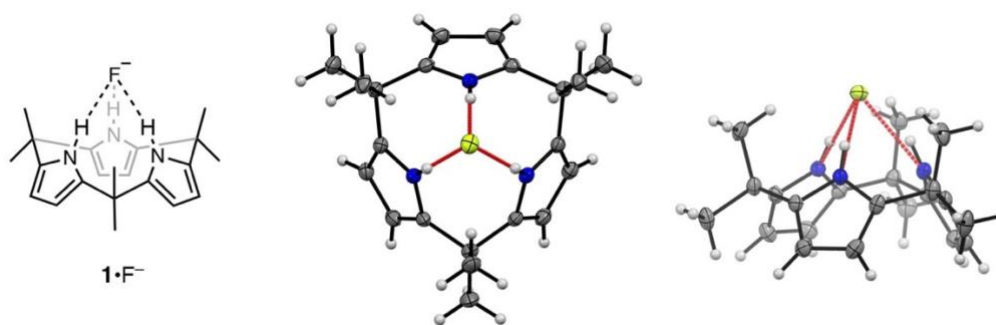


Figure 2-8. Crystal structure of **1**-TBAF complex. Counter cation and solvent molecule are omitted for clarity (C: gray, H: white, N: blue, O: red, F: yellow green).

Table 2-1. Association constants for calix[*n*]pyrroles with tetra-*n*-butylammonium halides in CD₂Cl₂.

anion	association constant (M ⁻¹)			
	calix[3]pyrrole 1	calix[4]pyrrole 14^a	calix[5]pyrrole 15^b	calix[6]pyrrole 2^c
F	230 ± 20	17170 ± 900	14000 ± 821	~3.2 × 10 ⁵ ^e
Cl	9.2 ± 0.2	350 ± 5.5	35 ± 3	1.2 × 10 ⁴ ± 10 ³ ^f
Br	1.9 ± 0.4	10 ± 0.5	– ^d	710 ± 25
I	< 1	< 10	– ^d	– ^d

^a reference 12. ^b reference 13. ^c reference 2. ^d Not reported. ^e Determined by a competition experiment using calix[4]pyrrole **14** as a competitor. ^f Determined with the Cram extraction method using D₂O/CD₂Cl₂ at 289 K.¹³

2.6. Conclusion

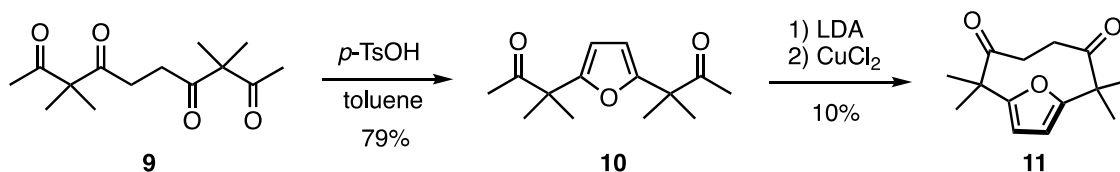
In conclusion, the synthesis of calix[3]pyrrole was achieved by Paal-Knorr pyrrole formation reaction-based strategy using cyclic hexaketone as a precursor. Calix[3]pyrrole has much larger strain compared with calix[4]pyrrole, calix[5]pyrrole, and calix[6]pyrrole, and the strain led to unique ring expansion reaction under acidic conditions, which were adopted as traditional oligopyrrole synthesis conditions. This strain and the ring expansion reaction under acidic conditions were found to be the reason why tripyrrolic macrocycles were not found in oligopyrrole macrocycle synthesis, which selectively provides tetrapyrrolic macrocycles selectively. Although the anion binding ability of calix[3]pyrrole is lower than that of the known calixpyrroles, the difference in anion binding ability can be applied to the switching of anion affinity during the ring expansion reaction. In addition, this rapid and high-yield ring expansion reaction would provide a new approach to large macrocyclic systems that are difficult to access with current methods.

2.7. Experimental Section

2.7.1. Reagents and Equipment

Solvents and reagents were purchased from FUJIFILM WAKO Pure Chemical Corporation, TCI Co., Ltd., Kanto Chemical Co., Inc., or Sigma-Aldrich Co., and used without further purification unless otherwise mentioned. Compounds **7** and **9** were prepared according to a reported procedure.^{3,8} All ¹H, ¹³C, and ¹¹B NMR spectra were recorded using JEOL JMN-ECS400 spectrometer and chemical shifts were reported in parts per million (ppm) relative to an internal standard tetramethylsilane ($\delta = 0.00$ ppm for ¹H NMR in CDCl₃), a solvent residual peak ($\delta = 5.32$ ppm for ¹H NMR in CD₂Cl₂ and $\delta = 77.16$ ppm for ¹³C NMR in CDCl₃), or an external standard BF₃•OEt₂ ($\delta = 0.00$ ppm for ¹¹B NMR). Infrared spectra were measured using a JASCO Co. FT/IR-4600. ESI-TOF-MS spectra were recorded on a Thermo Scientific Executive spectrometer. Elemental analyses were carried out using an Exceter Analytical, Inc. CE440 or MICRO CORDER JM10. Thin layer chromatography was performed on a silica gel sheet, MERCK silica gel 60 F254. Preparative scale separations were performed by means of gravity column chromatography over silica gel (Wakosil® 60. 64 ~ 210 μ m). Analytical HPLC chromatograms were recorded using a JASCO MD-2018 photodiode array detector quipped with a JASCO PU-2089 pump, JASCO AS-2059 sampler, JASCO CO-2060 column thermostat. Single crystal X-ray diffraction data were obtained using Rigaku XtaLAB P200 diffractometer equipped with a PILATUS200K detector, which uses a multilayer mirror (MoK α radiation $\lambda = 0.71073$ Å or CuK α radiation $\lambda = 1.54184$ Å) or a Rigaku XtaLAB Synergy-R/DW instrument equipped with a HyPix-6000HE detector, which uses a monochromated mirror. All structures were solved using a dual-space algorithm (SHELXT) and refined using full-matrix least-squares method (SHELXL).^{16,17}

2.7.2. Model reaction for the cyclization of oligoketone



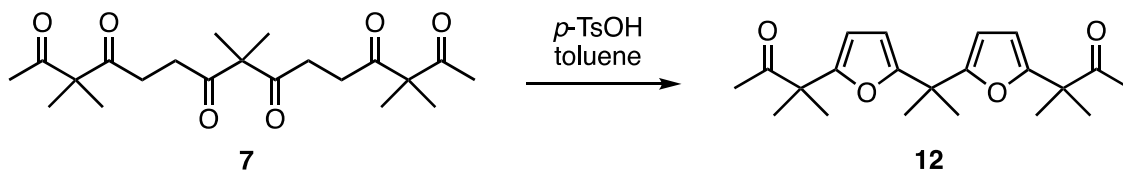
The cyclization of tetraketone **9** was found to be possible after formation of furan at 1,4-diketone moiety. The linear furan compound **10** was prepared according to the reported procedure.⁸ Cyclization of **10** was performed as follows.

In a 500 mL three-neck flask equipped with a dropping funnel and nitrogen gas inlet/outlet, a solution of lithium diisopropylamide (2.0 M in THF/heptane/ethylbenzene, 35.0 mL, 70.0 mmol) was cooled to -78 °C under N₂ atmosphere. A solution of compound **10** (5.00 g, 21.2 mmol) in anhydrous tetrahydrofuran (105 mL) was added dropwise using a dropping funnel over 15 min while keeping the solution temperature at -78 °C. After 15 min of stirring, a solution of copper(II) chloride (9.41 g, 70.0 mmol) in anhydrous *N,N*-dimethylformamide (154 mL) was added all at once. The reaction mixture was stirred for 1 h at -78 °C in a cooling bath, and then allowed to reach room temperature. The reaction was quenched by adding a 3% aqueous solution of hydrochloric acid (200 mL), transferred to a separatory funnel, and extracted with diethyl ether (250 mL × 3). The combined organic layer was washed with a 3% aqueous solution of hydrochloric acid (250 mL × 2) and dried over anhydrous sodium sulfate. After evaporation under reduced pressure, the crude product was purified by silica gel column chromatography (column diameter: 5.0 cm, height: 15 cm, eluent: Ethyl acetate/hexane = 1/10) to give furanophane **11** (592 mg, 2.52 mmol, 12% yield) as white solids

Characterization data for **11**

¹H NMR (400 MHz, CDCl₃, 298 K): δ = 6.27 (s, 2H, furyl), 2.17 (s, 4H, ethylene), 1.44 ppm (s, 12H, dimethylmethylene); ¹³C NMR (100 MHz, CDCl₃, 298 K): δ = 209.9, 158.8, 110.3, 51.2, 34.5, 21.4 ppm; IR (ATR, neat): 2923, 2867, 2851, 1712, 1693, 1457, 1259, 1029, 1015 cm⁻¹; mp: 86-91 °C; HRMS (ESI): *m/z* calcd. for C₁₄H₁₈O₃+Na⁺: 257.1148 [M+Na]⁺, found: 257.1148; elemental analysis (%) calcd. for C₁₄H₁₈O₃: C 71.77, H 7.74, N 0.00, found: C 71.75, H 7.82, N 0.02; *R*_f = 0.30 (silica gel, ethyl acetate/hexane = 1/10).

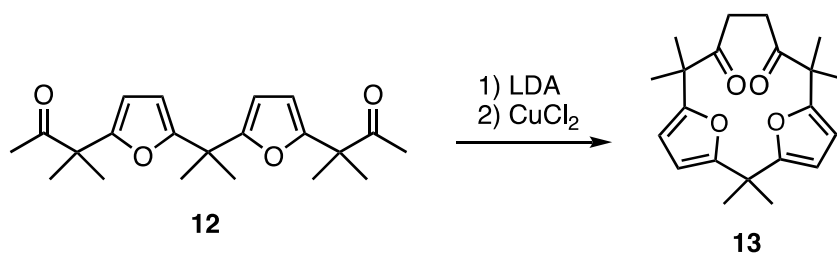
2.7.3. Synthesis of compound 12



In a 1.0 L round-bottomed flask equipped with a Dean-Stark apparatus, compound **7** (10.0 g, 26.3 mmol) and *p*-toluenesulfonic acid monohydrate (1.99 g, 10.5 mmol) were dissolved in toluene (400 mL) and heated to reflux for 5 h with azeotropic water removal. After cooling to room temperature, the reaction mixture was added to a saturated aqueous solution of sodium bicarbonate (400 mL) and transferred to a separatory funnel. The aqueous layer was extracted using toluene (400 mL \times 2), and the combined organic layer was washed with water (600 mL) and dried over anhydrous sodium sulfate. After concentration under reduced pressure, the mixture was purified using silica gel column chromatography (column diameter: 6.0 cm, height: 15 cm, eluent: hexane/ethyl acetate = 15/1) to give compound **12** (7.00 g, 77% yield) as an oil.

^1H NMR (400 MHz, CDCl_3 , 298 K): δ = 6.06 (d, 3J = 3.2 Hz, 2H, furyl), 5.94 (d, 3J = 3.2 Hz, 2H, furyl), 1.92 (s, 6H, acetyl), 1.58 (s, 6H, dimethylmethylene), 1.40 ppm (s, 12H, dimethylmethylene); ^{13}C NMR (100 MHz, CDCl_3 , 298 K): δ = 209.7, 159.5, 156.5, 105.9, 104.9, 49.2, 37.5, 26.3, 25.6, 23.2 ppm; IR (ATR, neat): 978, 2936, 2872, 1712, 1353, 1132, 1111, 1022, 956, 787 cm^{-1} ; HRMS (ESI): m/z calcd. for $\text{C}_{21}\text{H}_{28}\text{O}_4 + \text{Na}^+$: 367.1880 [$M + \text{Na}$] $^+$, found: 367.1880; elemental analysis (%) calcd. for $\text{C}_{21}\text{H}_{28}\text{O}_4$: C 73.23, H 8.19, N 0.00, found: C 73.16, H 8.26, N 0.00; R_f = 0.16 (silica gel, hexane/ethyl acetate = 15/1).

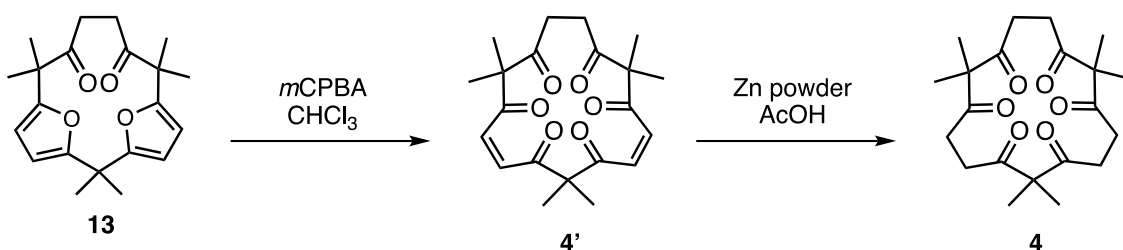
2.7.4. Synthesis of compound 10



In a 300 mL three-neck flask equipped with a dropping funnel, rubber septum, and an inert gas inlet/outlet, a solution of freshly distilled diisopropylamine (2.97 mL, 20.0 mmol) in anhydrous tetrahydrofuran (10 mL) was cooled to -78°C under N_2 atmosphere. 7.70 mL of *n*-butyllithium (2.6 M in *n*-hexane) was slowly added to the solution using a syringe. After stirring for 15 min, a solution of compound **12** (2.0 g, 5.8 mmol) in anhydrous tetrahydrofuran (58 mL) was added dropwise using a dropping funnel over 15 min while keeping the solution temperature at -78°C . After 15 min of stirring, a solution of copper(II) chloride (2.35 g, 17.5 mmol) in anhydrous *N,N*-dimethylformamide (84 mL) was added all at once. The reaction mixture was stirred for an hour at -78°C in a cooling bath, and then allowed to reach room temperature. The reaction was quenched by adding a 3% aqueous solution of hydrochloric acid (100 mL), transferred to a separatory funnel, and extracted with diethyl ether (100 mL \times 3). The combined organic layer was washed with a 3% aqueous solution of hydrochloric acid (50 mL \times 2) and dried over anhydrous sodium sulfate. After concentration under reduced pressure, the crude product was purified by silica gel column chromatography (column diameter: 4.5 cm, height: 12 cm, eluent: hexanes/dichloromethane = 1/1) to give compound **13** (830 mg, 42% yield) as a white solid.

^1H NMR (400 MHz, CDCl_3 , 298 K): δ = 6.08 (d, overlapping, 4H, furyl), 2.28 (s, 4H, ethylene), 1.57 (s, 6H, dimethylmethylene), 1.35 ppm (s, 12H, dimethylmethylene); ^{13}C NMR (100 MHz, CDCl_3 , 298 K): δ = 212.1, 159.8, 157.4, 106.0, 104.9, 49.5, 37.5, 32.8, 26.1, 22.8 ppm; IR (ATR, neat): 2971, 2936, 2871, 1708, 1555, 1023, 954, 787 cm^{-1} ; mp: 206-210 $^{\circ}\text{C}$; HRMS (ESI): m/z calcd. for $\text{C}_{21}\text{H}_{26}\text{O}_4+\text{Na}^+$: 365.1723 [$M+\text{Na}$] $^+$, found: 365.1720; elemental analysis (%) calcd. for $\text{C}_{21}\text{H}_{26}\text{O}_4$: C 73.66, H 7.65, N 0.00, found: C 73.42, H 7.66, N 0.03; R_f = 0.20 (silica gel, hexane/dichloromethane = 1/1).

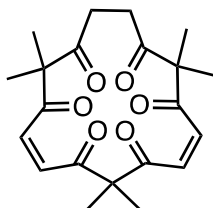
2.7.5. Synthesis of compound 4



In a 300 mL round-bottomed flask, cyclic difuran **13** (1.50 g, 4.38 mmol) was dissolved in chloroform (150 mL) and cooled at 0 °C using cooling bath. *meta*-Chloroperbenzoic acid (5.37 g, 21.8 mmol, 70% in water) was added to the solution and the reaction mixture was stirred at 0 °C. After 2 days of stirring, the reaction was quenched by adding a saturated aqueous solution of sodium bicarbonate (75 mL) followed by the addition of a saturated aqueous solution of sodium thiosulfate (75 mL). The organic layer was separated off and washed with a saturated aqueous solution of sodium bicarbonate (75 mL \times 3) and dried over anhydrous sodium sulfate. Evaporation of the solvent under reduced pressure gave crude **4'** that was used for the next reaction without further purification.

The crude **4'** was placed in 300 mL round-bottomed flask and dissolved in acetic acid (150 mL). To the solution, zinc powder (7.36 g, 113 mmol) was added. The resulting suspension was stirred for 40 min at room temperature. The reaction mixture was then filtered with suction and the solid residue on the funnel was washed with chloroform (75 mL) to remove insoluble materials. The filtrate was then poured into water (150 mL) and extracted with chloroform (75 mL \times 3). The combined organic layer was washed with a saturated aqueous solution of sodium bicarbonate (75 mL \times 5) and dried over anhydrous sodium sulfate. After concentrated under reduced pressure, the crude mixture was dissolved in hot ethanol (25 mL) and then cooled at 0 °C. The precipitated crystals were collected using suction filtration. The crystals on the funnel were further washed with cold ethanol (3 mL) and air-dried on the funnel to give compound **4** (471 mg, 28% yield from **13**) as colorless crystals.

Characterization data for 4'

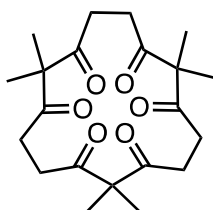


4'

For the characterization of 4', an analytical sample was obtained by silica gel column chromatography.

^1H NMR (400 MHz, CDCl_3 , 298 K): δ = 6.66 (d, 3J = 11.78 Hz, 2H, vinyl), 6.46 (d, 3J = 11.78, 2H, vinyl), 2.67 (s, 4H, ethylene), 1.48 (s, 6H, dimethylmethylene), 1.39 ppm (s, 12H, dimethylmethylene); ^{13}C NMR (100 MHz, CDCl_3 , 298 K): δ = 208.6, 201.3, 200.3, 137.0, 132.3, 62.8, 61.4, 34.5, 22.9, 20.9 ppm; IR (ATR, neat): 3054, 3037, 3008, 2979, 2942, 1693, 1671 cm^{-1} ; mp: 128-135 $^\circ\text{C}$; HRMS (ESI): m/z calcd. for $\text{C}_{21}\text{H}_{26}\text{O}_6+\text{Na}^+$: 397.1622 [$M+\text{Na}$] $^+$, found: 397.1620; elemental analysis (%) calcd. for $\text{C}_{21}\text{H}_{26}\text{O}_6$: C 67.36, H 7.00, N 0.00, found: C 67.04, H 6.99, N 0.05; R_f = 0.20 (silica gel, hexane/ethyl acetate = 3/1).

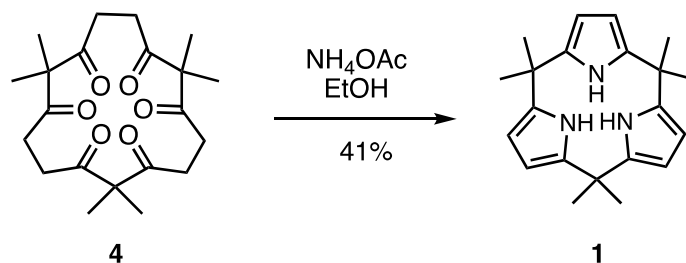
Characterization data for 4



4

^1H NMR (400 MHz, CDCl_3 , 298 K): δ = 6.66 (d, 3J = 11.78 Hz, 2H, vinyl), 6.46 (d, 3J = 11.78, 2H, vinyl), 2.67 (s, 4H, ethylene), 1.48 (s, 6H, dimethylmethylene), 1.39 ppm (s, 12H, dimethylmethylene); ^{13}C NMR (100 MHz, CDCl_3 , 298 K): δ = 209.7, 62.2, 33.7, 21.0 ppm; IR (ATR, neat): 2981, 2973, 2933, 1697, 1685, 1055, 1033 cm^{-1} ; mp: 182-185 $^\circ\text{C}$; HRMS (ESI): m/z calcd. for $\text{C}_{21}\text{H}_{30}\text{O}_6+\text{Na}^+$: 401.1935 [$M+\text{Na}$] $^+$, found: 401.1929; elemental analysis (%) calcd. for $\text{C}_{21}\text{H}_{30}\text{O}_6$: C 66.65, H 7.99, N 0.00, found: C 66.51, H 8.02, N 0.04; R_f = 0.15 (silica gel, hexane/ethyl acetate = 3/1).

2.7.6. Synthesis of calix[3]pyrrole **1**



In a 50 mL round-bottomed flask equipped with a reflux condenser, compound **4** (500 mg, 1.32 mmol) and ammonium acetate (6.10 g, 79.2 mmol) were dissolved in ethanol (10.0 mL), and heated at 90 °C in an oil bath for 1.5 h. After cooling to room temperature, the reaction mixture was diluted with chloroform (25 mL) and poured into water (50 mL). The aqueous layer was extracted with chloroform (25 mL \times 3), and the combined chloroform layer was washed with a saturated aqueous solution of sodium bicarbonate (25 mL \times 2) and dried over anhydrous sodium sulfate. After concentration under reduced pressure, the crude reaction mixture was purified using silica gel column chromatography (column diameter: 3.5 cm, height: 15 cm, eluent: hexanes/dichloromethane = 1/1) to give **1** (175 mg, 41% yield) as a colorless solid.

^1H NMR (400 MHz, CDCl_3 , 298 K): δ = 6.71 (brs, 3H, N-H), 5.83 (d, 4J = 2.8 Hz, 6H, pyrrolyl), 1.59 ppm (s, 18H, dimethylmethylene); ^{13}C NMR (100 MHz, CDCl_3 , 298 K): δ = 142.2, 103.6, 37.2, 26.7 ppm; IR (ATR, neat): 3443, 3419, 3402, 3346, 2986, 2925, 2867, 1230, 1034, 754 cm^{-1} ; mp: 120-125 °C; HRMS (ESI): m/z calcd. for $\text{C}_{21}\text{H}_{27}\text{N}_3\text{-H}^+$: 320.2132 [M-H] $^-$, found: 320.2131; R_f = 0.23 (silica gel, hexane/dichloromethane = 1/1).

2.7.7. Single crystal X-ray diffraction analyses

Crystallographic data for **11**

Single crystals of **11** suitable for X-ray diffraction analysis were obtained by slow evaporation of a *n*-hexane solution of **11**.

C₁₄H₁₈O₃, *M* = 234.28, crystal size: 0.62 × 0.36 × 0.20 mm³, monoclinic, space group *P*2₁/*n*, *a* = 11.3044(4), *b* = 8.8083(3), *c* = 13.4649(6) Å, β = 112.723(5)°, *V* = 1236.67(9) Å³, *Z* = 4, *T* = 123(2) K, μ = 0.087 mm⁻¹, *D*_{calc} = 1.258 g/cm³, 2.835° ≤ θ ≤ 26.491°, 2364 unique reflections out of 2548 with *I* > 2σ(*I*), GOF = 1.061, *R*₁ = 0.0372, *wR*₂ = 0.0935, CCDC: 2223944

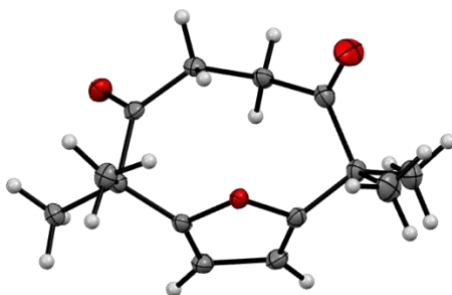


Figure 2-9. ORTEP drawing of the crystal structure of **11** at the 50% thermal probability levels (C: gray, H: white, O: red).

Crystallographic data for 13

Single crystals suitable for X-ray diffraction analysis were grown by vapor diffusion of hexanes into a dichloromethane solution of **13**.

$C_{21}H_{26}O_4$, $M = 342.42$, crystal size: $0.70 \times 0.08 \times 0.05 \text{ mm}^3$, monoclinic, space group $P2_1/c$, $a = 9.5315(4)$, $b = 17.0958(6)$, $c = 11.4593(4) \text{ \AA}$, $\alpha = \gamma = 90$, $\beta = 102.900(4)^\circ$, $V = 1820.15(12) \text{ \AA}^3$, $Z = 4$, $T = 123(2) \text{ K}$, $\mu = 0.085 \text{ mm}^{-1}$, $D_{\text{calc}} = 1.250 \text{ g/cm}^3$, $2.178^\circ \leq \theta \leq 26.497^\circ$, 3246 unique reflections out of 3770 with $I > 2\sigma(I)$, GOF = 1.046, $R_1 = 0.0343$, $wR_2 = 0.0901$, CCDC: 2080602

Crystallographic data for 4'

Single crystals suitable for X-ray diffraction analysis were grown by vapor diffusion of hexanes into a dichloromethane solution of **4'**.

$C_{21}H_{26}O_6$, $M = 374.42$, crystal size: $0.50 \times 0.33 \times 0.14 \text{ mm}^3$, triclinic, space group $P-1$, $a = 8.9992(2)$, $b = 10.9621(3)$, $c = 11.1990(3) \text{ \AA}$, $\alpha = 68.633(3)$, $\beta = 85.440(2)$, $\gamma = 69.242(2)^\circ$, $V = 960.50(5) \text{ \AA}^3$, $Z = 2$, $T = 123(2) \text{ K}$, $\mu = 0.094 \text{ mm}^{-1}$, $D_{\text{calc}} = 1.295 \text{ g/cm}^3$, $1.956^\circ \leq \theta \leq 25.242^\circ$, 3593 unique reflections out of 4151 with $I > 2\sigma(I)$, GOF = 1.050, $R_1 = 0.0346$, $wR_2 = 0.0869$, CCDC: 2080603

Crystallographic data for 4

Single crystals of **4** suitable for X-ray diffraction analysis were obtained by recrystallization from ethanol.

$C_{21}H_{30}O_6$, $M = 378.45$, crystal size: $0.60 \times 0.11 \times 0.11 \text{ mm}^3$, triclinic, space group $P-1$, $a = 10.2714(3)$, $b = 10.4682(4)$, $c = 10.5662(3) \text{ \AA}$, $\alpha = 74.552(3)$, $\beta = 74.987(2)$, $\gamma = 68.695(3)^\circ$, $V = 1003.44(6) \text{ \AA}^3$, $Z = 2$, $T = 123(2) \text{ K}$, $\mu = 0.091 \text{ mm}^{-1}$, $D_{\text{calc}} = 1.253 \text{ g/cm}^3$, $2.033^\circ \leq \theta \leq 25.242^\circ$, 3618 unique reflections out of 4329 with $I > 2\sigma(I)$, GOF = 1.061, $R_1 = 0.0367$, $wR_2 = 0.0909$, CCDC: 2080604

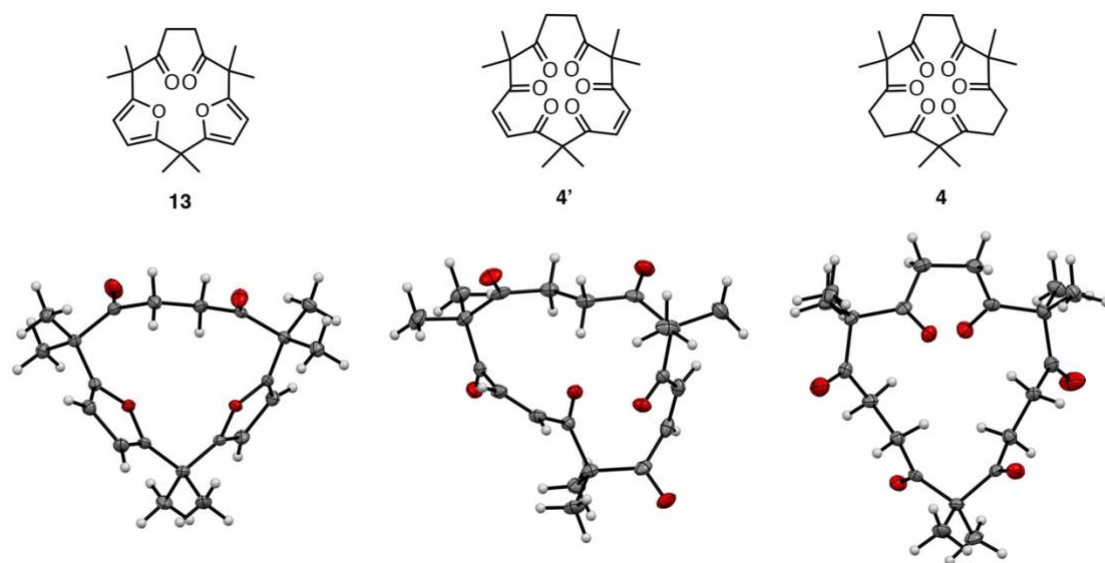


Figure 2-10. ORTEP drawing of the crystal structure of **13**, **4'**, and **4** at the 50% thermal probability levels (C: gray, H: white, O: red).

Crystallographic data for **1**

Single crystals suitable for X-ray diffraction analysis were grown by vapor diffusion of hexanes into a solution of **1** in dichloromethane that was not subject to drying; this gave crystals of the monohydrate of **1**, namely **1**•H₂O.

C₂₁H₂₇N₃•H₂O, *M* = 339.47, crystal size: 0.70 × 0.60 × 0.25 mm³, triclinic, space group *P*1, *a* = 10.3074(2), *b* = 13.1693(3), *c* = 14.4937(4) Å, α = 85.399(2), β = 81.088(2), γ = 81.505(2)°, *V* = 1919.01(8) Å³, *Z* = 4, *T* = 123(2) K, μ = 0.073 mm⁻¹, *D*_{calc} = 1.175 g/cm³, 2.019° ≤ θ ≤ 25.242°, 7129 unique reflections out of 8286 with *I* > 2σ(*I*), GOF = 1.064, *R*₁ = 0.0401, *wR*₂ = 0.1061, CCDC: 2080605

Crystallographic data for **1**-TBAF

Fluoride complex **1**-TBAF crystallized upon slow concentration of a dichloromethane solution containing calix[3]pyrrole **1** and tetra-*n*-butylammonium fluoride.

C₂₁H₂₇N₃•C₁₆H₃₆FN•CH₂Cl₂, *M* = 667.84, crystal size: 0.43 × 0.12 × 0.02 mm³, monoclinic, space group *P*2₁, *a* = 10.0875(4), *b* = 18.4506(5), *c* = 11.5037(5) Å, α = γ = 90, β = 115.734(5)°, *V* = 1928.72(14) Å³, *Z* = 2, *T* = 123(2) K, μ = 0.204 mm⁻¹, *D*_{calc} = 1.150 g/cm³, 1.965° ≤ θ ≤ 25.242°, 7595 unique reflections out of 7939 with *I* > 2σ(*I*), GOF = 1.044, *R*₁ = 0.0310, *wR*₂ = 0.0833, CCDC: 2080607

2.7.8. Deformation angles

Table 2-2. Deformation angles α and β determined from crystal structures.

Macrocycles	$\alpha/^\circ$	$\beta/^\circ$
calix[3]pyrrole 1	2.52	9.20
1 -TBAF	2.45	11.28
calix[4]pyrrole 14 ^a	0.38	1.78
calix[5]pyrrole 15 ^b	0.43	3.36
calix[6]pyrrole 2 ^c	0.41	3.59

^a reference 12, ^b reference 13, ^c reference 2.

2.7.9. Theoretical calculations

Theoretical optimization of the geometries of calix[*n*]pyrroles (*n* = 3, 4, 5, and 6) were performed using their crystal structures as the initial structures at the B3LYP/cc-pVTZ level of theory with Grimme's type dispersion.^{18,19} The average energy of each monomer unit in calix[*n*]pyrroles relative to that for calix[3]pyrrole **1** was evaluated at the same respective theory level using the equations below:

$$\Delta E_{\text{mon}} = (E_{\text{calix}[n]\text{pyrrole}} / n) - (E_{\text{calix}[3]\text{pyrrole}} / 3)$$

where ΔE_{mon} is the average relative energy of monomer unit in the calix[*n*]pyrroles, $E_{\text{calix}[n]\text{pyrrole}}$ is the energy of the calix[*n*]pyrroles, *n* is the number of monomers in the calix[*n*]pyrroles, and $E_{\text{calix}[3]\text{pyrrole}}$ is the energy of the calix[3]pyrrole **1**. All calculations were performed using Gaussian 16 Rev. C01.²⁰

2.7.10. Ring expansion reaction of **1** with TFA

HPLC analysis

To a stirred solution of calix[3]pyrrole **1** (3.3 mM, 1.5 mL) in CH₂Cl₂, trifluoroacetic acid was added as a 1.0 M CH₂Cl₂ solution (15 μL). After stirring the solution at room temperature for 5 sec, 10 sec, 30 sec, 1 min, 5 min, 10 min, 30 min, 1 h, 2 h, and 4 h, small aliquots of reaction solution were taken and immediately quenched via the addition of excess triethylamine (*ca.* 2 μL). The reaction mixtures were then analyzed by HPLC (see **Figure 2-4**).

¹H NMR spectral analysis

To a stirred solution of **1** (3.3 mM, 0.5 mL) in CH₂Cl₂, trifluoroacetic acid was added as a 1.0 M CH₂Cl₂ solution (5.0 μL). After stirring the solution for predetermined reaction time (5 sec, 30 sec, 30 min, or 4 h), the reaction was immediately quenched via the addition of a saturated aqueous solution of sodium bicarbonate. The organic phase was dried over anhydrous MgSO₄, and the solvent was evaporated off under reduced pressure. The residue was dissolved in CDCl₃ and analyzed by ¹H NMR spectroscopy (see **Figure 2-5**).

2.7.11. Ring expansion reaction of **1** with HCl

To a stirred solution of calix[3]pyrrole **1** (3.3 mM, 1.5 mL) in methanol, 12.0 M hydrochloric acid (12.6 μL) was added. After stirring the solution at room temperature for 5 sec, 10 sec, 30 sec, 1 min, 5 min, 10 min, 30 min, 1 h, 2 h, and 4 h, small aliquots of the reaction solution were removed and immediately quenched via the addition of excess triethylamine (*ca.* 20 μL). The reaction mixtures were then analyzed by HPLC (see **Figure 2-6**).

2.7.12. Anion binding experiments

General procedure for NMR spectroscopic titrations^{14,15}

For all anion-binding studies of **1** were performed in CD₂Cl₂ at 298 K. The chemical exchange between bound and unbound species proved fast compared to the NMR timescale, such that only averaged signals were observed. Thus, ¹H NMR spectral titration experiments were conducted by adding a solution of tetra-*n*-butylammonium (TBA) salt (1.0 M in CD₂Cl₂) into a solution of calix[3]pyrrole **1** (10 mM in CD₂Cl₂) in an NMR tube.

The corresponding association constants (*K*) were calculated from the changes in chemical shift of the NH proton of calix[3]pyrrole **1** using a non-linear curve-fitting method per the following equation:

$$\Delta\delta_{\text{obs}} = \frac{\Delta\delta_{\text{HG}}}{2K[\text{H}]_0} [1 + K[\text{H}]_0 + K[\text{G}]_0 - \{(1 + K[\text{H}]_0 + K[\text{G}]_0)^2 - 4K^2[\text{H}]_0[\text{G}]_0\}^{0.5}]$$

where $\Delta\delta_{\text{obs}}$ is the chemical shift change of NH proton signal of calix[3]pyrrole **1** at a salt concentration of $[\text{G}]_0$, $\Delta\delta_{\text{HG}}$ is the chemical shift change of **1** between free and completely complexed forms. $[\text{G}]_0$ is the fixed initial concentration of TBA salt, and $[\text{H}]_0$ is the initial concentration of calix[3]pyrrole **1**.

To obtain insights into the association stoichiometry, Job's plot analyses were conducted by changing the mole fractions of the calix[3]pyrrole **1** and TBAF at a total concentration of 10.0 mM. The chemical shift changes for the NH proton signals of calix[3]pyrrole **1** were used for the associated calculations.

NMR spectroscopic titration of **1** with TBACl

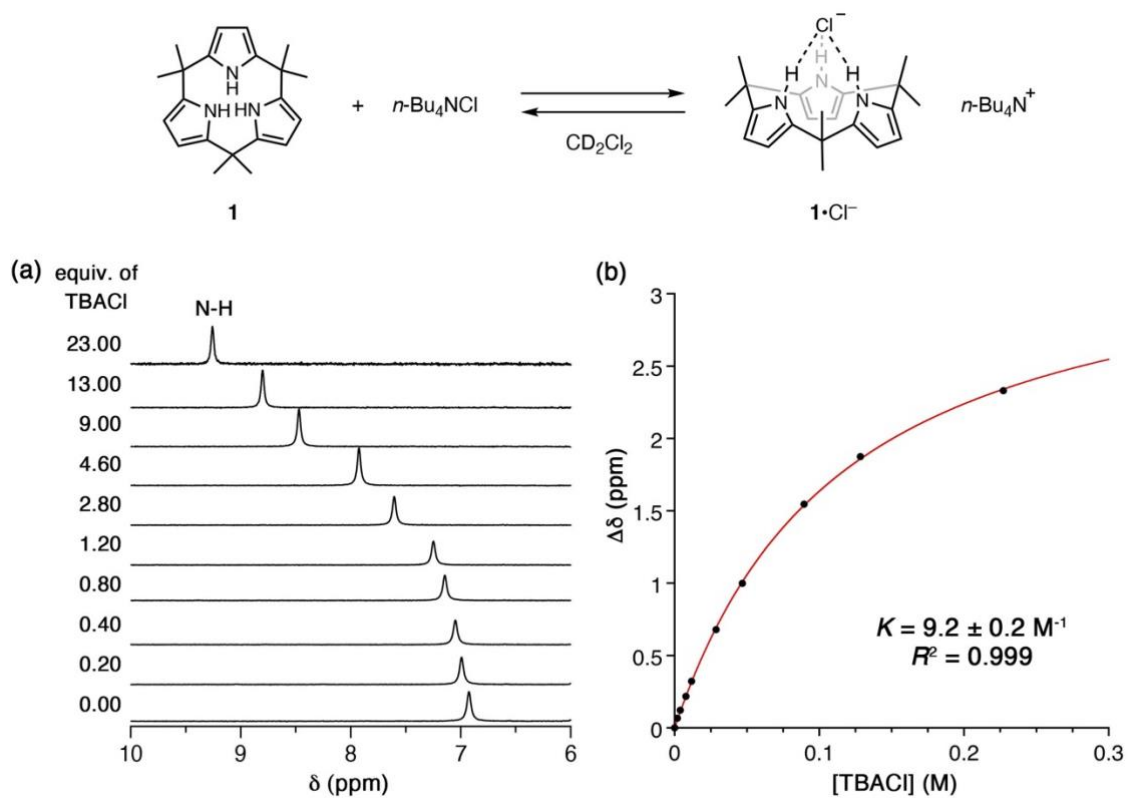


Figure 2-11. Chloride anion binding by calix[3]pyrrole **1**. (a) ^1H NMR spectra of **1** in 6.0 mM dichloromethane- d_2 solution titrated with TBACl (from 0.0 to 23.0 equivalent) and (b) non-linear curve fitting analysis of the chemical shift changes for the NH protons of **1** with the addition of TBACl.

NMR spectroscopic titration of **1** with TBABr

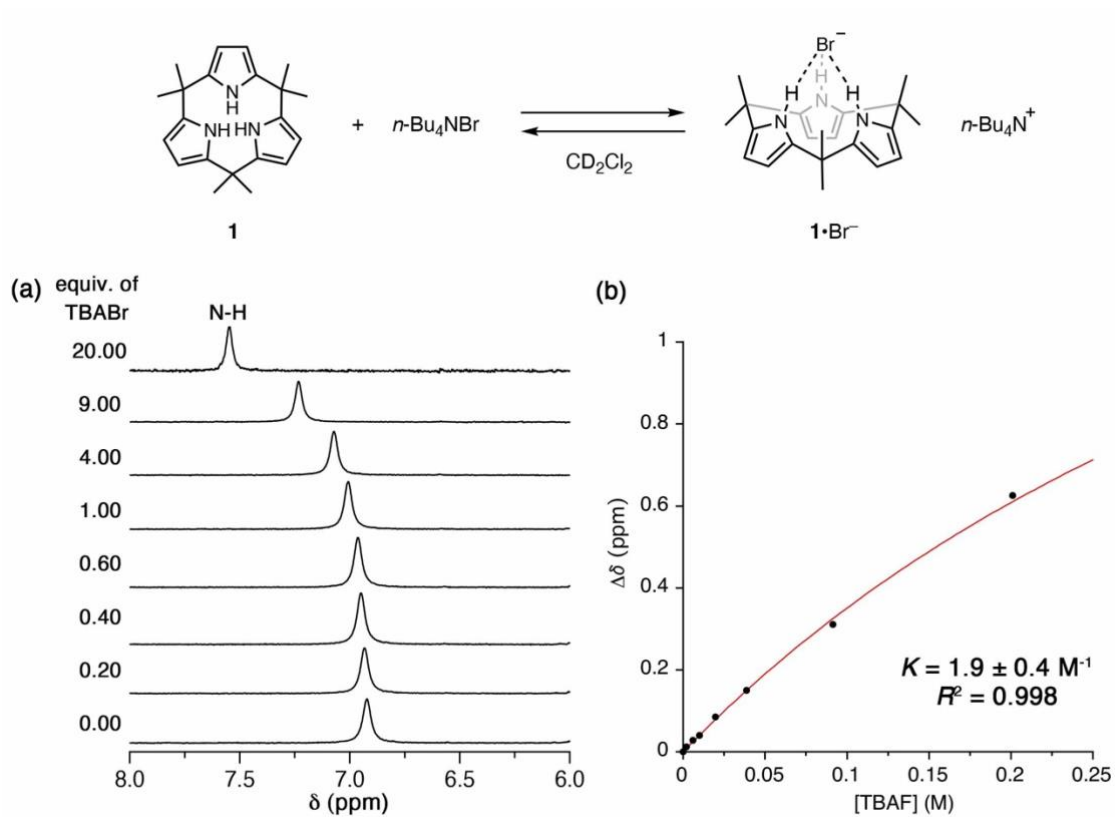


Figure 2-12. Bromide anion binding by calix[3]pyrrole **1**. (a) ^1H NMR spectra of **1** in 6.0 mM dichloromethane- d_2 solution titrated with TBABr (from 0.0 to 20.0 equivalent) and (b) non-linear curve fitting analysis of the chemical shift changes for the NH protons of **1** with the addition of TBABr.

NMR spectroscopic titration of **1** with TBAI

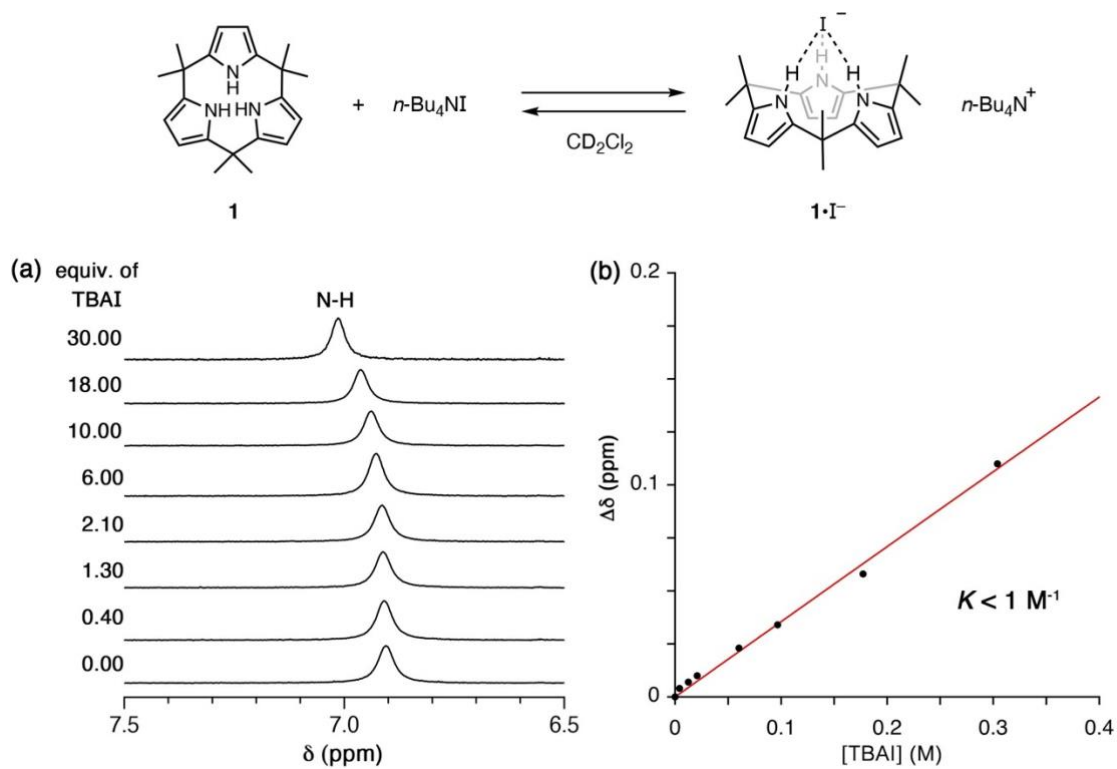


Figure 2-13. Iodide anion binding by calix[3]pyrrole **1**. (a) ¹H NMR spectra of **1** in 6.0 mM dichloromethane-*d*₂ solution titrated with TBAI (from 0.0 to 30.0 equivalent) and (b) non-linear curve fitting analysis of the chemical shift changes for the NH protons of **1** with the addition of TBAI.

2.8. References

1. G. Cafeo, F. H. Kohnke, G. L. L. Torre, M. F. Parisi, R. P. Nascone, A. J. P. White, D. J. Williams, Calix[6]pyrrole and Hybrid Calix[*n*]furan[*m*]pyrroles ($n+m=6$): Syntheses and Host–Guest Chemistry, *Chem. Eur. J.*, **2002**, *8*, 3148–3156.
2. Y. Kobuke, K. Hanji, K. Horiguchi, M. Asada, Y. Nakayama, J. Furukawa, Macrocyclic ligands composed of tetrahydrofuran for selective transport of monovalent cations through liquid membranes, *J. Am. Chem. Soc.*, **1976**, *98*, 7414–7419.
3. Y. Manabe, M. Uesaka, T. Yoneda, Y. Inokuma, Two-Step Transformation of Aliphatic Polyketones into π -Conjugated Polyimines, *J. Org. Chem.*, **2019**, *84*, 9957–9964.
4. Y. Ito, T. Konoike, T. Harada, T. Saegusa, Synthesis of 1,4-diketones by Oxidative Coupling of Ketone Enolates with CuCl_2 , *J. Am. Chem. Soc.*, **1977**, *99*, 1487–1493.
5. Y. Ito, T. Konoike, T. Saegusa, Synthesis of 1,4-diketones by the reaction of silyl enol ether with silver oxide. Regiospecific formation of silver(I) enolate intermediates, *J. Am. Chem. Soc.*, **1975**, *97*, 649–651.
6. E. Baciocchi, A. Casu, R. Ruzziconi, Synthesis of unsymmetrical 1,4-diketones by the ceric ammonium nitrate promoted cross-coupling of trimethylsilyl enol ethers, *Tetrahedron Lett.*, **1989**, *30*, 3707–3710.
7. V. V. Zhadankin, M. Mulikin, R. Tykwinski, B. Berglund, R. Caple, N. S. Zefirov, A. S. Koz'min, Carbon-carbon bond formation in reactions of $\text{PhIO}\cdot\text{HBF}_4$ -silyl enol ether adduct with alkenes or silyl enol ethers, *J. Org. Chem.*, **1989**, *54*, 2605–2608.
8. M. Uesaka, Y. Saito, S. Yoshioka, Y. Domoto, M. Fujita, Y. Inokuma, Oligoacetylacetones as Shapable Carbon Chains and Their Transformation to Oligoimines for Construction of Metal-organic Architectures, *Commun. Chem.*, **2018**, *1*, article number 23.
9. Y. Tobe, K. Ueda, K. Kakiuchi, Y. Odaira, Y. Kai, N. Kasai, Synthesis, structure, and reactivities of [6]paracyclophanes, *Tetrahedron*, **1986**, *42*, 1851–1858.
10. J. L. Lindsey, I. C. Schreiman, H. C. Hsu, P. C. Keamey, A. M. Marguerettaz, Rothemund and Adler-Longo reactions revisited: synthesis of tetraphenylporphyrins under equilibrium conditions, *J. Org. Chem.*, **1987**, *52*, 827–836.

11. A. Baeyer, Über ein Condensationsproduct von Pyrrol mit Aceton, *Ber. Dtsch. Chem. Ges.*, **1886**, *19*, 2184–2185.
12. P. A. Gale, J. L. Sessler, V. Král, V. Lynch, Calix[4]pyrrole: Old Yet New Anion-Binding Agents, *J. Am. Chem. Soc.*, **1996**, *118*, 5140–5141.
13. G. Cafeo, F. H. Kohnke, M. F. Parisi, R. P. Nascone, G. L. La Torre, D. J. Williams, The Elusive β -Unsubstituted Calix[5]pyrrole Finally Captured, *Org. Lett.*, **2002**, *4*, 2695–2697.
14. P. Thordarson, Determining association constants from titration experiments in supramolecular chemistry, *Chem. Soc. Rev.*, **2011**, *40*, 1305–1323.
15. L. Fielding, Determination of Association Constants (K_a) from Solution NMR Data, *Tetrahedron*, **2000**, *56*, 6151–6170.
16. G. M. Sheldrick, *SHELXT* – Integrated space-group and crystal-structure determination, *Acta Crystallogr. Sect. A*, **2015**, *71*, 3–8.
17. G. M. Sheldrick, Crystal structure refinement with *SHELXL*, *Acta Crystallogr. Sect. C*, **2015**, *71*, 3–8.
18. S. Grimme, J. Antony, S. Ehrlich, H. Krieg, A consistent and accurate *ab initio* parametrization of density functional dispersion correction (DFT-D) for the 94 elements H-Pu, *J. Chem. Phys.*, **2010**, *132*, 154104.
19. S. Grimme, S. Ehrlich, L. Goerigk, Effect of the damping function in dispersion corrected density functional theory, *J. Comput. Chem.*, **2011**, *32*, 1456–1465.
20. Gaussian 16, Revision C.01, M. J. Frisch, G. W. Trucks, H. B. Schlegel, G. E. Scuseria, M. A. Robb, J. R. Cheeseman, G. Scalmani, V. Barone, G. A. Petersson, H. Nakatsuji, X. Li, M. Caricato, A. V. Marenich, J. Bloino, B. G. Janesko, R. Gomperts, B. Mennucci, H. P. Hratchian, J. V. Ortiz, A. F. Izmaylov, J. L. Sonnenberg, D. Williams-Young, F. Ding, F. Lipparini, F. Egidi, J. Goings, B. Peng, A. Petrone, T. Henderson, D. Ranasinghe, V. G. Zakrzewski, J. Gao, N. Rega, G. Zheng, W. Liang, M. Hada, M. Ehara, K. Toyota, R. Fukuda, J. Hasegawa, M. Ishida, T. Nakajima, Y. Honda, O. Kitao, H. Nakai, T. Vreven, K. Throssell, J. A. Montgomery, Jr., J. E. Peralta, F. Ogliaro, M. J. Bearpark, J. J. Heyd, E. N. Brothers, K. N. Kudin, V. N. Staroverov, T. A. Keith, R. Kobayashi, J. Normand, K. Raghavachari, A. P. Rendell, J. C. Burant, S. S. Iyengar, J. Tomasi, M. Cossi, J. M. Millam, M. Klene, C. Adamo, R. Cammi, J. W. Ochterski, R. L. Martin, K. Morokuma, O. Farkas, J. B. Foresman, and D. J. Fox, Gaussian, Inc., Wallingford CT, 2016.

Chapter 3

Scope and Mechanistic Analysis of Ring Expansion

Reactions of Calix[3]pyrrole and Its Analogues

Abstract

The scope and mechanism of the ring expansion reaction was investigated using furan-embedded analogues of calix[3]pyrrole. The analogues calix[*n*]furan[*m*]pyrrole ($n + m = 3$) were prepared in a manner similar to the preparation of calix[3]pyrrole. They have different degrees of macrocyclic strain, which decreased as the number of pyrroles decreased. The reactivity also decreased as the macrocyclic strain decreased, suggesting the effect of strain in the reaction. Based on the experimental observations and computational study, the reaction mechanism for the ring expansion reaction was proposed to include two steps: the ring cleavage to release macrocyclic strain and cyclodimerization.

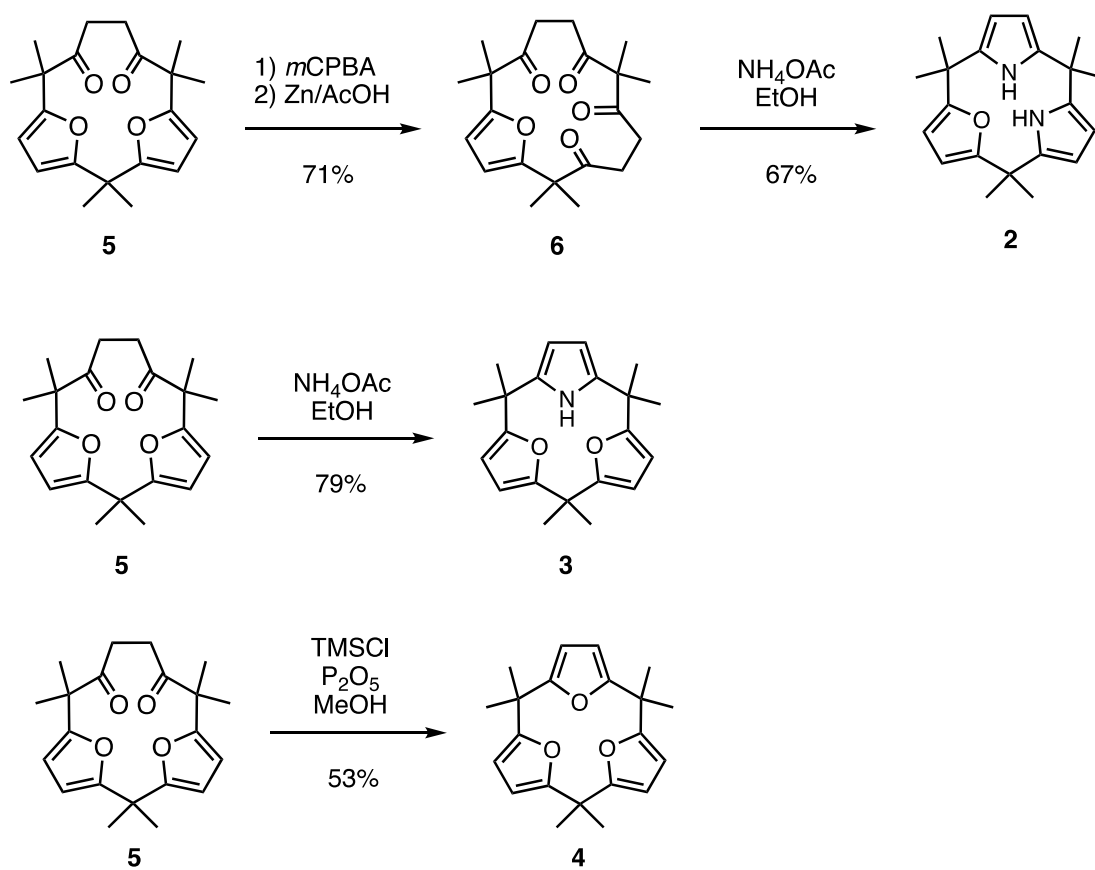
3.1. Introduction

As shown in the previous chapter, calix[3]pyrrole was found to undergo a rapid ring expansion reaction under acidic conditions to give a double-sized macrocycle, calix[6]pyrrole. There are several examples of reactions called “ring expansion reactions”,¹⁻³ but a double expansion of a macrocycle is quite rare. Although it is easy to assume that the highly strained structure of calix[3]pyrrole induces the reactivity, the relationship between macrocyclic strain and ring expansion reaction is unclear. It is better to understand in depth this unique ring expansion reaction of calix[3]pyrrole and generalize it as a method to access large macrocycles. In this chapter, the scope and reaction mechanism of ring expansion has been investigated using calix[3]pyrrole analogues with different degrees of strain.

In this context, the author envisioned that the strain of calix[3]pyrrole **1** can be varied by replacing pyrrole with furan to reduce the steric hindrance. Since furan is also accessible via a Paak-Knorr type reaction from 1,4-diketone, calix[3]pyrrole analogues with different numbers of pyrroles and furans can be prepared from the same precursor as calix[3]pyrrole **1**. In this work, calix[*n*]furan[*m*]pyrroles ($n + m = 3$, **2-4**) were prepared and their macrocyclic strain and reactivity in the ring expansion reaction were investigated. It was found that the smaller the ring strain, the lower the reactivity in the ring expansion reaction. Furthermore, increasing the strain by *N*-methylation also made an inert macrocycle active in ring expansion. In addition, the isolation of the reaction intermediate was possible, suggesting that the ring expansion reaction proceeds through ring cleavage to give a linear intermediate, and dimerization followed by intramolecular cyclization.

3.2. Synthesis of Furan Embedded Analogues of Calix[3]pyrrole

Furan-embedded calix[3]pyrrole analogues, calix[1]furan[2]pyrrole **2**, calix[2]furan[1]pyrrole **3**, and calix[3]furan **4** were prepared from cyclic difuran **5** synthesized in Chapter 2. For the synthesis of **2**, cyclic difuran **5** was treated with 1.5 eq. of *m*CPBA in chloroform to yield enedione **6'**, which was then reduced with zinc in acetic acid to furnish cyclic monofuran **6** in 71% yield over 2 steps. Paal-Knorr pyrrole formation reaction of this using ammonium acetate in ethanol gave **2** in 67% yield. Calix[2]furan[1]pyrrole **3** and calix[3]furan **4** were prepared directly from cyclic difuran **5** by Paal-Knorr type reaction in 79% and 51% yield, respectively.



Scheme 3-1. Synthesis of calix[1]furan[2]pyrrole **2**, calix[2]furan[1]pyrrole **3**, and calix[3]furan **4** from compound **5**.

Single crystal X-ray diffraction analysis of them revealed the different conformations in the solid state (**Figure 3-1**). **2** was adopted in a partial-cone conformation like **1**, with one pyrrole and furan facing in the same direction and another pyrrole facing in the opposite direction. This conformation could be the result of steric repulsion between two pyrrole NHs. On the other hand, **3** and **4** were adopted in a cone conformation in which all three heteroatoms face in the same direction. This difference in conformation seems to reflect the decrease in steric repulsion at the center of the macrocycles as the number of pyrroles decreases.

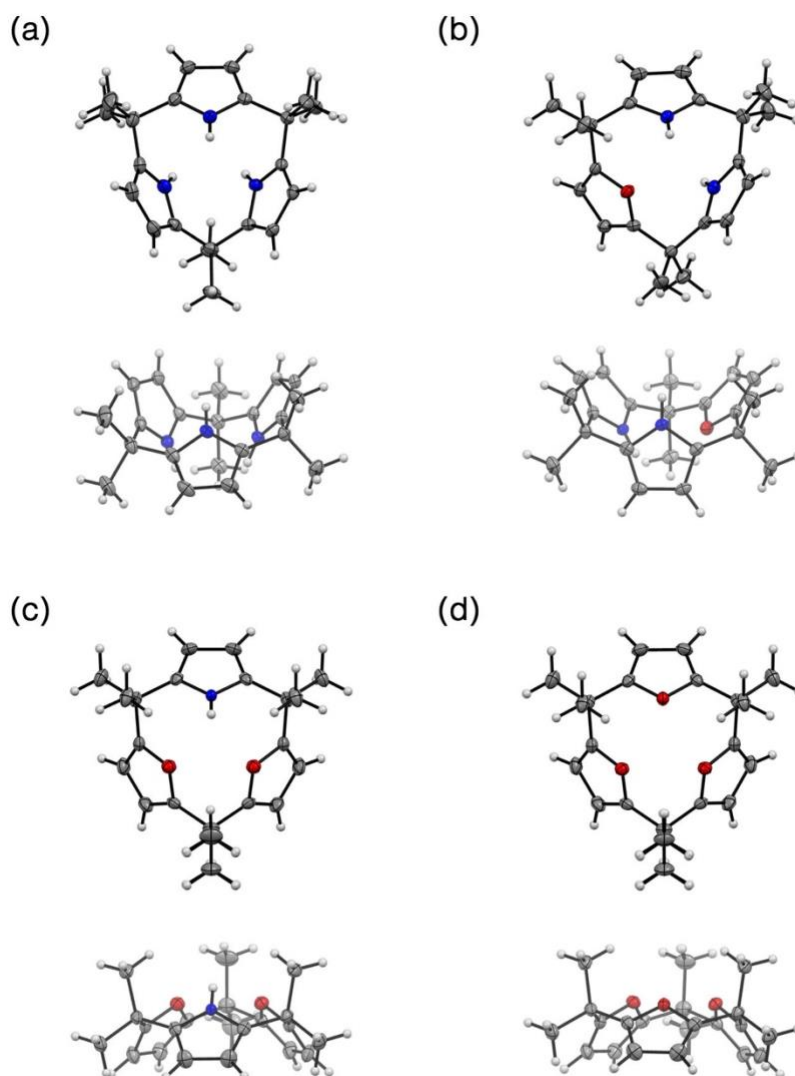


Figure 3-1. Crystal structures of (a) **1** (b) **2**, (c) **3**, and (d) **4** (top and side view, C: gray, H: white, N: blue, O: red).

Although **1** and **2** adopted the partial-cone conformation, and **3** and **4** adopted the cone conformation in the solid-state structure, all of them showed time-averaged structure in ^1H NMR analysis, suggesting that aromatic ring flipping in these macrocycles is fast on the NMR time scale at room temperature.

To compare the possible conformations for **1–4**, structure optimization and energy calculations were performed (**Figure 3-2**). For calix[3]pyrrole **1**, the partial-cone conformation was thought to be more stable than the cone conformation because the DFT optimization converged to the partial-cone conformation even when starting from the cone conformation. For calix[1]furan[2]pyrrole **2**, the partial-cone conformation, in which one pyrrole faces the opposite side of another pyrrole and furan, was found to be the most stable. As expected from the chemical structure, conformations in which two pyrroles face the same side were energetically unfavorable: the partial-cone conformation in which two pyrroles face the same side of the macrocycle was the least stable (7.2 kcal/mol higher than the most stable conformation), and the cone conformation was also destabilized by 5.7 kcal/mol compared to the most stable conformation. On the other hand, the cone conformation was calculated to be the most stable among three possible conformations of calix[2]furan[1]pyrrole **3**. The energy difference among three conformations was relatively small compared to that of **2**, and the most stable cone conformation was 2.1 and 3.3 kcal/mol more stable than partial-cone conformations. Similarly, calix[3]furan **4** was calculated to be more stable in the cone conformation than in the partial-cone conformation, although the energy difference was only 1.1 kcal/mol.

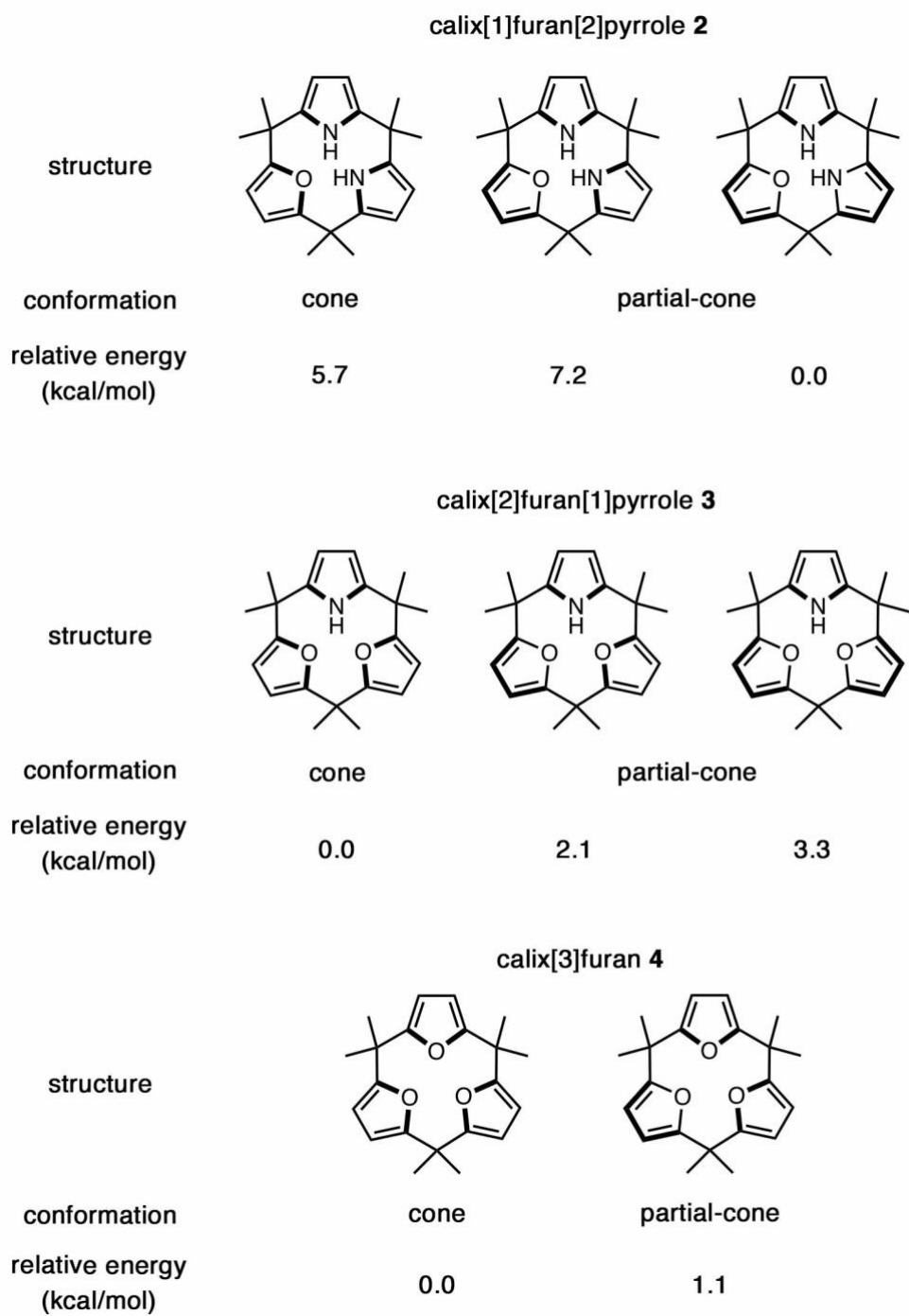


Figure 3-2. Comparison of energy for possible conformations of 2–4.

3.3. Comparison of Strain and Reactivity in Ring Expansion Reaction

The newly synthesized calix[3]-type macrocycles were measured in their deformation angles α and β according to the definition introduced in Section 2.3⁴ (**Figure 3-3**). Since **2** and **3** contain both furan and pyrrole, α and β are averaged independently for pyrrole and furan (**Table 3-1**). The deformation angles of **1** are $\alpha = 2.52^\circ$ and $\beta = 9.20^\circ$ (as shown in section 2.3), and $\alpha = 2.49^\circ$ and $\beta = 8.52^\circ$ around pyrroles in **2**, $\alpha = 2.48^\circ$ and $\beta = 6.17^\circ$ around pyrrole in **3**, indicating that the deformation angles around pyrroles decreases as the number of pyrroles decreases. Compared to the deformation angles around pyrroles, the angles around furan were relatively smaller ($\alpha = 2.14^\circ$ and $\beta = 5.78^\circ$ in **2**, $\alpha = 2.31^\circ$ and $\beta = 7.15^\circ$ in **3**, and $\alpha = 1.95^\circ$ and $\beta = 6.53^\circ$ in **4**), with no obvious correlation between these angles and number of pyrroles.

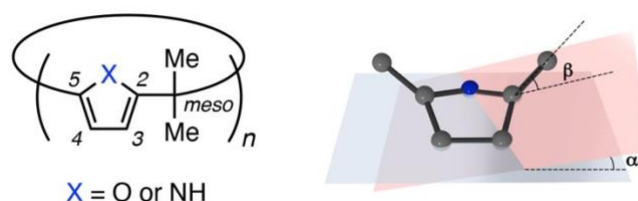
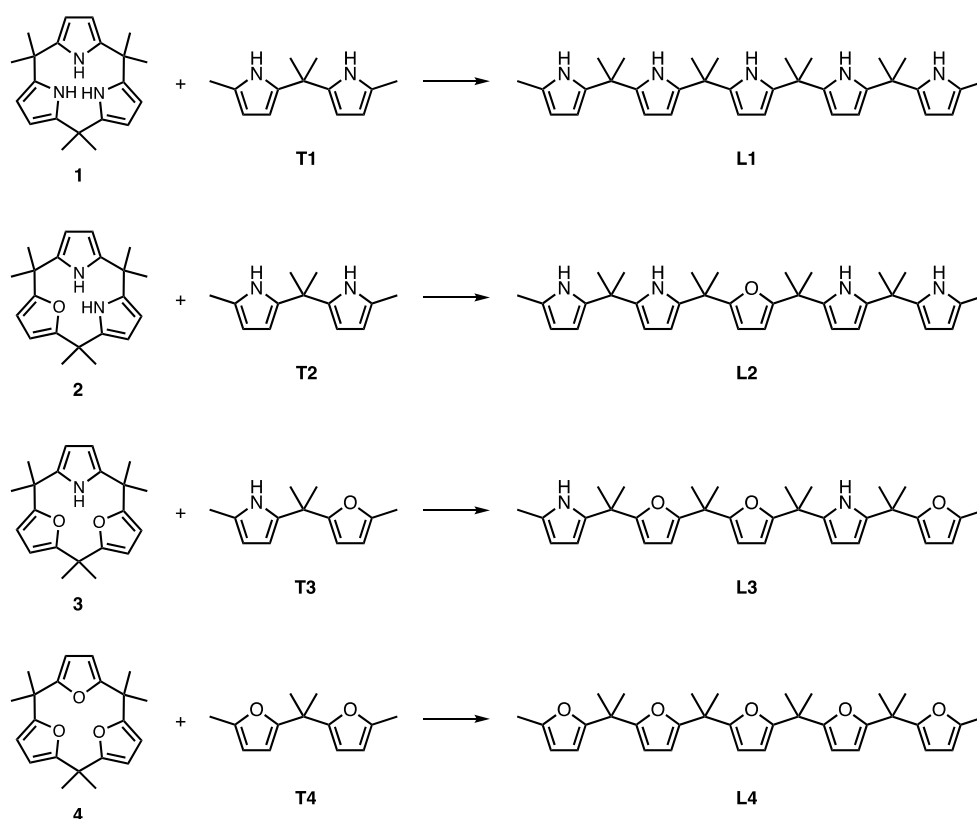


Figure 3-3. Definition of deformation angles α and β .

Table 3-1. Deformation angles α and β about pyrrole and furan rings in **1–4**.

	1	2	3	4
Pyrrole α ($^\circ$)	2.52	2.49	2.48	
Pyrrole β ($^\circ$)	9.20	8.52	6.17	
Furan α ($^\circ$)		2.14	2.31	1.95
Furan β ($^\circ$)		5.78	7.15	6.53

Theoretical calculations were also performed to evaluate the strains in these macrocycles, and a similar trend was observed. The strain energies were calculated by the energy change in virtual ring-opening reaction of **1–4** using terminal units **T1–T4** to give the linear form **L1–L4** (Scheme 3-2). The calculated strain energies were -20 kcal/mol for **1**, -17.7 kcal/mol for **2**, -12.2 kcal/mol for **3**, and -16.4 kcal/mol for **4** (Table 3-2). It was observed that the calculated strain energies decrease as the number of pyrroles decreases for the pyrrole-containing analogues **1–3**, while **4** has a higher strain energy, possibly due to the electrostatic repulsion between the oxygen atoms in **4**.

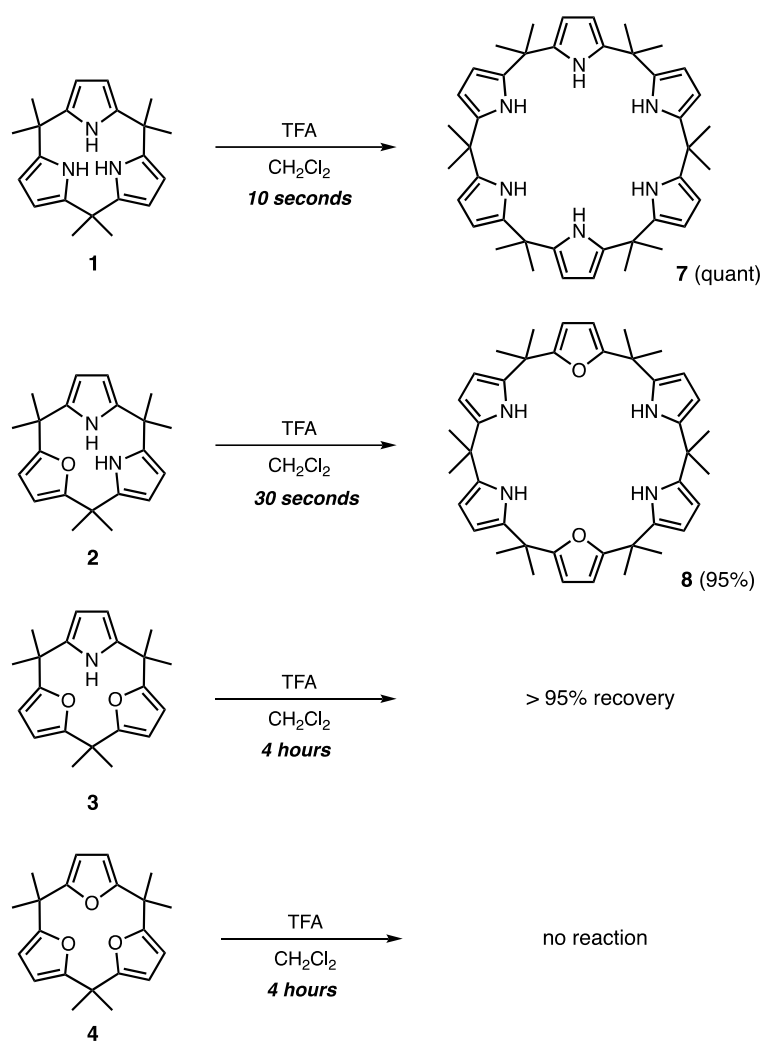


Scheme 3-2. Virtual ring-opening reaction for evaluation of strain energy in **1–4**.

Table 3-2. Calculated strain energies of **1–4**.

	1	2	3	4
Strain energy (kcal/mol)	-20.0	-17.7	-12.2	-16.4

The difference in macrocyclic strain affected the reactivity in the ring expansion reaction (**Scheme 3-3**). When **2** was subjected to the ring expansion reaction conditions, trifluoroacetic acid in dichloromethane, **2** was consumed and the formation of calix[2]furan[4]pyrrole **8** was observed. After 30 seconds, **2** was completely consumed to give **8** in 95% yield (**Figure 3-4**). Considering that **1** completely disappeared within 10 seconds to give calix[6]pyrrole **7** quantitatively, it can be said that **2** is less reactive than **1**. It should be noted that **8** was observed as a single isomer shown in Figure 3-4, whereas there are three possible isomers in macrocycles consisting of two furans and four pyrroles. Prolonging of the reaction time resulted in scrambling over hours, as observed in ^1H NMR spectrum, but it appeared to retain the calix[6]-sized macrocycle, unlike **7**, which underwent scrambling to give calix[4]pyrrole. Under the same conditions, **3** was much less reactive. More than 95% of **3** was recovered after 4 h, and only traces of what appears to be ring expanded product were observed in the ^1H NMR spectrum, HPLC chromatogram, and HR-ESI mass spectrum (**Figure 3-5**). **4** was inert under the same ring expansion reaction conditions, with no observable change in ^1H NMR and HPLC over 4 hours (**Figure 3-6**). Although **4** was inert under acidic conditions perhaps because of the difference in reactivity between pyrrole and furan, the reactivity in the ring expansion reaction decreased as the macrocyclic strain decreased.



Scheme 3-3. Comparison of reactivity in ring expansion reaction.

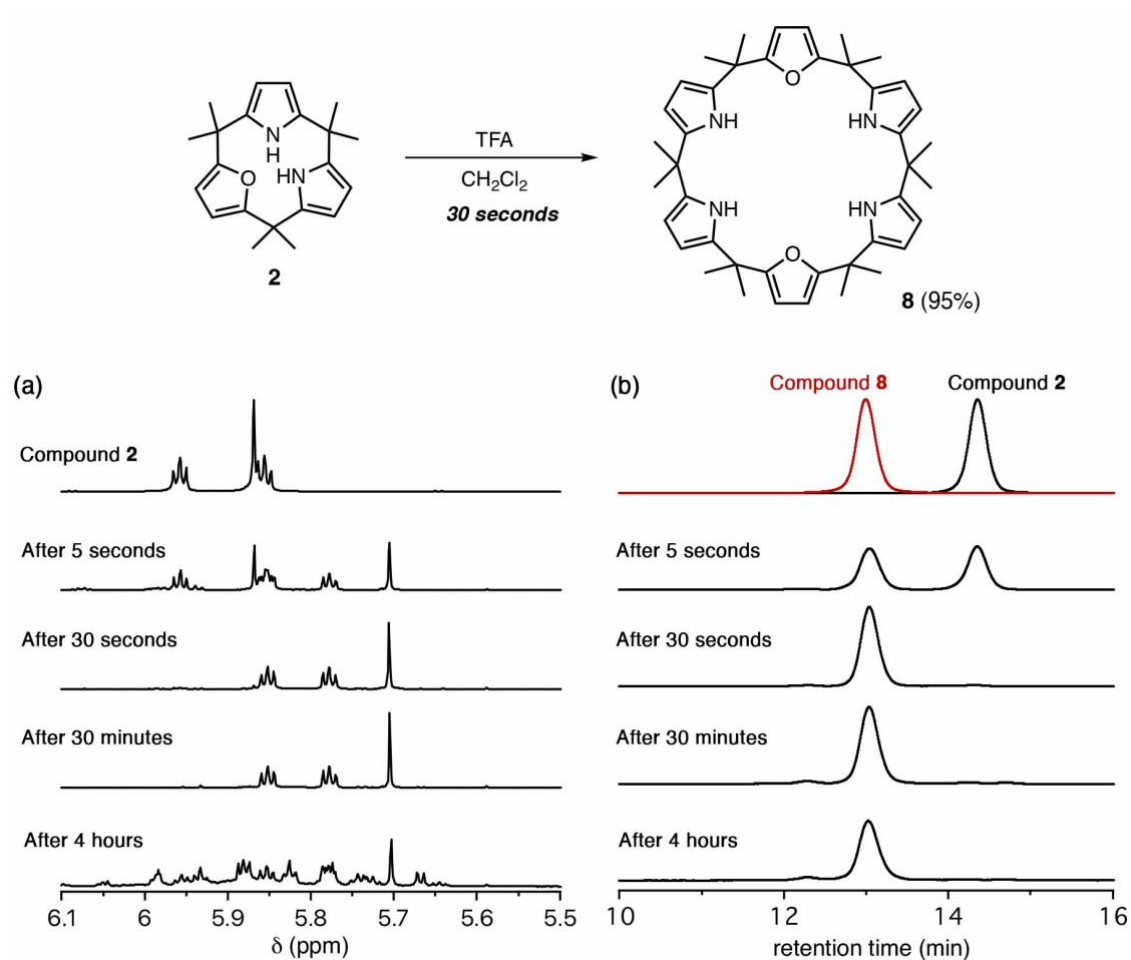


Figure 3-4. Ring expansion reaction of **2** by TFA in dichloromethane. (a) ¹H NMR spectra and (b) HPLC chromatogram measured before the reaction and at 5 sec, 30 sec, 30 min, and 4 h of the reaction (Column: TOSOH TSKgel G2000HXL×2, mobile phase: chloroform, detection: absorption at 245 nm, flow rate: 1.0 mL/min).

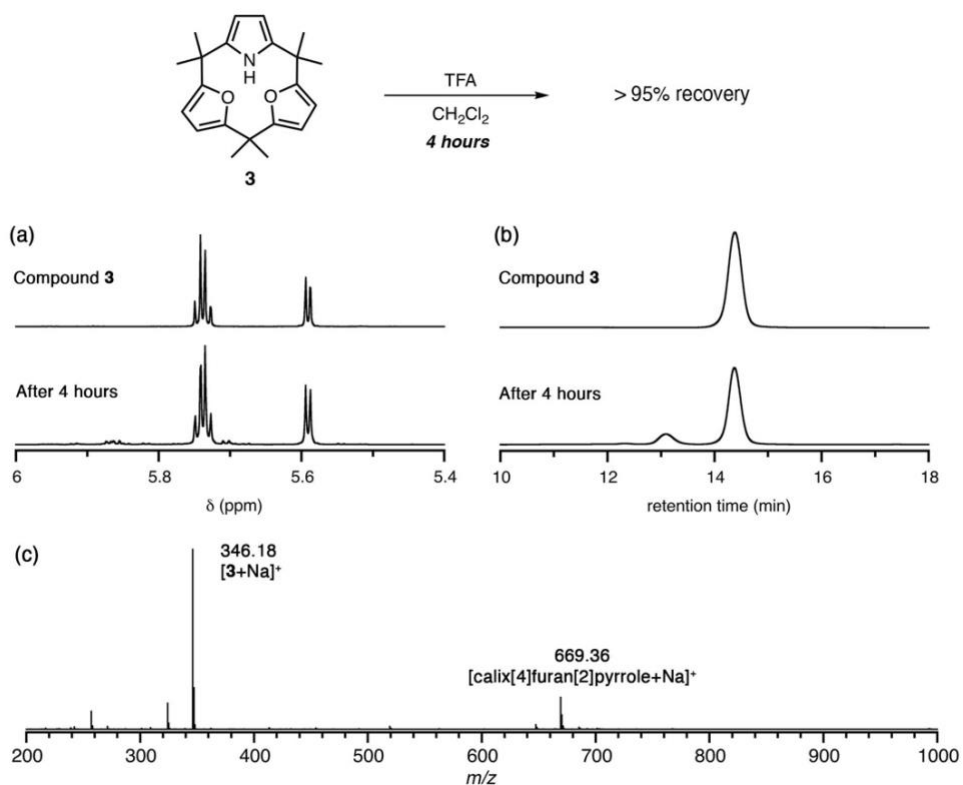


Figure 3-5. Reactivity test of **3** by TFA in dichloromethane. (a) ¹H NMR spectra and (b) HPLC chromatogram measured before and after the reaction (Column: TOSOH TSKgel G2000HXL×2, mobile phase: chloroform, detection: absorption at 245 nm, flow rate: 1.0 mL/min). (c) HR-ESI mass spectrum of reaction mixture after 4 h.

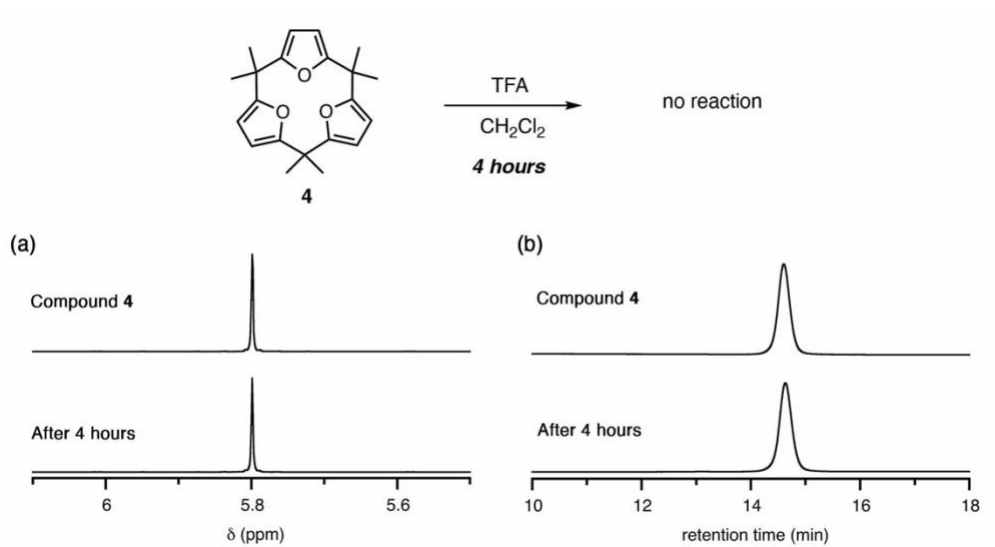


Figure 3-6. Reactivity test of **4** by TFA in dichloromethane. (a) ¹H NMR spectra and (b) HPLC chromatogram measured before and after the reaction (Column: TOSOH TSKgel G2000HXL×2, mobile phase: chloroform, detection: absorption at 245 nm, flow rate: 1.0 mL/min).

Although calix[3]furan **4** caused no reaction with TFA in dichloromethane, it was hydrolyzed to give **5** by the treatment with hydrochloric acid in ethanol (**Figure 3-7**). In this reaction, hydrolysis of one of the three furans proceeded, but prolonging the reaction time did not furnish further hydrolyzed products **6** or cyclic hexaketone compound. On the other hand, treatment of calix[4]furan under the same reaction conditions did not result in hydrolysis. In this sense, this hydrolysis of **4** can also be said to be caused by macrocyclic strain.

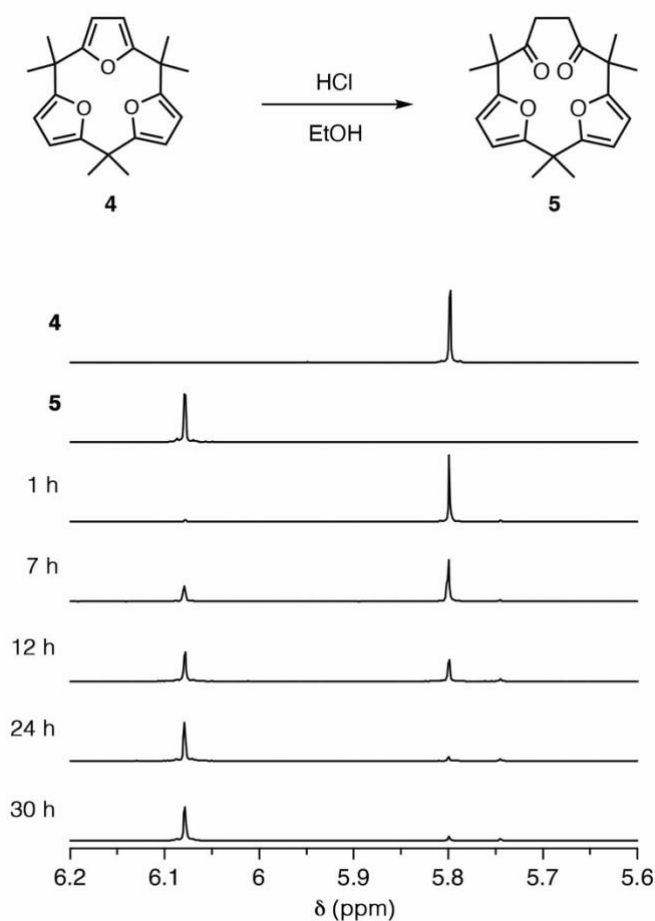


Figure 3-7. Hydrolysis of **4** to **5** by hydrochloric acid in ethanol (¹H NMR spectra, CDCl₃, 298 K).

3.4. Increased Strain upon *N*-methylation and Its Ring Expansion Reaction

Since the difference in macrocyclic strain affected the reactivity in its ring expansion reaction, it was considered that **3** could become reactive in the ring expansion reaction if its macrocyclic strain was increased. To increase the macrocyclic strain in **3**, *N*-methylation was performed using iodomethane and sodium hydride in DMF to afford **3-Me** in 82% yield (**Figure 3-8a**). In the ^1H NMR spectrum of **3-Me**, methyl protons were observed as five peaks at $\delta = 2.24, 1.48, 1.57, 1.63,$ and 1.66 ppm, suggesting that aromatic ring flipping is slow on the NMR time scale due to increased steric repulsion at the center of the macrocycle. Single crystal X-ray diffraction analysis revealed that **3-Me** adopted in a partial-cone conformation with the *N*-methyl group facing the opposite side of the oxygen atoms to minimize the steric repulsion of *N*-Me (**Figure 3-8b**). The angle between the mean-plane of the pyrrole ring and the mean-plane of bridging (*meso*) carbons was 74.1° in **3-Me**, while that of **3** was 44.7° , indicating that the steric repulsion was increased by *N*-methylation (**Figure 3-9**). The deformation angles α and β in **3-Me** were measured to be $\alpha = 2.03^\circ$ and $\beta = 11.70^\circ$ around pyrrole and $\alpha = 1.91^\circ$ and $\beta = 5.49^\circ$ around furans, indicating significant increase in angle β by *N*-methylation.

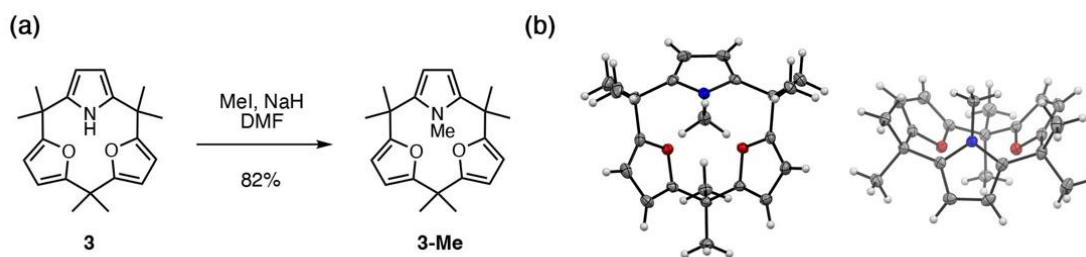


Figure 3-8. (a) *N*-methylation reaction of **3** and (b) the crystal structure of **3-Me** (C: gray, H: white, N: blue, O: red).

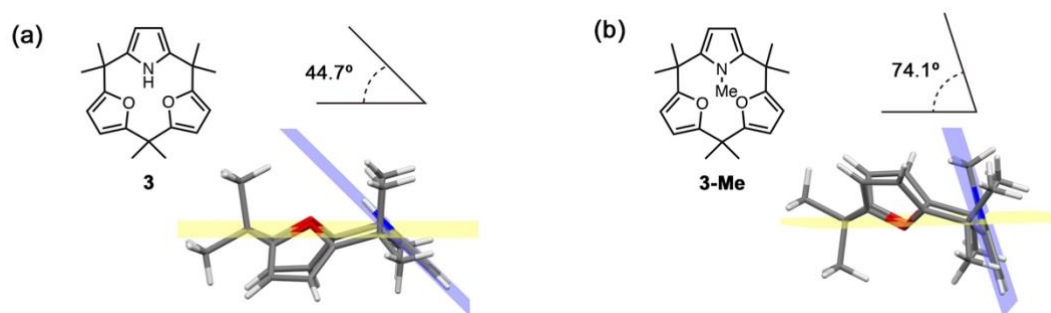


Figure 3-9. The comparison of the angle between mean-plane of pyrrole ring and mean-plane of bridging carbons in **3** and **3-Me**.

When **3-Me** was treated with trifluoroacetic acid in dichloromethane, it disappeared after 30 seconds and several new signals were observed in the HPLC chromatogram (**Figure 3-10**). Among the newly observed species, compound **9** observed as a fraction at 13.8 minutes, had the same molecular weight as the starting material. ^1H NMR spectroscopic analysis of this fraction revealed that compound **9** is a ring cleaved product of **3-Me** containing two furans and one *N*-methyl pyrrole connected by dimethylmethylene, and isopropylidene at one end (**Figure 3-11**). The 2D-NOESY spectrum of compound **9** showed the correlation between α -proton of heteroaromatic ring observed at 6.44 ppm and *N*-methyl group at 3.19 ppm, showing that *N*-methylpyrrole is at the terminal and has α -proton.

HPLC chromatograms showed further changes in the reaction mixture over 1 hour. The major fraction of the resulting mixture was separated and analyzed by ^1H NMR spectrum and HR-ESI mass spectrum to show that two isomers of calix[6]-type ring-expanded product **10** and **11** were formed in a 2:1 ratio (**Figure 3-12**). The structure of each isomer was determined by single crystal X-ray diffraction analysis after chromatographic separation. The major isomer **10** was determined to be a doubly *N*-confused *N,N'*-dimethylcalix[4]furan[2]pyrrole, in which two *N*-methylpyrroles are connected at α - β and α - β manner with C_{2h} symmetry. The minor isomer **11** was determined to have the same formula as **10** but *N*-methylpyrroles are connected at α - β and β - α manner with C_{2v} symmetry. The observed *N*-confusion could be induced by steric repulsion between the *N*-methyl group and the neighboring dimethylmethylene moiety. Such a rearrangement of a α -substituent to β -position is known for *N*-substituted pyrroles.^{5,6}

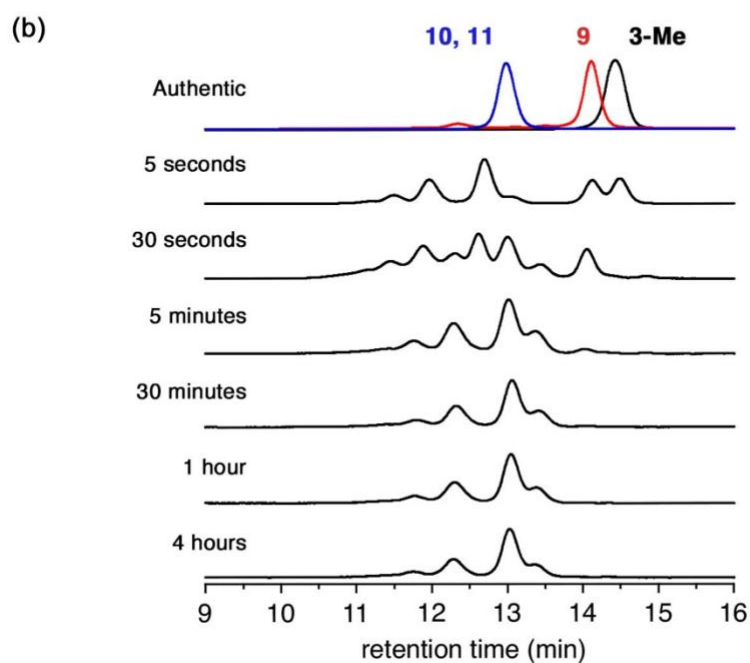
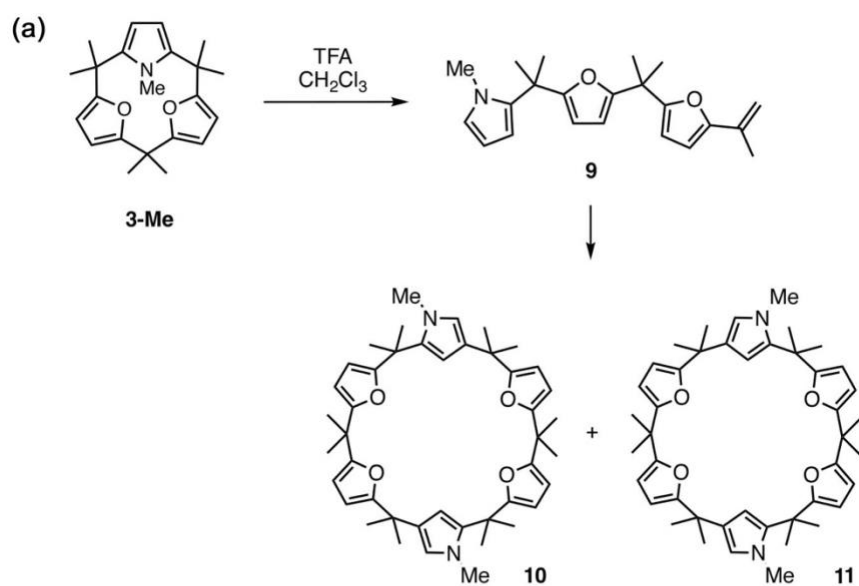


Figure 3-10. (a) Ring expansion reaction of **3-Me** by TFA in dichloromethane and (b) HPLC chromatograms corresponding to the reaction (Column: TOSOH TSKgel G2000HXL×2, mobile phase: chloroform, detection: absorption at 245 nm, flow rate: 1.0 mL/min).

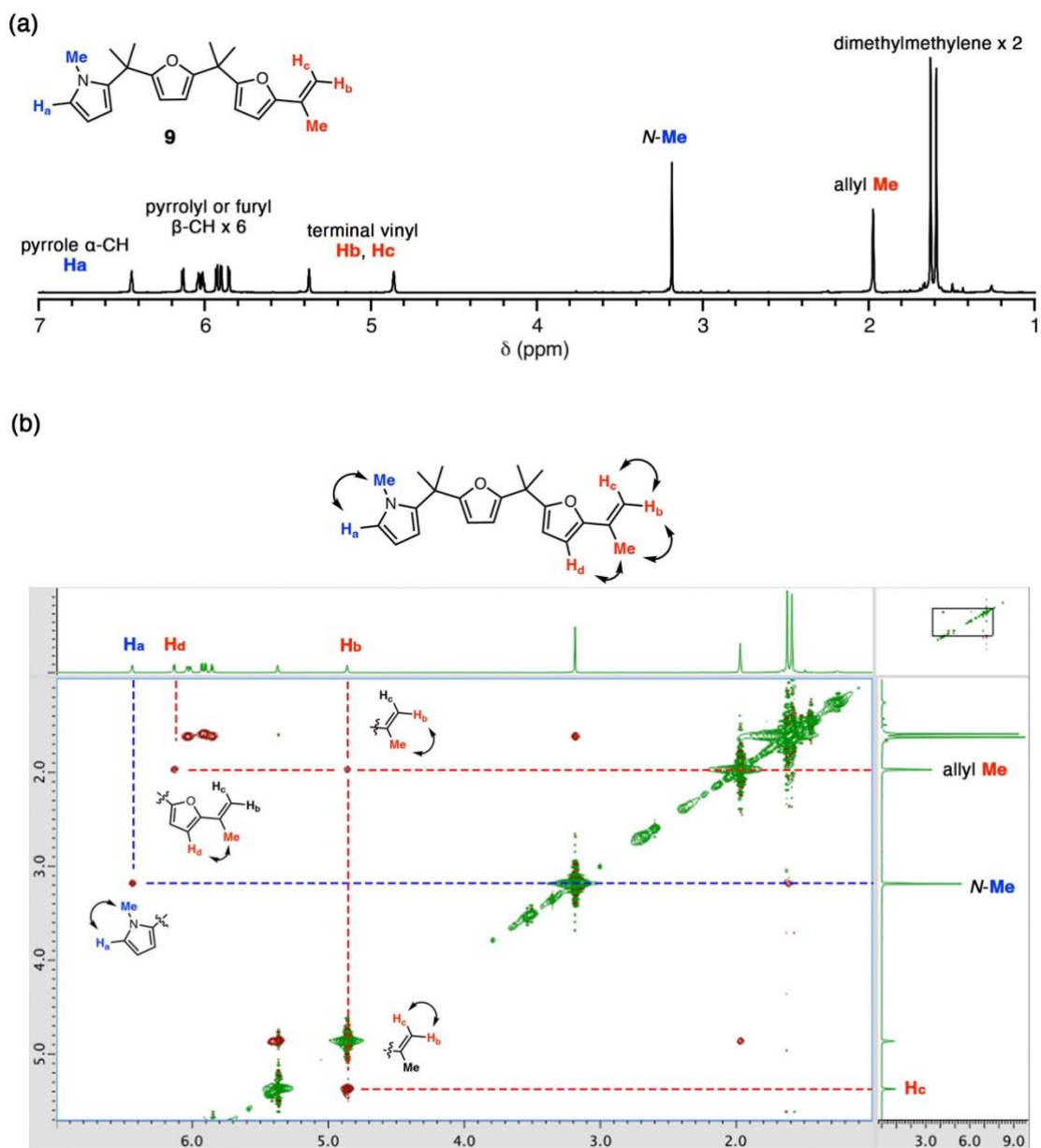


Figure 3-11. (a) ^1H NMR spectrum and (b) 2D-NOESY spectrum of compound **9** in chloroform-*d* at 298 K.

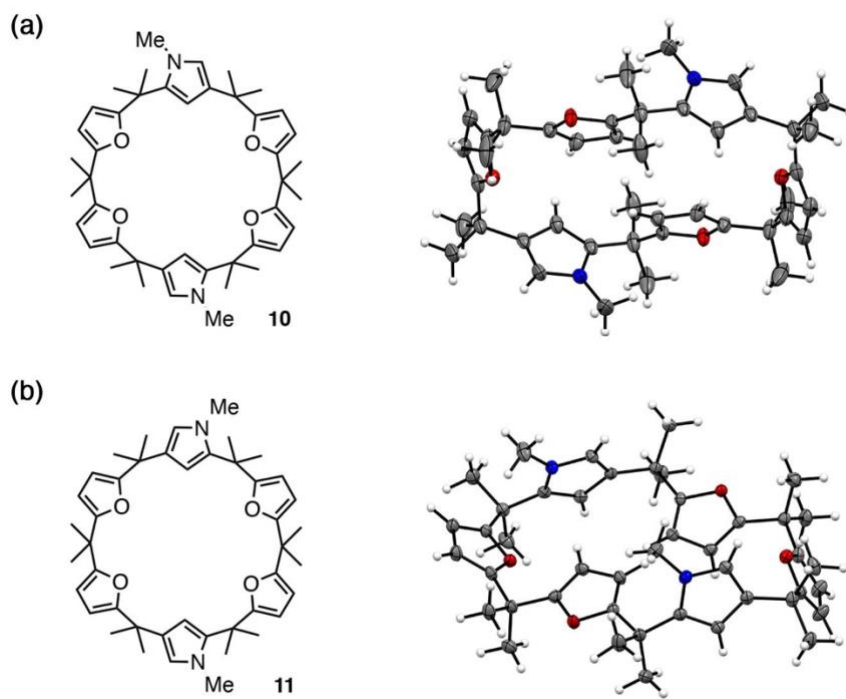


Figure 3-12. Crystal structure of **10** and **11** (C: gray, H: white, N: blue, O: red).

Furthermore, HR-ESI mass spectra of fractions at 15 seconds of the reaction were measured to reveal that there are compounds with double, triple, and quadruple the molecular weight of **3-Me**. The mixture obtained after 1 hour of reaction time also contained compounds with double, triple, and quadruple the molecular weight of **3-Me**, but the retention time of these compounds was different from that observed at 15 seconds of reaction time (**Figure 3-13**). It can be deduced that the compounds observed at the early stage of the reaction have linear structures and those observed at the late stage of the reaction are cyclic compounds. An attempt was made to characterize these products, but it was found to be difficult due to the existence of isomers depending on the connectivity around the pyrrole rings, such as **10** and **11**.

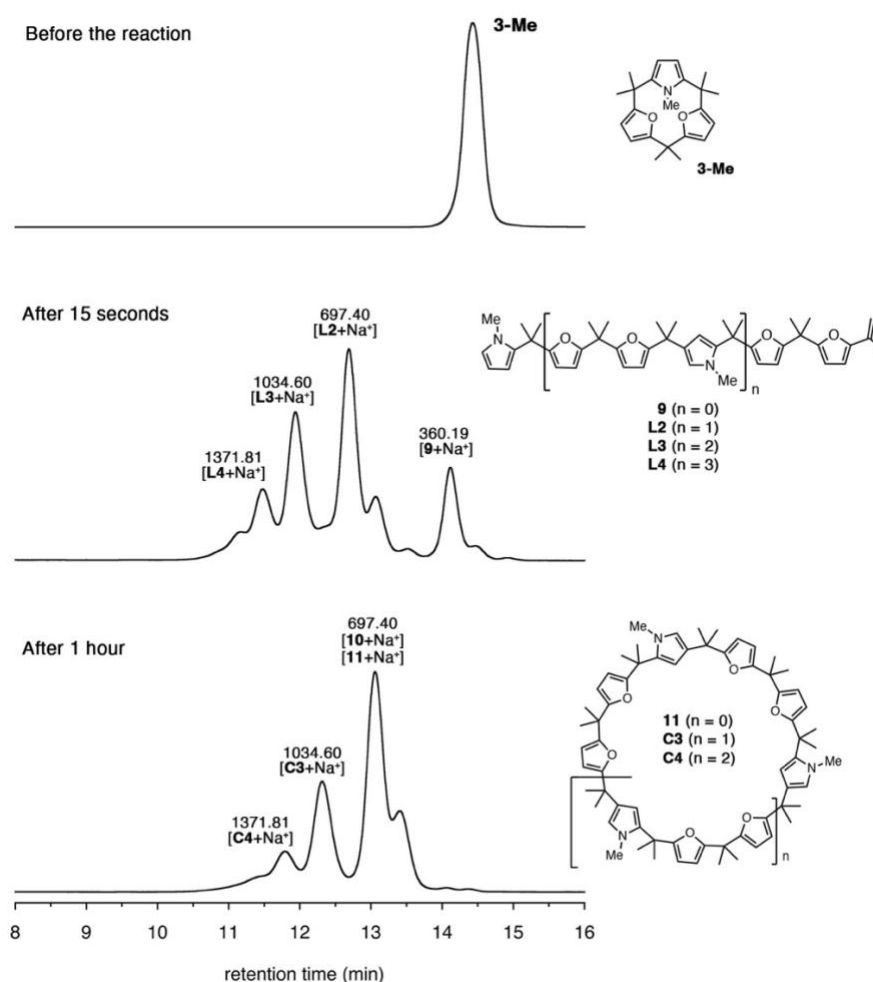
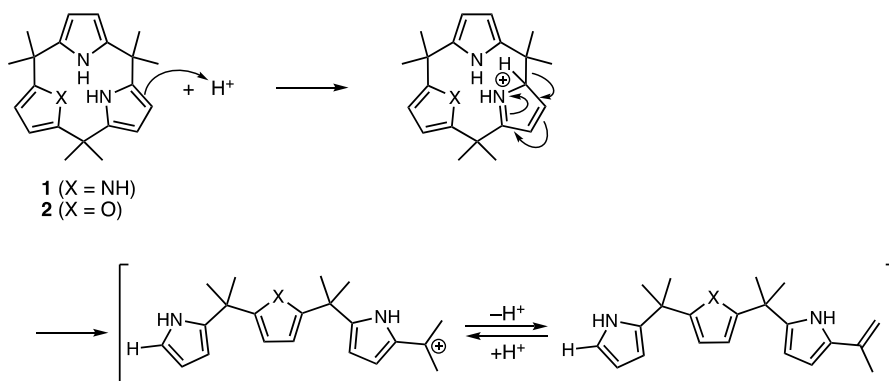


Figure 3-13. HPLC chromatograms of the reaction mixture after 15 sec and 1 h, and ESI-mass analysis of each observed peaks with proposed structures. (HPLC conditions; Column: TOSOH TSKgel G2000HXL \times 2, mobile phase: chloroform, detection: UV absorption at 245 nm, flow rate: 1.0 mL/min, ESI-MS; methanol, positive mode.)

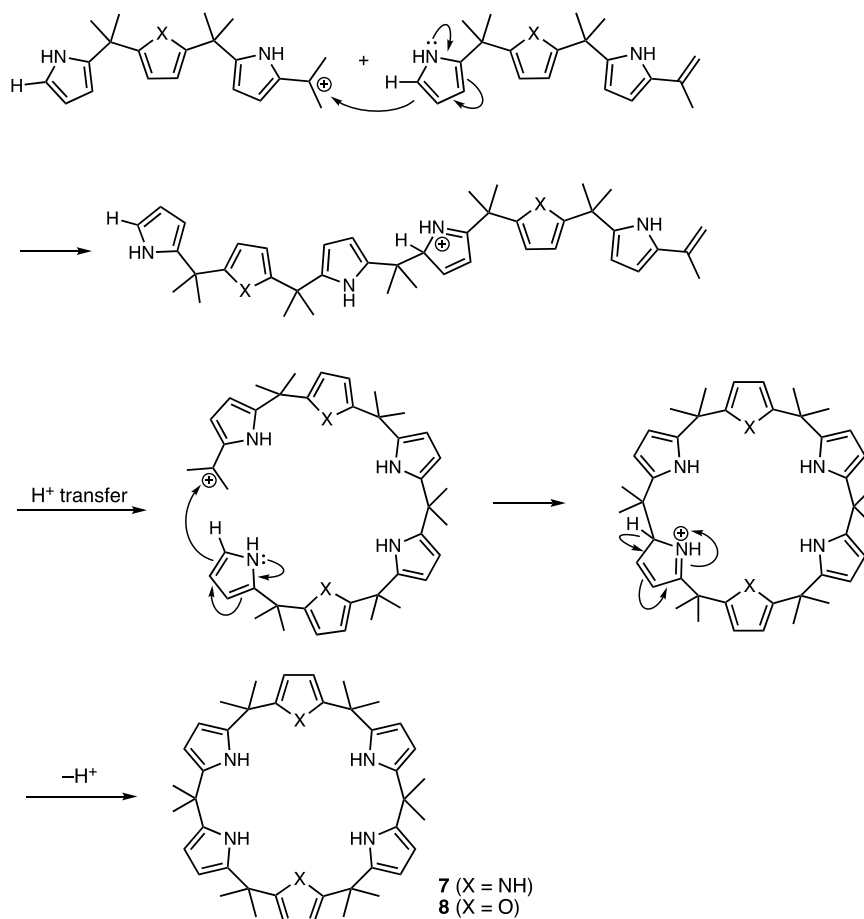
3.5. Reaction Mechanism Analysis

Since compound **9** was obtained in the middle of the ring expansion reaction of **3-Me**, the reaction mechanism for the ring expansion reaction of calix[3]pyrrole was proposed as follows: (1) Protonation of pyrrole leads to the retro Friedel-Crafts reaction to give ring cleaved product driven by the release of macrocyclic strain. (2) A linear intermediate reacts with another linear intermediate to form linearly dimerized species, which is then cyclized by aromatic electrophilic substitution reaction (**Scheme 3-4**). In the case of calix[3]pyrrole **1**, for example, **1** is protonated by acid and undergoes ring cleavage to release the macrocyclic strain to form linear tripyrrolic intermediate. This intermediate is difficult to reconstruct calix[3]pyrrole **1** due to the large macrocyclic strain of **1**. The reactive linear intermediate then undergoes dimerization by intermolecular aromatic electrophilic substitution reaction to give linear hexapyrrolic compound, which can be cyclized by intramolecular reaction to give calix[6]pyrrole **7**. Although **7** can also undergo ring cleavage by acid, it can go back to **7** because **7** is not much strained. Therefore, calix[6]pyrrole **7** remained in the ring expansion reaction conditions for more than 1 hour. During repeated ring formation/cleavage of **7**, linear oligopyrrolic species are assumed to be fragmented into shorter chains and then converged to thermodynamically favored calix[4]pyrrole. Linear intermediates are expected to be much more reactive than macrocycles such as calix[6]pyrrole **7** and calix[4]pyrrole, so only cyclic products were observed in ^1H NMR and GPC-HPLC analyses.

Ring Cleavage



Cyclodimerization



Scheme 3-4. Proposed reaction mechanism for the ring expansion reaction of **1** or **2** to give **7** or **8**.

In light of this proposed mechanism, the observed selectivity in the ring cleavage of **3-Me** was investigated theoretically (**Figure 3-14a**). Among three possible cations, the *N*-methylpyrrole-protonated cation **12c** is much more energetically favored than the other two types of furan-protonated cations **12a** and **12b**, reflecting the electron-rich nature of *N*-methylpyrrole. The linear cation **13c** formed from **12c** was also more favorable than **13a** and **13b** formed from **12a** and **12b**, respectively. Therefore, the theoretical calculation results supported the experimental observation that only compound **9** was observed as a ring cleaved intermediate.

Considering the proposed reaction mechanism, the selective formation of **8** in the ring expansion reaction of **2** can also be attributed to the site-selective ring cleavage, since the selective formation of a linear intermediate can yield the cyclodimerized ring expanded product as a single isomer. To investigate the selectivity in the ring cleavage of **2**, a similar computational analysis was performed (**Figure 3-14b**). Among three possible protonated states, the furan-protonated cation **14e** had the highest energy (23.0 kcal/mol), and the energy difference between two pyrrole-protonated cations **14d** and **14f** is only 1.5 kcal/mol. This is reasonable because furan is more electron deficient than pyrrole. On the other hand, the linear cation **15d**, which is cleaved between pyrrole and furan after protonation at pyrrole is the least favorable (10.6 kcal/mol) compared to the other two linear cations **15e** (6.8 kcal/mol) and **15f** (5.5 kcal/mol), indicating that the cation adjacent to pyrrole is more stable than that adjacent to furan. Overall, pathway F, in which ring cleavage occurs between pyrroles, is the most realistic pathway.

Based on these experimental observations and theoretical calculations, it could be said that the ring expansion reaction of calix[3]pyrrole and analogues is triggered by the macrocyclic strain. Although the degree of strain affects the reactivity, the types of aromatic rings included in the macrocycle also affect the reactivity. Electron-rich pyrrole would be advantageous for protonation and cation stabilization.

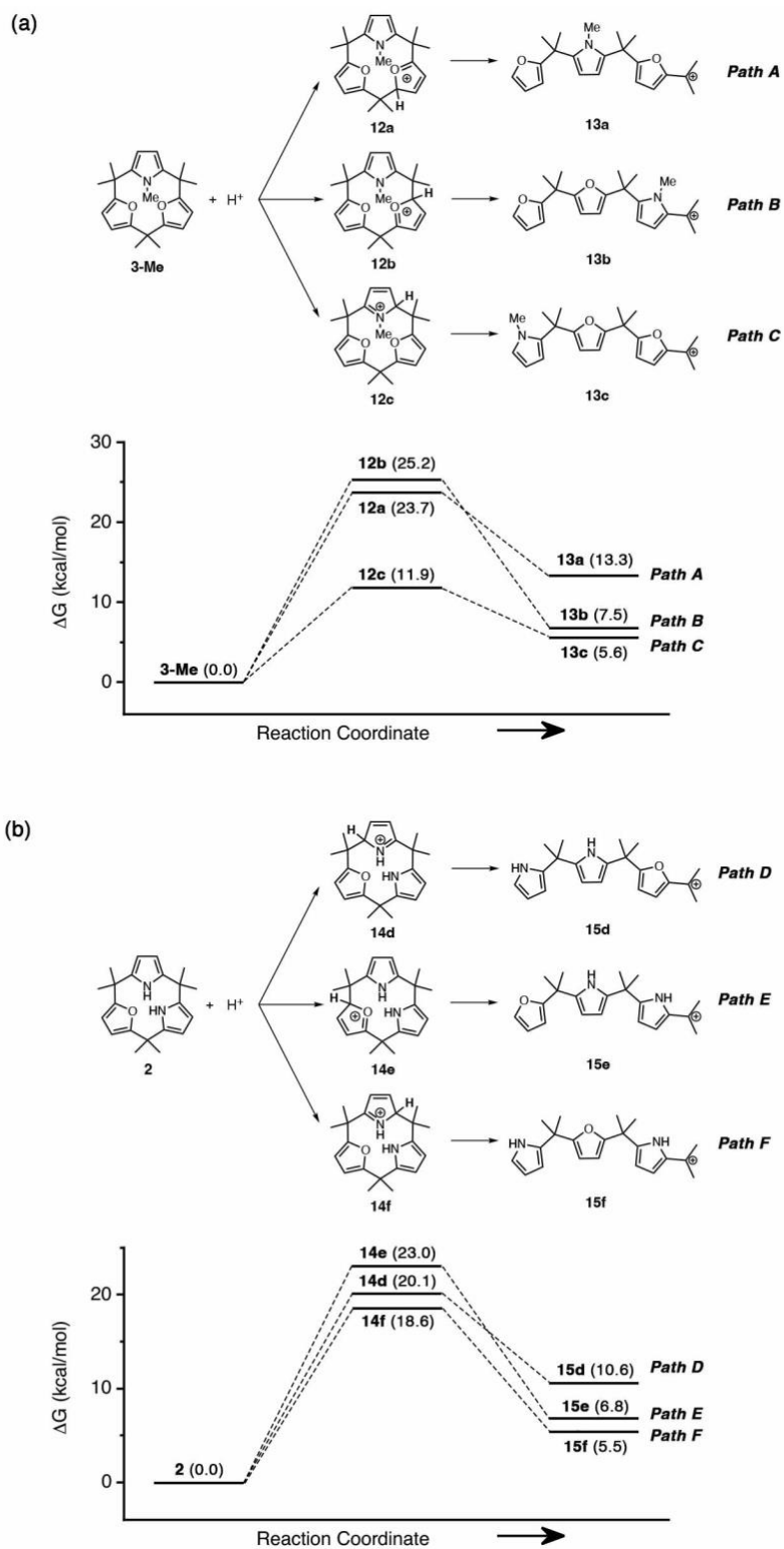


Figure 3-14. Relative free energy diagrams of possible pathways for protonation and ring cleavage of (a) **3-Me** and (b) **2** using TFA as a proton source.

To prove the reaction mechanism, a scrambling experiment using **1** and **2** was investigated (**Figure 3-15**). When the ring expansion reaction was performed using 1:1 mixture of **1** and **2**, the cross-coupled product calix[1]furan[5]pyrrole **16** was obtained in 35% yield along with the homo-coupled products **7** and **8**. Since no other isomers were observed, it can be said that site-selective ring cleavage of **2** gives a linear intermediate such as **15f**.

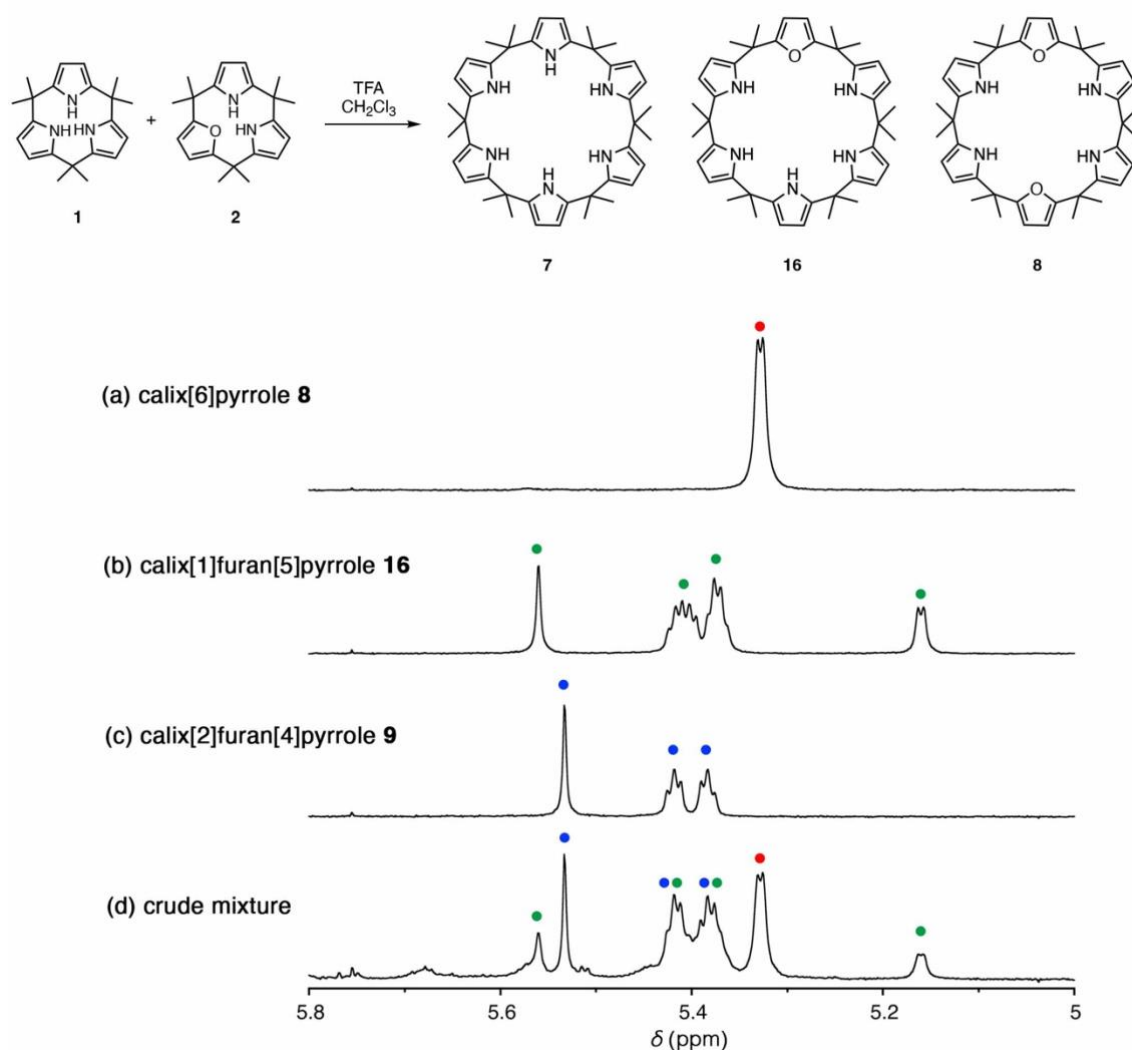


Figure 3-15. Scrambling experiment using a mixture of **1** and **2**. ¹H NMR spectra of (a) **7**, (b) **16**, (c) **8**, and (d) crude mixture after the scrambling experiment measured in DMSO-*d*₆ (400 MHz, 298 K).

3.6. Conclusion

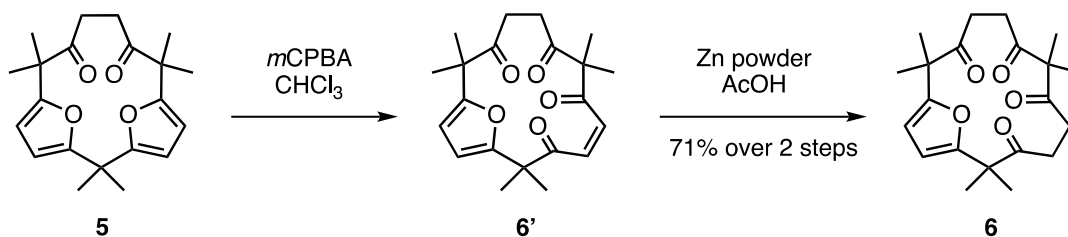
By synthesizing the furan-embedded calix[3]pyrrole analogues with different degrees of strain, the author elucidated the reaction mechanism and scope of the strain-induced ring expansion reaction. It was found that the ring expansion reaction of calix[3]pyrrole proceeds through two steps, the first step is protonation and ring cleavage driven by strain release, and the second step is recombination and cyclization by Friedel-Crafts type mechanism. Since ring cleavage is site-selective in furan-pyrrole mixed analogues, the ring expansion reaction gave the product with a defined sequence of furan and pyrrole. Such heteroaromatics-mixed macrocyclic systems are difficult to synthesize or isolate by traditional synthesis, so the strain-induced ring expansion reaction would be a new tool to access new macrocyclic systems that have been difficult to access.

3.7. Experimental Section

3.7.1. Reagents and equipment

Solvents and reagents were purchased from FUJIFILM WAKO Pure Chemical Industries Ltd., TCI Co., Ltd., Kanto Chemical Co., Inc., or Sigma-Aldrich Co., and used without further purification unless otherwise mentioned. Compounds **1** and **5** were prepared following the procedure described in Chapter 2. Compounds **7**, **8**, and **16** were prepared according to a reported procedure⁷. All ¹H and ¹³C NMR spectra were recorded using JEOL JMN-ECS400 spectrometer and chemical shifts were reported in parts per million (ppm) relative to an internal standard tetramethylsilane ($\delta = 0.00$ ppm for ¹H NMR in CDCl₃) or a solvent residual peak ($\delta = 2.50$ ppm for ¹H NMR in DMSO-*d*₆ and $\delta = 77.16$ ppm for ¹³C NMR in CDCl₃). Infrared spectra were measured using a JASCO Co. FT/IR-4600. ESI-TOF-MS spectra were recorded on a Thermo Scientific Executive spectrometer. Elemental analyses were carried out using an Exceter Analytical, Inc. CE440 or MICRO CORDER JM10. Thin layer chromatography was performed on a silica gel sheet, MERCK silica gel 60 F254. Preparative scale separations were performed by means of gravity column chromatography over silica gel (Wakosil[®] 60. 64 ~ 210 μ m). Analytical HPLC chromatograms were recorded using a JASCO MD-2018 photodiode array detector quipped with a JASCO PU-2089 pump, JASCO AS-2059 sampler, JASCO CO-2060 column thermostat. Single crystal X-ray diffraction data were obtained using Rigaku XtaLAB P200 diffractometer equipped with a PILATUS200K detector, which uses a multilayer mirror (MoK α radiation $\lambda = 0.71073$ Å) or a Rigaku XtaLAB Synergy-R/DW instrument equipped with a HyPix-6000HE detector, which uses a monochromated mirror. All structures were solved using a dual-space algorithm (SHELXT) and refined using full-matrix least-squares method (SHELXL).^{8,9}

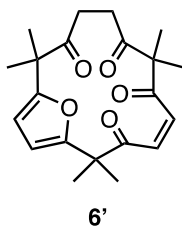
3.7.2. Synthesis of compound 6



In a 200 mL round-bottomed flask, compound **5** (1.00 g, 2.92 mmol) was dissolved in chloroform (100 mL). *m*-Chloroperbenzoic acid (contains 30% water, 2.16 g, 8.76 mmol) was added to the solution with stirring. After 1 hour stirring at room temperature, the reaction solution was poured into a mixture of a saturated aqueous solution of sodium thiosulfate (50 mL) and a saturated aqueous solution of sodium bicarbonate (50 mL). The organic layer was separated, washed with saturated aqueous solution of sodium bicarbonate (50 mL \times 3), and dried over anhydrous sodium sulfate. Evaporation of the solvent gave crude **6'** which was used without isolation.

The crude product **6'** was dissolved in acetic acid (100 mL) in a 200 mL round-bottomed flask. After addition of zinc powder (2.48 g, 38.0 mmol), the resulting suspension was vigorously stirred for 30 minutes at ambient temperature. Solid materials were removed by suction filtration, and wash on a funnel with chloroform (50 mL). The filtrate was poured into water (100 mL), and the aqueous layer was extracted using chloroform (50 mL \times 3). Combined organic layer was washed with saturated aqueous solution of sodium bicarbonate (50 mL \times 5), dried over anhydrous sodium sulfate, and concentrated under reduced pressure. The resulting pale-yellow solid was subjected to silica gel column chromatography (diameter: 4.0 cm, height: 10 cm, eluent: hexane/ethyl acetate =3/1) to give 749 mg (71% yield) of compound **6** as a colorless solid.

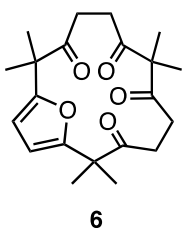
Characterization data for compound 6'



Analytical sample of compound **6'** was obtained by purification of crude **6'** using silica gel column chromatography (hexane/ethyl acetate = 5/1).

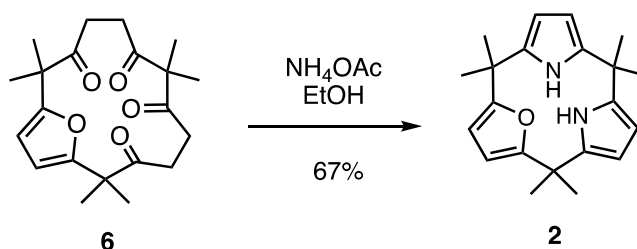
^1H NMR (CDCl_3 , 400 MHz, 298 K): δ = 6.28 (d, 1H, vinyl, J = 12 Hz), 6.28 (d, 1H, furyl, J = 3.2 Hz), 6.23 (d, 1H, vinyl, J = 12 Hz), 6.17 (d, 1H, furyl, J = 3.2 Hz), 2.67–2.71 (m, 2H, ethylene), 2.27–2.32 (m, 2H, ethylene), 1.47 (s, 6H, dimethylmethylene), 1.45 (s, 6H, dimethylmethylene), 1.38 ppm (s, 6H, dimethylmethylene); ^{13}C NMR (CDCl_3 , 100 MHz, 298 K): δ = 210.9 (C=O), 210.7 (C=O), 203.6 (C=O), 198.3 (C=O), 159.7 (C=C), 155.5 (C=C), 140.3 (C=C), 126.6 (C=C), 107.9 (C=C), 106.2 (C=C), 62.5 ($\text{C}(\text{CH}_3)_2$), 49.8 ($\text{C}(\text{CH}_3)_2$), 48.7 ($\text{C}(\text{CH}_3)_2$), 36.6 (CH_2), 32.6 (CH_2), 23.1 (CH_3), 22.8 (CH_3), 21.8 ppm (CH_3); IR(ATR, neat): 2974, 2934, 2871, 1709, 1694, 1058, 790 cm^{-1} ; m.p. 173–179 $^\circ\text{C}$; HRMS(ESI): m/z calcd. for $\text{C}_{21}\text{H}_{26}\text{O}_5\text{Na}^+$: 381.1673 [$M+\text{Na}$] $^+$; found 381.1669; R_f = 0.28 (hexane/ethyl acetate = 5/1).

Characterization data for compound 6



^1H NMR (CDCl_3 , 400 MHz, 298 K): δ = 6.21 (s, 2H, furyl), 2.62–2.66 (m, 4H, ethylene), 2.42–2.46 (m, 4H, ethylene), 1.44 (s, 12H, dimethylmethylene), 1.31 ppm (s, 6H, dimethylmethylene); ^{13}C NMR (CDCl_3 , 100 MHz, 298 K): δ = 210.5 (C=O), 209.4 (C=O), 156.9 (C=C), 107.1 (C=C), 62.7 ($\text{C}(\text{CH}_3)_2$), 49.5 ($\text{C}(\text{CH}_3)_2$), 33.3 (CH_2), 32.9 (CH_2), 22.5 (CH_3), 20.7 ppm (CH_3); IR(ATR, neat): 2973, 2929, 2869, 1720, 1707, 1701, 1686, 1365, 1062, 1038, 956, 806 cm^{-1} ; m.p. 116–118 $^\circ\text{C}$; HRMS(ESI): m/z calcd. for $\text{C}_{21}\text{H}_{28}\text{O}_5\text{Na}^+$: 383.1829 [$M+\text{Na}$] $^+$; found 383.1831; elemental analysis calcd.(%) for $\text{C}_{21}\text{H}_{28}\text{O}_5$: C, 69.98; H, 7.83; N, 0.00; found C, 69.84; H, 7.88; N, 0.01; R_f = 0.29 (hexane/ethyl acetate = 3/1).

3.7.3. Synthesis of calix[1]furan[2]pyrrole 2

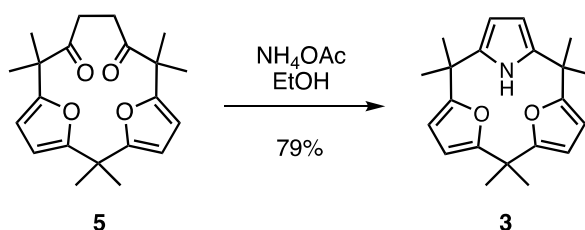


In a 50 mL round-bottomed flask equipped with a reflux condenser, compound **6** (600 mg, 1.66 mmol) was dissolved in absolute ethanol (12.0 mL), and added ammonium acetate (5.12 g, 66.4 mmol). The resulting mixture was heated to reflux for 1 h with magnetic stirring. After removal of ethanol by evaporation, the residue was diluted with chloroform (40 mL), washed with water (60 mL) and then with saturated aqueous solution of sodium bicarbonate (60 mL). The organic layer was dried over anhydrous sodium sulfate, and the solvent was removed using a rotary evaporator. The residue was chromatographed on silica gel (diameter: 3.5 cm, height: 15 cm, eluent; hexane/dichloromethane = 1/1) to give calix[1]furan[2]pyrrole **2** (357 mg, 67% yield) as a colorless solid.

Characterization data for compound 2

^1H NMR (CDCl_3 , 400 MHz, 298 K): δ = 7.01 (brs, 2H, NH), 5.96 (dd, 2H, pyrrolyl, J = 3.2, 2.8 Hz), 5.87 (s, 2H, furyl), 5.86 (dd, 2H, pyrrolyl, J = 3.2, 2.8 Hz), 1.60 (s, 6H, dimethylmethylene), 1.57 ppm (s, 12H, dimethylmethylene); ^{13}C NMR (CDCl_3 , 100 MHz, 298 K): δ = 161.5 (C=C), 142.1 (C=C), 139.4 (C=C), 104.4 (C=C), 103.9 (C=C), 103.1 (C=C), 37.57 ($\text{C}(\text{CH}_3)_2$), 37.55 ($\text{C}(\text{CH}_3)_2$), 28.8 (CH_3), 26.1 ppm (CH_3); IR(ATR, neat): 3438, 3327, 2965, 2927, 1221, 1038, 10210 756 cm^{-1} ; m.p. 110–119 $^\circ\text{C}$; HRMS(ESI): m/z calcd. for $\text{C}_{21}\text{H}_{26}\text{ON}_2\text{Na}^+$: 345.1937 [$M+\text{Na}$] $^+$; found 345.1940; elemental analysis calcd.(%) for $\text{C}_{21}\text{H}_{26}\text{O}_5 \cdot (\text{H}_2\text{O})_{0.5}$: C, 76.10; H, 8.21; N, 8.45; found C, 76.14; H, 8.28; N, 8.42; R_f = 0.52 (hexane/dichloromethane = 1/1).

3.7.4. Synthesis of calix[2]furan[1]pyrrole **3**

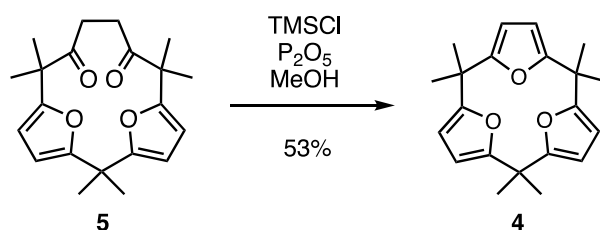


In a 20 mL round-bottomed flask equipped with a reflux condenser, compound **5** (200 mg, 0.58 mmol) and ammonium acetate (894 mg, 11.6 mmol) were placed and added absolute ethanol (4.0 mL). The mixture was heated to reflux for 5 h with magnetic stirring. The reaction solution was concentrated under reduced pressure, and the residue was dissolved in chloroform (40 mL). The organic solution was washed with water (20 mL \times 2), dried over anhydrous sodium sulfate, and the solvent was removed under reduced pressure. The crude product was purified by silica gel column chromatography (diameter: 2.0 cm, height: 10 cm, eluent: hexane/dichloromethane = 4/1) to give calix[2]furan[1]pyrrole **3** (149 mg, 79% yield) as colorless crystals.

Characterization data for compound **3**

^1H NMR (CDCl_3 , 400 MHz, 298 K): δ = 10.34 (brs, 1H, N-H), 5.75 (d, 2H, furyl, J = 3.2 Hz), 5.73 (d, 2H, furyl, J = 3.2 Hz), 5.59 (d, 2H, pyrrolyl, J = 2.8 Hz), 1.69 (s, 6H, dimethylmethylene), 1.67 ppm (s, 12H, dimethylmethylene); ^{13}C NMR (CDCl_3 , 100 MHz, 298 K): δ = 162.7 (C=C), 160.3 (C=C), 139.9 (C=C), 103.0 (C=C), 102.8 (C=C), 100.7 (C=C), 38.0 ($\text{C}(\text{CH}_3)_2$), 37.2 ($\text{C}(\text{CH}_3)_2$), 25.6 (CH_3), 24.3 ppm (CH_3); IR(ATR, neat): 3461, 2972, 2929, 2871, 1017, 773, 754, 731, 722 cm^{-1} ; m.p. 164-167 $^\circ\text{C}$; HRMS(ESI): m/z calcd. for $\text{C}_{21}\text{H}_{26}\text{NO}_2^+$: 324.1958 [$M+\text{H}$] $^+$; found 324.1960; elemental analysis calcd.(%) for $\text{C}_{21}\text{H}_{25}\text{NO}_2$; C, 77.98; H, 7.79; N, 4.33; found C, 77.85; H, 7.83; N, 4.30; R_f = 0.55 (hexane/dichloromethane = 4/1).

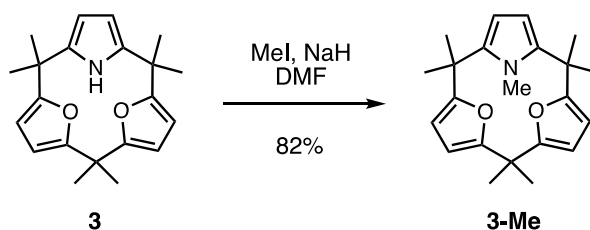
3.7.5. Synthesis of calix[3]furan **4**



In a 30 mL round-bottomed flask equipped with a reflux condenser, compound **5** (100 mg, 0.29 mmol) and phosphorus pentoxide (100 mg, 0.70 mmol) were suspended in dry methanol (1.5 mL) under nitrogen atmosphere. After addition of chlorotrimethylsilane (7.5 mL, 59 mmol) via syringe, the suspension was heated to reflux for 30 min with magnetic stirring. After cooled to room temperature, the reaction mixture was diluted with diethyl ether (20 mL) and slowly poured into saturated aqueous solution of sodium bicarbonate (20 mL) with the care for the gas generation. The organic layer was separated, washed with saturated aqueous solution of sodium bicarbonate (20 mL \times 2), and dried over anhydrous sodium sulfate. After concentrated under reduced pressure, the crude mixture was purified by silica gel column chromatography (diameter: 2.0 cm, height: 12 cm, eluent: hexane/dichloromethane = 4/1) to give calix[3]furan **4** (51 mg, 53% yield) as a colorless crystal.

¹H NMR (CDCl₃, 400 MHz, 298 K): δ = 5.80 (s, 6H, furyl), 1.63 ppm (s, 12H, dimethylmethylene); ¹³C NMR (CDCl₃, 100 MHz, 298 K): δ = 160.7 (C=C), 102.7 (C=C), 38.2 (C(CH₃)₂), 24.8 ppm (CH₃); IR(ATR, neat): 2971, 2932, 2869, 1533 cm⁻¹; m.p. 85–90 °C; HRMS(ESI): *m/z* calcd. for C₂₁H₂₄O₃Na⁺: 347.1618 [*M*+Na]⁺; found 347.1615; elemental analysis calcd.(%) for C₂₁H₂₄O₃; C, 77.75; H, 7.46; N, 0.00; found C, 77.57; H, 7.46; N, 0.03; *R*_f = 0.54 (hexane/dichloromethane = 4/1).

3.7.6. Synthesis of compound 3-Me

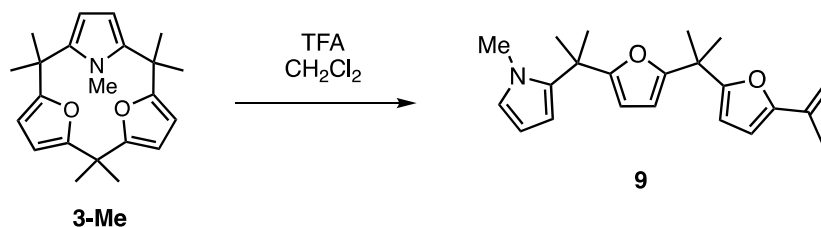


In a 100 mL two-necked flask equipped with inert gas inlet/outlet and rubber septum, compound **3** (800 mg, 2.47 mmol) and sodium hydride (1.98 g, 49.4 mmol, 60% dispersion in mineral oil) were placed under nitrogen atmosphere. *N,N*-dimethylformamide (DMF, 58 mL) was added to the flask via syringe. After addition of iodomethane (3.1 mL, 49.4 mmol) via syringe, the suspension was stirred at room temperature for 2 hours. The reaction mixture was slowly poured into water (100 mL) with the care for the heat generation. Crude product was extracted from the mixture with diethyl ether (100 mL \times 1, then 50 mL \times 2). Combined organic layer was washed with brine, dried over anhydrous sodium sulfate, and concentrated under reduced pressure. The crude product was purified by silica gel column chromatography (diameter: 4.2 cm, height: 10 cm, eluent: hexane/dichloromethane = 4/1) to give compound **3-Me** (684 mg, 82% yield) as a colorless solid.

Characterization data for compound 3-Me

^1H NMR (CDCl_3 , 400 MHz, 298 K): δ = 6.13 (s, 2H, pyrrolyl), 5.91 (d, 2H, furyl, J = 3.2 Hz), 5.83 (d, 2H, furyl, J = 3.2 Hz), 2.24 (s, 3H, *N*-methyl), 1.66 (s, 6H, methyl), 1.63 (s, 6H, methyl), 1.57 (s, 3H, methyl), 1.48 ppm (s, 3H, methyl); ^{13}C NMR (CDCl_3 , 100 MHz, 298 K): δ = 162.5 (C=C), 160.7 (C=C), 140.8 (C=C), 105.5 (C=C), 103.6 (C=C), 102.3 (C=C), 38.3 (C(CH₃)₂), 37.7 (C(CH₃)₂), 31.0 (CH₃), 29.5 (CH₃), 26.0 (CH₃), 25.8 (CH₃), 21.7 ppm (CH₃), IR(ATR, neat): 2996, 2969, 2927, 2870, 1015, 770 cm^{-1} ; m.p. 146–148 $^\circ\text{C}$; HRMS(ESI): calcd. for $\text{C}_{22}\text{H}_{27}\text{NO}_2\text{Na}^+$: 360.1934 [$M+\text{Na}$] $^+$; found 360.1935; elemental analysis calcd.(%) for $\text{C}_{22}\text{H}_{27}\text{NO}_2$: C, 78.30; H, 8.06; N, 4.15; found C, 78.20; H, 8.19; N, 4.10; R_f = 0.33 (hexane/dichloromethane = 4/1).

3.7.7. Isolation and characterization of **9**

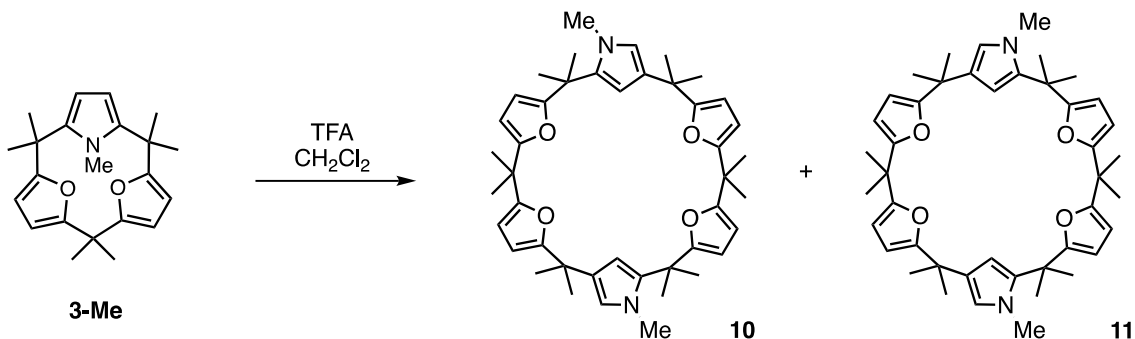


In a 300 mL round-bottomed flask, compound **3-Me** (100 mg, 0.29 mmol) was dissolved in dichloromethane (90 mL). After addition of trifluoroacetic acid (69 μ L, 0.90 mmol), resulting solution was stirred for 15 seconds at room temperature. Then the reaction was immediately quenched by addition of triethylamine (2.5 mL). The reaction solution was washed with saturated aqueous solution of sodium bicarbonate (50 mL \times 2), dried over anhydrous sodium sulfate, and concentrated under reduced pressure. Purification of **9** was conducted by recycling gel permeation chromatography using chloroform as an eluent (*ca.* 15 mg, 15% yield).

Characterization data for compound **9**

¹H NMR (CDCl₃, 400 MHz, 298 K): δ = 6.44 (dd, 1H, pyrrolyl-a, J = 1.8 Hz, 2.7 Hz), 6.13 (d, 1H, furyl-b, J = 3.2 Hz), 6.04 (dd, 1H, pyrrolyl-b, J = 1.8 Hz, 3.7 Hz), 6.01 (dd, 1H, pyrrolyl-b, J = 2.7 Hz, 3.7 Hz), 5.93 (d, 1H, furyl-b, J = 3.2 Hz), 5.90 (d, 1H, furyl-b, J = 3.2 Hz), 5.86 (d, 1H, furyl-b, J = 3.2 Hz), 5.37 (brs, 1H, vinyl), 4.86 (dd, 1H, vinyl, J = 1.4 Hz, 1.8 Hz), 3.19 (s, 3H, *N*-methyl), 1.97 (s, 3H, allyl), 1.63 (s, 6H, dimethylmethylene), 1.59 ppm (s, 6H, dimethylmethylene); ¹³C NMR (CDCl₃, 100 MHz, 298 K): δ = 159.9 (C=C), 159.7 (C=C), 158.1 (C=C), 153.6 (C=C), 138.2 (C=C), 133.0 (C=C), 123.4 (C=C), 108.9 (C=C), 106.9 (C=C), 105.83 (C=C), 105.75 (C=C), 105.6 (C=C), 104.7 (C=C), 104.6 (C=C), 37.6 (C(CH₃)₂), 36.6 (C(CH₃)₂), 35.1 (NCH₃), 28.6 (C(CH₃)₂), 26.4 (C(CH₃)₂), 19.3 ppm (C=C-CH₃); HRMS(ESI): m/z calcd. for C₂₂H₂₇O₂NNa⁺: 360.1934 [M +Na]⁺; found 360.1933.

3.7.8. Synthesis of macrocycles **10** and **11**



In a 300 mL round-bottomed flask, compound **3-Me** (200 mg, 0.59 mmol) was dissolved in dichloromethane (179 mL). After addition of trifluoroacetic acid (137 μL , 1.79 mmol), the reaction solution was stirred for 1 h at room temperature. The reaction was then quenched by addition of triethylamine (2.5 mL). The solution was then washed with saturated aqueous solution of sodium bicarbonate (50 mL \times 2), dried over anhydrous sodium sulfate, and concentrated under reduced pressure. Residual solid was chromatographed on silica gel column (diameter: 3 cm, height: 15 cm, eluent: hexane/dichloromethane = 3/1) to give **10** and **11** as an isomeric mixture (100 mg, 50%, **10:11** = 64:36 determined from ^1H NMR spectrum, see **Figure 3-16**).

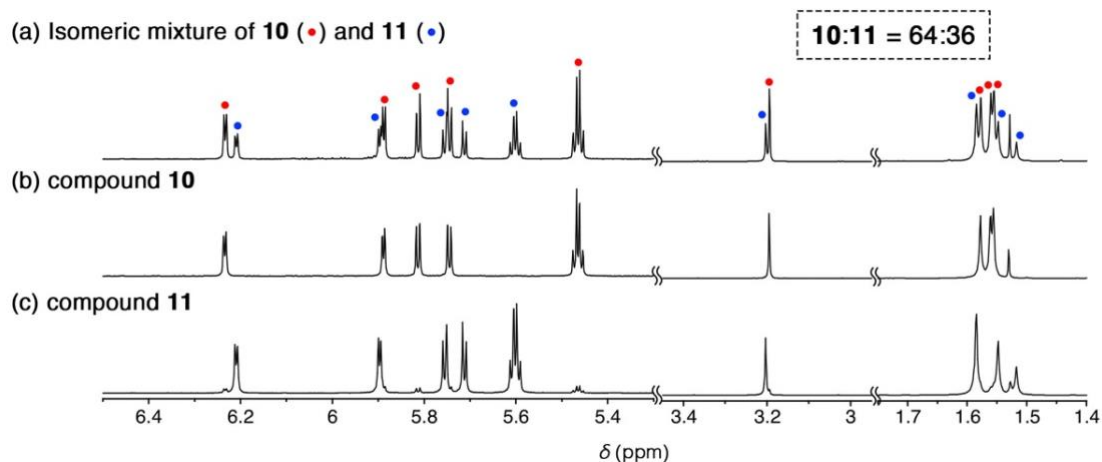


Figure 3-16. ^1H NMR spectra of (a) a mixture of **10** and **11** obtained after the first chromatographic separation, (b) isolated **10**, and (c) isolated **11** (chloroform-*d*, 400 MHz, 298 K)

Since compounds **10** and **11** have similar R_f values on silica gel, only a few milligrams of each component were isolated after repeated silica gel column chromatography (eluent: hexane/toluene = 1/1) for structural analysis.

Characterization data for **10**

^1H NMR (CDCl_3 , 400 MHz, 298 K): δ = 6.23 (d, 2H, pyrrolyl- α , J = 2.3 Hz), 5.89 (d, 2H, pyrrolyl- β , J = 2.3 Hz), 5.81 (d, 2H, furyl- β , J = 3.2 Hz), 5.75 (d, 2H, furyl- β , J = 3.2 Hz), 5.47 (d, 2H, furyl- β , J = 3.2 Hz), 5.46 (d, 2H, furyl- β , J = 3.2 Hz), 3.20 (s, 6H, *N*-Me), 1.58 (s, 12H, dimethylmethylene), 1.560 (s, 12H, dimethylmethylene), 1.556 ppm (s, 12H, dimethylmethylene); ^{13}C NMR (CDCl_3 , 100 MHz, 298 K): δ = 162.7 (C=C), 159.0 (C=C), 158.6 (C=C), 157.8 (C=C), 137.3 (C=C), 129.3 (C=C), 119.9 (C=C), 104.9 (C=C, overlapping), 104.6 (C=C), 104.0 (C=C), 102.7 (C=C), 37.7 (C(CH₃)₂), 36.7 (C(CH₃)₂), 35.5 (NCH₃), 35.4 (C(CH₃)₂), 28.3 (C(CH₃)₂), 28.2 (C(CH₃)₂), 26.5 ppm (C(CH₃)₂); HRMS(ESI): calcd. for $\text{C}_{44}\text{H}_{54}\text{N}_2\text{O}_4\text{Na}^+$: 697.3976 [$M+\text{Na}$]⁺; found 697.3960; R_f = 0.30 (hexane/toluene = 1/1).

Characterization data for **11**

^1H NMR (CDCl_3 , 400 MHz, 298 K): δ = 6.21 (d, 2H, pyrrolyl- α , J = 2.3 Hz), 5.90 (d, 2H, pyrrolyl- β , J = 2.3 Hz), 5.76 (d, 2H, furyl- β , J = 3.2 Hz), 5.71 (d, 2H, furyl- β , J = 3.2 Hz), 5.61 (d, 2H, furyl- β , J = 3.2 Hz), 5.60 (d, 2H, furyl- β , J = 3.2 Hz), 3.20 (s, 6H, *N*-Me), 1.59 (s, 12H, dimethylmethylene, s, 6H, dimethylmethylene, overlapping), 1.55 (s, 12H, dimethylmethylene), 1.52 ppm (s, 6H, dimethylmethylene); ^{13}C NMR (CDCl_3 , 100 MHz, 298 K): δ = 162.5 (C=C), 159.3 (C=C), 158.19 (C=C), 158.16 (C=C), 137.0 (C=C), 128.9 (C=C), 120.1 (C=C), 105.1 (C=C), 104.7 (C=C), 104.4 (C=C), 104.1 (C=C), 103.5 (C=C), 37.9 (C(CH₃)₂), 36.6 (C(CH₃)₂), 35.6 (C(CH₃)₂), 35.3 (NCH₃), 28.4 (C(CH₃)₂), 28.2 (C(CH₃)₂), 27.3 (C(CH₃)₂), 26.5 ppm (C(CH₃)₂); HRMS(ESI): calcd. for $\text{C}_{44}\text{H}_{54}\text{N}_2\text{O}_4\text{Na}^+$: 697.3976 [$M+\text{Na}$]⁺; found 697.3958; R_f = 0.27 (hexane/toluene = 1/1).

3.7.9. Single crystal X-ray diffraction analyses

Crystallographic data for 6

Single crystals of **6** suitable for X-ray diffraction analysis were obtained by slow evaporation of a methanol solution of **6**.

$C_{21}H_{28}O_5$, $M = 360.43$, crystal size: $0.45 \times 0.24 \times 0.11 \text{ mm}^3$, triclinic, space group $P\bar{1}$, $a = 9.9880(2)$, $b = 12.3967(3)$, $c = 16.7198(4) \text{ \AA}$, $\alpha = 88.015(2)$, $\beta = 83.096(2)$, $\gamma = 89.960(2)^\circ$, $V = 2053.96(8) \text{ \AA}^3$, $Z = 4$, $T = 123(2) \text{ K}$, $\mu = 0.082 \text{ mm}^{-1}$, $D_{\text{calc}} = 1.166 \text{ g/cm}^3$, $1.644^\circ \leq \theta \leq 27.498^\circ$, 7735 unique reflections out of 9009 with $I > 2\sigma(I)$, GOF = 1.045, $R_1 = 0.0546$, $wR_2 = 0.1525$, CCDC: 2127626

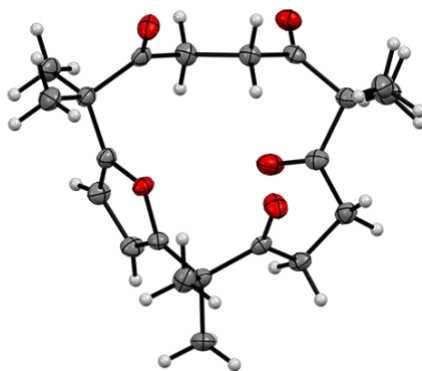


Figure 3-17. ORTEP drawing of the crystal structure of **6** at the 50% thermal probability levels (C: gray, H: white, O: red).

Crystallographic data for 2

Single crystals of **2** suitable for X-ray diffraction analysis were obtained by slow evaporation of a methanol solution of **2**.

(C₂₁H₂₆N₂O)₂•H₂O, $M = 662.89$, crystal size: $0.54 \times 0.30 \times 0.10$ mm³, triclinic, space group $P\bar{1}$, $a = 10.9348(2)$, $b = 12.4101(2)$, $c = 14.8887(2)$ Å, $\alpha = 87.972(2)$, $\beta = 81.500(2)$, $\gamma = 68.029(2)^\circ$, $V = 1852.67(6)$ Å³, $Z = 2$, $T = 123(2)$ K, $\mu = 0.075$ mm⁻¹, $D_{\text{calc}} = 1.188$ g/cm³, $1.770^\circ \leq \theta \leq 27.499^\circ$, 6883 unique reflections out of 8129 with $I > 2\sigma(I)$, GOF = 1.084, $R_1 = 0.0408$, $wR_2 = 0.1082$, CCDC: 2127623

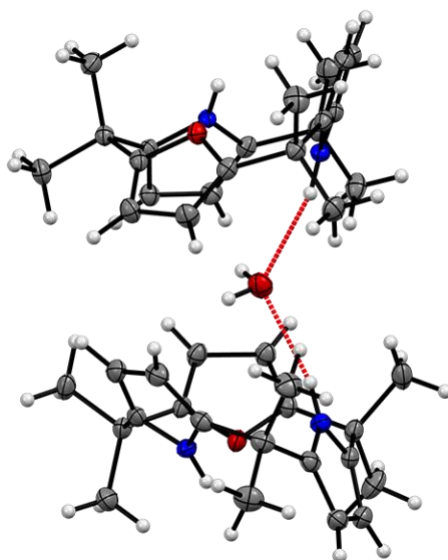


Figure 3-18. ORTEP drawing of the asymmetric unit for crystal structure of **2**•H₂O at the 50% thermal probability levels (C: gray, H: white, N: blue, O: red). The red dotted lines show presumed hydrogen bonds between oxygen atom and pyrrole NH.

Crystallographic data for 3

Single crystals of **3** suitable for X-ray diffraction analysis were grown by vapor diffusion of hexane into a dichloromethane solution of **3**.

$C_{21}H_{25}NO_2$, $M = 323.42$, crystal size: $0.56 \times 0.37 \times 0.15 \text{ mm}^3$, orthorhombic, space group $Pnma$, $a = 10.2822(6)$, $b = 16.8541(10)$, $c = 10.2716(7) \text{ \AA}$, $a = b = c = 90^\circ$, $V = 1780.04(19) \text{ \AA}^3$, $Z = 4$, $T = 123(2) \text{ K}$, $\mu = 0.077 \text{ mm}^{-1}$, $D_{\text{calc}} = 1.207 \text{ g/cm}^3$, $2.417^\circ \leq \theta \leq 26.489^\circ$, 1691 unique reflections out of 1887 with $I > 2\sigma(I)$, GOF = 1.093, $R_1 = 0.0416$, $wR_2 = 0.1137$, CCDC: 2127624

Crystallographic data for 4

Single crystals suitable for X-ray diffraction analysis were obtained by slow evaporation of a methanol solution of **4**.

$C_{21}H_{24}O_3$, $M = 324.40$, crystal size: $0.80 \times 0.60 \times 0.10 \text{ mm}^3$, orthorhombic, space group $Pnma$, $a = 10.2015(8)$, $b = 16.5522(12)$, $c = 10.4282(7) \text{ \AA}$, $a = b = c = 90^\circ$, $V = 1760.9(2) \text{ \AA}^3$, $Z = 4$, $T = 123(2) \text{ K}$, $\mu = 0.080 \text{ mm}^{-1}$, $D_{\text{calc}} = 1.224 \text{ g/cm}^3$, $2.308^\circ \leq \theta \leq 25.242^\circ$, 1643 unique reflections out of 1974 with $I > 2\sigma(I)$, GOF = 1.063, $R_1 = 0.0404$, $wR_2 = 0.1049$, CCDC: 2080606

Crystallographic data for 3-Me

Single crystals of **3-Me** suitable for X-ray diffraction analysis were obtained by slow evaporation of a dichloromethane solution of **3-Me**.

$C_{22}H_{27}NO_2$, $M = 337.44$, crystal size: $0.55 \times 0.19 \times 0.16 \text{ mm}^3$, triclinic, space group $P-1$, $a = 9.7363(2)$, $b = 10.4441(2)$, $c = 10.8166(2) \text{ \AA}$, $\alpha = 97.177(2)$, $\beta = 105.930(2)$, $\gamma = 114.819(2)^\circ$, $V = 922.93(4) \text{ \AA}^3$, $Z = 2$, $T = 123(2) \text{ K}$, $\mu = 0.077 \text{ mm}^{-1}$, $D_{\text{calc}} = 1.214 \text{ g/cm}^3$, $2.037^\circ \leq \theta \leq 26.988^\circ$, 3395 unique reflections out of 3909 with $I > 2\sigma(I)$, GOF = 1.069, $R_1 = 0.0373$, $wR_2 = 0.0937$, CCDC: 2127625

Crystallographic data for 10

Single crystals of **10** suitable for X-ray diffraction analysis were grown by vapor diffusion of methanol into a dichloromethane solution of **10**.

$C_{44}H_{54}N_2O_4$, $M = 674.89$, crystal size: $0.22 \times 0.06 \times 0.03 \text{ mm}^3$, triclinic, space group $P-1$, $a = 6.9663(4)$, $b = 11.8577(8)$, $c = 12.9052(9) \text{ \AA}$, $\alpha = 107.659(6)$, $\beta = 102.976(5)$, $\gamma = 93.403(5)^\circ$, $V = 980.48(12) \text{ \AA}^3$, $Z = 1$, $T = 123(2) \text{ K}$, $\mu = 0.072 \text{ mm}^{-1}$, $D_{\text{calc}} = 1.143 \text{ g/cm}^3$, $1.713^\circ \leq \theta \leq 26.499^\circ$, 3234 unique reflections out of 4061 with $I > 2\sigma(I)$, GOF = 1.061, $R_1 = 0.0758$, $wR_2 = 0.2117$, CCDC: 2127627

Crystallographic data for 11

Single crystals of **11** suitable for X-ray diffraction analysis were grown by vapor diffusion of hexane into a dichloromethane solution of **11**.

$C_{44}H_{54}N_2O_4 \cdot (C_6H_{14})_{0.424} \cdot (CH_2Cl_2)_{0.136}$, $M = 723.18$, crystal size: $0.55 \times 0.21 \times 0.20 \text{ mm}^3$, triclinic, space group $P-1$, $a = 12.8545(4)$, $b = 13.6755(4)$, $c = 14.8304(5) \text{ \AA}$, $\alpha = 110.186(3)$, $\beta = 98.026(3)$, $\gamma = 115.491(3)^\circ$, $V = 2077.07(13) \text{ \AA}^3$, $Z = 2$, $T = 123(2) \text{ K}$, $\mu = 0.090 \text{ mm}^{-1}$, $D_{\text{calc}} = 1.156 \text{ g/cm}^3$, $1.799^\circ \leq \theta \leq 27.499^\circ$, 7798 unique reflections out of 9318 with $I > 2\sigma(I)$, GOF = 1.100, $R_1 = 0.0415$, $wR_2 = 0.1155$, CCDC: 2127628

3.7.10. Computational study on the energy of cone and partial-cone conformations

All structures were optimized and calculated their energy at the B3LYP/6-31G(d) level of theory using Gaussian 16 Rev. C01.¹⁰

3.7.11. Computational study on macrocyclic strains

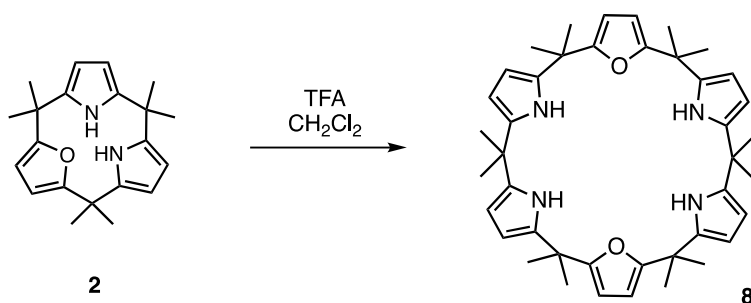
All calculations were performed at the B3LYP/cc-pVTZ level of theory with Grimme's type dispersion correction,^{11,12} followed by frequency analysis to confirm that the obtained optimized structures were stable structures using Gaussian 16 Rev. C01.¹⁰ The polarizable continuum model (IEFPCM)¹³ was also employed in all calculations to include solvation effect of CH₂Cl₂ solvent. In order to evaluate strain energy, the geometries of **1-4** and **3-Me** were optimized using their crystal structures as the initial structures, and the corresponding linear forms of **1-4** and **3-Me** were also optimized. To construct the linear forms, the ring-opened form were terminated by the neighbor units such as pyrrole, furan, and *N*-methylpyrrole in each ring. In addition, the molecules consisting of two units used to terminate the ring-opened form were also optimized. The evaluation scheme of each structure is shown in the Scheme 3-2.

According to the evaluation scheme of the strain energy as shown in Scheme S1, the strain energy was defined as the following equation:

$$\Delta E_{\text{strain}} = (E_{\text{linear}}) - (E_{\text{ring}} + E_{\text{terminal}})$$

where ΔE_{strain} is the ring strain energy, E_{linear} is the energy in the linear form, E_{ring} is the energy in the ring form, and E_{terminal} is the energy of a molecule consisting of terminating units.

3.7.12. Strain-induced ring expansion reaction of **2**



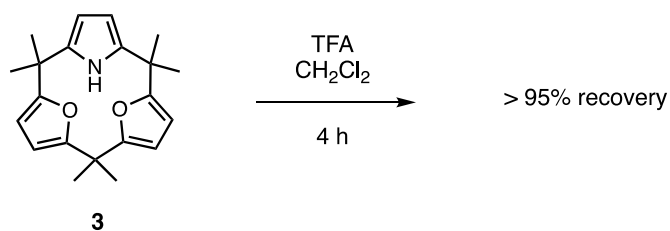
NMR spectral analysis

To a stirred solution of calix[1]furan[2]pyrrole **2** (3.3 mM, 5.0 mL) in CH_2Cl_2 , trifluoroacetic acid was added as a 1.0 M dichloromethane solution (50 μL). After stirring the solution for predetermined periods (5 sec, 30 sec, 30 min, and 4 h), the reaction was immediately quenched by the addition of a saturated aqueous solution of sodium bicarbonate. The organic phase was dried over anhydrous magnesium sulfate, and the solvent was evaporated off under reduced pressure. The residue was dissolved in CDCl_3 and analyzed by ^1H NMR spectroscopy.

HPLC analysis

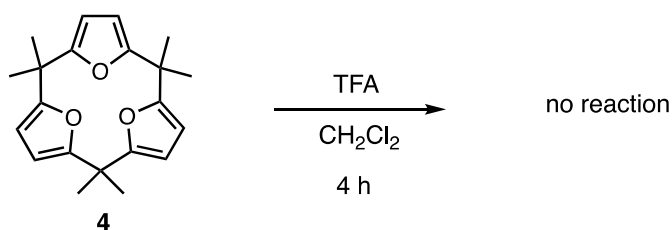
To a stirred solution of calix[1]furan[2]pyrrole **2** (3.3 mM, 1.5 mL) in CH_2Cl_2 , trifluoroacetic acid was added as a 1.0 M CH_2Cl_2 solution (15 μL). After stirring the solution at room temperature for 5 sec, 10 sec, 30 sec, 1 min, 5 min, 30 min, and 4 h, small aliquots of reaction solution were taken and immediately quenched by the addition of excess triethylamine (*ca.* 2 μL). The reaction mixtures were then analyzed by HPLC.

3.7.13. Acid stability test for 3



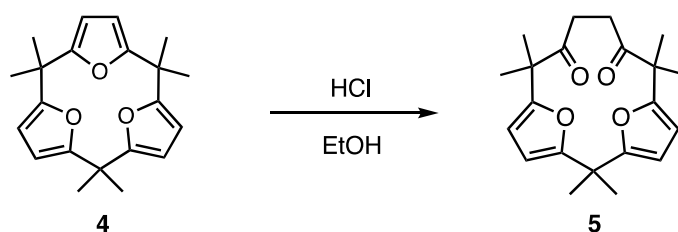
To a stirred solution of **3** (3.3 mM, 1.5 mL) in CH₂Cl₂, trifluoroacetic acid was added as a 1.0 M CH₂Cl₂ solution (15 μL). After stirring the solution at room temperature for 4 h, the reaction was quenched by adding saturated aqueous solution of sodium bicarbonate. The reaction mixture was then dried over anhydrous sodium sulfate and concentrated under reduced pressure. The residue was then analyzed by ¹H NMR, HPLC, and ESI-MS. Recovery rate of compound **3** was calculated by NMR analysis. Note that NMR analysis also confirmed that minor fraction at 13.1 min on HPCL chromatogram (see **Figure 3-6**) contained several minor products which could not be separated.

3.7.14. Acid stability for 4



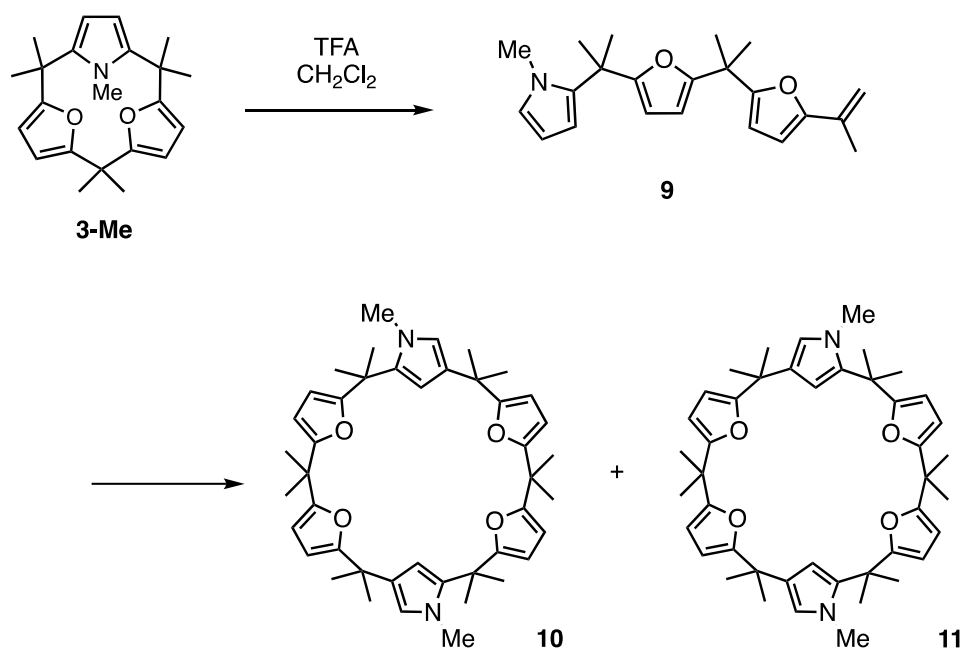
To a stirred solution of **4** (3.3 mM, 1.5 mL) in CH₂Cl₂, trifluoroacetic acid was added as a 1.0 M CH₂Cl₂ solution (15 μL). After stirring the solution at room temperature for 4 h, the reaction was quenched by addition of saturated aqueous solution of sodium bicarbonate. The reaction mixture was then dried over anhydrous sodium sulfate and concentrated under reduced pressure. The residue was then analyzed by ¹H NMR and HPLC.

3.7.15. Hydrolysis of 4



In a 10 mL round bottomed flask, 12 M hydrochloric acid (0.4 mL) was added to a stirred solution of calix[3]furan **4** in ethanol (0.75 mL, 133 mM). After stirring the solution at room temperature for 1, 7, 12, 24, and 30 h, small aliquots of the solution were removed and immediately quenched via the addition of saturated aqueous solution of sodium bicarbonate. The products were extracted with Et₂O, dried over anhydrous magnesium sulfate, and the solvent evaporated off. The residue was dissolved in CDCl₃ and analyzed by ¹H NMR spectroscopy.

3.7.16. Ring cleavage and expansion reaction of 3-Me



To a stirred dichloromethane solution of **3-Me** (3.3 mM, 1.5 mL), a 1.0 M dichloromethane solution of trifluoroacetic acid (15 μ L) was added at room temperature. After stirring the solution for 5 sec, 10 sec, 30 sec, 1 min, 5 min, 10 min, 30 min, 1 h, and 4 h, small aliquots of reaction solution were taken and immediately quenched by addition of excess triethylamine (*ca.* 2 μ L). The reaction mixtures were then analyzed by HPLC.

3.7.17. Theoretical calculation on reaction mechanism analysis

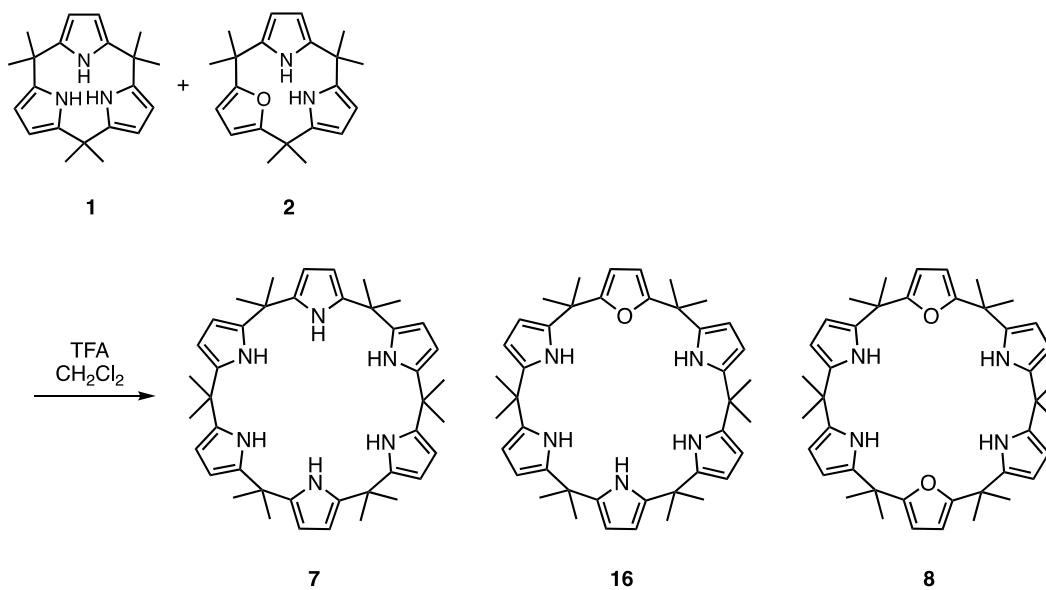
All calculations were performed at the B3LYP/cc-pVTZ level of theory with Grimme's type dispersion correction,^{11,12} followed by frequency analysis to confirm that the obtained optimized structures were stable structures and obtain thermal corrections using Gaussian 16 Rev. C01.¹⁰ The polarizable continuum model (IEFPCM)¹³ was also employed in all calculations to include solvation effect of CH₂Cl₂ solvent. As shown in Figure3-13, all structures of the ring forms of **2** and **3-Me**, respective protonated structures in the ring forms and linear forms, and trifluoroacetic acid (TFA) and trifluoroacetate were optimized. The relative free energies to the ring form of **2** or **3-Me** was defined as the following equations:

$$\Delta G_1 = (G_{\text{ring+H}} + G_{\text{TFA-H}}) - (G_{\text{ring}} + G_{\text{TFA}}),$$

$$\Delta G_2 = (G_{\text{linear+H}} + G_{\text{TFA-H}}) - (G_{\text{ring}} + G_{\text{TFA}}),$$

where ΔG_1 is the relative free energy of protonated ring form, ΔG_2 is the relative free energy of protonated linear form, G_{ring} is the free energy in the ring form, G_{linear} is the free energy in the linear form, $G_{\text{ring+H}}$ is the free energy in the protonated ring form, $G_{\text{linear+H}}$ is the free energy in the protonated linear form, $G_{\text{TFA-H}}$ is the free energy of trifluoroacetate, and G_{TFA} is the free energy of TFA.

3.7.18. Scrambling experiment using a mixture of **1** and **2**



In a 20 mL round-bottomed flask, **1** (1.0 mg, 3.3 μmol) and **2** (1.0 mg, 3.3 μmol) were dissolved in dichloromethane (2.0 mL). After addition of a 1.0 M dichloromethane solution of trifluoroacetic acid (20 μL , 20 μmol) the solution was stirred for 1 minute at room temperature. The reaction was then quenched with triethylamine (15 μL). The solution was washed with saturated aqueous solution of sodium bicarbonate (5 mL \times 2) and dried over anhydrous magnesium sulfate. After evaporation of the solvent, reaction products were analyzed by ¹H NMR. NMR yields (**7**, 51% (based on **1**); **16**, 35%; **8**, 60% (based on **2**)) were determined using 1,3,5-trichlorobenzene as an internal standard.

3.8. References

1. B. Biletskyi, P. Colonna, K. Masson, J.-L. Parrain, L. Commeiras, G. Chouraqui, Small rings in the bigger picture: ring expansion of three- and four-membered rings to access larger all-carbon cyclic systems, *Chem. Soc. Rev.*, **2021**, *50*, 7513–7538.
2. J. R. Donald, W. P. Unsworth, Ring -Expansion Reactions in the Synthesis of Macrocycles and Medium-Sized Rings, *Chem. Eur. J.*, **2017**, *23*, 8780–8799.
3. K. T. Mortensen, T. J. Osberger, T. A. King, H. F. Sore, D. R. Spring, Strategies for the Diversity-Oriented Synthesis of Macrocycles, *Chem. Rev.*, **2019**, *119*, 10288–10317.
4. Y. Tobe, K. Ueda, K. Kakiuchi, Y. Odaira, Y. Kai, N. Kasai, Synthesis, structure, and reactivities of [6]paracyclophanes, *Tetrahedron*, **1986**, *42*, 1851–1858.
5. D.-S. Choi, S. Huang, M. Huang, T. S. Barnard, R. D. Adams, J. M. Seminario, J. M. Tour, Revised Structures of *N*-Substituted Dibrominated Pyrrole Derivatives and Their Polymeric Products. Termaleimide Models with Low Optical Band Gaps, *J. Org. Chem.*, **1998**, *63*, 2646–2655.
6. C. Zonta, Fabrizio Fabris, O. D. Lucchi, The Pyrrole Approach toward the Synthesis of Fully Functionalized Cup-Shaped Molecules, *Org. Lett.*, **2005**, *7*, 1003–1006.
7. G. Cafeo, F. H. Kohnke, G. L. L. Torre, M. F. Parisi, R. P. Nascone, A. J. P. White, D. J. Williams, Calix[6]pyrrole and Hybrid Calix[*n*]furan[*m*]pyrroles ($n+m=6$): Syntheses and Host–Guest Chemistry, *Chem. Eur. J.*, **2002**, *8*, 3148–3156
8. G. M. Sheldrick, *SHELXT* – Integrated space-group and crystal-structure determination, *Acta Crystallogr. Sect. A*, **2015**, *71*, 3–8.
9. G. M. Sheldrick, Crystal structure refinement with *SHELXL*, *Acta Crystallogr. Sect. C*, **2015**, *71*, 3–8.
10. Gaussian 16, Revision C.01, M. J. Frisch, G. W. Trucks, H. B. Schlegel, G. E. Scuseria, M. A. Robb, J. R. Cheeseman, G. Scalmani, V. Barone, G. A. Petersson, H. Nakatsuji, X. Li, M. Caricato, A. V. Marenich, J. Bloino, B. G. Janesko, R. Gomperts, B. Mennucci, H. P. Hratchian, J. V. Ortiz, A. F. Izmaylov, J. L. Sonnenberg, D. Williams-Young, F. Ding, F. Lipparini, F. Egidi, J. Goings, B. Peng, A. Petrone, T. Henderson, D. Ranasinghe, V. G. Zakrzewski, J. Gao, N. Rega, G. Zheng, W. Liang, M. Hada, M. Ehara, K. Toyota, R. Fukuda, J. Hasegawa, M. Ishida, T. Nakajima, Y. Honda, O. Kitao, H. Nakai, T. Vreven, K. Throssell, J. A. Montgomery, Jr., J. E. Peralta, F. Ogliaro, M. J. Bearpark, J. J. Heyd, E. N. Brothers, K. N. Kudin, V. N. Staroverov, T. A. Keith, R. Kobayashi, J. Normand, K. Raghavachari, A. P. Rendell, J. C. Burant, S. S. Iyengar, J. Tomasi, M. Cossi, J. M.

Millam, M. Klene, C. Adamo, R. Cammi, J. W. Ochterski, R. L. Martin, K. Morokuma, O. Farkas, J. B. Foresman, and D. J. Fox, Gaussian, Inc., Wallingford CT, 2016. S. Grimme, J. Antony, S. Ehrlich, H. Krieg, A consistent and accurate *ab initio* parametrization of density functional dispersion correction (DFT-D) for the 94 elements H-Pu, *J. Chem. Phys.*, **2010**, *132*, 154104.

11. S. Grimme, S. Ehrlich, L. Goerigk, Effect of the damping function in dispersion corrected density functional theory, *J. Comput. Chem.*, **2011**, *32*, 1456–1465.
12. E. Cancès, B. Mennucci, J. Tomasi, A new integral equation formalism for the polarizable continuum model: Theoretical background and applications to isotropic and anisotropic dielectrics, *J. Chem. Phys.*, **1997**, *107*, 3032–3041.

Chapter 4

Construction of Chiral System by Controlling Aromatic Ring Inversion in Calix[3]pyrrole

Abstract

The chirality of calix[1]furan[1]pyrrole[1]thiophene, an asymmetric analogue of calix[3]pyrrole was investigated. This macrocycle showed the existence of separable enantiomers, which underwent racemization in solution at room temperature. Since racemization occurs via aromatic ring inversion, *N*-methylation was performed to suppress ring flipping. As a result, the *N*-methylated analogue showed no observable racemization over one month in solution. The change in racemization behavior upon *N*-methylation was supported by MD simulations, and *N*-methylation in the presence of chiral ammonium afforded *N*-methylated product with a slight stereoselectivity. Calix[1]furan[1]pyrrole[1]thiophene also underwent a ring expansion reaction under acidic conditions to give double-, triple-, and quadruple-sized macrocycles that lost chirality due to free aromatic ring inversions.

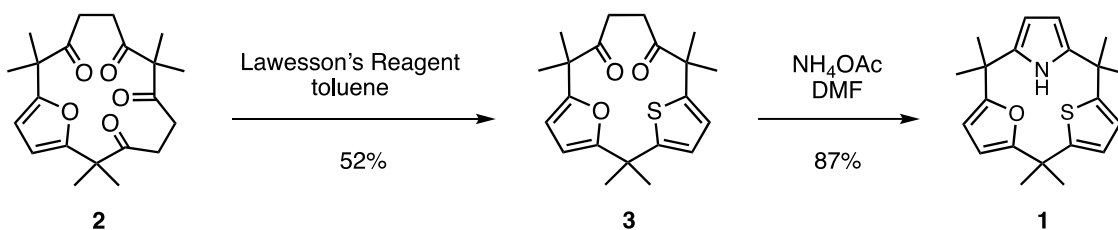
4.1. Introduction

In the previous sections, calix[3]pyrrole and its analogues tended to be non-planar as indicated by their crystal structures. In addition, *N*-methylated calix[2]furan[1]pyrrole showed a slower aromatic ring inversion on the NMR time scale. Thus, if calix[3]pyrrole skeletons were constructed with three different aromatic rings, and their aromatic ring inversion was slow enough, the molecule would have no stereogenic center, but would belong to the C_1 point group, and thus be chiral. Such chirality of a macrocyclic structure, where racemization occurs via macrocyclic inversion and ring cleavage leads to the formation of achiral products, is called “inherent chirality”, which was first introduced by Böhmer to describe the chirality of asymmetrically substituted calix[4]arene¹. Although an increasing number of inherently chiral molecules have been reported²⁻⁵, it is unclear how much inversion barrier is sufficient to make the macrocycle chiral. Therefore, a new motif for inherently chiral macrocycles would help to understand the requirements for inherently chiral macrocycles.

In this work, calix[1]furan[1]pyrrole[1]thiophene was prepared as an asymmetric derivative of calix[3]pyrrole. Thiophene ring is accessible from 1,4-diketone structure, and sulfur with a large atomic radius is expected to suppress its aromatic ring inversion. Indeed, calix[1]furan[1]pyrrole[1]thiophene was separable into the pair of enantiomers, but they underwent racemization in solution. This racemization was successfully suppressed by *N*-methylation, allowing the optical resolution of the enantiomers. *N*-methylation in the presence of a chiral ammonium salt afforded asymmetrically *N*-methylated product, although the *ee* was only modest. Furthermore, calix[1]furan[1]pyrrole[1]thiophene underwent strain-induced ring expansion reaction under acidic conditions, to afford calix[*n*]furan[*n*]pyrrole[*n*]thiophene, where $n = 2, 3, 4$. Not only was it confirmed that ring expanded products are achiral, but also the synthetic application of the ring expansion reaction of the calix[3]-type macrocycle was demonstrated.

4.2. Preparation and Chirality of Calix[1]furan[1]pyrrole[1]thiophene

Calix[1]furan[1]pyrrole[1]thiophene **1** was prepared from the cyclic monofuran **2** prepared in section 2.2. Compound **2** was first treated with Lawesson's reagent in toluene to give thiophene containing macrocycle **3** in 52% yield. Then **3** was converted to calix[1]furan[1]pyrrole[1]thiophene **1** using ammonium acetate in DMF in 87% yield. The formation of **1** was confirmed by HR-ESI mass spectroscopic analysis, which showed a peak of **1** as a sodium adduct ($[1+Na^+]$ at $m/z = 381.1485$, calculated for $C_{21}H_{26}O_3S+Na^+$, $m/z = 381.1494$). The 1H NMR spectrum of **1** showed six methyl protons individually at 1.4–1.8 ppm, suggesting that the aromatic ring inversion of **1** is slower on the NMR time scale. Since the 1H NMR spectra of calix[3]pyrrole and calix[1]furan[2]pyrrole indicated fast aromatic ring inversion on the NMR time scale, the introduction of thiophene not only makes the macrocycle asymmetric but also slows down the aromatic ring inversion.



Scheme 4-1. Synthesis of calix[1]furan[1]pyrrole[1]thiophene **1** from **2**.

Single crystal X-ray diffraction analysis of **1** revealed that it adopts the partial-cone conformation with a C_1 symmetric structure in which thiophene faces the opposite side to pyrrole and furan (**Figure 4-1a**). Only one enantiomer was found in the crystal structure, and its relative configuration was determined to be (R^*, R^*, S^*) with respect to thiophene, furan, and pyrrole planes based on the definition of planar chirality. Since there can be eight conformational isomers of **1** with respect to planar chirality on each aromatic ring, the relative energies were calculated and compared. Considering the pairs of enantiomers, energy calculations were performed on four isomers, namely (R^*, R^*, R^*) , (R^*, R^*, S^*) , (S^*, R^*, S^*) , and (R^*, S^*, S^*) . It was found that the observed isomer (R^*, R^*, S^*) is the most stable as 2.4 kcal/mol that of other isomers (**Figure 4-1b**) This might be due to steric hindrance of sulfur is the largest, NH is the second largest, and oxygen is the smallest among three heteroatoms. Therefore, **1** prefers (R^*, R^*, S^*) configuration, in which NH and sulfur atom are opposite to each other, and the furan oxygen atom faces the same direction as NH, not thiophene.

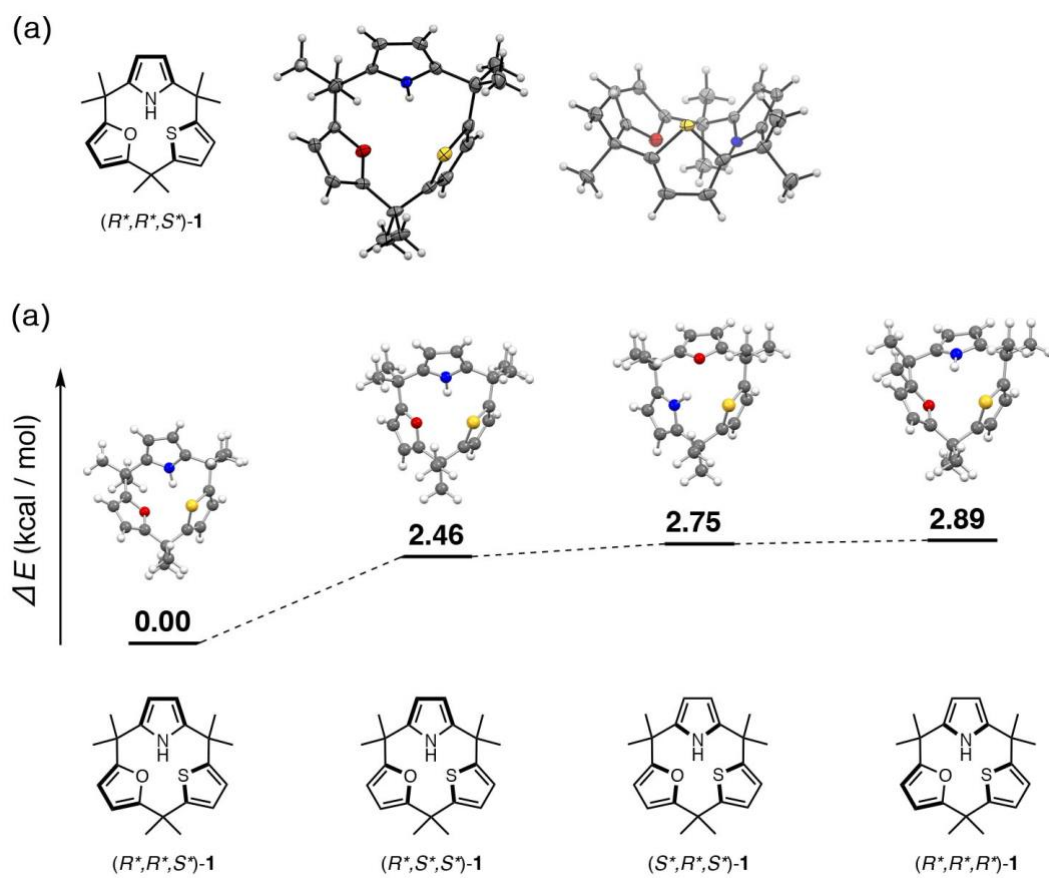


Figure 4-1. (a) Single crystal structure of **1** viewed from top and side, and (b) relative energy comparison between conformational isomers of **1** (gray: C, white: H, red: O, blue: N, yellow: S).

When **1** was analyzed by HPLC on a chiral column (CHIRALPAC IG-3) using hexane/*i*-PrOH (*v/v* = 1/1) as eluent, two peaks were observed at 14.1 and 14.6 minutes (**Figure 4-2**). The CD spectra of each fraction showed mirror-image spectra, indicating that these fractions are enantiomers. Although these enantiomers were separable by chiral HPLC, the enantiomeric excess of the separated fraction decayed after being kept in solution at room temperature (**Figure 4-3**). This observation can be ascribed to the racemization via aromatic ring inversion, so enantiomeric excess determined from the peak area of the HPLC chromatogram was plotted against time to calculate the rate constant *k* and half-life *t*_{1/2} in hexane/*i*-PrOH (*v/v* = 1/1). Curve fitting using a first-order kinetic model^{5,6} gave *k* and *t*_{1/2} as $4.5 \times 10^{-5} \text{ s}^{-1}$ and 2.1 h, respectively. Eyring plot analysis after determination of the racemization kinetics at different temperatures revealed the activation enthalpy and entropy to be $\Delta H = 76.6 \text{ kJ/mol}$ and $\Delta S = -70.4 \text{ J/mol}\cdot\text{K}$, respectively. The activation barrier for racemization at 298 K was calculated to be 97.6 kJ/mol, which is not sufficient to suppress racemization at room temperature. The racemization rates were also determined in different solvent systems. The half-life *t*_{1/2} in *n*-hexane was 2.5 h, while those in dichloromethane, methanol, and DMF were 1.7 h, 0.5 h, and 4.2 min, respectively.

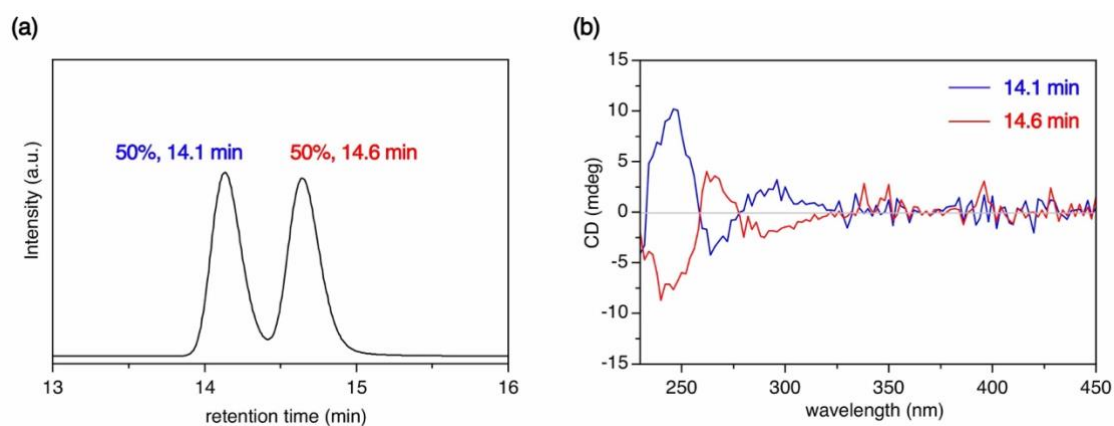


Figure 4-2. (a) HPLC analysis of **1** using chiral stationary state and (b) CD spectra of each fraction measured using CD detector equipped in HPLC system (column: DAICEL CHIRALPAC IG-3 \times 2, mobile phase: *n*-hexane/*i*-PrOH (*v/v* = 1/1), detection: UV absorption at 254 nm, flow rate: 0.5 mL/min, column temperature: 10 °C.)

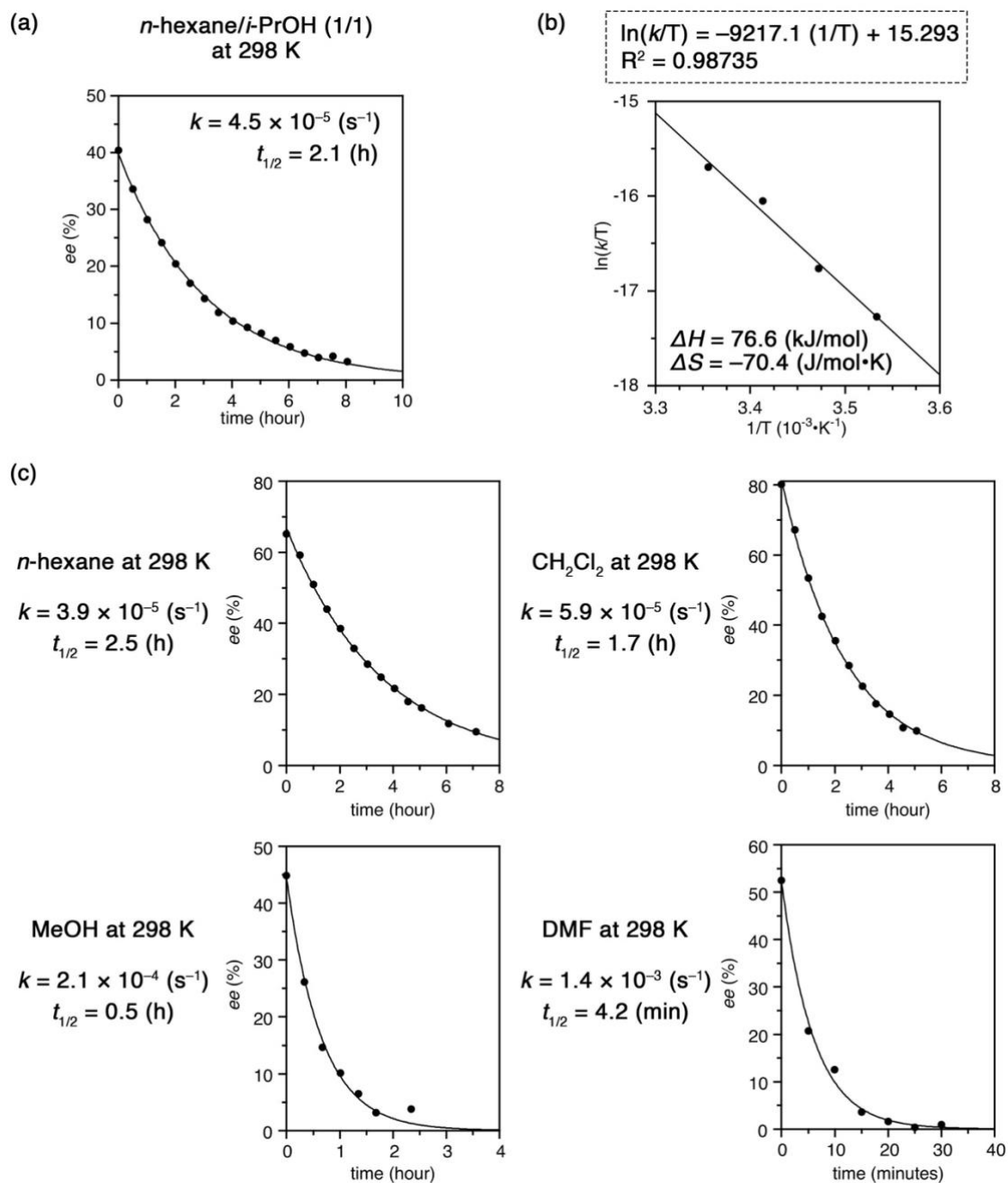


Figure 4-3. (a) Decay of enantiomeric excess of **1** in *n*-hexane/*i*-PrOH (v/v = 1/1) at 298 K, (b) Eyring plot analysis for racemization of **1**, and (c) decay of enantiomeric excess of **1** in *n*-hexane, dichloromethane, MeOH, and DMF.

4.3. Suppression of Racemization by *N*-Methylation

To suppress racemization of **1** via aromatic ring inversion, *N*-methylation of **1** was performed. Treatment of **1** with sodium hydride and iodomethane in DMF at room temperature afforded **1-Me** in 50% yield (Figure 4-4a). The ^1H NMR spectrum showed signals similar to those of **1**, except for the *N*-methyl group at 2.39 ppm instead of NH proton signal. Although the aromatic ring inversion was shown to be slower on the NMR time scale (six signals assigned to methyl groups were observed), no diastereomer was observed in its ^1H NMR spectrum. **1-Me** showed two peaks in HPLC analysis using a chiral column (CHIRALPAK IJ-5) and methanol as eluent. The enantiomers were separated and found to be configurationally stable, as no detectable racemization was found in the HPLC chromatogram measured after being kept in methanol at room temperature over one month, demonstrating the effective suppression of aromatic ring inversion by *N*-methylation (Figure 4-4b). The enantiomers were also confirmed by the mirror-imaged CD spectra measured in *n*-hexane (Figure 4-4c).

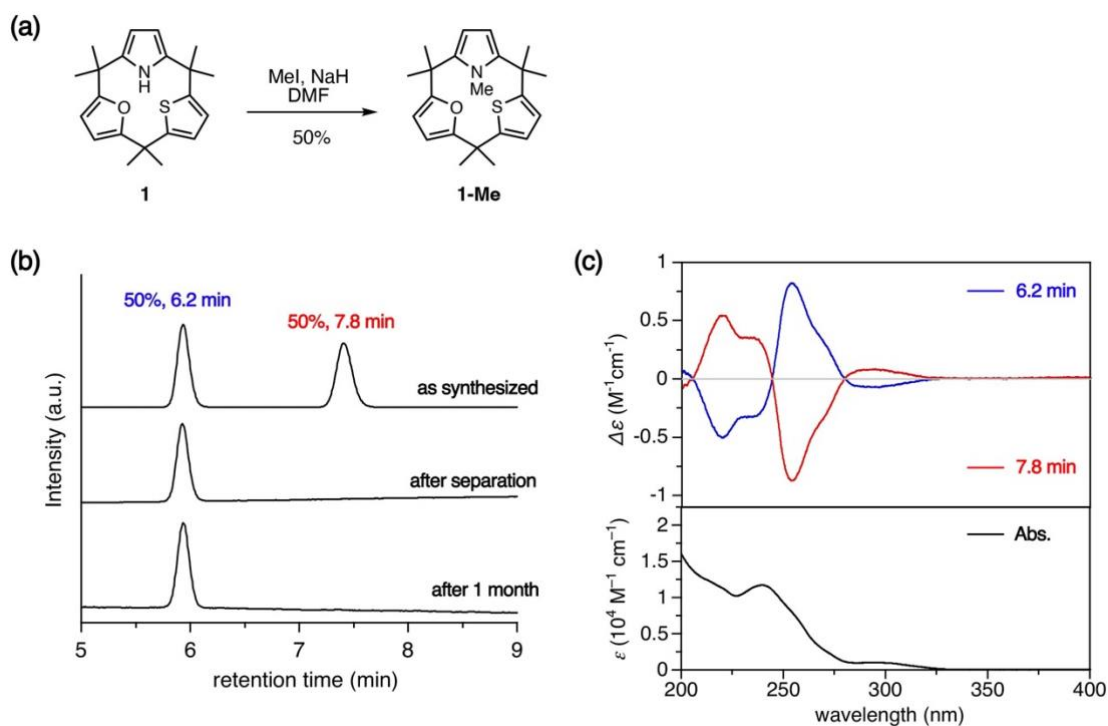


Figure 4-4. (a) *N*-methylation reaction of **1**, (b) configurational stability of **1-Me** determined using chiral HPLC (column: DAICEL CHIRALPAC IJ-5, mobile phase: MeOH, detection: UV absorption at 254 nm, flow rate: 1.0 mL/min, column temperature: 40 °C), and (c) CD spectra for enantiomers and absorption spectra of **1-Me** in *n*-hexane.

Since **1-Me** is configurationally stable, a single crystal of the pure enantiomer was obtained from the first fraction observed at 6.2 minutes in the chiral HPLC chromatogram. X-ray diffraction analysis of the single crystal revealed that **1-Me** adopts a partial-cone conformation, with the *N*-methylated pyrrole facing the opposite side of furan and thiophene, reflecting the greater steric hindrance of the *N*-methyl group than the sulfur atom (**Figure 4-5**). From this structure, the absolute configuration was determined as (*R,S,S*) based on the planar chirality around the thiophene, furan, and pyrrole planes, respectively.

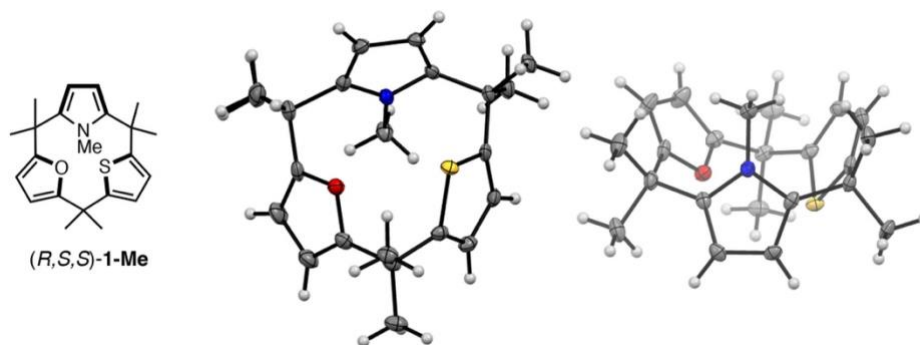


Figure 4-5. Crystal structure of (*R,S,S*)-**1-Me** viewed from top and side. (gray: C, white: H, red: O, blue: N, yellow: S).

Given the different racemization behaviors of **1** and **1-Me**, the molecular dynamics simulations were performed in *n*-hexane for 25 ns to investigate their aromatic ring inversion motions. The distances d_X between heteroatoms ($X = S, N, O$) and the plane defined by the three bridging carbons were plotted as a function of time (**Figure 4-6**). While pyrrole and furan rings in **1** flipped frequently on this time scale, the thiophene ring did not flip, indicating that thiophene ring flipping is the rate-determining step in the racemization of **1**. This relatively slower motion of thiophene ring can be attributed to the larger size and weight of the sulfur atom compared with those of oxygen or nitrogen. When the same MD simulation was performed on **1-Me**, the ring flipping of the pyrrole was not observed on this time scale, nor was that of thiophene. In addition, the ring flipping of furan was observed, but to some extent suppressed compared to that observed in **1**.

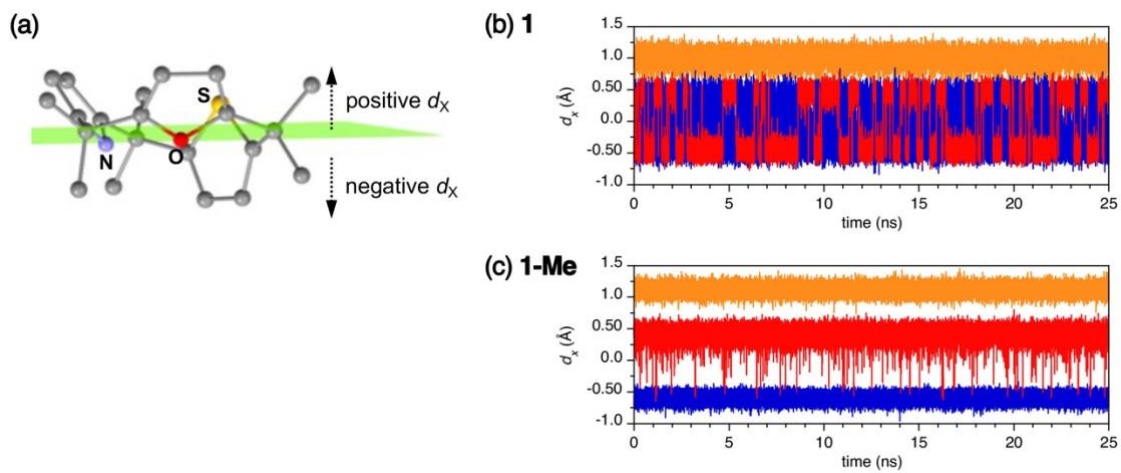


Figure 4-6. (a) Illustration of d_x and (b) molecular dynamics (MD) simulation of aromatic ring flipping in **1** and (c) **1-Me**

Since *N*-methylation effectively suppressed racemization of **1**, and the racemization rate of **1** in DMF (reaction solvent) is fast ($t_{1/2} < 5$ min), dynamic kinetic resolution during *N*-methylation reaction with chiral cation was investigated. The author envisioned that after deprotonation of pyrrolic NH by base, the formed anion can be paired with chiral cation to form diastereomeric salt, which allows enantio-enrichment. Therefore, *N*-methylation in the presence of a chiral cation was expected to give **1-Me** enantioselective fashion. When **1** was subjected to *N*-methylation conditions in the presence of the chiral ammonium salt **4**,⁷ (*R,S,S*)-**1-Me** was obtained in 48% yield with 10% *ee* (Figure 4-7). Although the *ee* was modest, it was suggested that the enantioselective molecular recognition of **1** with a specific substrate can be achieved. Other conditions for *N*-methylation were investigated to improve the *ee* but were not successful.

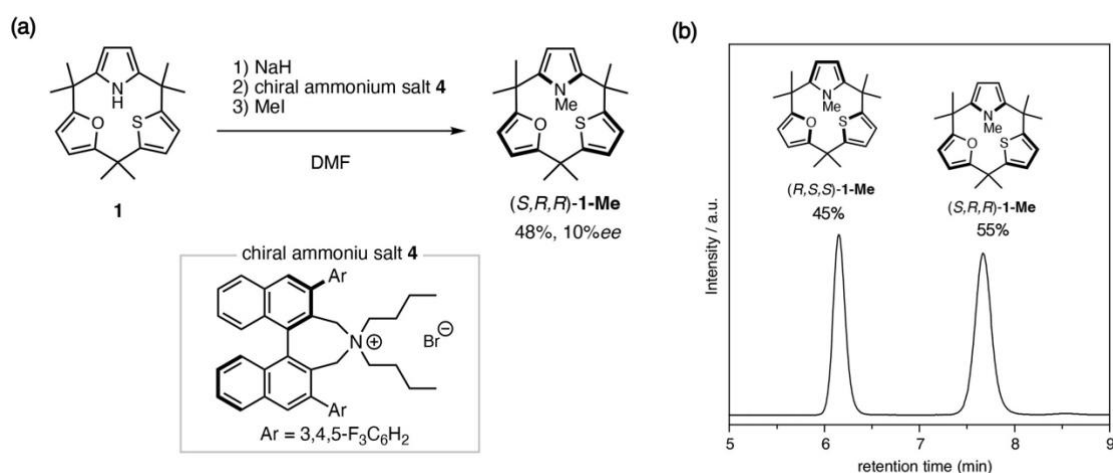


Figure 4-7. (a) *N*-methylation of **1** in the presence of chiral ammonium salt **7** and (b) analysis of product using chiral HPLC (column: DAICEL CHIRALPAC IJ-5, mobile phase: MeOH, detection: UV absorption at 254 nm, flow rate: 1.0 mL/min, column temperature: 40 °C).

4.4. Strain-Induced Ring Expansion Reaction of Calix[1]furan[1]pyrrole[1]thiophene

Macrocyclic ring size is a critical parameter that affects an aromatic ring inversion barrier. In order to obtain a larger macrocycle, the strain-induced ring expansion reaction of **1** was investigated. When **1** was treated with trifluoroacetic acid in dichloromethane for 1 h, GPC-HPLC analysis indicated the formation of larger molecules compared to the starting material **1**. After separation of fractions by preparative-scale GPC, calix[2]furan[2]pyrrole[2]thiophene **5**, calix[3]furan[3]pyrrole[3]thiophene **6**, and calix[4]furan[4]pyrrole[4]thiophene **7** were isolated in 30%, 16%, and 7% yield, respectively (**Figure 4-8**). Since ^1H NMR analysis of the separated products showed no evidence of other positional isomers of **5**, **6**, and **7**, this ring expansion reaction appears to be regioselective. This would be due to the site-selective ring cleavage of **1** by acid giving a single linear intermediate as suggested in the ring expansion reaction of calix[1]furan[2]pyrrole in chapter 3, which is then oligomerized and cyclized to give macrocyclic products.

In this reaction, it took more than 30 minutes for all of the starting material **1** to be consumed, while calix[3]pyrrole and calix[1]furan[2]pyrrole were consumed within 1 minute. It is assumed that the activation energy for ring cleavage is relatively higher in **1** than in calix[3]pyrrole and calix[1]furan[2]pyrrole. Furthermore, this reaction of **1** gave not only double- but also triple- and quadruple-sized products, while calix[3]pyrrole and calix[1]furan[2]pyrrole gave only double-sized products. This would be due to the difference in the number of pyrroles because pyrrole can interact with anion (conjugate base) using NH to promote intramolecular reaction.

Because diffraction grade single crystals of **5** and **7** were obtained, X-ray diffraction analysis was performed. The crystal structure of **5** and **7** indicated that they have repeating sequences of pyrrole, furan, and thiophene in their calix[6]- and calix[12]-size macrocycles. Although **5**, **6**, and **7** were analyzed by chiral stationary state HPLC, no separable enantiomers were observed, probably because of their rapid aromatic ring inversions.

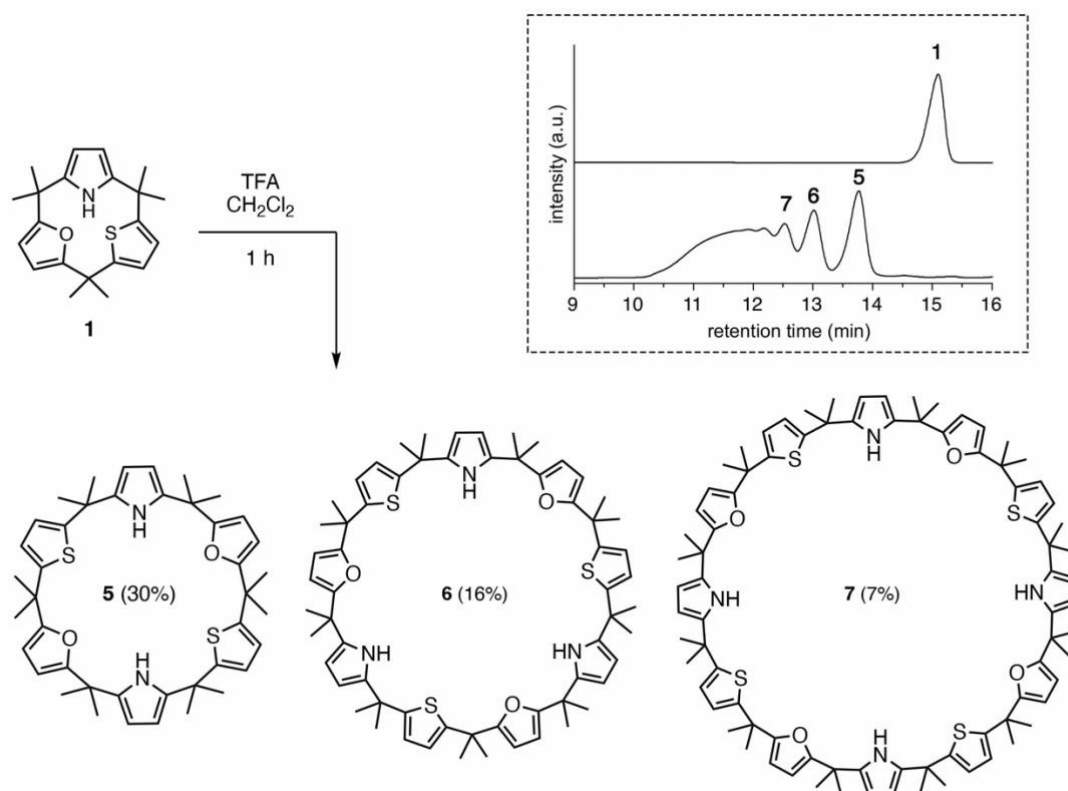


Figure 4-8. Strain-induced ring expansion reaction of **1** by TFA in dichloromethane. Inset shows GPC-HPLC chromatograms of reaction mixture (Column: TOSOH TSKgel G2000HXL×2, mobile phase: chloroform, detection: absorption at 245 nm, flow rate: 1.0 mL/min).

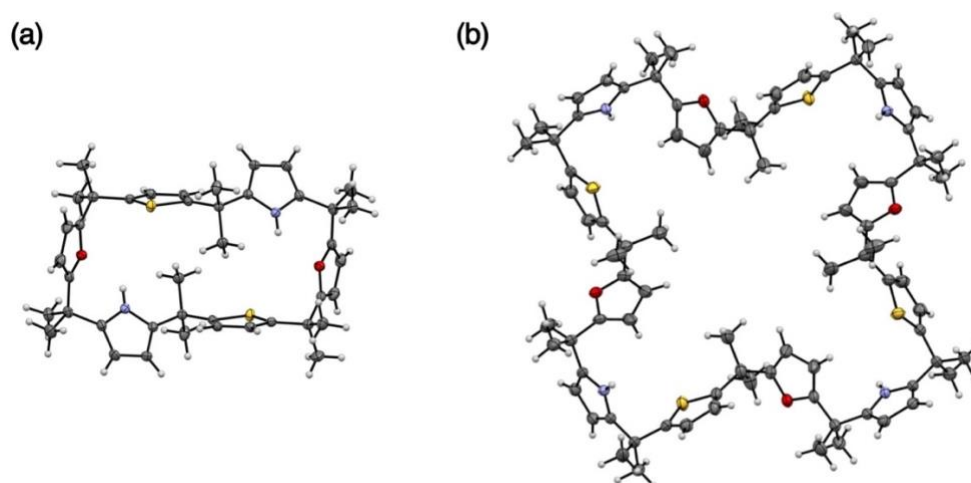


Figure 4-10. Crystal structure of (a) **5** and (b) **7** (gray: C, white: H, red: O, blue: N, yellow: S). Solvent molecule is omitted for clearly.

4.5. Conclusion

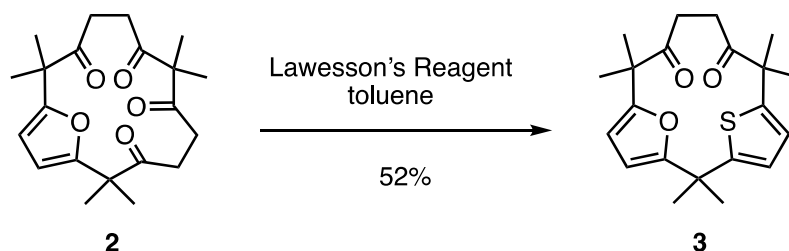
In conclusion, the introduction of furan and thiophene into the calix[3]pyrrole core afforded the construction of a chiral macrocycle, whose chirality is derived from its suppressed aromatic ring inversion. Although calix[1]furan[1]pyrrole[1]thiophene **1** underwent racemization via aromatic ring inversion in solution, *N*-methylation successfully suppressed the ring inversion to give the configurationally stable macrocycle **1-Me**. The difference of aromatic ring inversion was not only confirmed by the experimental racemization behavior but also supported by the result of MD simulation. The suppression of racemization by *N*-methylation was also applied to enantioselective molecular recognition although the observed enantiomeric excess was only 10% *ee*. The strain-induced ring expansion reaction of **1** gave two-, three-, and four-fold expanded products **5**, **6**, and **7**, whose ring inversions were fast enough to allow them being racemic mixtures. In this context, these results suggest that the calix[3]pyrrole-type macrocycle is a promising framework for inherently chiral macrocycles, and their aromatic ring inversion behavior is controlled by appropriate functionalization.

4.6. Experimental Section

4.6.1. Reagents and equipment

Solvents and reagents were purchased from FUJIFILM WAKO Pure Chemical Industries Ltd., TCI Co., Ltd., Kanto Chemical Co., Inc., or Sigma-Aldrich Co., and used without further purification unless otherwise mentioned. Compound **2** was prepared according to a procedure introduced in Chapter 3. All ^1H and ^{13}C NMR spectra were recorded using JEOL JMN-ECS400 spectrometer and chemical shifts were reported in parts per million (ppm) relative to an internal standard tetramethylsilane ($\delta = 0.00$ ppm for ^1H NMR in CDCl_3) or a solvent residual peak ($\delta = 77.16$ ppm for ^{13}C NMR in CDCl_3). Infrared spectra were measured using a JASCO Co. FT/IR-4600. ESI-TOF-MS spectra were recorded on a Thermo Scientific Executive spectrometer. Elemental analyses were carried out using an Exceter Analytical, Inc. CE440 or MICRO CORDER JM10. Thin layer chromatography was performed on silica gel sheets, MERCK silica gel 60 F254 or alumina plates, WAKO alumina 60 F254. Preparative scale separations were performed by means of gravity column chromatography over silica gel (Wakosil[®] 60, 64 ~ 210 μm) or alumina. UV/Vis absorption spectra were recorded on a JASCO V-770 spectrophotometer. Fluorescence spectra were recorded on a HITACHI F-7000 fluorescence spectrophotometer. Fluorescence quantum yields were measured using a Hamamatsu Photonics Quantaurus QY C11347-01 instrument. Circular dichroism spectra were recorded on a JASCO J-1500 spectrophotometer. Analytical HPLC chromatograms were recorded using a JASCO MD-2018 photodiode array detector quipped with a JASCO PU-2089 pump, JASCO AS-2059 sampler, and JASCO CO-2060 column thermostat. Single crystal X-ray diffraction data were obtained using Rigaku XtaLAB P200 diffractometer equipped with a Rigaku XtaLAB Synergy-R/DW instrument equipped with a HyPix-6000HE detector with a monochromated mirror (MoK_α radiation $\lambda = 0.71073$ Å). All structures were solved using a dual-space algorithm (SHELXT) and refined using full-matrix least-squares methods (SHELXL).^{8,9}

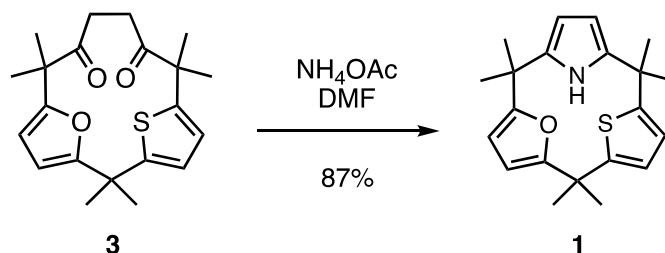
4.6.2. Synthesis of compound 3



Compound **2** (500 mg, 1.39 mmol) and Lawesson's reagent (670 mg, 1.66 mmol) were placed in a 50 mL Schlenk tube. After evacuation and backfill with nitrogen gas, dry toluene (16 mL) was added to the tube via syringe. The resulting suspension was heated at 60 °C for 50 minutes with magnetic stirring. After cooled to room temperature, the reaction mixture was passed through silica gel plug using ethyl acetate as the eluent before being concentrated under reduced pressure. The resulting mixture was then purified by silica gel column chromatography (column diameter: 3 cm, height: 15 cm, eluent: CH₂Cl₂) to give crude **3**, which was washed with 15 mL of *n*-hexane to give 260 mg (52% yield) of purified **3** as a colorless solid.

¹H NMR (400 MHz, CDCl₃, 298 K): δ = 6.80 (d, J = 3.8 Hz, 1H, thienyl), 6.75 (d, J = 3.8 Hz, 1H, thienyl), 6.03 (d, J = 3.0 Hz, 1H, furyl), 6.01 (d, 1H, J = 3.0 Hz, furyl), 2.28 (m, 4H, ethylene), 1.71 (s, 6H, dimethylmethylene), 1.46 (s, 6H, dimethylmethylene), 1.31 ppm (s, 6H, dimethylmethylene); ¹³C NMR (100 MHz, CDCl₃, 298 K): δ = 212.2, 210.5, 162.3, 157.6, 154.5, 148.2, 124.0, 123.3, 105.7, 103.4, 51.6, 49.3, 39.7, 35.6, 31.3, 27.1, 23.9, 22.9 ppm; IR (ATR, neat): 2974, 2932, 2868, 1702, 1551, 1431, 1364, 1250, 1065, 1019 cm⁻¹; mp: 169-175 °C; HRMS (ESI): m/z calcd. For C₂₁H₂₆O₃S+Na⁺: 381.1494 [M+Na]⁺, found: 381.1485; elemental analysis (%) calcd. For C₂₁H₂₆O₃S: C 70.36, H 7.31, N 0.00, found: C 69.97, H 7.31, N 0.04; R_f = 0.20 (silica gel, CH₂Cl₂).

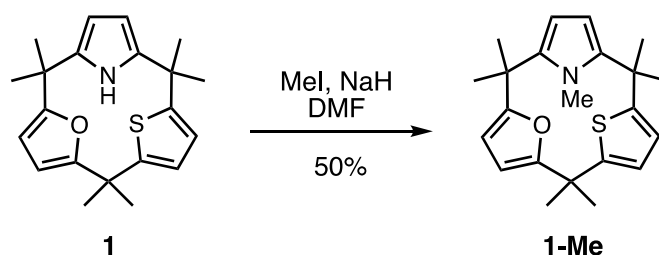
4.6.3. Synthesis of calix[1]furan[1]pyrrole[1]thiophene 1



In a 100 mL round-bottomed flask equipped with a reflux condenser, compound **3** (334 mg, 0.93 mmol), ammonium acetate (12.9 g, 167 mmol), and *N,N*-dimethylformamide (DMF, 6.6 mL) were heated at 120 °C in an oil bath for 6 h with magnetic stirring. After allowing to cool to room temperature, the reaction mixture was diluted with chloroform (100 mL) and washed with water (100 mL). The aqueous layer was then extracted with chloroform (100 mL \times 2), and the combined organic layer was further washed with a saturated aqueous solution of sodium bicarbonate (100 mL \times 2) and brine (100 mL), and dried over anhydrous sodium sulfate. After removal of the volatiles under reduced pressure, the residue was chromatographed over silica gel (column diameter: 3 cm, height: 5 cm, eluent: CH₂Cl₂/*n*-hexane = 1/1) to give compound **1** (275 mg, 87% yield) as a colorless solid.

¹H NMR (400 MHz, CDCl₃, 298 K): δ = 7.09 (brs, 1H, N-H), 6.95 (d, J = 3.7 Hz, 1H, thienyl), 6.89 (d, J = 3.7 Hz, 1H, thienyl), 5.83 (d, J = 3.0 Hz, 1H, furyl), 5.75 (d, J = 3.0 Hz, 1H, furyl), 5.68 (dd, J = 3.1, 3.1 Hz, 1H, pyrrolyl), 5.65 (dd, J = 3.1, 3.1 Hz, 1H, pyrrolyl), 1.74 (s, 6H, methyl), 1.67 (s, 3H, methyl), 1.65 (s, 3H, methyl), 1.58 (s, 3H, methyl), 1.45 ppm (s, 3H, methyl); ¹³C NMR (100 MHz, CDCl₃, 298 K): δ = 163.1, 160.9, 160.7, 159.3, 144.4, 137.9, 123.5, 122.6, 103.1, 102.6, 101.7, 101.2, 41.4, 41.2, 36.6, 28.2, 28.0, 27.5, 27.1, 27.0, 22.8 ppm; UV/Vis (*n*-hexane): λ_{max} (ϵ) = 220 (13600), 244 nm (8900 mol⁻¹ L cm⁻¹); IR (ATR, neat): 3426, 2966, 2927, 2868, 1536, 1458, 1362, 1213, 1105, 1036, 1016 cm⁻¹; mp: 130-134 °C; HRMS (ESI): m/z calcd. For C₂₁H₂₅ONS+Na⁺: 362.1549 [M+Na]⁺, found: 362.1545; elemental analysis (%) calcd. For C₂₁H₂₅ONS: C 74.30, H 7.42, N 4.13, found: C 74.11, H 7.48, N 4.08; R_f = 0.60 (silica gel, CH₂Cl₂/*n*-hexane = 1/1).

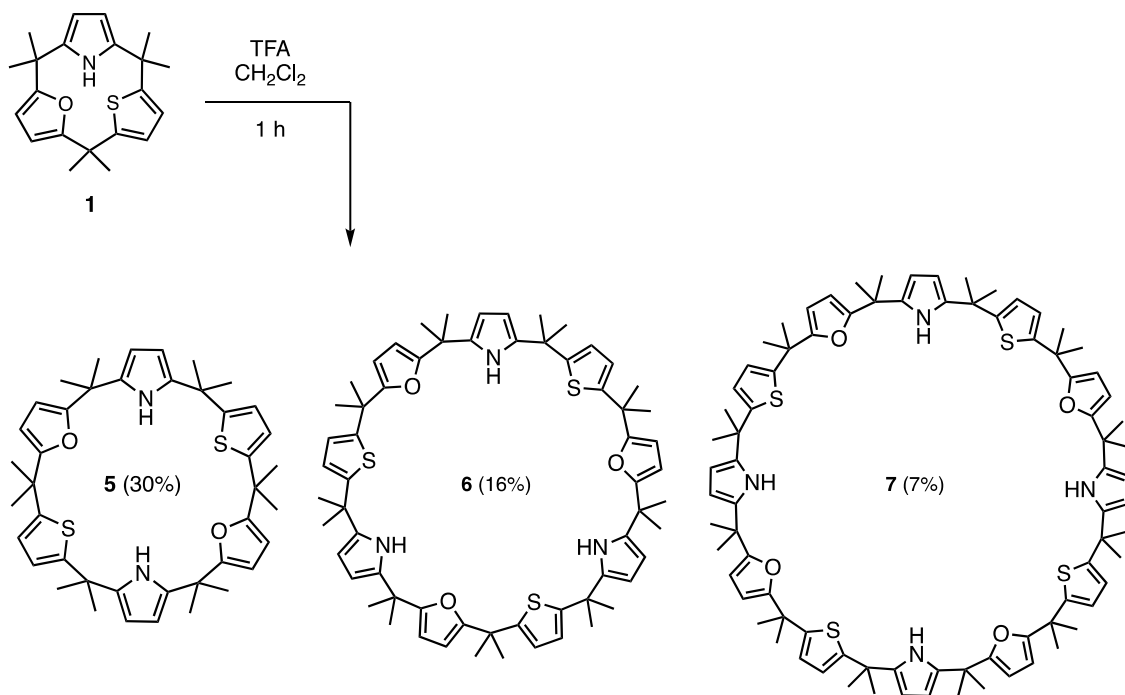
4.6.4. *N*-methylation of **1**



Calix[1]furan[1]pyrrole[1]thiophene **1** (100 mg, 0.295 mmol) and sodium hydride (60% dispersion in mineral oil, 240 mg, 6.00 mmol) were placed in a 25 mL Schlenk tube, which was then evacuated and backfilled with nitrogen gas three times. To the Schlenk tube, dry *N,N*-dimethylformamide (7.0 mL) was added followed by the addition of iodomethane (380 μ L, 6.10 mmol) via syringe. After stirring magnetically for 2 hours at room temperature, the reaction mixture was slowly poured into water (20 mL) [Caution: exothermic]. After extracting with diethyl ether (20 mL \times 3), the combined organic layer was washed with brine (20 mL), dried over anhydrous sodium sulfate, and concentrated under reduced pressure. The resulting mixture was then subjected to alumina column chromatography (column diameter: 2 cm, height: 10 cm, eluent: CH₂Cl₂/*n*-hexane = 1/39) to give crude **1-Me**, which was washed with 0.5 mL of MeOH to afford 52 mg (50 % yield) of compound **1-Me** as a colorless solid.

¹H NMR (400 MHz, CDCl₃, 298 K): δ = 6.64 (d, *J* = 3.7 Hz, 1H, thienyl), 6.39 (d, *J* = 3.7 Hz, 1H, thienyl), 6.10 (d, *J* = 3.7 Hz, 1H, furyl), 6.04 (d, *J* = 3.7 Hz, 1H, furyl), 5.79 (d, *J* = 3.0 Hz, 1H, pyrrolyl), 5.78 (d, *J* = 3.0 Hz, 1H, pyrrolyl), 2.39 (s, 3H, *N*-methyl), 1.81 (s, 3H, methyl), 1.77 (s, 3H, methyl), 1.74 (s, 3H, methyl), 1.63 (s, 3H, methyl), 1.62 (s, 3H, methyl), 1.54 ppm (s, 3H, methyl); ¹³C NMR (100 MHz, CDCl₃, 298 K): δ = 163.0, 161.9, 159.8, 159.7, 146.1, 142.7, 122.6, 119.1, 105.6, 104.7, 103.2, 101.4, 41.8, 40.8, 38.1, 32.2, 31.1, 30.9, 27.2, 25.5, 24.9, 22.8 ppm; UV/Vis (*n*-hexane): λ_{max} (ϵ) = 240 (11600), 295 nm (1000 mol⁻¹ L cm⁻¹); IR (ATR, neat): 2965, 2919, 2870, 1365, 1234, 744 cm⁻¹; mp: 153-157 °C; HRMS (ESI): *m/z* calcd. For C₂₂H₂₇ONS+Na⁺: 376.1706 [*M*+Na]⁺, found: 376.1703; elemental analysis (%) calcd. For C₂₂H₂₇ONS: C 74.75, H 7.70, N 3.96, found: C 74.60, H 7.71, N 3.91; *R*_f = 0.30 (alumina, CH₂Cl₂/*n*-hexane = 1/39).

4.6.5. Ring expansion reaction of **1**



In a 200 mL round-bottom flask, compound **1** (100 mg, 0.29 mmol) was dissolved in CH₂Cl₂ (88 mL). After addition of trifluoroacetic acid (1.0 mmol as a 1.0 M CH₂Cl₂ solution), the solution was stirred for 1 h at room temperature. The reaction was quenched with 2.5 mL of triethylamine and the volatiles were evaporated off. The residue was separated by gel permeation chromatography using a recycling HPLC, followed by purification by silica gel column chromatography (column diameter = 2.0 cm, height = 15.0 cm eluent: CH₂Cl₂/*n*-hexane = 2/3) to afford calix[2]furan[2]pyrrole[2]thiophene **5** (30 mg, 44 μmol, 30% yield), calix[3]furan[3]pyrrole[3]thiophene **6** (16 mg, 15 μmol, 16% yield), and calix[4]furan[4]pyrrole[4]thiophene **7** (7 mg, 5 μmol, 7% yield) as white solids.

Characterization data for compound 5

¹H NMR (400 MHz, CDCl₃, 298 K): δ = 7.94 (brs, 2H, N-H), 6.39 (m, 4H, thienyl), 5.94 (dd, J = 3.0 Hz, 2H, pyrrolyl), 5.91 (dd, J = 3.0 Hz, 2H, pyrrolyl), 5.82 (d, J = 3.0 Hz, 2H, furyl), 5.80 (d, J = 3.0 Hz, 2H, furyl), 1.63 (s, 12H, dimethylmethylene), 1.61 (s, 12H, dimethylmethylene), 1.56 ppm (s, 12H, dimethylmethylene); ¹³C NMR (100 MHz, CDCl₃, 298 K): δ = 160.0, 159.8, 152.4, 151.0, 138.9, 137.2, 122.8, 122.3, 104.7, 103.7, 102.7, 102.3, 39.1, 38.0, 36.3, 31.3, 30.1, 27.9 ppm; HRMS (ESI): m/z calcd. For C₄₂H₅₀O₂N₂S₂+Na⁺: 701.3192 [M +Na]⁺; found: 701.3206; R_f = 0.29 (silica gel, CH₂Cl₂/*n*-hexane = 1/2).

Characterization data for compound 6

¹H NMR (400 MHz, CDCl₃, 298 K): δ = 7.90 (brs, 3H, N-H), 6.40 (d, J = 3.7 Hz, 3H, thienyl), 6.37 (d, J = 3.7 Hz, 3H, thienyl), 5.91 (dd, J = 3.0, 3.0 Hz, 3H, pyrrolyl), 5.88 (dd, J = 3.0, 3.0 Hz, 3H, pyrrolyl), 5.82 (s, 6H, furyl), 1.61 (s, 18H, dimethylmethylene), 1.56 (s, 18H, dimethylmethylene), 1.55 ppm (s, 18H, dimethylmethylene); ¹³C NMR (100 MHz, CDCl₃, 298 K): δ = 159.9, 159.8, 152.9, 151.1, 138.6, 137.3, 122.2, 122.1, 104.5, 103.8, 103.1, 102.4, 38.9, 38.1, 36.3, 31.3, 29.9, 27.9 ppm; HRMS (ESI): m/z calcd. For C₆₃H₇₅O₃N₃S₃+Na⁺: 1040.4863 [M +Na]⁺; found: 1040.4845; R_f = 0.29 (silica gel, CH₂Cl₂/*n*-hexane = 2/3).

Characterization data for compound 7

¹H NMR (400 MHz, CDCl₃, 298 K): δ = 7.86 (brs, 4H, N-H), 6.41 (d, J = 3.7 Hz, 4H, thienyl), 6.37 (d, J = 3.7 Hz, 4H, thienyl), 5.90 (dd, J = 3.2, 3.2 Hz, 4H, pyrrolyl), 5.87 (dd, J = 3.2, 3.2 Hz, 4H, pyrrolyl), 5.82 (d, J = 3.0 Hz, 4H, furyl), 5.80 (d, J = 3.0 Hz, 4H, furyl), 1.60 (s, 24H, dimethylmethylene), 1.57 (s, 24H, dimethylmethylene), 1.54 ppm (s, 24H, dimethylmethylene); ¹³C NMR (100 MHz, CDCl₃, 298 K): δ = 159.9, 159.8, 152.9, 151.2, 138.5, 137.3, 122.1, 104.5, 103.9, 103.2, 102.5, 38.9, 38.1, 36.3, 31.3, 29.8, 27.9 ppm; HRMS (ESI): m/z calcd. For C₈₄H₁₀₀O₄N₄S₄+Na⁺: 1379.6503 [M +Na]⁺; found: 1379.6520; R_f = 0.29 (silica gel, CH₂Cl₂/*n*-hexane = 2/3).

4.6.6. Single crystal X-ray diffraction analyses

Crystallographic data for 1

Single crystals suitable for X-ray diffraction analysis were grown from an *n*-hexane solution of **1** by slow evaporation.

C₂₁H₂₅NOS, *M* = 339.48, crystal size: 0.10 × 0.05 × 0.05 mm³, orthorhombic, space group *P*2₁2₁2₁, *a* = 10.0298(6), *b* = 11.2729(6), *c* = 16.4583(9) Å, $\alpha = \beta = \gamma = 90^\circ$, *V* = 1860.86(18) Å³, *Z* = 4, *T* = 123(2) K, $\mu = 0.181 \text{ mm}^{-1}$, *D*_{calc} = 1.212 g/cm³, 2.190° ≤ θ ≤ 30.707°, 3976 unique reflections out of 4367 with *I* > 2σ(*I*), GOF = 1.042, *R*₁ = 0.0374, *wR*₂ = 0.0986, CCDC: 2237091

Crystallographic data for (R,S,S)-1-Me

Single crystals suitable for X-ray diffraction analysis were grown by vapor diffusion of MeOH into a CH₂Cl₂ solution of (R,S,S)-**1-Me**.

C₂₂H₂₇NOS, *M* = 353.50, crystal size: 0.35 × 0.17 × 0.04 mm³, monoclinic, space group *P*2₁, *a* = 16.1698(5), *b* = 6.6113(2), *c* = 17.7006(5) Å, $\alpha = \gamma = 90^\circ$, $\beta = 92.757(3)^\circ$, *V* = 1890.06(10) Å³, *Z* = 4, *T* = 123(2) K, $\mu = 0.181 \text{ mm}^{-1}$, *D*_{calc} = 1.242 g/cm³, 1.666° ≤ θ ≤ 27.496°, 8212 unique reflections out of 8511 with *I* > 2σ(*I*), GOF = 1.156, *R*₁ = 0.0533, *wR*₂ = 0.1372, Flack = 0.07(2), CCDC: 2237092

Crystallographic data for 5

Single crystals suitable for X-ray diffraction analysis were grown by slow evaporation of a CH₂Cl₂/MeOH solution of **5**.

C₄₂H₅₀N₂O₂S₂, *M* = 678.96, crystal size: 0.50 × 0.05 × 0.02 mm³, triclinic, space group *P*-1, *a* = 6.5240(3), *b* = 10.6250(5), *c* = 13.7581(6) Å, $\alpha = 71.881(4)^\circ$, $\beta = 89.567(3)^\circ$, $\gamma = 84.284(4)^\circ$, *V* = 901.60(7) Å³, *Z* = 1, *T* = 123(2) K, $\mu = 1.631 \text{ mm}^{-1}$, *D*_{calc} = 1.250 g/cm³, 3.381° ≤ θ ≤ 69.990°, 3139 unique reflections out of 3371 with *I* > 2σ(*I*), GOF = 1.222, *R*₁ = 0.0595, *wR*₂ = 0.1823, CCDC: 2237424

Crystallographic data for 7

Single crystals suitable for X-ray diffraction analysis were grown by slow evaporation of a CH₂Cl₂/MeOH solution of 7.

C₈₄H₁₀₀N₄O₄S₄•(CH₃OH)₄, $M = 1486.08$, crystal size: $0.10 \times 0.05 \times 0.05$ mm³, tetragonal, space group $I4_1/a$, $a = 36.7837(6)$, $b = 36.7837(6)$, $c = 6.5185(2)$ Å, $\alpha = \beta = \gamma = 90^\circ$, $V = 8819.8(4)$ Å³, $Z = 4$, $T = 123(2)$ K, $\mu = 1.406$ mm⁻¹, $D_{\text{calc}} = 1.119$ g/cm³, $3.398^\circ \leq \theta \leq 69.963^\circ$, 3119 unique reflections out of 4142 with $I > 2\sigma(I)$, GOF = 1.066, $R_1 = 0.0676$, $wR_2 = 0.2118$, CCDC: 2237412

4.6.7. Computational analyses

Geometry optimization and stability analysis for stereoisomers of **1**

Theoretical calculations were performed with Gaussian 16 Rev. C01.¹⁰ The optimized structure of (*R*^{*},*R*^{*},*S*^{*})-**1** was obtained at the B3LYP/cc-pVTZ level of theory with Grimme's D3BJ dispersion correction using the single crystal X-ray structure (CCDC deposition number: 2237091) as the input.^{11,12} The initial structures of the stereoisomers (*R*^{*},*S*^{*},*S*^{*})-**1**, (*S*^{*},*R*^{*},*S*^{*})-**1**, and (*R*^{*},*R*^{*},*R*^{*})-**1** were modified from the crystal structure of (*R*^{*},*R*^{*},*S*^{*})-**1**, and structural optimizations carried out under the same conditions as above. Optimization allowed the energies (ΔE) of the stereoisomers of **1** to be calculated relative to the most stable stereoisomer (*R*^{*},*R*^{*},*S*^{*})-**1** (see Figure 4-1).

Molecular dynamics simulation for **1** and **1-Me**

All the classical molecular dynamics (MD) simulations were performed using the GROMACS version 2020.5.^{13,14} The electronic charges were calculated *via* single-point energy calculation at HF/6-31G(d) level of theory using the optimized structures. The restrained electrostatic potential (RESP) charge method was employed to derive the partial charge.¹⁵ The topology files of the macrocycles and solvent were generated by the Antechamber utility from Ambergtools21¹⁶, with the general amber force fields (GAFF)¹⁷. For the simulation of calix[1]pyrrole[1]furan[1]thiophene, one (*R*^{*},*R*^{*},*S*^{*})-**1** and calix[1]furan[1]*N*-methylpyrrole[1]thiophene, one (*R*,*S*,*S*)-**1-Me** was taken into a cubic box of 29.15 × 29.15 × 29.15 Å³ and 29.20 × 29.20 × 29.20 Å³ consisting of 129 and 132 *n*-hexane molecules as a solvent, respectively. The systems were minimized using the steepest-descent method, with a force tolerance of 10.0 kJ·mol⁻¹·nm⁻¹. Two-step equilibration of the systems, NVT followed by NPT ensembles, were carried out. The V-rescale thermostat¹⁸ with a 0.1 ps coupling time was used for NVT equilibration for 50 ps, and then the Berendsen barostat¹⁹ with a 2.0 ps coupling time and the V-rescale thermostat with the previous setting was used for NPT equilibration for 200 ps. The equilibration process enabled the desired temperature (298.0 K) and pressure (1 atm) and the equilibrated density for the systems, (*R*^{*},*R*^{*},*S*^{*})-**1** and (*R*,*S*,*S*)-**1-Me** were computed to be 648.9 and 648.7 kg·m⁻³, respectively, (density of *n*-hexane = 655 kg·m⁻³). The MD simulations were performed for 25.0 ns in the NPT ensemble at pressure P of 1.0 atm and temperature T of 298.0 K, with a 0.2 fs time-step. The V-rescale¹⁸ thermostat, with a 0.1 ps coupling time, and the Parrinello-Rahman isotropic barostat^{20,21}, with a 2.0 ps coupling time, were used to regulate the temperature and pressure, respectively. A cutoff distance of 1.2 nm was considered for both the van der Waals (vdW) and Coulomb interactions,

and the particle-mesh Ewald (PME)²² method was employed using a grid spacing of 0.16 nm, with a PME order of 4. The isothermal compressibility of *n*-hexane was considered as $1.674 \times 10^{-4} \text{ bar}^{-1}$.²³

As inferred a fast conformational change of calix[1]pyrrole[1]furan[1]thiophene, an MD simulation considering one (R^*, R^*, S^*)-**1** in *n*-hexane solvent was performed for 25 ns to deduce the dynamic behavior of (R^*, R^*, S^*)-**1**. To analyze the relative orientation of each hetero ring, a plane was defined by the three *meso*-carbon atoms in **1**, shown by the green plane in Figure 4-7a and Figure 4-11. The perpendicular distances, d_X ($X = \text{O}, \text{N}$ and S), to this green plane were measured. Figure 4-7b presents the evolution of d_X over the MD simulation for 25 ns, where a change in the sign of d_X indicates the flipping of the heteroaromatic rings from one side of the green plane to the opposite side. Such flipping of the heterocycles can account for the racemization of **1**. The author observed the continuous flipping of the pyrrole and furan rings, which was confirmed by the changes of the sign of d_X ($X = \text{O}$ and N). For the thiophene case, there was no alteration in the sign of d_S , although a fluctuation in d_S was observed during the MD simulation.

A similar analysis for the calix[1]furan[1]*N*-methylpyrrole[1]thiophene, (R, S, S)-**1-Me** was performed and the perpendicular distances, d_X ($X = \text{O}, \text{N}$ and S) were again determined from a similarly defined green plane (see Figure S2) consisting of the *meso*-carbon atoms with respect to time of the MD analysis. In case of the (R, S, S)-**1-Me**, there was no alteration of the sign of d_S , with small fluctuation of d_S , which is similar to the (R^*, R^*, S^*)-**1**. In contrast to (R^*, R^*, S^*)-**1**, the flipping of the other two heterocycles was hindered. The d_N showed no change of sign and always stayed on the same side of the plane from the beginning to the end of the MD simulation. The additional Me-group on the N-atom in (R, S, S)-**1-Me** caused hindrance and was considered to account for the absence of pyrrole ring flipping. On the other hand, the furan flips more freely, which was supported by the plot. Although the alteration of the sign of d_O was observed in Figure 4-7c, the furan ring instantly went back to its original side. Overall, the heterocycles do not flip effectively with only small fluctuations being seen during the MD simulation.

4.6.8. Racemization kinetics of **1**

General equations

Determination of enantiomerization rate constant and half-life for racemization

The time course of the racemization of **1** was analyzed using the equations given below, assuming first-order kinetics.^{5,6}

The rate constant for conversion of one enantiomer A into another B is assumed to be the same as the rate for conversion in the opposite direction and can be described by a rate constant, k . Under this assumption, the change in population of each enantiomer can be described as follows:

$$\frac{d[A]}{dt} = -k([A] - [B]) \quad (4.1)$$

$$\frac{d[B]}{dt} = k([A] - [B]) \quad (4.2)$$

Taking the difference of the above two equations give the following equation:

$$\frac{d([A] - [B])}{dt} = -2k([A] - [B]) \quad (4.3)$$

which in turn, can be written in terms of enantiomeric excess, ee , as follows:

$$\frac{d(ee)}{dt} = -2k(ee) \quad (4.4)$$

since the total concentration of the two enantiomers, $([A] + [B])$, is constant, and ee is defined according to the following relation:

$$ee = \frac{([A] - [B])}{([A] + [B])} \quad (4.5)$$

Rearranging equation (4.4) and integrating yields the following linear relationship:

$$(ee_t) = (ee_0)e^{-2kt} \quad (4.6)$$

where (ee_0) is the initial enantiomeric excess.

From a plot of the enantiomeric excess as a function of time according to equation (4.6), the value of k can be calculated.

The half-life for the racemization process, $t_{1/2}$, can be calculated by rearranging equation (4.6):

$$t_{1/2} = \frac{\ln(2)}{2k} \quad (4.7)$$

Determination of the activation enthalpy and entropy of racemization

Using the rate constants determined at several temperatures, the activation energy for enantiomerization were obtained using the Eyring equation:

$$k = \left(\frac{k_B T}{h}\right) e^{-\frac{\Delta G(T)}{RT}} \quad (4.8)$$

where k_B is the Boltzmann constant, h is Planck's constant, and ΔG is the free energy of activation for enantiomerization, which can be divided into enthalpic (ΔH) and entropic (ΔS) terms as follows:

$$\Delta G(T) = \Delta H - T\Delta S \quad (4.9)$$

From equation (8) and (9), the following equation can be derived:

$$\ln\left(\frac{k}{T}\right) = -\left(\frac{\Delta H}{R}\right)\left(\frac{1}{T}\right) + \left(\frac{\Delta S}{R}\right) + \ln\left(\frac{k_B}{h}\right) \quad (4.10)$$

The values for ΔH and ΔS were determined from the kinetic data obtained from a plot of $\ln(k/T)$ as a function of $1/T$ following in accord with equation (4.10).

The equation (4.10) is a straight line with negative slope, $-\left(\frac{\Delta H}{R}\right)\left(\frac{1}{T}\right)$, and a y-intercept, $\left(\frac{\Delta S}{R}\right) + \ln\left(\frac{k_B}{h}\right)$. From this equation, the ΔH and ΔS of racemization can be determined.

Racemization kinetics of **1** in *n*-hexane/*i*-PrOH (v/v = 1/1)

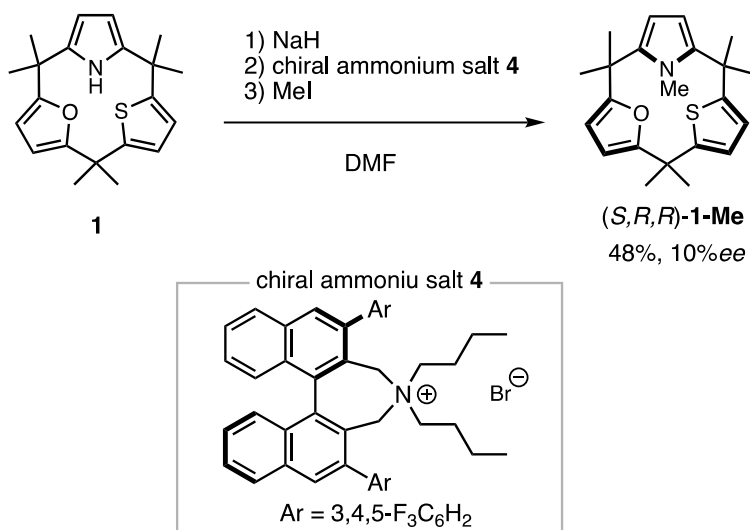
Analytical samples were separated using analytical HPLC. Separated samples were then kept at various temperature (298, 293, 288, and 283 K), and the enantiomeric excess was analyzed using chiral HPLC. The enantiomeric excess values recorded at various times, *ee* (%) were plotted as a function of time. The rate constant for enantiomerization k (s⁻¹) and half-life $t_{1/2}$ (h) were estimated by curve fitting the decrease of *ee* (%) using equation (4.6) and (4.7) described above.

From k value at each temperature and equation (4.10) described above, the ΔH and ΔS of racemization were determined to be 76.6 (kJ/mol) and -70.4 (J/mol•K), respectively.

Racemization kinetics of **1** in different solvents

Analytical samples were separated using analytical HPLC. Separated samples were then evaporated to dryness below room temperature and then dissolved in a given solvent (*n*-hexane, CH₂Cl₂, MeOH, or *N,N*-dimethylformamide). After keeping at 25 °C, the solvent was evaporated off below room temperature. The residue was dissolved in *n*-hexane/*i*-PrOH (v/v = 1/1) to analyze the enantiomeric excess using chiral HPLC. The enantiomeric excess values recorded at various times, *ee* (%) were plotted as a function of time. The rate constant for enantiomerization k (s⁻¹) and half-life $t_{1/2}$ (h or min) were estimated by curve fitting the decrease of *ee* (%) using equations (4.6) and (4.7) provided above.

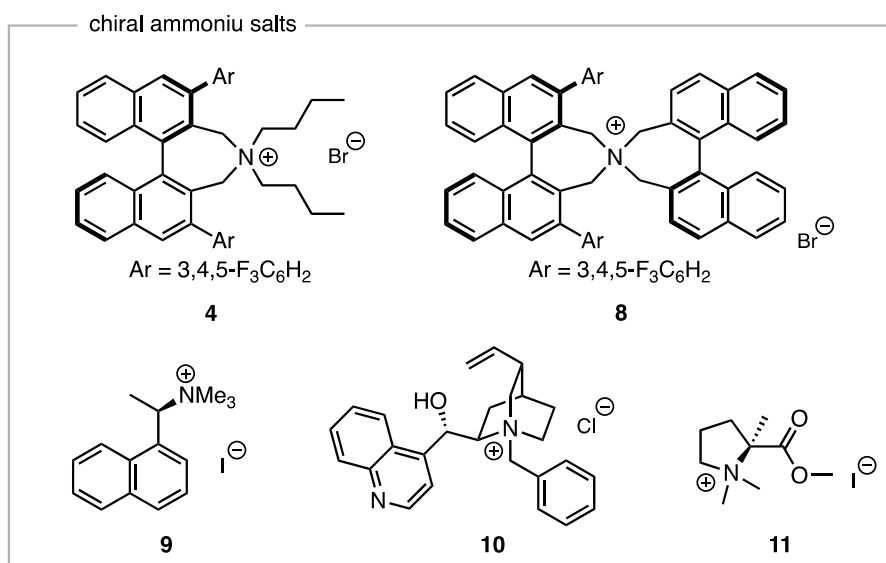
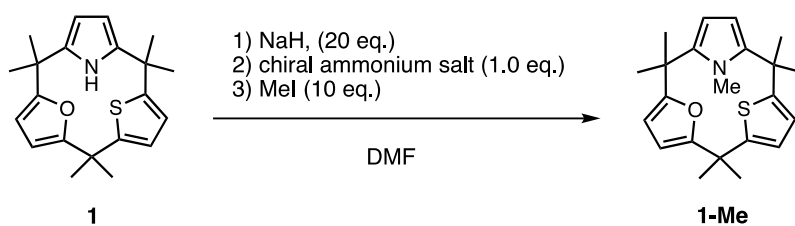
4.6.9. Methylation of **1** in the presence of chiral ammonium salt **4**



Experimental Procedure

Compound **1** (20 mg, 0.060 mmol) and sodium hydride (49 mg, 0.12 mmol, 60% dispersion in mineral oil) were placed in a 25 mL Schlenk tube under a nitrogen atmosphere. Anhydrous *N,N*-dimethylformamide (1.4 mL) was added to the Schlenk tube via syringe. The suspension was stirred at room temperature for 10 minutes. After that, chiral ammonium salt **4** (40 mg, 0.060 mmol) was added and the reaction mixture was stirred for an additional 10 min at room temperature. Following the subsequent addition of iodomethane (0.20 mL, 0.30 mmol) via syringe, the resulting suspension was stirred at room temperature for 2 h. The reaction mixture was slowly quenched with 10 wt% NaOH aq. (1 mL) [Caution: Exothermic]. Water (20 mL) was added, and the reaction mixture extracted with CH₂Cl₂ (20 mL × 3). The combined organic layer was washed with brine (20 mL) and dried over anhydrous sodium sulfate. The residual organic salts were removed by passing through an alumina plug (3 cm) and the resulting solution concentrated under reduced pressure. The crude product obtained in this way was purified by alumina column chromatography (column diameter: 2.0 cm, height: 10 cm, eluent: CH₂Cl₂/*n*-hexane = 1/39) to remove residual mineral oil. The solid obtained in this way was washed with MeOH (0.2 mL) to afford 10 mg of a white solid corresponding to compound **1-Me** in 48% yield. The as-synthesized compound **1-Me** was analyzed by HPLC and the enantiomer **(S,R,R)-1-Me** was calculated to have been formed in 10% ee.

4.6.10. *N*-methylation of **1** using several chiral salts



Entry	Chiral salt	Temp. (°C)	Time (h)	% <i>ee</i> ^a
1		25	2	10
2	4	40	1	5
3		15	6	9
4		10	9	5
5	8	25	2	0
6	9	25	2	0
7	10	25	2	0
8	11	25	2	0

^a Determined from HPLC analysis (column: CHIRALPAK IJ-5, eluent: MeOH, temperature: 40 °C, flow rate: 1.0 mL/min).

4.7. References

1. V. Böhmer, D. Kraft, M. Tabatabai, Inherently Chiral Calixarenes, *J. Incl. Phenom. Mol. Recognit. Chem.*, **1994**, *19*, 17–39.
2. A. Szumna, Inherently chiral concave molecules—from synthesis to applications, *Chem. Soc. Rev.*, **2010**, *39*, 4274–4285
3. G. E. Arnott, Inherently Chiral Calixarenes: Synthesis and Applications, *Chem. Eur. J.*, **2017**, *24*, 1744–1754.
4. M. Tang, X. Yang, Catalytic Enantioselective Synthesis of Inherently Chiral Molecules: Recent Advances, *Eur. J. Org. Chem.*, **2023**, e202300738.
5. M. Rickhaus, L. Jundt, M. Mayor, Determining Inversion Barriers in Atropisomers – A Tutorial for Organic Chemists, *Chimia*, **2016**, *70*, 192–202.
6. S. Kulyk, S. M. D. Paul, M. A. Marx, T. M. Peakman, C. R. Smith, Atropisomeric Racemization Kinetics of MRTX1719 Using Chiral Solvating Agent-Assisted ¹⁹F NMR Spectroscopy, *ACS Omega*, **2022**, *36*, 32062–32067.
7. M. Kitamura, S. Shirakawa, K. Maruoka, Powerful Chiral Phase-Transfer Catalysts for the Asymmetric Synthesis of α -Alkyl- and α,α -Dialkyl- α -amino acids, *Angew. Chem. Int. Ed.*, **2005**, *44*, 1549–1551.
8. G. M. Sheldrick, *SHELXT* – Integrated space-group and crystal-structure determination, *Acta Crystallogr. Sect. A*, **2015**, *71*, 3–8.
9. G. M. Sheldrick, Crystal structure refinement with *SHELXL*, *Acta Crystallogr. Sect. C*, **2015**, *71*, 3–8.
10. Gaussian 16, Revision C.01, M. J. Frisch, G. W. Trucks, H. B. Schlegel, G. E. Scuseria, M. A. Robb, J. R. Cheeseman, G. Scalmani, V. Barone, G. A. Petersson, H. Nakatsuji, X. Li, M. Caricato, A. V. Marenich, J. Bloino, B. G. Janesko, R. Gomperts, B. Mennucci, H. P. Hratchian, J. V. Ortiz, A. F. Izmaylov, J. L. Sonnenberg, D. Williams-Young, F. Ding, F. Lipparini, F. Egidi, J. Goings, B. Peng, A. Petrone, T. Henderson, D. Ranasinghe, V. G. Zakrzewski, J. Gao, N. Rega, G. Zheng, W. Liang, M. Hada, M. Ehara, K. Toyota, R. Fukuda, J. Hasegawa, M. Ishida, T. Nakajima, Y. Honda, O. Kitao, H. Nakai, T. Vreven, K. Throssell, J. A. Montgomery, Jr., J. E. Peralta, F. Ogliaro, M. J. Bearpark, J. J. Heyd, E. N. Brothers, K. N. Kudin, V. N. Staroverov, T. A. Keith, R. Kobayashi, J. Normand, K. Raghavachari, A. P. Rendell, J. C. Burant, S. S. Iyengar, J. Tomasi, M. Cossi, J. M. Millam, M. Klene, C. Adamo, R. Cammi, J. W. Ochterski, R. L. Martin, K. Morokuma, O. Farkas, J. B. Foresman, and D. J. Fox, Gaussian, Inc., Wallingford CT, 2016.

11. S. Grimme, J. Antony, S. Ehrlich, H. Krieg, A consistent and accurate *ab initio* parametrization of density functional dispersion correction (DFT-D) for the 94 elements H-Pu, *J. Chem. Phys.*, **2010**, *132*, 154104.
12. S. Grimme, S. Ehrlich, L. Goerigk, Effect of the damping function in dispersion corrected density functional theory, *J. Comput. Chem.*, **2011**, *32*, 1456–1465.
13. D. V. D. Spoel, E. Lindahl, B. Hess, G. Groenhof, E. A. Mark, H. J. C. Berendsen, GROMACS: Fast, flexible, and free, *J. Comput. Chem.*, **2005**, *26*, 1701–1718.
14. B. Hess, C. Kutzner, D. V. D. Spoel, E. Lindahl, GROMACS 4: Algorithms for Highly Efficient, Load-Balanced, and Scalable Molecular Simulation, *J. Chem. Theory Comput.*, **2008**, *4*, 435–447.
15. C. I. Bayly, P. Cieplak, W. Cornell, P. A. Kollman, A well behaved electrostatic potential based method using charge restraints for deriving atomic charges: the RESP model, *J. Phys. Chem.*, **1993**, *97*, 10269–10280.
16. D.A. Case, H.M. Aktulga, K. Belfon, I.Y. Ben-Shalom, S.R. Brozell, D.S. Cerutti, T.E. Cheatham, III, G.A. Cisneros, V.W.D. Cruzeiro, T.A. Darden, R.E. Duke, G. Giambasu, M.K. Gilson, H. Gohlke, A.W. Goetz, R. Harris, S. Izadi, S.A. Izmailov, C. Jin, K. Kasavajhala, M.C. Kaymak, E. King, A. Kovalenko, T. Kurtzman, T.S. Lee, S. LeGrand, P. Li, C. Lin, J. Liu, T. Luchko, R. Luo, M. Machado, V. Man, M. Manathunga, K.M. Merz, Y. Miao, O. Mikhailovskii, G. Monard, H. Nguyen, K. A. O’Hearn, A. Onufriev, F. Pan, S. Pantano, R. Qi, A. Rahnamoun, D.R. Roe, A. Roitberg, C. Sagui, S. Schott-Verdugo, J. Shen, C.L. Simmerling, N.R. Skrynnikov, J. Smith, J. Swails, R.C. Walker, J. Wang, H. Wei, R.M. Wolf, X. Wu, Y. Xue, D.M. York, S. Zhao, and P.A. Kollman (2021), Amber 2021, University of California, San Francisco.
17. J. Wang, R. M. Wolf, J. W. Caldwell, P. A. Kollman, D. A. Case, Development and testing of a general amber force field, *J. Comput. Chem.*, **2004**, *25*, 1157–1174.
18. G. Bussi, D. Donadio, M. Parrinello, Canonical sampling through velocity rescaling, *J. Chem. Phys.*, **2007**, *126*, 014101.
19. H. J. C. Berendsen, J. P. M. Postma, W. F. V. Gunsteren, A. DiNola, J. R. Haak, Molecular dynamics with coupling to an external bath, *J. Chem. Phys.*, **1984**, *81* 3684–3690.
20. M. Parrinello, A. Rahman, Polymorphic transitions in single crystals: A new molecular dynamic method, *J. Appl. Phys.*, **1981**, *52*, 7182–7190.
21. S. Nosé, M. L. Klein, Constant pressure molecular dynamics for molecular systems, *Mol. Phys.*, **1983**, *50*, 1055–1076.

22. U. Essmann, L. Perera, M. L. Berkowitz, A smooth particle mesh Ewald method, *J. Chem. Phys.*, **1995**, *103*, 8577–8593.
23. The isothermal compressibility of *n*-hexane at 298 K and 1 atm. is taken from http://www.ddbst.com/en/EED/PCP/CMPT_C89.php (last accessed on 17th January 2023)

Chapter 5

Acid-Stability of Calix[3]pyrrole-Boron Complex and Application to the Design of Highly Acid Stable BODIPY Dye

Abstract

The stability of the calix[3]pyrrole boron complex under acidic conditions was investigated to show that it forms adducts with acid by protonation of pyrrole and coordination of conjugate base on boron center. This unique protonation behavior was then applied for the design of acid stable BODIPY. The designed BODIPY, consisting of tripyrrolic macrocycle structure with boron at the center, showed remarkable stability against acid and fluorescence turn-on upon protonation under acidic conditions. The stability and fluorescence in acidic solution were then applied to the staining of strongly acidic materials, which cannot be stained by conventional BODIPYs due to decomposition.

5.1. Introduction

As introduced in Chapters 2–4, calix[3]pyrrole and derivatives with sufficient macrocyclic strain were found to undergo strain-induced ring expansion reaction under acidic conditions. This reactivity helped to understand why tripyrrolic macrocycles were never found in the acid-catalyzed condensation reaction of pyrrole and carbonyl compounds. On the other hand, subporphyrins, a class of conjugated tripyrrolic macrocycles, are known to be obtained in acid-catalyzed condensation reaction using a boron complex of pyrroles as a precursor^{1,2,3}. Therefore, it can be assumed that the boron atom has any stabilization effect on tripyrrolic macrocycles. In this sense, complexation with boron might stabilize calix[3]pyrrole against acid, and detailed analysis of it would supply information about the role of boron stabilizing tripyrrolic macrocycles.

In this work, the boron complex of calix[3]pyrrole was prepared and its stability under acidic conditions was investigated. The boron complex showed stability under acidic conditions and recovered after neutralization. By direct analysis in the presence of TFA by NMR spectroscopy, it was found that calix[3]pyrrole boron complex formed adduct with TFA by protonation at pyrrole and coordination of conjugate base to boron atom. Even with stronger acid, MsOH, calix[3]pyrrole boron complex was doubly protonated to form cationic complex, still keeping the boron atom at the center of the tripyrrolic macrocycle. This protonation behavior was then applied to the design of an acid stable boron dipyrromethene (BODIPY) dye, which exhibited high acid stability as well as fluorescence turn-on upon protonation. This acid stable BODIPY could be used to dye highly acidic polymer resin, NafionTM, which could not be stained by conventional BODIPY, or acidic organogel with sulfonic acid functional groups.

5.2. Acid-stability of Calix[3]pyrrole Boron Complex

The boron complex of calix[3]pyrrole **2** was prepared by treating calix[3]pyrrole **1** with boron tribromide after deprotonation with *n*-butyllithium in 25% yield (**Figure 5-1a**). In the ^1H NMR spectrum of **2**, only two peaks were observed at 5.95 and 1.69 ppm, which are assignable to pyrrole β -protons and methyl protons, indicating highly symmetric structure of **2**. Single crystal X-ray diffraction analysis revealed that **2** has a shallow bowl-shaped structure with a trigonal planar structure of the boron center (**Figure 5-1b**). When boron complex **2** was treated with TFA in dichloromethane, under which conditions calix[3]pyrrole underwent ring expansion reaction, **2** was recovered after neutralization even after 4 hours of reaction time, showing the improved stability against acid by complexation with boron (**Figure 5-2**).

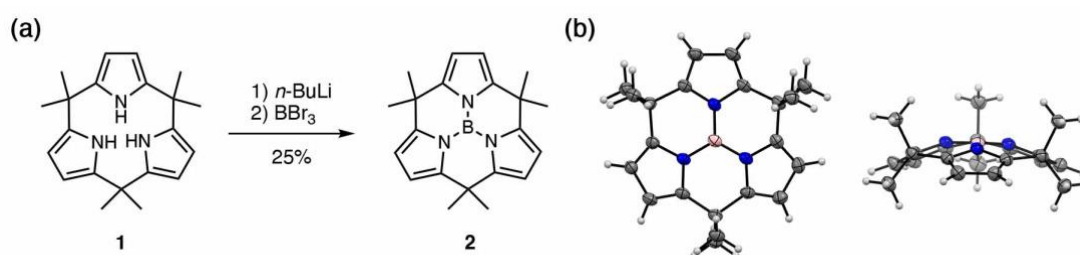


Figure 5-1. (a) Synthesis of boron-calix[3]pyrrole **2** and (b) crystal structure of **2**.

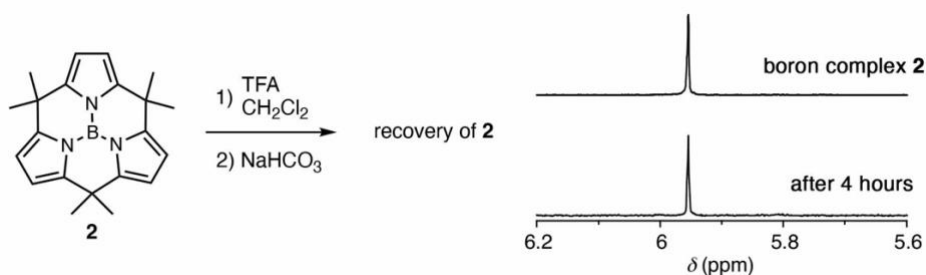


Figure 5-2. ^1H NMR spectrum corresponds to the stability test of **1** (CDCl₃, 400 MHz, 298 K)

For a detailed analysis of this acid stability, the chloroform-*d* solution of **2** with 3.3 equivalents of trifluoroacetic acid was analyzed by ^1H NMR spectroscopy. The ^1H NMR spectrum showed the formation of the TFA adduct **3**, with the appearance of a pair of doublets observed at 3.6–4.0 ppm attributed to the methylene proton of the *3H*-pyrrole, as well as asymmetrically observed pyrrole β -protons at 5.8–6.2 ppm and methyl groups at 1.6–1.8 ppm (**Figure 5-3**). The ^{11}B NMR spectrum showed the signal shift from 22.8 ppm for **2** to -4.3 ppm for **3** corresponding to the change in boron coordination from trigonal planar to tetrahedral. Although **3** was observed as a mixture with **1** in solution at a molar ratio of **2:3** = 34:66 at 25 °C, the ratio of **3** decreased to 51% and 40% at 40 °C and 50 °C, respectively, indicating that **2** and **3** are in equilibrium.

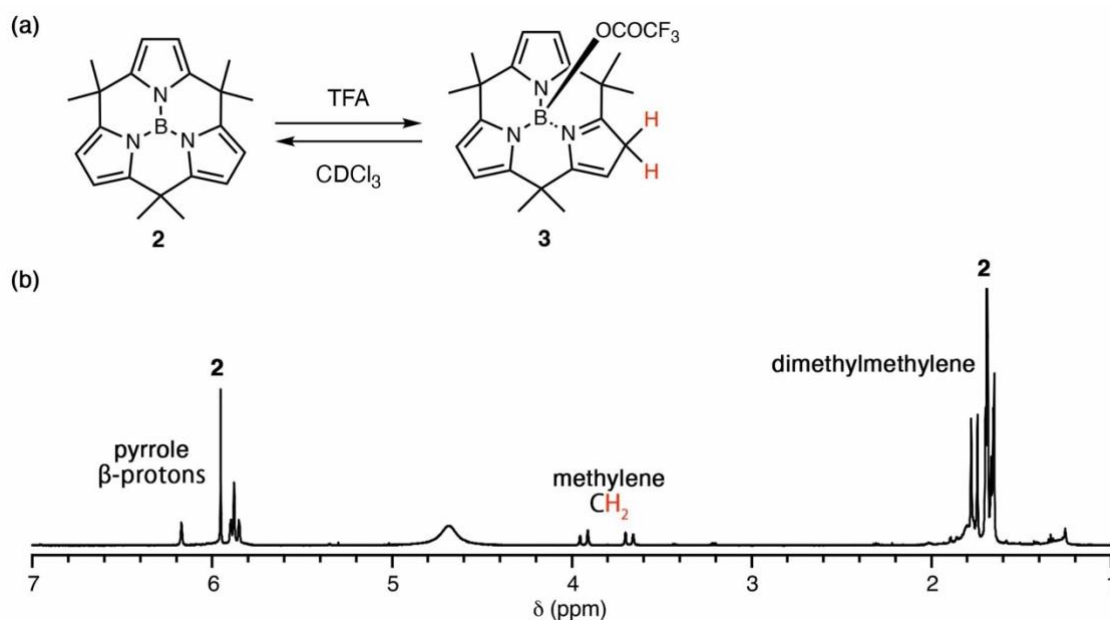


Figure 5-3. (a) Reaction scheme for the formation of **3** upon addition of TFA and (b) ^1H NMR spectrum of **3** prepared by dissolving **2** in chloroform-*d* (6.0 mM) in the presence of 3.3 equivalent of TFA (400 MHz, 298 K).

Slow evaporation of chloroform solution of **1** in the presence of excess amount of TFA gave a diffraction grade crystal of **3**. X-ray diffraction analysis of the single crystal of **3** confirms that one of the three pyrroles was protonated at the β -position to give a $3H$ -pyrrole ring, and a tetrahedral coordination of boron center bounded to the trifluoroacetate anion (**Figure 5-4**). One of the three B–N bonds was 1.531(5) Å, which is significantly longer than the other two bonds (1.490(4) and 1.493(4) Å). The C–C distances around the pyrrole ring, which has a longer B–N bond were 1.436(15) Å at C(2)–C(3), 1.516(11) Å at C(3)–C(4), and 1.389(16) Å at C(4)–C(5), indicating the $3H$ -pyrrole structure. From these analyses, it can be said that a pyrrole acts as a base to accept proton, and boron acid as an acid upon addition of TFA.

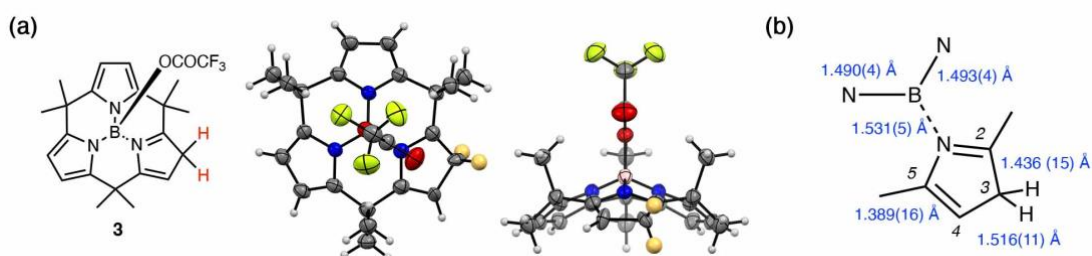


Figure 5-4. (a) Crystal structure of **3** and (b) selected bond length in **3**.

Although pyrrole tends to be protonated at the α -position, the observed state was protonated at the β -position. This may be due to the steric effect of the neighboring dimethylmethylene. In fact, comparison of DFT calculated energy for α -protonated monoadducts and β -protonated monoadduct (OH at the boron atom for ease of calculation) suggests that the β -protonated adduct is more than 20 kcal/mol stable compared to the α -protonated monoadducts. The optimized geometry suggested that the steric repulsion between proton and dimethylmethylene moiety or deformation of the tripyrrolic macrocycle skeleton is the reason for destabilization of α -protonated monoadducts.

Further addition of trifluoroacetic acid to the mixture of **2** and **3** resulted in a further change in the spectrum, and the exclusive formation of **4** was observed after addition of 25 equivalents of TFA (**Figure 5-5a**). The ^1H NMR spectrum of **4** showed signals from pyrrole β -protons at 8.14, 7.16, and 6.08 ppm as a pair of doublets and a singlet, methyl protons at 1.84, 1.83, 1.79 and -0.25 ppm as four singlets, and pyrrole α -protons at 5.90 ppm (**Figure 5-5b**). The ^{11}B NMR spectrum showed a signal at -3.55 ppm indicating that the boron atom is in the tetrahedral coordination mode. Further structural analysis using HMQC and HMBC confirmed the structure of **4**, that two pyrroles are protonated at the α -position (**Figure 5-5c,d**). While many possible structures exist as doubly protonated forms of **2**, DFT calculations supported that **4** is the most favorable isomer among them. The formation of **4** was also reversible process because **4** was observed when the mixture of **2** and **3** was cooled to -50 °C. Therefore, it was assumed that the first protonation can occur at both α - and β -position of pyrrole in an equilibrium, while only the most energetically favored **3** was observed in ^1H NMR spectra. When an excess amount of TFA was added, a second protonation occurred, and again only the most stable isomer **4** was observed in the ^1H NMR spectra. This would be the reason why the protonation site is different between **3** and **4**.

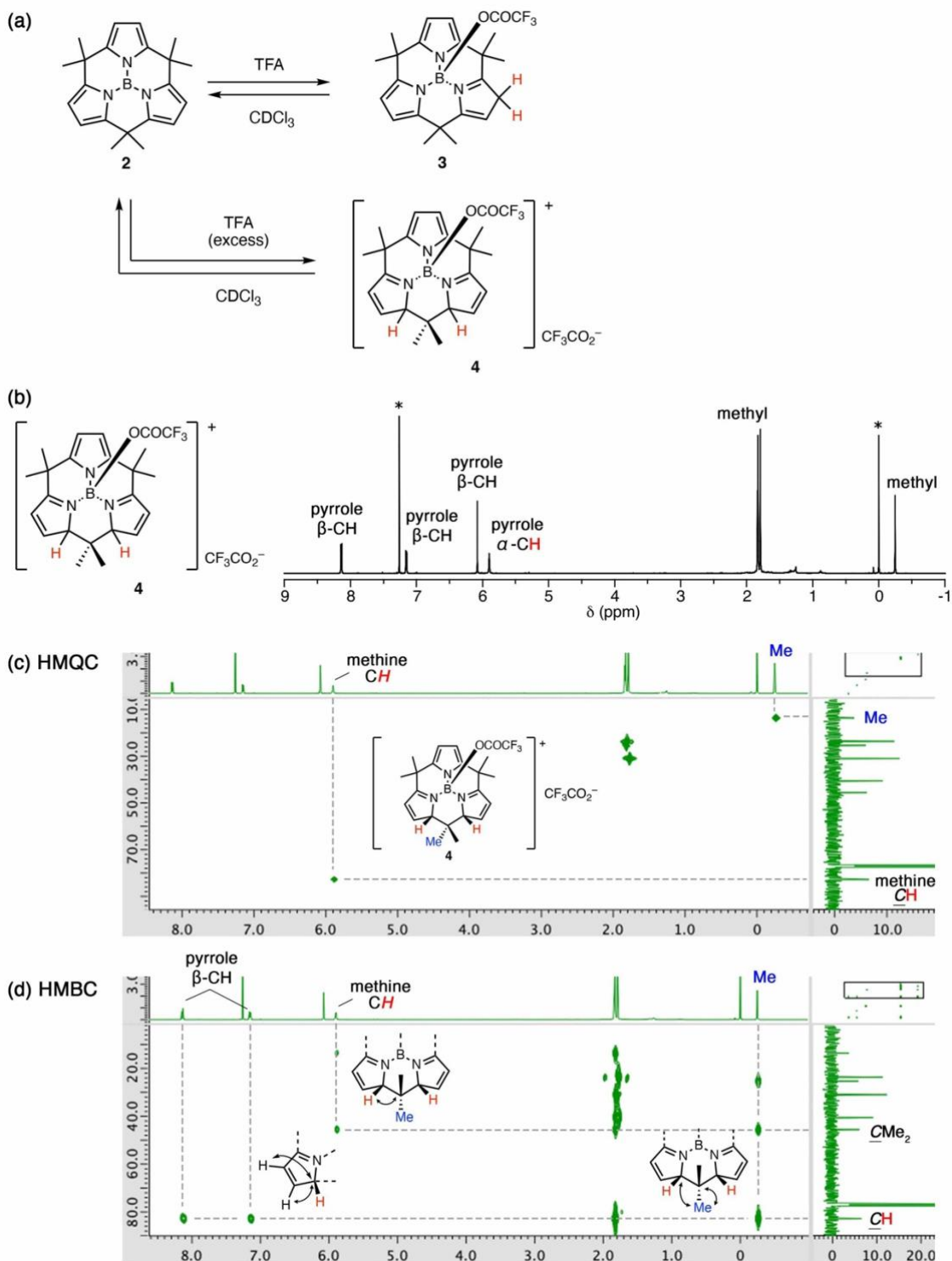


Figure 5-5. (a) Reaction of **2** and TFA, (b) ^1H NMR spectrum of **4** prepared by the addition of TFA (25 eq.) to the solution of **2** (6.0 mM) in chloroform-*d* (400 MHz, 298 K, *: solvent and internal standard TMS), and (c) HMQC and (d) HMBC spectra of **4** in chloroform-*d*.

When methanesulfonic acid (MsOH) was used instead of TFA, the formation of a doubly protonated cationic complex **5** similar to **4** was observed (**Figure 5-6a**). In this case, no monoprotonated species were found even with less than 1 equivalent of MsOH. In the ^1H NMR spectrum, a characteristic signal of the methine proton was observed at 6.14 ppm for 2*H*-pyrroles in the presence of 3.0 equivalents of MsOH. This result indicates that the protonated form **5** is sufficiently stable to retain the boron atom coordinated by the tripyrrolic macrocycle skeleton.

On the other hand, monoprotonated compound **6** was observed when acetic acid was added to the chloroform-*d* solution of **2**. Although only a very small amount of adduct **6** was observed at room temperature with an excess amount of acetic acid, the formation of **6** was favored at lower temperatures, and exclusive formation of **6** was observed at $-50\text{ }^\circ\text{C}$ (**Figure 5-6b**). Doubly protonated species such as **3** or **4** were not observed even with a large excess of acetic acid. The addition of water to the chloroform-*d* solution of **2** also furnished monoprotonated compound **7**, and the ratio of **7** to **2** increased as with decreasing temperature. Exclusive formation of **7** was observed below $-50\text{ }^\circ\text{C}$ (**Figure 5-6c**).

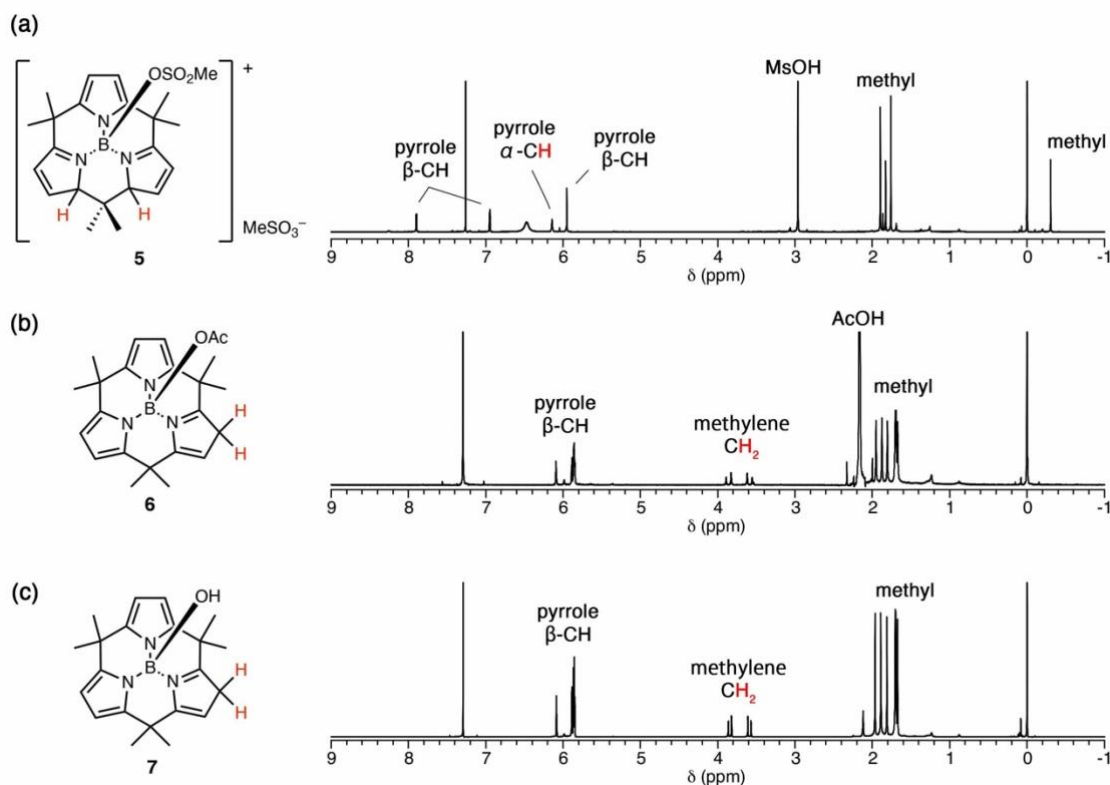
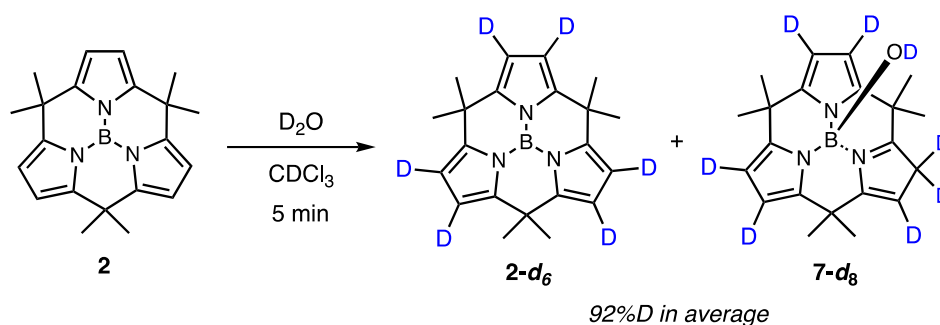


Figure 5-6. (a) ^1H NMR spectra of **5**, (b) **6**, and (c) **7** in chloroform-*d* prepared by adding MsOH (3.0 eq.), AcOH (30 eq.), and water (1.0 eq.), respectively, measured at 298 K (**5**) and 223 K (**6** and **7**).

In D₂O saturated chloroform solution, **2** caused rapid H/D exchange reaction via reversible D₂O adduct formation, and 92% deuteration of the pyrrole β-proton was observed after 5 minutes at 298 K (Scheme 5-2). The van't Hoff analysis⁴ of equilibrium between **2** and **7** gave physical parameters of $\Delta H = -56.5 \text{ kJ mol}^{-1}$, $\Delta S = -151 \text{ J mol}^{-1} \text{ K}^{-1}$, and $\Delta G = -11.46 \text{ kJ mol}^{-1}$ at 298 K (Figure 5-7). Although protonation at pyrrole β-position causes dearomatization of the pyrrole ring, the formation of **7** is favored even at room temperature, perhaps due to the increased basicity of pyrrole upon coordination of a fourth ligand to the boron atom.



Scheme 5-2. H/D exchange reaction of **2** upon addition of D₂O

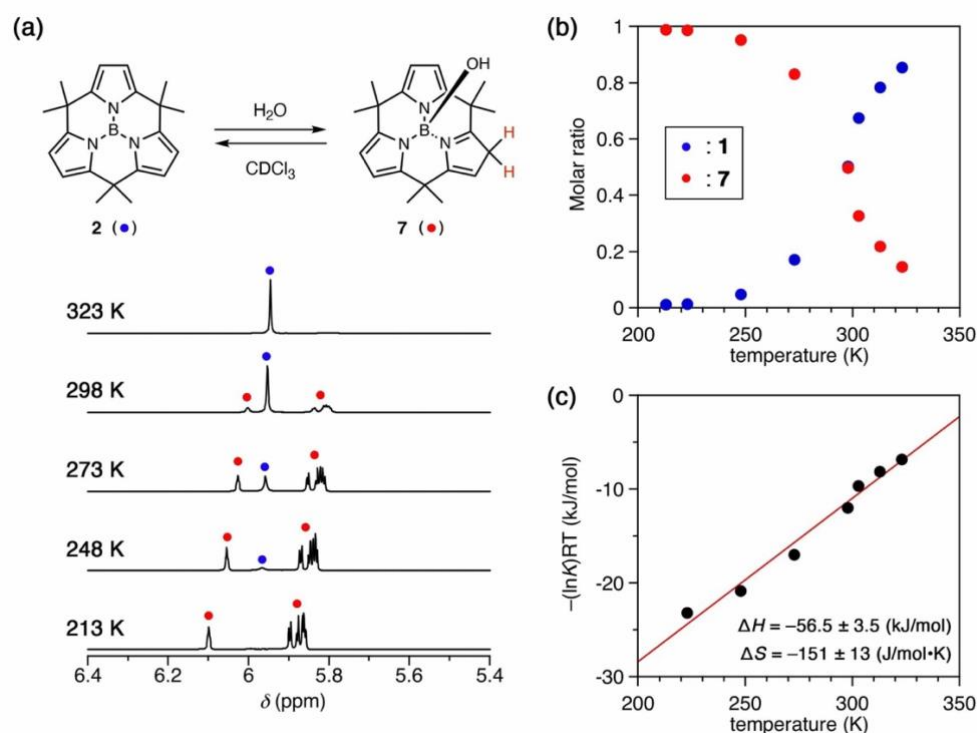
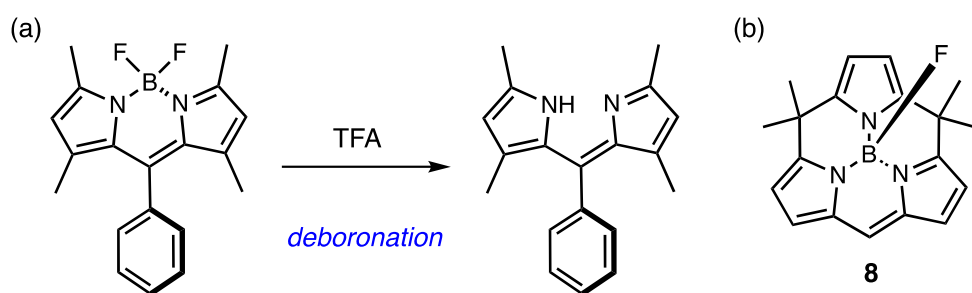


Figure 5-7. (a) ¹H NMR spectra (pyrrolyl proton region) of **2** in chloroform-*d* containing 1 equiv. of water measured at various temperature, (b) plot of molar ratio **2**:**7** versus temperature, and (c) van't Hoff plot for the equilibrium between **2** and **7**.

5.3. Design and Synthesis of Cyclic BODIPY Dye

The unusual protonation behavior of **2** under acidic conditions prompted the author to apply it to the design of acid resistant chromophore. Boron dipyrromethene (BODIPY) is the boron complex of dipyrromethene and regarded as a fluorescent probe characterized by its intense absorption/fluorescence band, narrow Stokes shift, and high fluorescence quantum yield.^{5,6,7} While BODIPYs are widely used as fluorescent chromophores, it is also known that BODIPYs tend to undergo deboronation under acidic conditions, which results in the loss of fluorescent character (**Scheme 5-3**).^{8,9,10} There are many BODIPYs that can be used as pH indicators, i.e., acid/base responsive BODIPYs are known.¹¹ However, most of them are used in near-neutral or weakly acidic pH range, and BODIPYs that can be used in highly acidic conditions (pH ~ 1) have hardly been investigated.¹²⁻¹⁴ As acid-stable fluorophores, several examples based on oxazine^{15,16}, cyanine^{17,18}, rhodamine^{19,20}, and so on, have been reported to date. Although such acid-stable fluorophores are already known, acid-stable BODIPY, with characteristic fluorescence properties as introduced above, would be a new candidate for staining of strongly acidic materials. In this sense, cyclic BODIPY **8** was designed, which is expected to show remarkably high acid stability by combining BODIPY skeleton and calix[3]pyrrole boron complex **2**.



Scheme 5-3. (a) Deboronation of BODIPY under acidic conditions and (b) structure of newly designed cyclic BODIPY **8**.

The synthesis of cyclic BODIPY **8** was started from tripyrrane **9**²¹ (**Figure 5-8a**). Tripyrrane **9** was directly complexed with boron atom using borane triethylamine to give **10** in 98% yield. Boron complex **10** was then subjected to the macrocyclization reaction using triethyl orthoformate to afford methoxy-cyclic BODIPY **11** in 10% yield. Since the methoxy group on the boron atom appeared to be prone to axial ligand exchange, it was fluorinated with boron trifluoride etherate to give **8** as a more stable compound. In the ¹¹B NMR spectrum of **8**, a doublet signal observed at -2.69 ppm with $J_{B-F} = 40$ Hz confirmed the formation of the B-F bond. Single crystal X-ray diffraction analysis of **8** revealed tetrahedral coordination on the boron atom with three nitrogen and one fluoride atom (**Figure 5-8b**). The bond length around the dipyrromethene skeleton revealed its effectively conjugated structure.

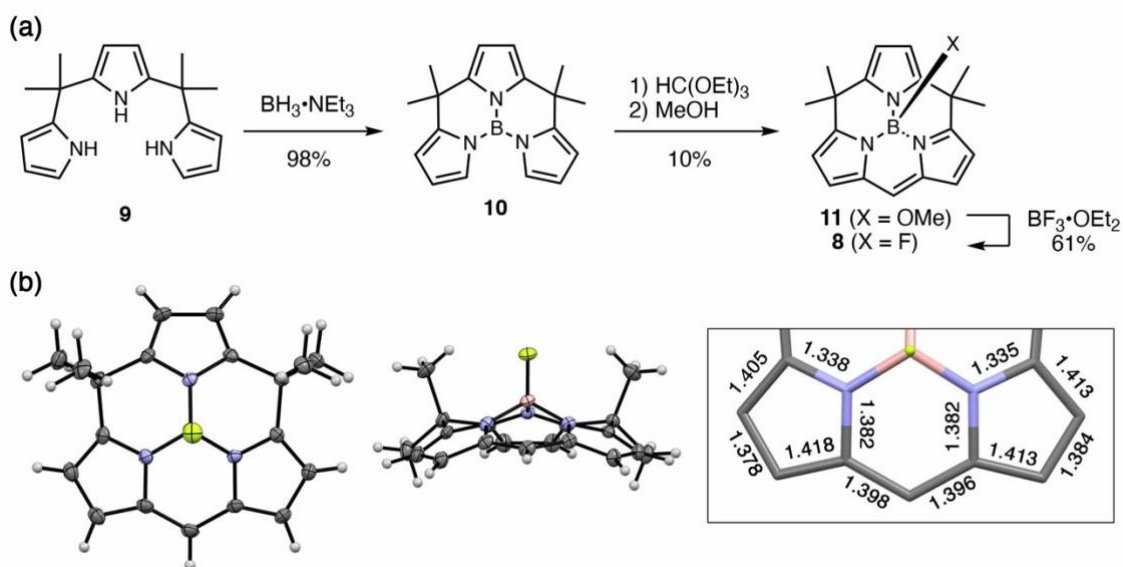


Figure 5-8. (a) Synthesis of cyclic BODIPY **8** and (b) crystal structure of **8**. The inset shows the selected bond lengths (Å) around dipyrromethene moiety.

The UV-Vis absorption spectrum of **8** measured in dichloromethane showed an intense absorption band with absorption maximum at 539 nm with an absorption coefficient of $\epsilon = 3.3 \times 10^4 \text{ M}^{-1} \text{ cm}^{-1}$ (**Figure 5-9**). However, no fluorescence emission was observed. When TFA was added to the dichloromethane solution of **8** as a brief acid stability check, no obvious change in the absorption spectrum was observed while it showed intense fluorescence emission at 557 nm with a small Stokes shift, which is a common property of BODIPYs. The fluorescence intensity increased upon addition of TFA up to 5% (v/v), where the fluorescence quantum yield and fluorescence lifetime were 0.89 and 11.1 ns, respectively.

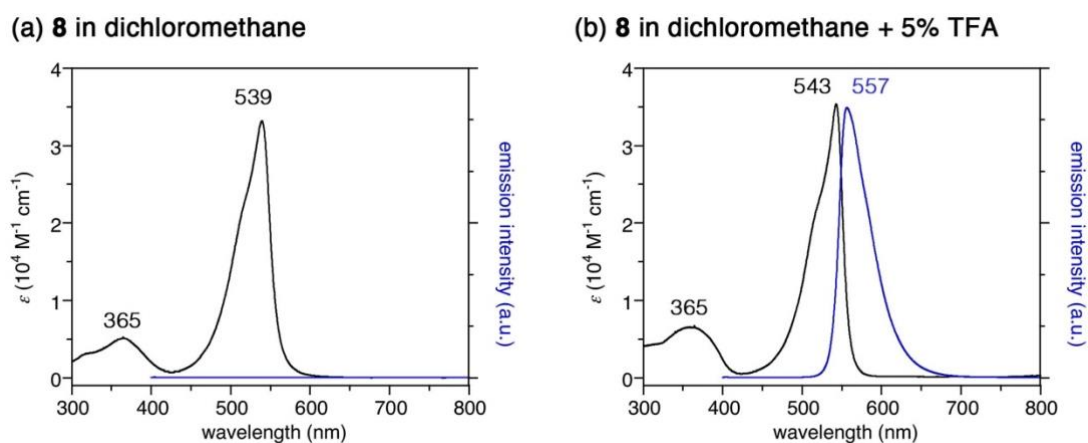


Figure 5-9. (a) UV-Vis absorption spectra (black line) and emission spectra (blue line) of **8** in dichloromethane and (b) with 5% (v/v) TFA (excitation wavelength: 360 nm).

Since the change in fluorescence property seemed to be due to protonation by acid additio, it was analyzed in detail by NMR spectroscopy (**Figure 5-10**). ^1H NMR spectrum of **8** in chloroform-*d* showed a pair of doublets at 6.91 and 6.26 ppm and a singlet at 7.17 ppm attributable to β -protons and a *meso*-proton of dipyrromethene moiety, respectively, and a singlet at 5.83 ppm that assignable to β -proton of an opposite pyrrole ring. Upon addition of TFA, broadening of the signal of pyrrole β -proton and low-field shift of other peaks were observed, suggesting the time-averaged C_s symmetric structure due to the reversible protonation at β -position of pyrrole in fast equilibrium. On the other hand, desymmetrization of signals was observed upon cooling to $-50\text{ }^\circ\text{C}$, and a pair of doublets assignable to the methylene protons of 3*H*-pyrrole generated by the protonation of pyrrole ring at the β -position was found at $-50\text{ }^\circ\text{C}$. Based on this observation, it can be said that protonation at the β -position of pyrrole ring occurred to afford $\mathbf{8}\cdot\text{H}^+$ by the addition of TFA. When MsOH or trifluoromethanesulfonic acid (TfOH) was used instead of TFA, similar change in the spectra was observed and no deboronation was observed. The acid dissociation constant of the protonated form $\mathbf{8}\cdot\text{H}^+$ was determined to be 3.22 in acetonitrile-*d*₃ using MsOH acid and 4-nitroaniline as a reference base.

Based on the protonation behavior of **8** by acid, the change in fluorescence property can be attributed to the protonation of the pyrrole ring. It was suggested that the fluorescence quenching observed in **8** under neutral conditions was caused by photoinduced electron transfer from pyrrole moiety to dipyrromethene moiety in the excited state as reported for several BODIPY analogues^{22,23}. Molecular orbital calculations of **8** indicated that HOMO-1 and LUMO of **8** are laying on the dipyrromethene moiety, while HOMO is on the pyrrole ring (**Figure 5-11**). On the other hand, HOMO and LUMO are on the dipyrromethene moiety in $\mathbf{8}\cdot\text{H}^+$. This molecular orbital analysis suggests that it is possible that electron transfer from dipyrromethene moiety to pyrrole ring may interfere with emission in **8**, but not in $\mathbf{8}\cdot\text{H}^+$.

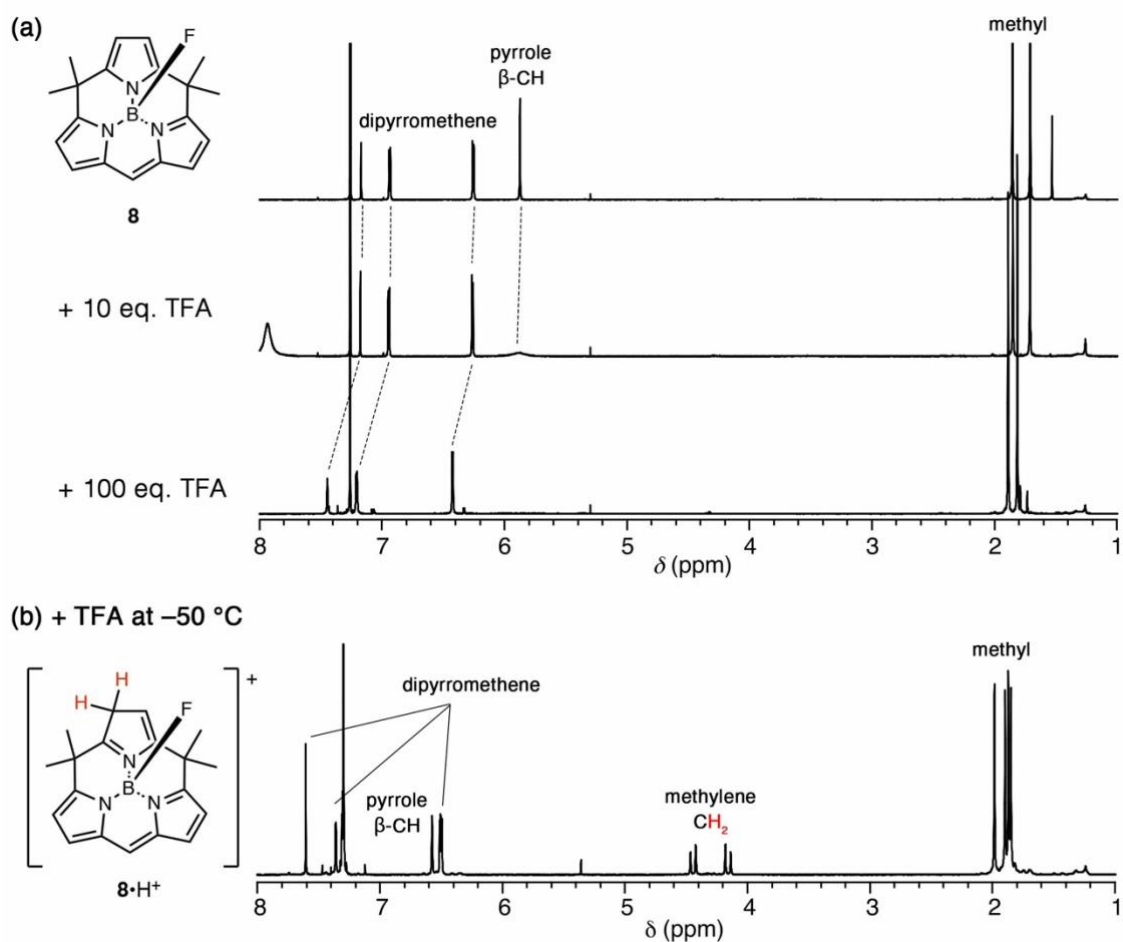


Figure 5-10. Analysis of protonation behavior of **8** upon addition of TFA in chloroform-*d*. (a) Comparison of ^1H NMR spectra before addition of TFA and after addition of 10 and 100 equiv. of TFA measured at 298 K. (b) ^1H NMR spectrum of **8** after addition of 100 equiv. of TFA measured at 223 K, suggesting the formation of **8** $\cdot\text{H}^+$.

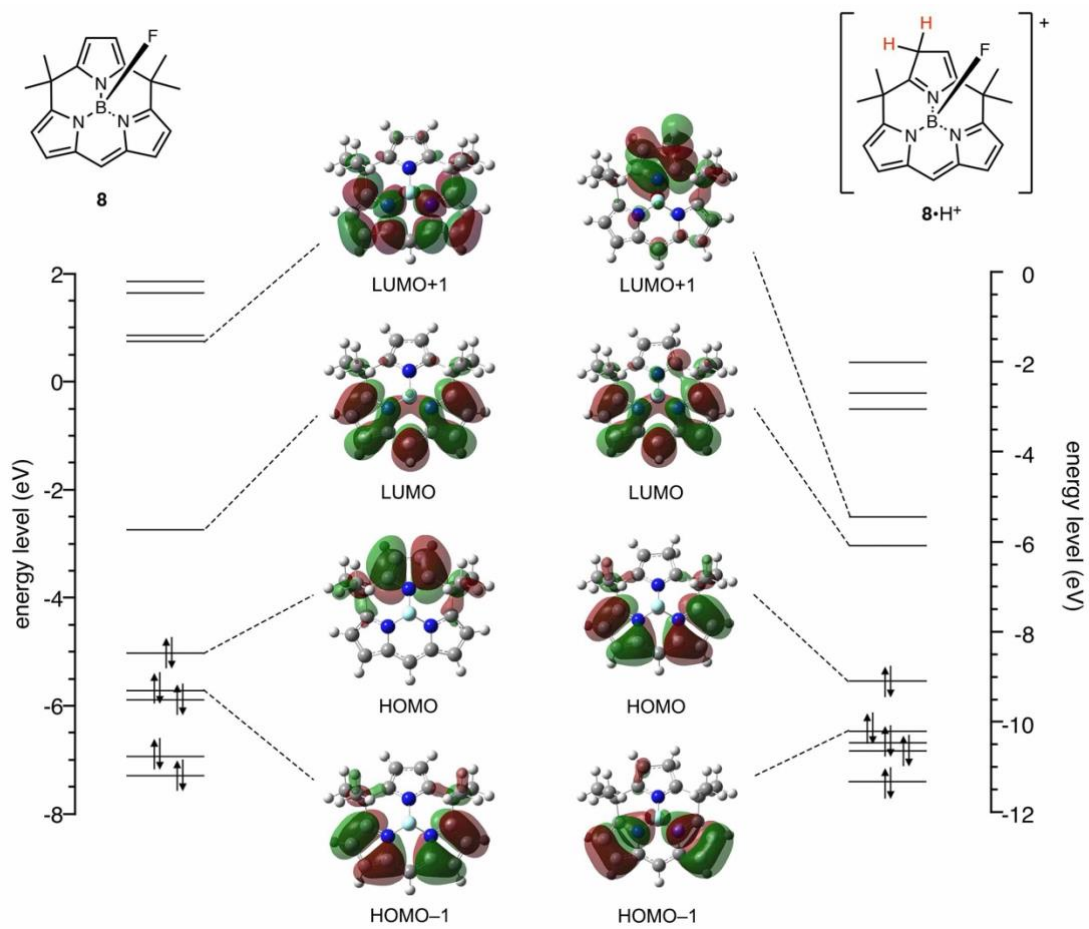


Figure 5-11. Frontier molecular orbital diagram of **8** and **8•H⁺** calculated at B3LYP 6-31G(d,p)/B3LYP6-31G(d,p) levels of theory.

5.4. Acid Resistance of cyclic BODIPY

The acid stability of **8** was then tested in neat acids and compared with commercial pentamethyl BODIPY **12** (Figure 5-12). In acetic acid, **12** remained strongly emissive ($\Phi_F = 0.86$) while **8** was not emissive due to the low acidity of acetic acid ($pK_a = 12.6$ in DMSO²⁴), which is not sufficient to protonate **8**. The emission from **12** became weaker in neat TFA ($\Phi_F = 0.29$) whose acidity is much stronger than acetic acid ($pK_a = 3.45$ in DMSO²⁴), and it became not emissive in stronger acids, MsOH ($pK_a = 1.8$ in DMSO²⁴), sulfuric acid ($pK_a = 1.4$ in DMSO²⁴), and trifluoromethanesulfonic acid (TfOH, $pK_a = 0.3$ in DMSO²⁴). From the change of absorption spectra, it was assumed that a deboronation occurred and fluorescent character was lost. On the other hand, **8** remained highly emissive even in neat TFA with high fluorescence quantum yield ($\Phi_F = 0.68$). Comparable fluorescence quantum yield was observed in neat MsOH or sulfuric acid with $\Phi_F = 0.62$ and 0.54 , respectively. However, a distinct blue shift in both absorption and emission spectra was observed when **8** was dissolved in TfOH.

Although **8** showed an explicit change in optical spectra in TfOH, the absorption band around 540 nm recovered after removal of TfOH and dissolved in neutral solvent. Therefore, it was suggested that the spectral change is the result of multiple protonation by super-acidic TfOH, and not the result of deboronation. ¹H NMR spectrum of **8** measured in TfOH/CD₂Cl₂ (v/v = 3/1) indicated signals around 2 and 7-8 ppm, that can be assigned as methyl groups and pyrrole or dipyrromethene moiety respectively along with set of doublets around 4-5 ppm, implying that **8** is multiply protonated by TfOH (Figure 5-13a). Furthermore, at several fluorescence lifetime were found (0.04, 2.46, and 5.97 ns at 430 nm and 0.07, 4.15, and 13.5 ns at 550 nm, respectively) when the emission lifetime was measured at 550 nm, indicating that multiple components are mixed. Indeed, **8** was recovered after neutralization although **12** was not recovered because of deboronation (Figure 5-13b). Since **8** was found to be protonated at β -position of pyrrole in acids like TFA or MsOH, it was suggested that further protonation occurs at dipyrromethene moiety to shorten the conjugation system by TfOH, much stronger acid than TFA or MsOH.

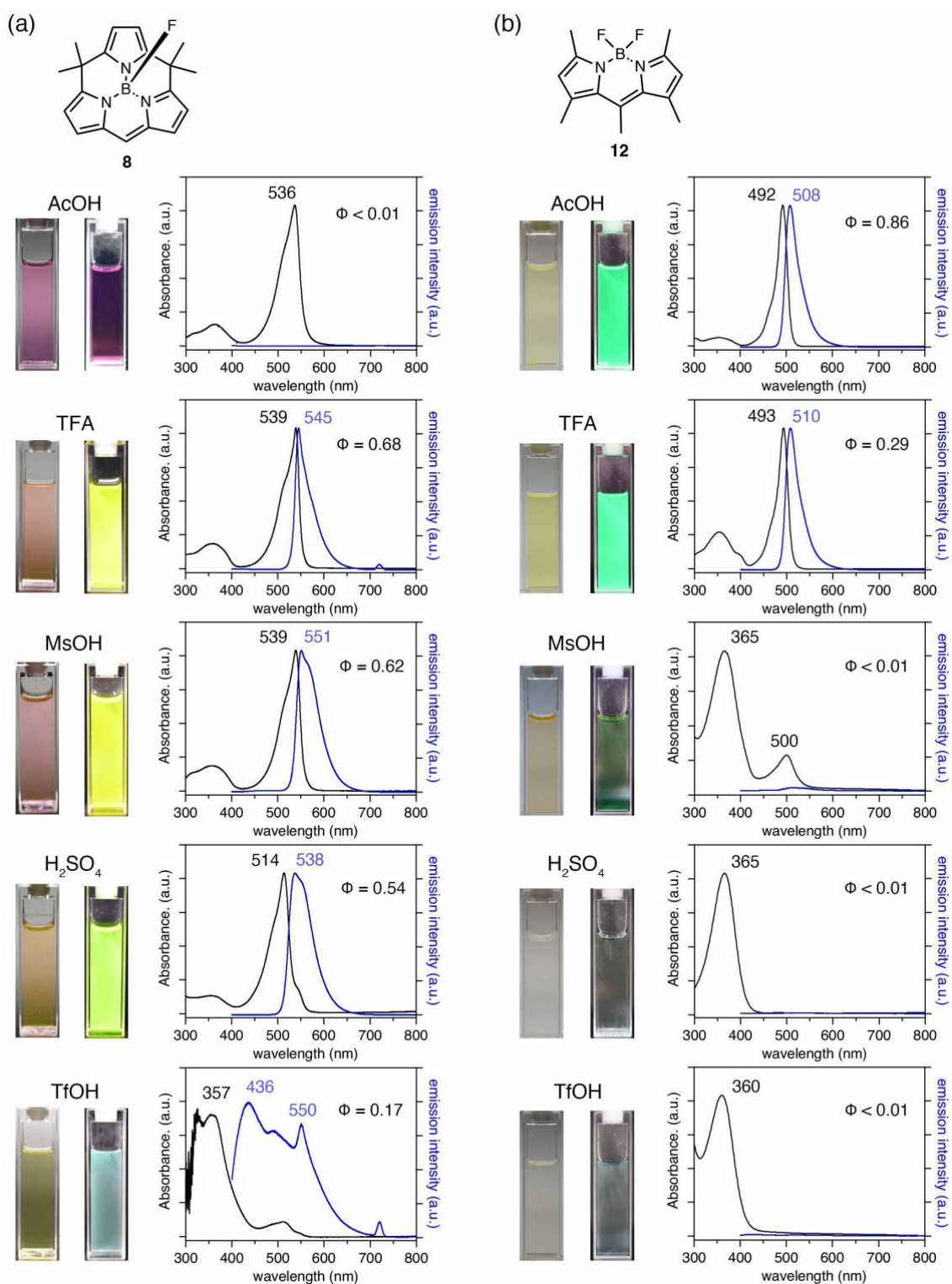


Figure 5-12. (a) BODIPY **8** and (b) **12** in neat acids: Photographs taken under room light (left) and UV light (right), and UV-Vis absorption (black line) and fluorescence emission (blue line) spectra (Excitation wavelength: 360 nm).

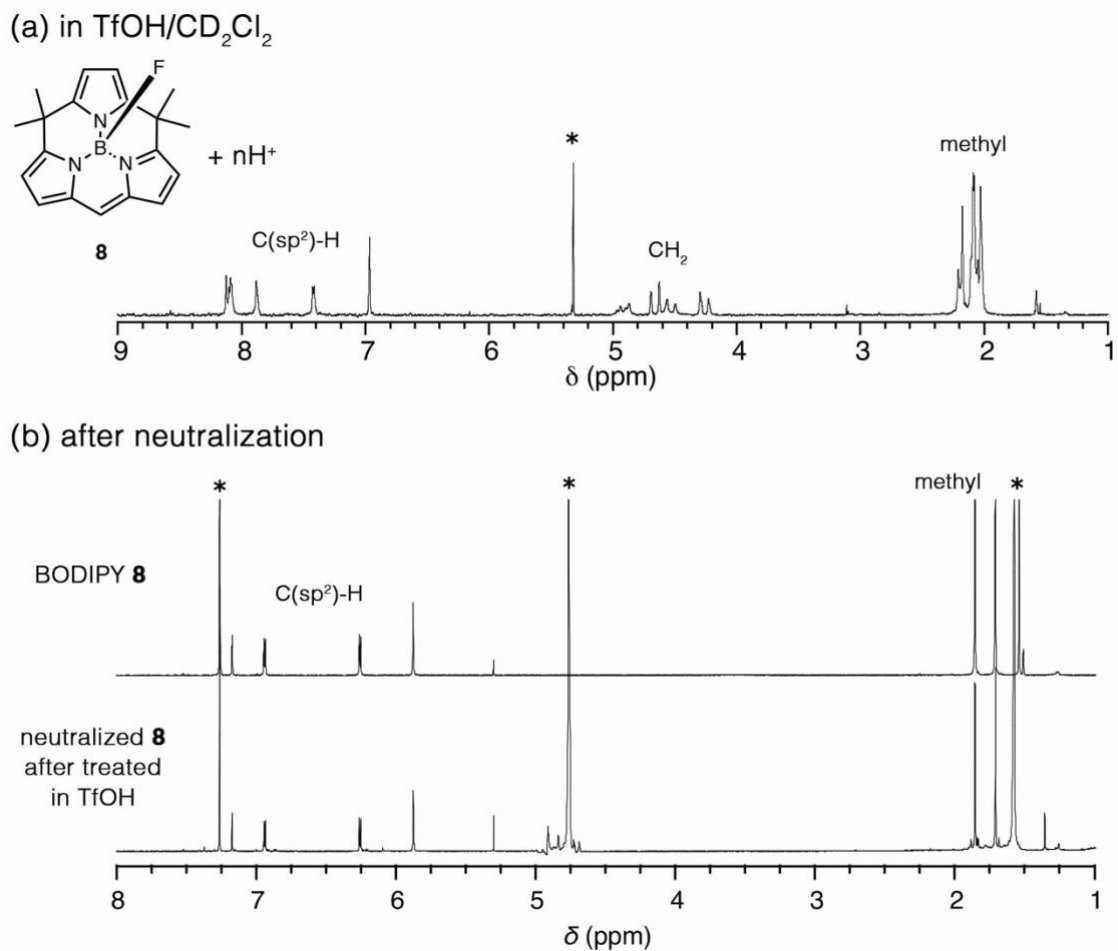


Figure 5-13. (a) ¹H NMR spectrum of **8** in TfOH/dichloromethane-*d*₂ (v/v = 3/1) suggesting that multiple protonation is occurring (400 MHz, 298 K). (b) Comparison of ¹H NMR spectra of **8** before and after dissolved in TfOH and neutralized. (CDCl₃, 298 K, 400 MHz). Asterisks denotes solvent signals.

The acid resistance of **8** was further investigated using various acids. When dissolved in hydrofluoric acid (50% aqueous solution) which is known to corrode glass, **8** showed intense absorption at 536 nm and emission signal at 551 nm, indicating that **8** was present in solution in its protonated form (**Figure 5-14a**). Although hydrofluoric acid is reported to be a weak acid ($pK_a = 15$ in DMSO²⁵) when diluted, it is also reported that acidity of hydrogen fluoride increases with increasing concentration.^{26,27} Thus, 50% hydrofluoric acid has sufficient acidity to protonate **8**. Similar protonation behavior was observed when aqueous solution of HBF₄ ($pK_a = 3.4$ in DMF²⁸) or HPF₆ ($pK_a \sim 0$ in DMSO²⁹), known as corrosive strong Brønsted acid, was used instead of hydrofluoric acid. **8** showed intense absorption band at 536 nm in both with slightly stronger absorption around 360 nm in the case of HPF₆, and emission band at 553 and 554 nm respectively (**Figure 5-14b, c**), again indicating no obvious change in **8**. In contrast, no fluorescence was observed in aqueous hydroiodic acid solution (**Figure 5-14d**). The absorption spectrum of **8** in 55% hydroiodic acid showed absorption band at 544 nm with broad absorption band below 400 nm due to iodine formed in HI solution. Therefore, **8** can exist in hydroiodic acid solution without deboronation despite reducing character of HI, but the fluorescence of protonated **8**•H⁺ should be quenched by the counter anion I⁻.³⁰

Stability was also investigated using fluorosulfonic acid, which has a higher acidity than H₂SO₄ (Hammett acidity $H_0 = -12.6$ for FSO₃H and -11 for H₂SO₄, respectively³¹). While both absorption and emission spectra of **8** in fluorosulfonic acid showed blue-shifted signals like those observed in sulfuric acid, these absorption and emission bands had narrow Stokes shifts characteristic of BODIPY (**Figure 5-14e**). This observation implied that BODIPY structure is retained but there should be some change in chemical structure other than protonation. After the removal of fluorosulfonic acid by neutralization, NMR analysis suggested that substitution occurred at one CH in the dipyrromethene moiety to give desymmetrized NMR signals as well as the loss of one CH signal. Therefore, **8** was found to retain the BODIPY structure even in fluorosulfonic acid, although a substitution reaction occurs.

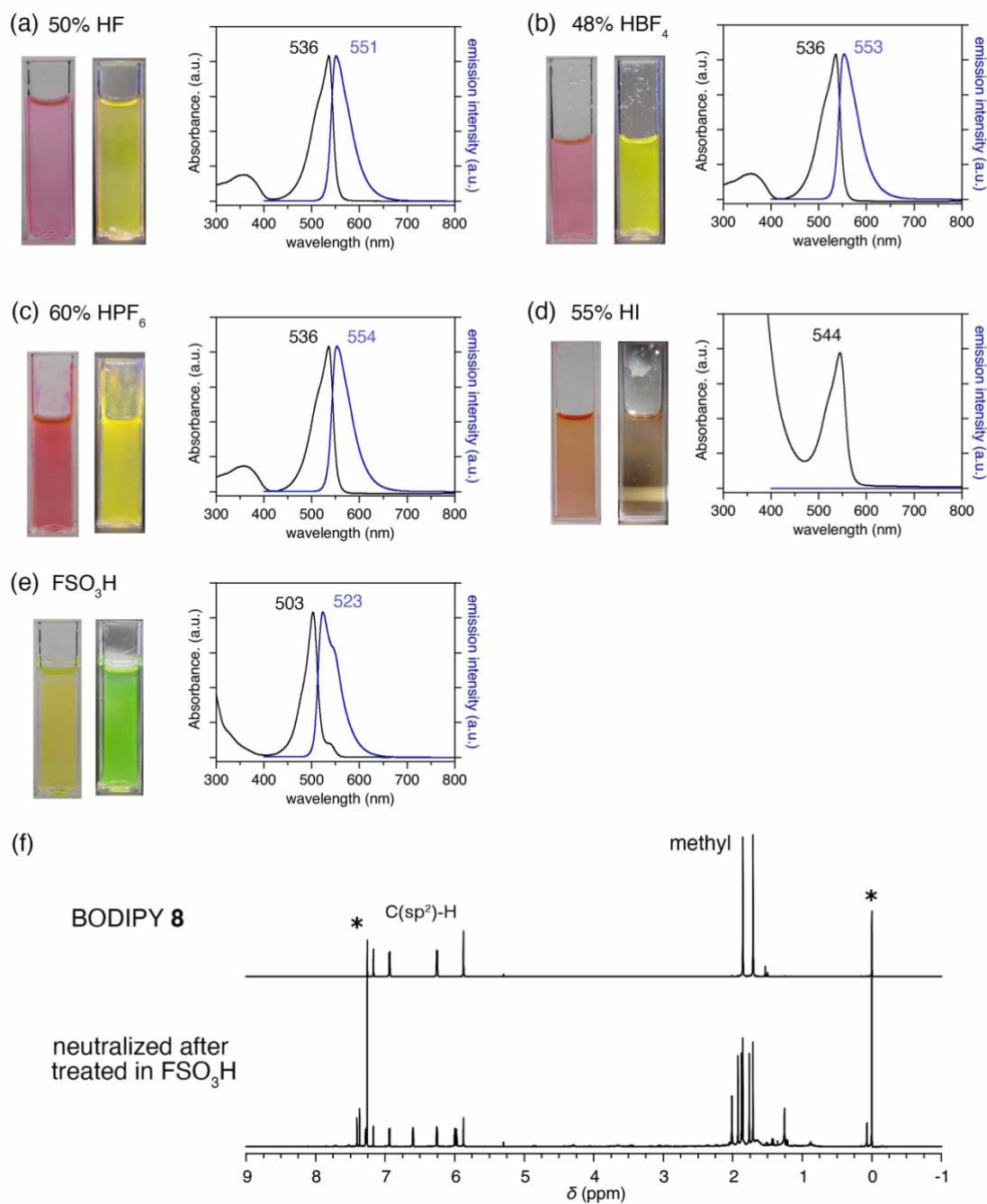


Figure 5-14. BODIPY **8** in (a) 50% hydrofluoric acid, (b) 48% HBF₄, (c) 60% HPF₆, (d) 55% hydroiodic acid, and (e) neat fluorosulfonic acid: Photographs taken under room light (left) and UV light (right), and UV-Vis absorption (black line) and fluorescence emission (blue line) spectra (Excitation wavelength: 360 nm). (e) Comparison of ¹H NMR spectra before and after treated in FSO₃H (CDCl₃, 400 MHz, 298 K).

5.5. Application of cyclic BODIPY to Stain Strongly Acidic Materials

Encouraged by the remarkable stability of **8** in acid, it was used to stain strongly acidic resin, Nafion³² (**Figure 5-15**). Nafion is composed of perfluorinated polyethylene with sulfonic acid side chain. Thus, Nafion is regarded as a solid super acid and is used as a proton conducting material³³, an ion exchange membrane³⁴, and solid acid catalyst.³⁵ When Nafion beads were immersed in the toluene solution of BODIPY **12**, staining of the beads was observed, but not emissive under irradiation of UV light (365 nm), indicating that **12** is deboronated in the superacidic resin and loses its fluorescence. In contrast, immersion of Nafion beads in the toluene solution of **8** resulted in coloration of the beads, and it showed fluorescence under irradiation of UV light (365 nm). This observation showed that the remarkable stability of cyclic BODIPY **8** under acidic conditions allows the use of **8** for staining strongly acidic materials that are difficult to be stained with conventional BODIPY due to deboronation.

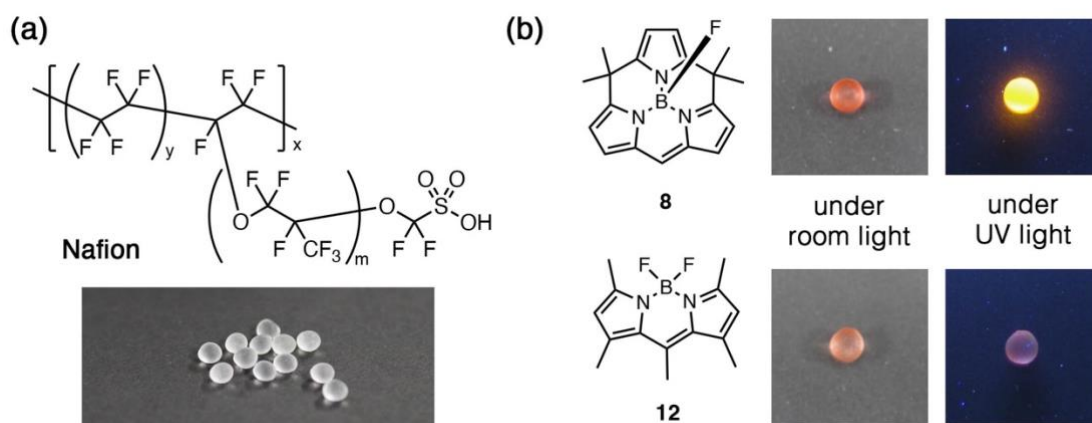


Figure 5-15. (a) The chemical structure and appearance of Nafion beads and (b) photographs of Nafion beads after immersed in toluene solution of **12** and **8** taken under room light and UV light (365 nm).

8 was also used to stain acidic hydrogel containing sulfonic acid groups in its network structure. The gel was prepared by two-step protocols: the first network was formed by polymerization of 2-acrylamide-2-methylpropanesulfonic acid and *N,N'*-methylene(bis)acrylamide, and the second network was formed from *N,N*-dimethylacrylamide and *N,N'*-methylene(bis)acrylamide by polymerization in the presence of the first network gel in water to give transparent hydrogel (**Figure 5-16a**). When the hydrogel was stained with BODIPY **8**, a pink gel was obtained which emitted yellow fluorescence upon irradiation with 365 nm UV light (**Figure 5-16b**). The gel stained by commercial BODIPY **12** also emitted fluorescence and it seemed that emission from **12** was much stronger than that from **8**, perhaps due to the elevating effect of the solvent. While **12** could also be used to stain the gel, it is assumed that **8** would be used to monitor the neutralization of the gel because it changes fluorescence character by protonation. When the hydrogel stained with **8** was immersed in 0.1 M ethanol solution of triethylamine, the diffusion of triethylamine was observed as a gradual quenching of the fluorescence of **8** (**Figure 5-16c**).

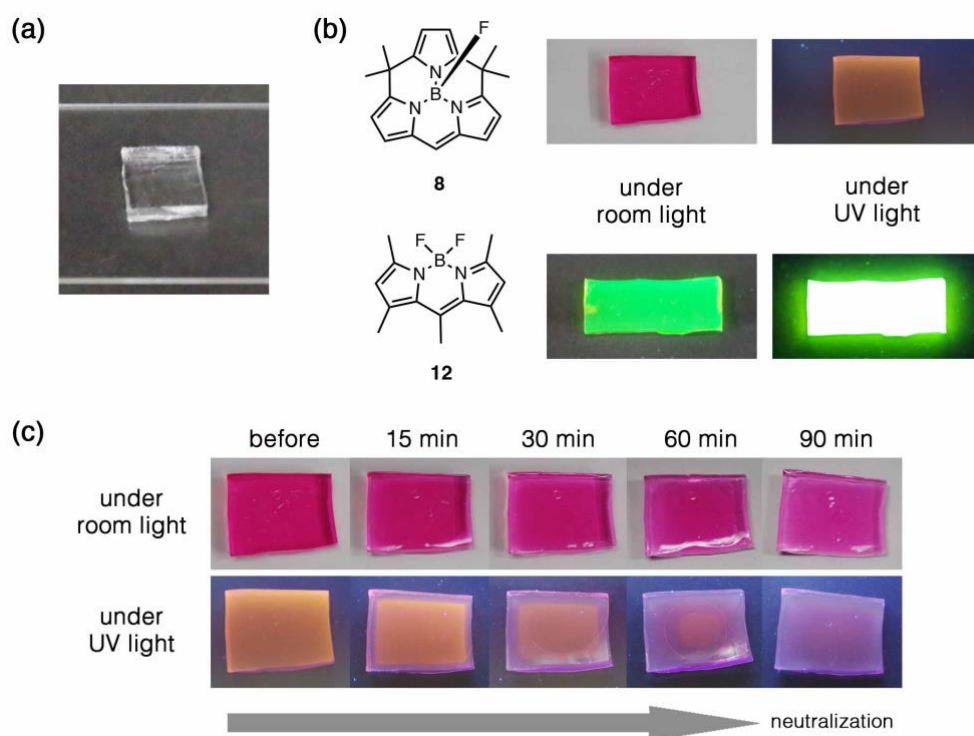


Figure 5-16. Photographs of acrylamide-based hydrogel with sulfonic acid functional groups: (a) before stained, (b) after stained using **8** and **12**, and (c) visualization of diffusion of triethylamine.

5.6. Conclusion

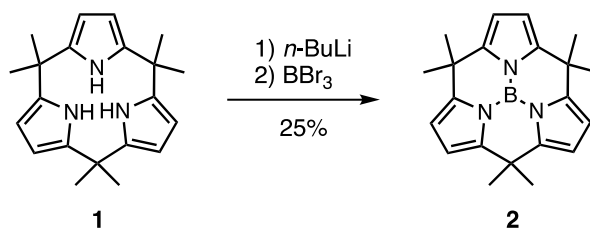
In conclusion, calix[3]pyrrole boron complex **2** was found to be stable under acidic conditions due to its amphoteric nature. It reversibly forms an adduct with acids by protonation of pyrrole and coordination of conjugate base to the boron center without deboronation or ring cleavage. This protonation gimmick had been applied to design highly acid-stable cyclic BODIPY **8**, which does not undergo deboronation even in neat TfOH, and exhibits fluorescence turn-on upon protonation. **8** could be used to stain super-acidic resin which cannot be stained with conventional BODIPY **12**. BODIPY **8** was also used to stain acidic gel and allowing neutralization to be visualized by fluorescence quenching. The cyclic BODIPY **8** designed and prepared herein is expected to be used to stain strongly acidic materials and visualize their acidity or neutralization process.

5.7. Experimental Section

5.7.1. Reagents and equipment

Solvents and reagents were purchased from WAKO Pure Chemical Industries Ltd., TCI Co., Ltd., Kanto Chemical Co., Inc., or Sigma-Aldrich Co., and used without further purification unless otherwise mentioned. Compound **1** was prepared according to the procedure described in Chapter 2, and compound **9** was prepared according to a reported procedure¹¹. All ¹H and ¹³C NMR spectra were recorded using JEOL JMN-ECS400 or JMN-ECZ600R spectrometer, and chemical shifts were reported in parts per million (ppm) relative to an internal standard tetramethylsilane ($\delta = 0.00$ ppm for ¹H NMR in CDCl₃), external standard boron trifluoride ethyl etherate ($\delta = 0.00$ ppm for ¹¹B NMR in CDCl₃), external standard hexafluorobenzene (-162.9 ppm for ¹⁹F NMR in CDCl₃) or a solvent residual peak ($\delta = 77.16$ ppm for ¹³C NMR in CDCl₃). Thin layer chromatography was performed on a silica gel sheet, MERCK silica gel 60 F254. Preparative scale separations were performed by means of gravity column chromatography over silica gel (Wakosil® 60. 64 ~ 210 μm). Infrared spectra were measured using a JASCO Co. FT/IR-4600. ESI-TOF-MS spectra were recorded on a Thermo Scientific Executive spectrometer. Elemental analyses were carried out using an Exceter Analytical, Inc. CE440 or MICRO CORDER JM10. UV/Vis absorption spectra were recorded on a JASCO V-770 spectrophotometer. Fluorescence spectra were recorded on a HITACHI F-7000 fluorescence spectrophotometer. Fluorescence quantum yields were measured by a Hamamatsu Photonics Quantaaurus QY C11347-01 Single crystal X-ray diffraction data were obtained using Rigaku XtaLAB P200 diffractometer equipped with a PILATUS200K detector, which uses a multilayer mirror (MoK α radiation $\lambda = 0.71073$ Å) or a Rigaku XtaLAB Synergy-R/DW instrument equipped with a HyPix-6000HE detector, which uses a monochromated mirror. All structures were solved using a dual-space algorithm (SHELXT) and refined using full-matrix least-squares method (SHELXL).^{36,37}

5.7.2. Synthesis of calix[3]pyrrole boron complex **2**

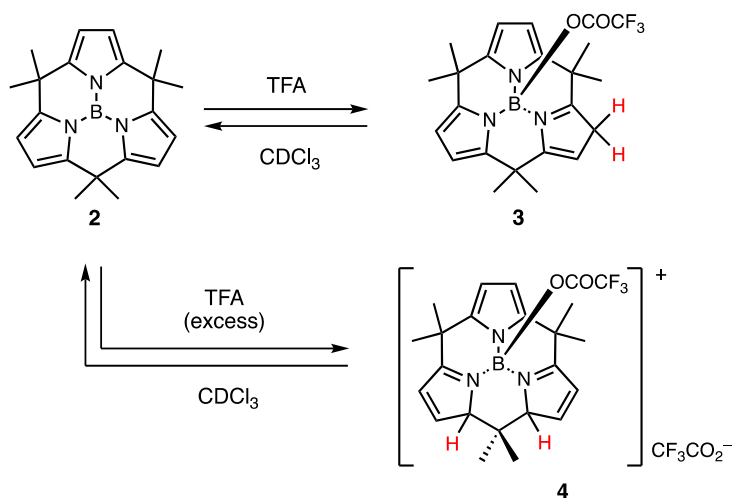


To a two-neck flask equipped with a rubber septum and inert gas inlet/outlet, calix[3]pyrrole **1** (60.0 mg, 0.19 μmol) and anhydrous toluene (15 mL) were added under nitrogen atmosphere and the mixture was cooled at $-78\text{ }^{\circ}\text{C}$ with stirring in a cooling bath. A solution of *n*-butyl lithium (2.6 M in *n*-hexane, 0.30 mL, 0.76 mmol) was slowly added to the solution via syringe and stirred for 30 min at $-78\text{ }^{\circ}\text{C}$. Then boron tribromide (70 μL , 0.76 mmol) was slowly added via syringe. The resulting solution was then taken out from the cooling bath and stirred for 30 min at room temperature. The reaction was quenched by the addition of water (40 mL), extracted with toluene (20 mL \times 3), dried over anhydrous sodium sulfate, and concentrated under reduced pressure. The resulting solid was purified by sublimation (4 torr, $140\text{ }^{\circ}\text{C}$) to give the boron complex **2** (16.2 mg, 25% yield) as a white solid.

Characterization data for **2**

^1H NMR (CDCl_3 , 400 MHz, 298 K): δ 5.95 (s, 6H, pyrrolyl), 1.69 (s, 18H, dimethylmethylene); ^{13}C NMR (CDCl_3 , 100 MHz, 298 K); δ 144.4, 106.8, 37.7, 30.5; ^{11}B NMR (CDCl_3 , 128 MHz, 298 K); δ 22.81; IR (ATR, neat): 2967, 1559, 1504, 1380, 1358, 1240, 1213, 1160, cm^{-1} ; HR-ESI-TOF-MS (m/z): $[\text{M}+\text{OH}]^-$ calcd. for $\text{C}_{21}\text{H}_{25}\text{BN}_3\text{O}$, 346.2095, found, 346.2092.

5.7.3. Formation of TFA adducts **3** and **4**



Sample of TFA adducts **3** and **4** were prepared by the addition of TFA into the solution of **2** in chloroform-*d* (6.6 mM). Upon addition of TFA (~ 3 equivalent), formation of adduct **3** was observed. Further addition of TFA (~ 25 equivalent) led to the formation of adduct **4** (Figure 5-15).

Characterization data for **3**

¹H NMR (CDCl₃, 600 MHz, 298 K): δ = 6.17 (br, 1H, pyrrolyl), 5.91–5.84 (m, 4H, pyrrolyl \times 4, overlapping) 3.94 (dd, 1H, methylene, J = 25.5, 1.4 Hz), 3.68 (dd, 1H, methylene, J = 25.5 Hz, 1.4 Hz), 1.78 (s, 3H, methyl), 1.75 (s, 3H, methyl), 170 (3H, methyl, overlapped with methyl proton of residual **1**), 1.66–1.64 ppm (s, 6H, 2 \times methyl), one methyl group was not found maybe due to overlapped with methyl proton signal of residual **1**; ¹¹B NMR (CDCl₃, 192 MHz, 298 K): δ = -2.18 ppm.

Characterization data for **4**

¹H NMR (CDCl₃, 600 MHz, 298 K): δ = 8.14 (d, 2H, vinyl, ² J = 5.5 Hz), 7.16 (d, 2H, vinyl, ² J = 5.5 Hz), 6.08 (s, 2H, pyrrolyl), 5.90 (br, 2H, methine), 1.84 (s, 3H, methyl), 1.83 (s, 6H, methyl), 1.79 (s, 6H, methyl) -0.25 ppm (s, 3H, methyl); ¹³C NMR (CDCl₃, 150 MHz, 298 K): δ = 197.2, 160.9, 134.9, 128.6, 107.6, 82.9, 45.7, 40.6, 31.1, 25.4, 23.7, 13.7 ppm (Peaks from trifluoroacetate moiety was not confirmed due to low intensity); ¹¹B NMR (CDCl₃, 192 MHz, 298 K): δ = -3.55 ppm; HR-ESI-TOF-MS: m/z = 443.2105 (calcd. for C₂₃H₂₆¹⁰BF₃N₃O₂, 443.2107 [**3**-CF₃COO]⁺).

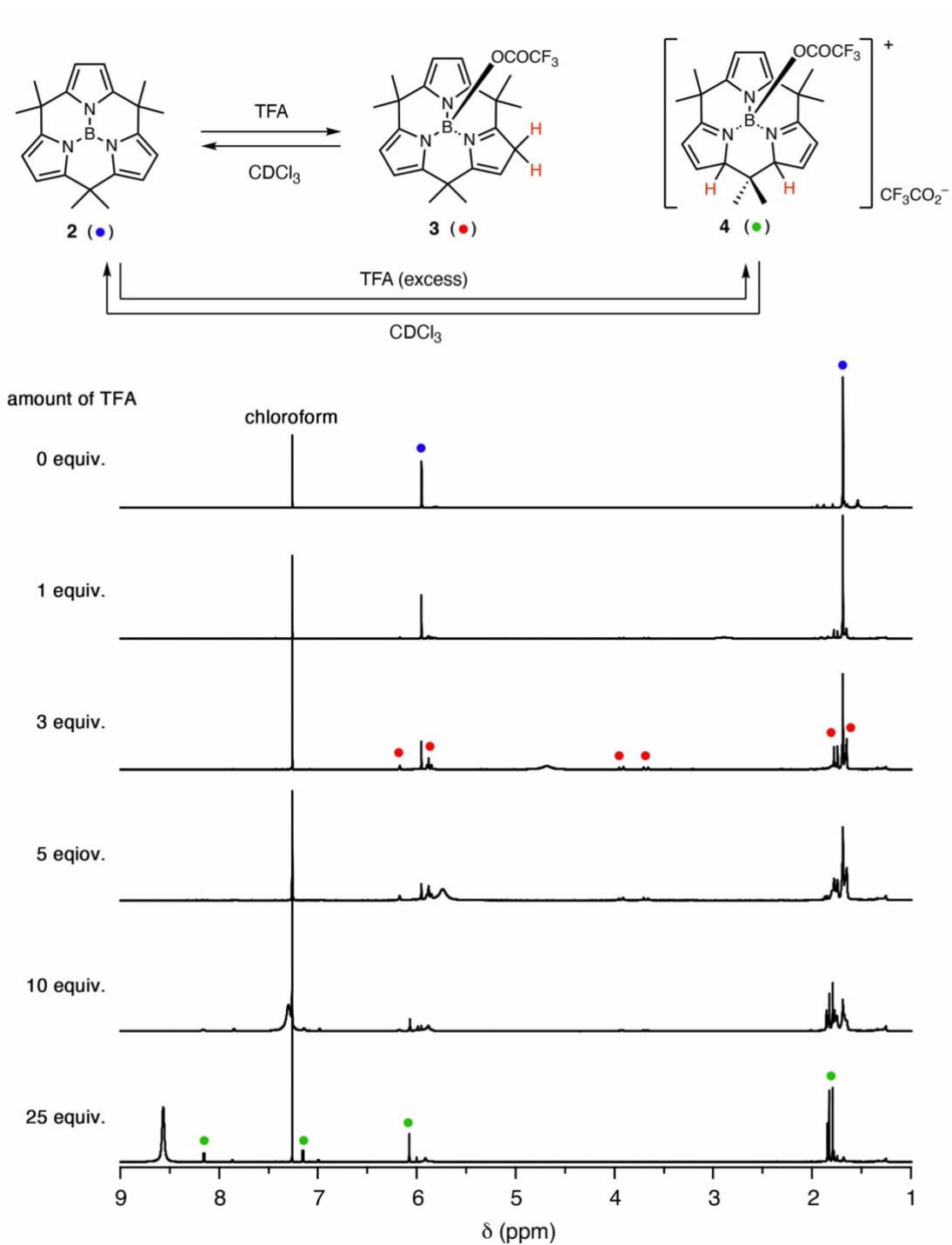


Figure 5-17. Changes in ^1H NMR spectra of **2** in chloroform-*d* (6.0 mM) upon addition of TFA (0 – 25 equivalent).

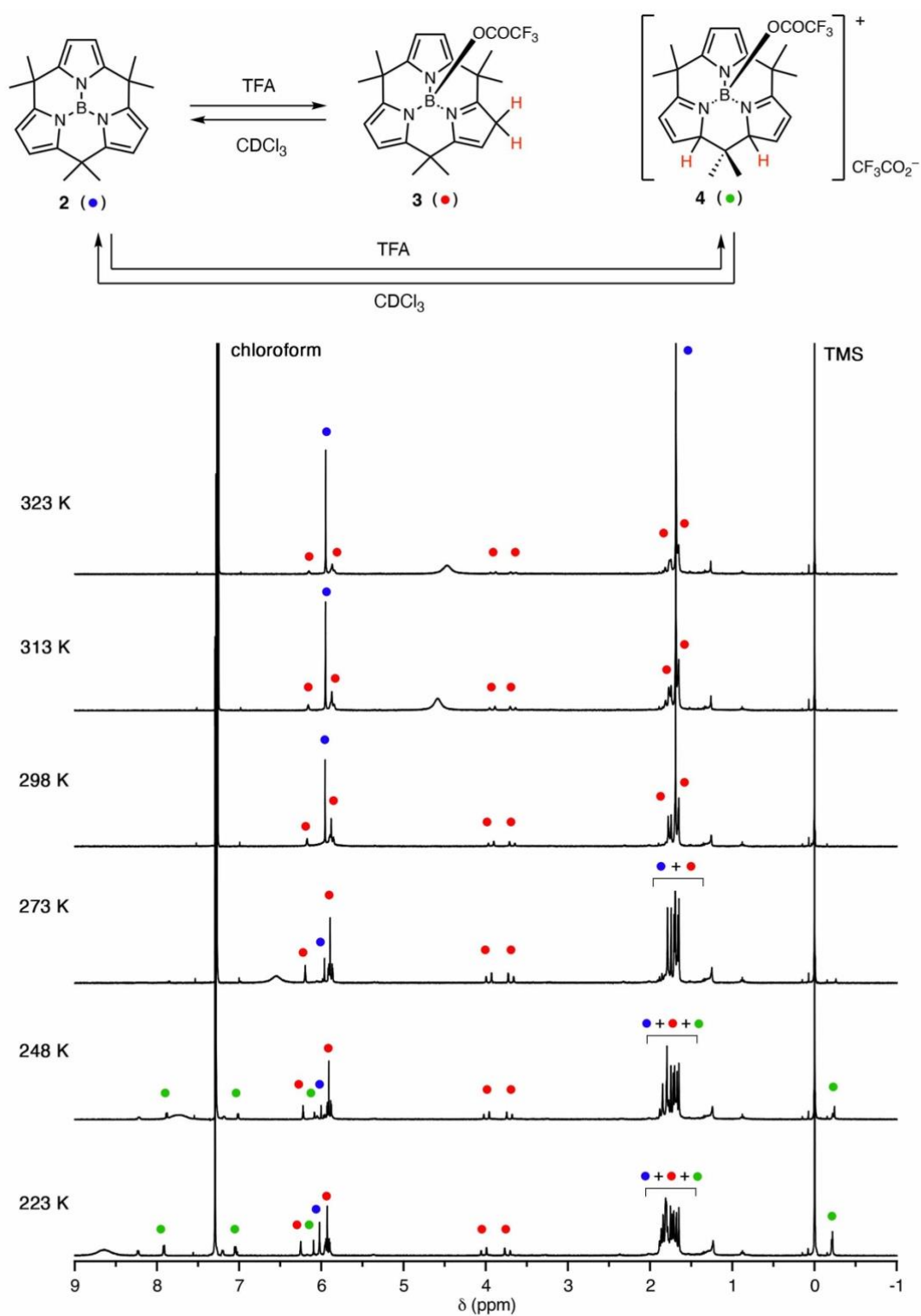
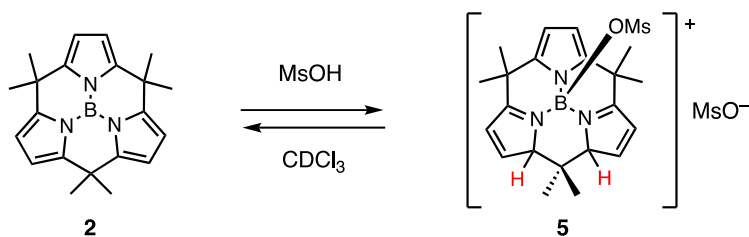


Figure 5-18. Changes in ^1H NMR spectra of **2** in chloroform-*d* (6.0 mM) with TFA (3 equivalent) at various temperature.

5.7.4. Formation of MsOH adduct **5**



Sample of MsOH adduct **5** was prepared by the addition of MsOH into the solution of **2** in chloroform-*d* (6.6 mM). Upon addition of MsOH (~ 3 equivalent), formation of adduct **5** was observed. Unlike TFA, mono-adduct was not observed even with the addition of small amount of MsOH (**Figure 5-17**).

Characterization data for **5**

^1H NMR (CDCl_3 , 400 MHz, 298 K): $\delta = 7.90$ (d, 2H, vinyl, $J = 5.4$ Hz), 6.95 (dd, 2H, vinyl, $J = 0.9, 5.4$ Hz), 6.14 (br, 2H, methine), 5.95 (s, 2H, pyrrolyl), 2.96 (methanesulfonyl overlapped with methanesulfonic acid), 1.90 (s, 6H, methyl), 1.83 (s, 3H, methyl), 1.76 (s, 6H, methyl), -0.22 ppm (s, 3H, methyl); ^{13}C NMR (CDCl_3 , 100 MHz, 298 K): $\delta = 196.4, 161.2, 135.1, 128.6, 107.4, 81.7, 43.4, 40.6, 40.1, 30.8, 25.6, 23.9, 13.9$ ppm; ^{11}B NMR (CDCl_3 , 128 MHz, 298 K): $\delta = -4.37$ ppm; HR-ESI-TOF-MS: $m/z = 425.2064$ (calcd. for $\text{C}_{22}\text{H}_{29}^{10}\text{BN}_3\text{O}_3\text{S}$, 425.2059 [**5**-Me SO_3^-] $^+$).

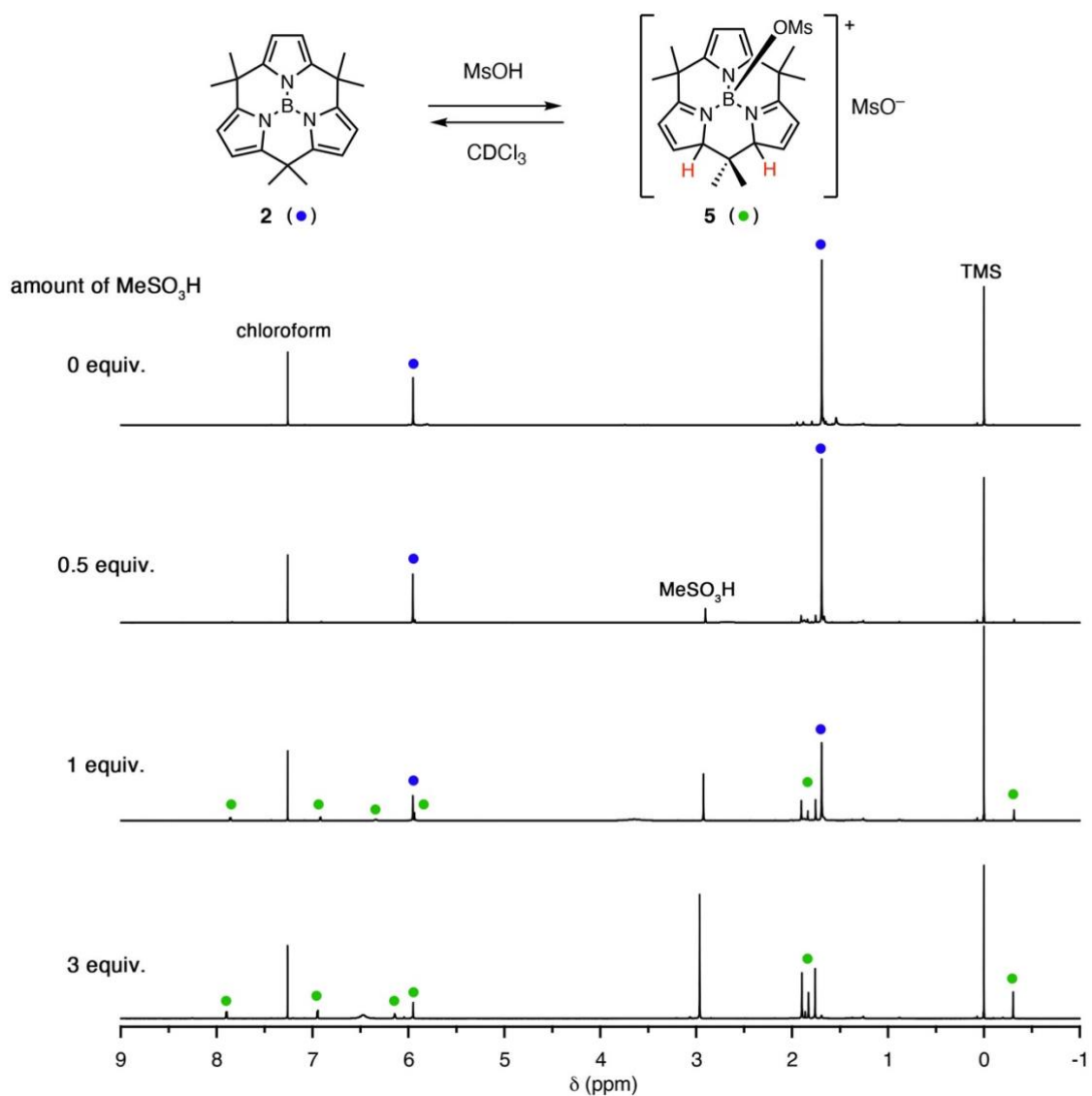
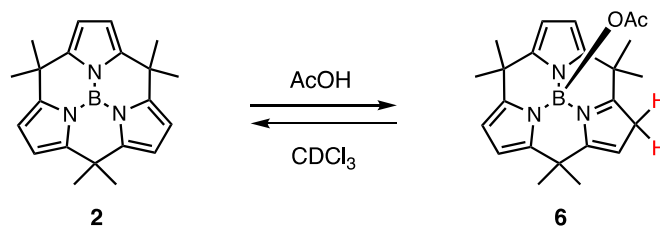


Figure 5-19. Changes in ¹H NMR spectra of **2** in chloroform-*d* (6.0 mM) upon addition of MsOH (0 – 3 equivalent)

5.6.5. Formation of AcOH adduct **6**



Sample of AcOH adduct **6** was prepared by the addition of AcOH into the solution of **2** in chloroform-*d* (6.6 mM). While formation of **6** was not observed even with large excess amount of AcOH (30 equiv.) at 25 °C, decrease of temperature led to the formation of **6**, and almost exclusive formation of **6** was observed with 30 equiv. of AcOH at -50 °C (**Figure 5-18**). The characterization data was measured at -50 °C with 30 equiv. of AcOH.

Characterization data for **6**

¹H NMR (CDCl₃, 600 MHz, 223 K): δ = 6.12 (br, 1H, vinyl), 5.90 (d, 1H, pyrrolyl, J = 3.1 Hz), 5.89–5.85 (m, 3H, pyrrolyl \times 3, overlapping), 3.87 (dd, 1H, methylene, J = 1.4 and 25.5 Hz), 3.60 (dd, 1H, methylene, J = 2.1 and 25.5 Hz), 2.20 (acetyl, overlapped with acetic acid), 1.94 (s, 3H, methyl), 1.86 (s, 3H, methyl), 1.80 (s, 3H, methyl), 1.72–1.65 ppm (9H, methyl \times 3, overlapping); ¹³C NMR (CDCl₃, 150 MHz, 298 K): δ = 193.2, 156.6, 143.1, 142.5, 135.3, 134.0, 115.0, 103.1, 102.0, 101.7, 101.5, 43.5, 40.4, 36.4, 36.1, 34.8, 31.9, 31.7, 25.1, 24.9 (2 CH₃ overlapping) ppm, peaks of axial acetyl group was overlapped with peaks of acetic acid (179.1 and 21.5 ppm); ¹¹B NMR (CDCl₃, 128 MHz, 298 K): δ = -2.48 ppm.

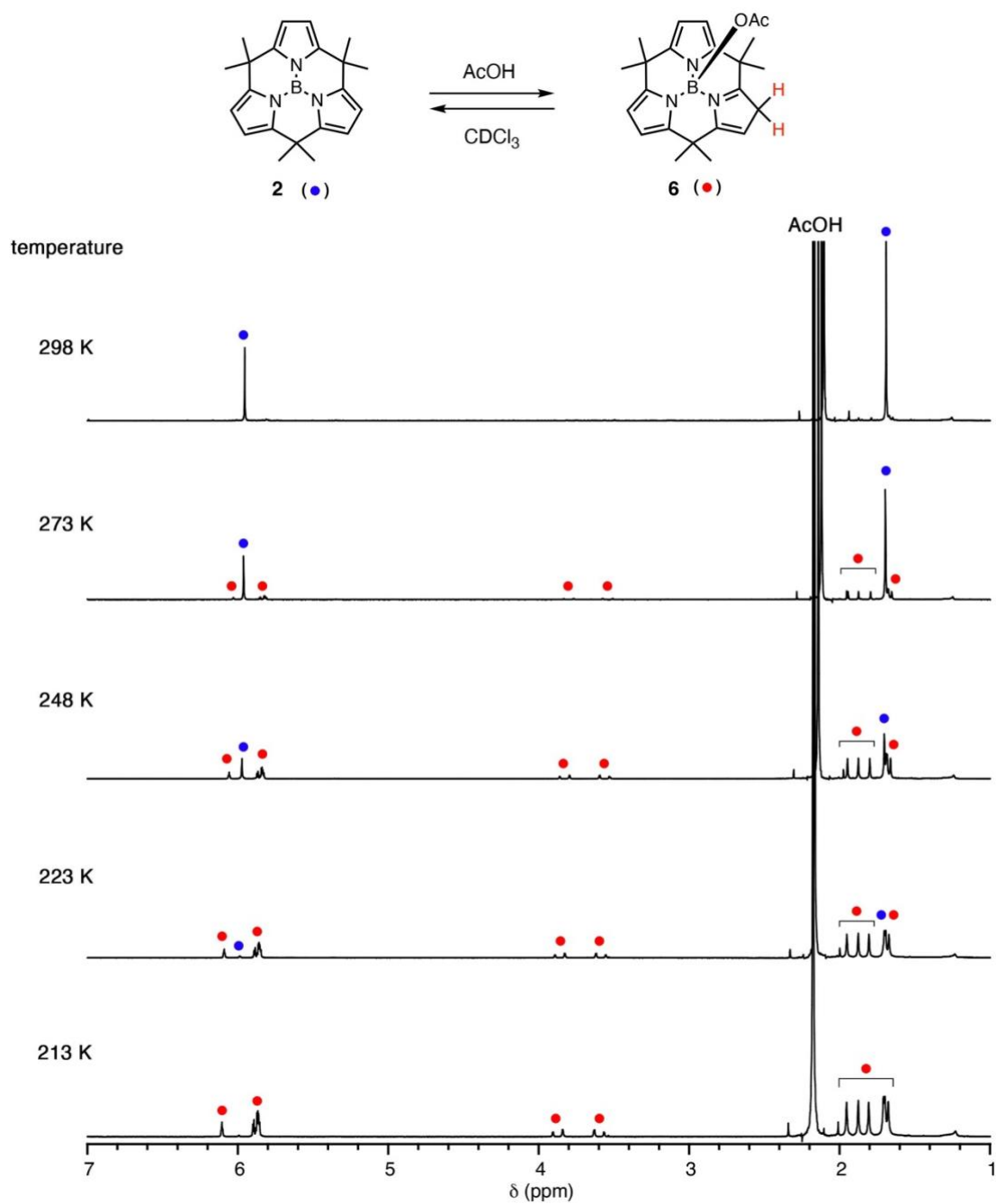
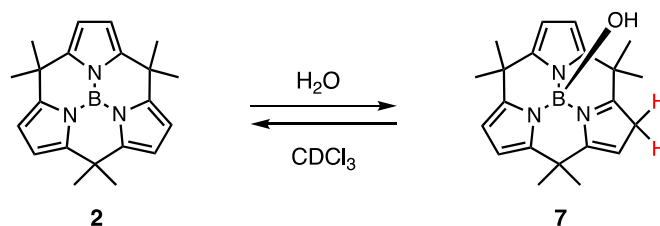


Figure 5-20. Change in ¹H NMR spectra of **2** in chloroform-*d* (6.0 mM) with 30 equiv. of AcOH at various temperature.

5.7.5. Formation of water adduct **7**

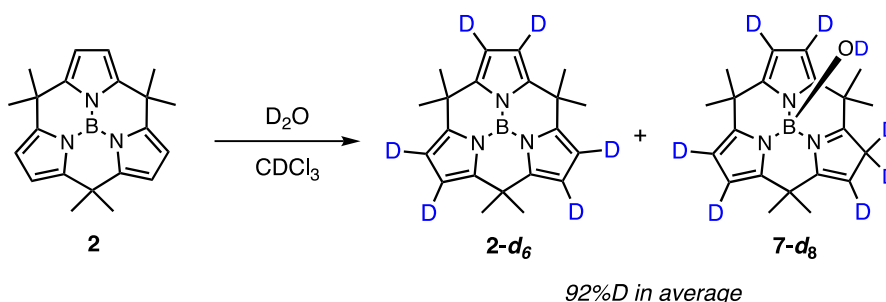


Sample of H₂O adduct **7** was prepared by the addition of H₂O into the solution of **1** in chloroform-*d* (15.5 mM). In chloroform-*d* containing 1 eq. of water, the formation of the adduct **7** was confirmed. Because the formation of **7** is favorable at lower temperature (see **Figure 5-7**), NMR spectra for characterization was recorded at 213 K.

Characterization data for **7**

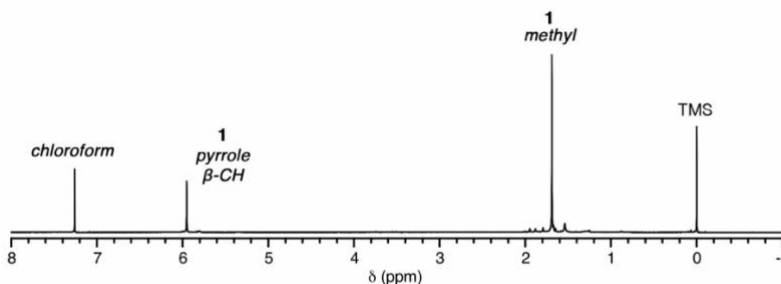
¹H NMR (CDCl₃, 600 MHz, 213 K): δ = 6.10 (br, 1H, vinyl), 5.90 (d, 1H, pyrrolyl, J = 2.8 Hz), 5.88 (d, 1H, pyrrolyl, J = 2.8 Hz), 5.87–5.85 (m, 2H, pyrrolyl \times 2, overlapping), 3.85 (dd, 1H, methylene, J = 25.5, 1.4 Hz), 3.60 (dd, 1H, methylene, J = 25.5, 1.4 Hz), 2.16 (s, 1H, OH), 1.97 (s, 3H, methyl), 1.89 (s, 3H, methyl), 1.81 (s, 3H, methyl), 1.72–1.67 ppm (9H, methyl \times 3); ¹³C NMR (CDCl₃, 150 MHz, 213 K): δ = 193.0, 156.8, 143.2, 142.6, 135.3, 133.9, 114.8, 103.1, 101.9, 101.6, 101.5, 43.4, 40.4, 36.4, 36.1, 34.9, 31.94, 31.88, 25.2, 24.8 (2 CH₃ overlapping) ppm; ¹¹B NMR (CDCl₃, 192 MHz, 213 K): δ = –2.16 ppm; HR-ESI-TOF-MS: m/z = 345.2132 (calcd. for C₂₁H₂₅OBN₃O, 345.2132 [M –H][–]).

5.7.6. H/D exchange reaction of **2** using D₂O



A 6.6 mM solution of complex **1** in chloroform-*d* was prepared. After addition of one drop of deuterium oxide, the solution was mixed by handshaking and immediately analyzed by ¹H NMR spectroscopy. The deuterium/proton ratio at β-position of pyrrole was calculated according to the ratio of integration value of methyl protons and β-protons.

(a) before addition of D₂O



(b) after addition of D₂O

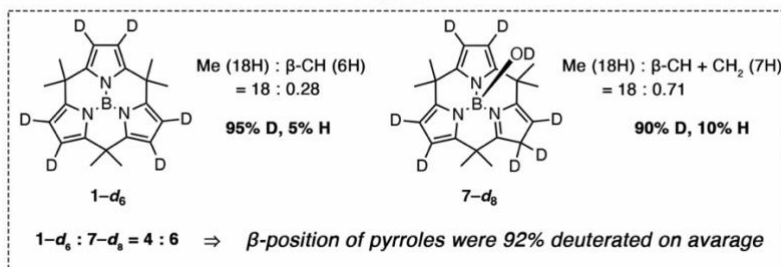
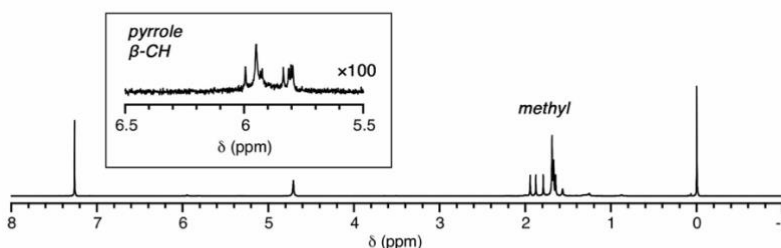


Figure 5-21. Comparison of ¹H NMR spectra recorded (a) before and (b) after addition of deuterium oxide into chloroform-*d* solution of **2**.

5.7.7. The van't Hoff plot analysis for the equilibrium between 2 and 7

A solution of **2** in chloroform-*d* (15.5 mM) with 3 equivalent amount of H₂O was measured ¹H NMR spectra at various temperatures (**Figure 5-7**). For each temperature, the equilibrium constant *K* was calculated based on the concentration of **2**, **7**, and H₂O as equation (5.1). Concentration of **2**, **7**, and H₂O were determined by integration for respective compounds.

$$K = \frac{[\mathbf{7}]}{[\mathbf{2}][\text{H}_2\text{O}]} \quad (5.1)$$

Temperature dependent change in equilibrium constant can be described as equation (5.2).

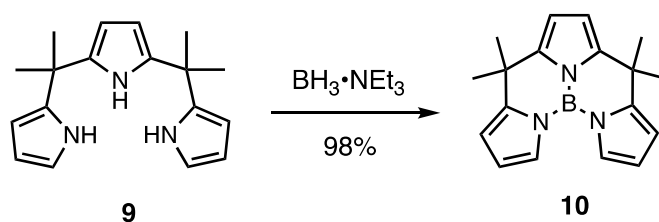
$$\Delta G = -RT\ln(K) \quad (5.2)$$

The plot of $\ln(K)$ as a function of T^{-1} was fit according to the equation (3.3).

$$\ln(K) = \frac{-\Delta H}{RT} + \frac{\Delta S}{R} \quad (5.3)$$

The enthalpy and entropy of the reaction were extracted from the slope and the intercept to determine ΔH and ΔS as -56.5 ± 3.5 (kJ/mol) and -151 ± 13 (J/mol•K), respectively (see Figure 5-8).

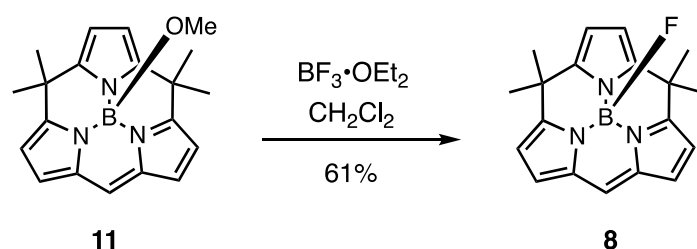
5.7.8. Synthesis of boron(III)-tripyrane **10**



In a 20 mL round-bottomed flask equipped with a reflux condenser, tripyrrane **9** (1.00 g, 3.55 mmol) and triethylamine borane (0.8 mL, 5.42 mmol) were placed and stirred at 150 °C for 3.5 hours. After completion of the reaction, all volatiles were removed under reduced pressure at 100 °C to give boron(III)-tripyrane **10** (1.01 g, 98% yield) as a sticky pale-yellow solid. **10** was used in the next reaction without further purification.

^1H NMR (CDCl_3 , 400 MHz, 298 K): δ = 7.40 (dd, 2H, α -pyrrolyl, 3J = 3.1 Hz, 5J = 1.4 Hz), 6.46 (dd, 2H, β -pyrrolyl, 3J = 3.1 Hz, 3J = 3.1 Hz), 6.32 (dd, 2H, β -pyrrolyl, 3J = 3.1 Hz, 5J = 1.4 Hz), 6.16 (s, 2H, β -pyrrolyl), 1.63 ppm (s, 12H, methyl); ^{13}C NMR (CDCl_3 , 100 MHz, 298 K): δ = 146.2, 139.4, 120.8, 114.4, 108.0, 106.8, 35.9, 33.6 ppm; ^{11}B NMR (CDCl_3 , 128 MHz, 298 K): δ = 20.70 ppm; HR-ESI-TOF-MS: m/z = 289.1859 (calcd. for $\text{C}_{18}\text{H}_{21}\text{N}_3^{10}\text{B}$, 289.1859 [$M+\text{H}$] $^+$); IR (ATR, neat): 2965, 2923, 2864, 1435, 1375, 1357, 1256, 1184 cm^{-1} .

5.7.10. Synthesis of F-cyclic BODIPY **8**



In a 50 mL round-bottomed flask, compound **11** (100 mg, 0.31 mmol) was dissolved in dichloromethane (150 mL). To the solution, boron trifluoride ethyl etherate (2.50 mL) was slowly added. The resulting solution was stirred at room temperature for 30 min. Then the solution was washed with saturated aqueous solution of sodium bicarbonate and dried over anhydrous sodium sulfate. After evaporation of the solvent, the crude mixture was purified by silica gel column chromatography (diameter: 2.0 cm, height: 6 cm, eluent: dichloromethane) to give compound **8** (60 mg, 61% yield) as a deep red solid.

^1H NMR (CDCl_3 , 400 MHz, 298 K): δ = 7.17 (s, 1H, vinyl), 6.94 (d, 2H, β -pyrrolyl, 3J = 4.0 Hz), 6.25 (d, 2H, β -pyrrolyl, 3J = 4.0 Hz), 5.87 (s, 2H, β -pyrrolyl), 1.85 (s, 6H, methyl), 1.71 ppm (s, 6H, methyl); ^{13}C NMR (CDCl_3 , 100 MHz, 298 K): δ = 168.9, 140.5, 133.0, 130.6, 128.5, 112.8, 102.9, 39.0, 33.0, 23.6 ppm; ^{11}B NMR (CDCl_3 , 128 MHz, 298 K): δ = -2.69 ppm (d, $^1J_{\text{B-F}}$ = 40 Hz); ^{19}F NMR (CDCl_3 , 376 MHz, 298 K) -152.8 ppm (q, $^1J_{\text{B-F}}$ = 40 Hz); UV/Vis (dichloromethane): λ_{max} (ϵ) = 365 (5200), 540 nm (33100 mol $^{-1}$ L cm $^{-1}$); IR (ATR, neat): 2963, 2922, 2859, 1542, 1421, 1400, 1260, 1224, 1205, 1106, 1040, 1016 cm $^{-1}$; R_f = 0.80 (dichloromethane).

5.7.11. X-ray crystallographic analyses

Crystallographic data for 3

Single crystals of **3** suitable for X-ray diffraction analysis were obtained from chloroform solution of **2** containing excess of TFA by slow evaporation of the solvent.

$C_{23}H_{25}BF_3N_3O_2$, $M = 443.27$, crystal size: $0.13 \times 0.10 \times 0.08 \text{ mm}^3$, monoclinic, space group $P2_1$, $a = 9.9243(2)$, $b = 10.3239(3)$, $c = 9.9264(2) \text{ \AA}$, $\alpha = 90$, $\beta = 93.7192(19)$, $\gamma = 90^\circ$, $V = 1014.89(4) \text{ \AA}^3$, $Z = 2$, $T = 123(2) \text{ K}$, $\mu = 0.935 \text{ mm}^{-1}$, $D_{\text{calc}} = 1.451 \text{ g/cm}^3$, $4.464^\circ \leq \theta \leq 75.901^\circ$, 3332 unique reflections out of 3594 with $I > 2\sigma(I)$, GOF = 1.045, $R_1 = 0.0492$, $wR_2 = 0.1394$.

Crystallographic data for 8

Single crystals of **8** suitable for X-ray diffraction analysis were obtained by slow evaporation of *n*-hexane/dichloromethane solution of **8**.

$C_{19}H_{19}FBN_3$, $M = 349.23$, crystal size: $0.30 \times 0.12 \times 0.10 \text{ mm}^3$, orthorhombic, space group $P2_12_12_1$, $a = 8.9872(4)$, $b = 14.3269(5)$, $c = 25.4310(11) \text{ \AA}$, $\alpha = \beta = \gamma = 90^\circ$, $V = 3274.5(2) \text{ \AA}^3$, $Z = 8$, $T = 123(2) \text{ K}$, $\mu = 0.085 \text{ mm}^{-1}$, $D_{\text{calc}} = 1.295 \text{ g/cm}^3$, $1.601^\circ \leq \theta \leq 30.668^\circ$, 6681 unique reflections out of 7338 with $I > 2\sigma(I)$, GOF = 1.042, $R_1 = 0.0356$, $wR_2 = 0.0921$.

Crystallographic data for 11

Single crystals of **11** suitable for X-ray diffraction analysis were obtained by slow evaporation of methanol/dichloromethane solution of **11**.

$C_{20}H_{24}BN_3O \cdot H_2O$, $M = 349.23$, crystal size: $0.25 \times 0.10 \times 0.03 \text{ mm}^3$, monoclinic, space group $P2_1/c$, $a = 8.7116(3)$, $b = 25.5062(6)$, $c = 9.0478(3) \text{ \AA}$, $\alpha = 90$, $\beta = 114.477(4)$, $\gamma = 90^\circ$, $V = 1829.74(11) \text{ \AA}^3$, $Z = 4$, $T = 123(2) \text{ K}$, $\mu = 0.652 \text{ mm}^{-1}$, $D_{\text{calc}} = 1.268 \text{ g/cm}^3$, $3.466^\circ \leq \theta \leq 76.067^\circ$, 3084 unique reflections out of 3704 with $I > 2\sigma(I)$, GOF = 1.034, $R_1 = 0.0535$, $wR_2 = 0.1283$.

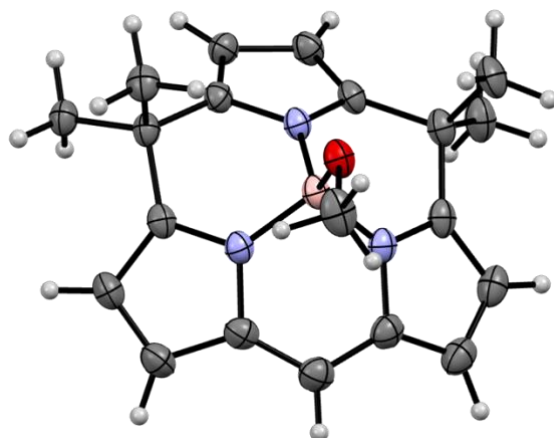


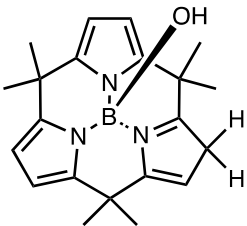
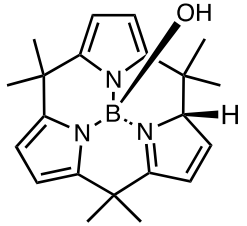
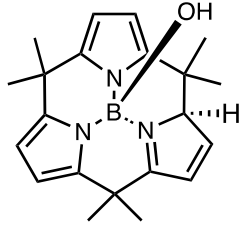
Figure 5-22. ORTEP drawing of the crystal structure of **11** at the 50% thermal probability levels (C: gray, H: white, N: blue, O: red, B: pink). Water molecules are omitted for clarity.

5.7.12. Computational analysis

Geometry optimization and stability analysis for isomers of 3

Theoretical calculations were performed with Gaussian 16 Rev. C01.³⁸ The initial structures of the isomers of **3** were modified from the crystal structure of **3** by adding/removing hydrogen, and structural optimizations carried out at the B3LYP/6-31G(d,p) level of theory. Optimization allowed the energies (ΔE) of the isomers of **3** to be calculated relative to **3**.

Table 5-1. Comparison of relative energy for isomers of **3**.

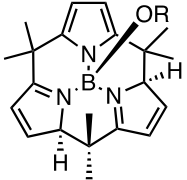
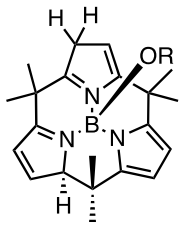
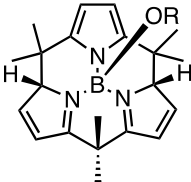
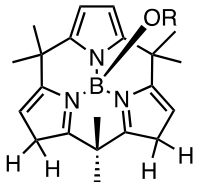
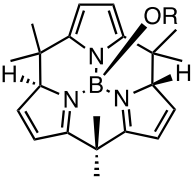
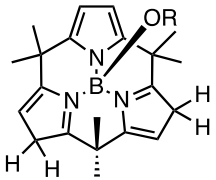
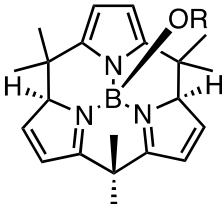
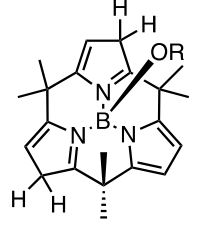
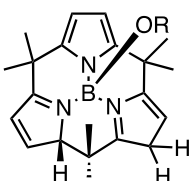
entry	structure	ΔE (kJ/mol)
1		0.00
2		21.6
3		37.1

Geometry optimization and stability analysis for isomers of **4**

Theoretical calculations were performed with Gaussian 16 Rev. C01.³⁸ The initial structures of the isomers were modified from the crystal structure of **3** by adding hydrogen, and structural optimizations carried out at the B3LYP/6-31G(d,p) level of theory. Optimization allowed the energies (ΔE) of the isomers of **4** to be calculated relative to **4**.

Table 5-2. Comparison of relative energy for isomers of **4**.

entry	structure	ΔE (kcal/mol)	entry	structure	ΔE (kcal/mol)
1		0.00	12		7.67
2		18.51	13		8.91
3		30.81	14		10.92
4		7.22	15		20.98
5		18.27	16		15.95
6		25.45	17		16.34

entry	structure	ΔE (kcal/mol)	entry	structure	ΔE (kcal/mol)
7		31.34	18		21.92
8		12.14	19		14.94
9		23.57	20		9.77
10		32.53	21		8.04
11		7.17			

Geometry optimization and energy calculation of **8** and **8**•H⁺

Theoretical calculations were performed with Gaussian 16 Rev. C01.³⁸ The structure of **8** was optimized at B3LYP/6-31G(d,p) level of theory using crystal structure as an initial state. The structure of **8**•H⁺ was obtained by modifying the crystal structure of **8**, and structural optimization was carried out at same level of theory. Energy calculations of them were carried out at B3LYP/6-31G(d,p) level of theory.

5.7.13. Analyses on protonation of **8**

Change in absorption and emission spectra of **8** with TFA

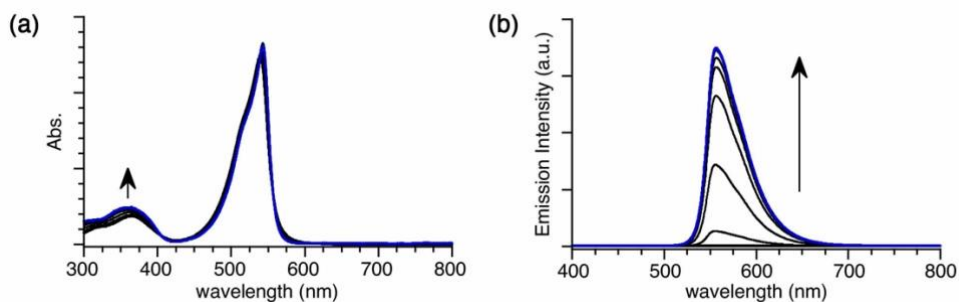


Figure 5-23. (a) UV-Vis absorption and (b) emission spectra of compound **8** in dichloromethane (15 μ M) with 0.0 (bold black line), 0.5, 1.0, 1.5, 2.0, 2.5, 3.0, 4.0, 5.0 (black lines), and 6.0% (bold blue line) of TFA ($\lambda_{\text{ex}} = 360$ nm).

Fluorescence lifetime of **8** in 5% TFA solution and neat TfOH

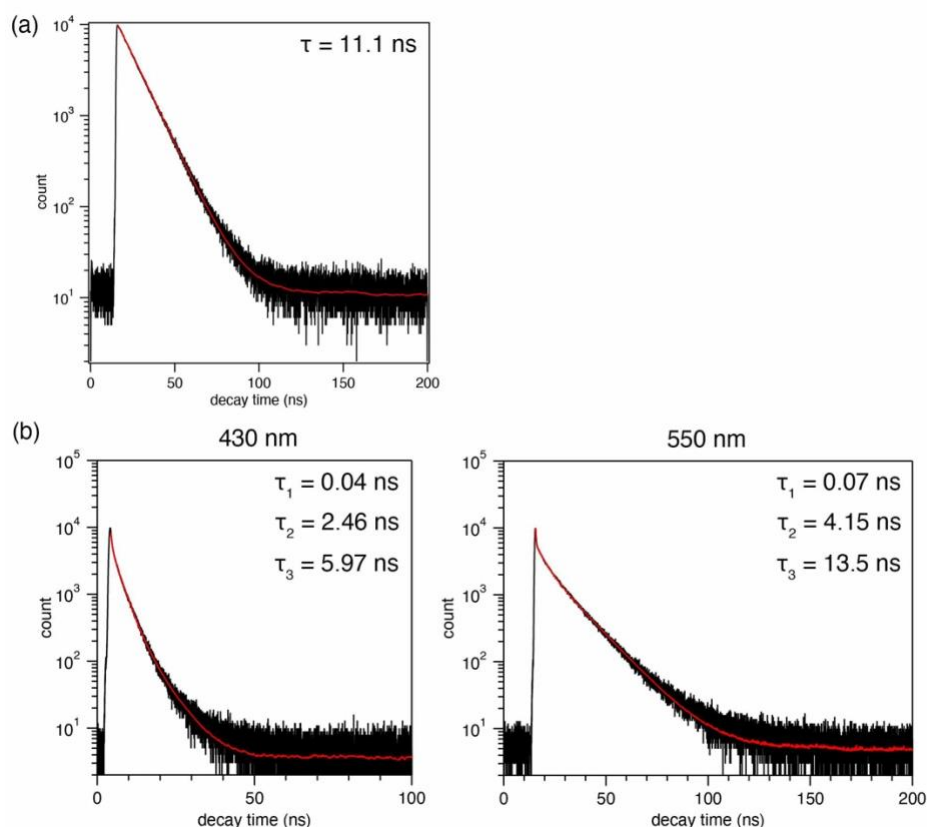


Figure 5-24. Fluorescence lifetime decay profiles of **8** in (a) dichloromethane with 5% TFA and (b) neat TfOH (detected at 430nm and 550 nm).

Structural analysis of $\mathbf{8}\cdot\mathbf{H}^+$ using $^1\mathbf{H}$ NMR spectroscopy.

Experimental procedure

In an NMR tube, chloroform-*d* solution of **8** (6.0 mM, 0.5 mL) was prepared and added TFA (100 equiv.). The resulting solution was then analyzed using $^1\mathbf{H}$ NMR spectroscopy at various temperature because $\mathbf{8}\cdot\mathbf{H}^+$ showed time-averaged C_s symmetric structure at 298 K, and characterization data for $\mathbf{8}\cdot\mathbf{H}^+$ was obtained at 223 K.

Characterization data for $\mathbf{8}\cdot\mathbf{H}^+$

$^1\mathbf{H}$ NMR (CDCl_3 , 600 MHz, 223 K): δ = 7.61 (s, 1H, vinyl), 7.36 (d, 1H, β -pyrrolyl, 3J = 4.1 Hz), 7.31 (d, 1H, β -pyrrolyl, 3J = 4.1 Hz), 6.57 (br, 1H, β -pyrrolyl) 6.51 (d, 1H, β -pyrrolyl, 3J = 4.1 Hz), 6.50 (d, 1H, β -pyrrolyl, 3J = 4.1 Hz), 4.44 (d, 1H, methylene, 2J = 26.2 Hz), 4.16 (d, 1H, methylene, 3J = 26.2 Hz), 1.98 (s, 3H, methyl), 1.90 (s, 3H, methyl), 1.87 (s, 3H, methyl), 1.85 ppm (s, 3H, methyl).

Determination of pK_{aH} value for $\mathbf{8}\cdot\mathbf{H}^+$

Equations

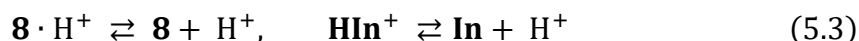
pK_{aH} of $\mathbf{8}\cdot\mathbf{H}^+$ was determined by relative measurement method³⁹ using an indicator with acid dissociation constant reported.

Acid dissociation constant of protonated base \mathbf{BH}^+ can typically be described as follows:



$$K_{aH} = \frac{[\mathbf{B}][\mathbf{H}^+]}{[\mathbf{HB}^+]} \quad (5.2)$$

Since $\mathbf{8}$ and indicator base were used in this relative measurement method, following two acid-base equilibrium exist:



where \mathbf{In} is indicator and \mathbf{HIn}^+ is protonated form of indicator base. The acid dissociation constants for these two bases are:

$$K_{aH}(\mathbf{8}\cdot\mathbf{H}^+) = \frac{[\mathbf{8}][\mathbf{H}^+]}{[\mathbf{8}\cdot\mathbf{H}^+]}, \quad K_{aH}(\mathbf{HIn}^+) = \frac{[\mathbf{In}][\mathbf{H}^+]}{[\mathbf{HIn}^+]} \quad (5.4)$$

As $\mathbf{8}$ and indicator exists in the same solution in relative measurement, the relative acidity ΔpK_{aH} can be described from equation (5.4) as follows:

$$\Delta pK_{aH} = pK_{aH}(\mathbf{8}\cdot\mathbf{H}^+) - pK_{aH}(\mathbf{HIn}^+) = -\log \frac{[\mathbf{8}][\mathbf{H}^+]}{[\mathbf{8}\cdot\mathbf{H}^+]} + \log \frac{[\mathbf{In}][\mathbf{H}^+]}{[\mathbf{HIn}^+]} \quad (5.5)$$

$$\Delta pK_{aH} = \log \frac{[\mathbf{8}\cdot\mathbf{H}^+]}{[\mathbf{8}]} \frac{[\mathbf{In}]}{[\mathbf{HIn}^+]} \quad (5.6)$$

From equations (5.5) and (5.6), $pK_{aH}(\mathbf{8}\cdot\mathbf{H}^+)$ can be described as:

$$pK_{aH}(\mathbf{8}\cdot\mathbf{H}^+) = pK_{aH}(\mathbf{HIn}^+) + \log \frac{[\mathbf{8}\cdot\mathbf{H}^+]}{[\mathbf{8}]} \frac{[\mathbf{In}]}{[\mathbf{HIn}^+]} \quad (5.7)$$

Experimental procedure

To a 0.5 mL solution of **8** in acetonitrile-*d*₃ (6.0 mM), 1.0 mg of 4-nitroaniline was added as indicator base. After measuring ¹H NMR spectrum of initial state, small aliquot of MsOH was added to the solution. Then ¹H NMR spectrum was measured again, and addition of acid and ¹H NMR measurement was repeated until chemical shift of peaks from **8** and 4-nitroaniline no longer changes.

Since $pK_{aH}(\mathbf{8}\cdot\mathbf{H}^+)$ can be described as equation (5.7), molar ratio of protonated/unprotonated species ($[\mathbf{8}\cdot\mathbf{H}^+]/[\mathbf{8}]$ and $[\mathbf{HIn}^+]/[\mathbf{In}]$) was calculated from chemical shift changes:

$$\frac{[\mathbf{8}\cdot\mathbf{H}^+]}{[\mathbf{8}]} = \frac{(\delta_{\mathbf{8}} - \delta_{obs(\mathbf{8})})}{(\delta_{obs(\mathbf{8})} - \delta_{\mathbf{8}\cdot\mathbf{H}^+})} \quad (5.8)$$

$$\frac{[\mathbf{HIn}^+]}{[\mathbf{In}]} = \frac{(\delta_{\mathbf{In}} - \delta_{obs(\mathbf{In})})}{(\delta_{obs(\mathbf{In})} - \delta_{\mathbf{HIn}^+})} \quad (5.9)$$

where $\delta_{\mathbf{8}}$ and $\delta_{\mathbf{In}}$ indicates chemical shift of each species at initial state, $\delta_{\mathbf{8}\cdot\mathbf{H}^+}$ and $\delta_{\mathbf{HIn}^+}$ indicates chemical shift of each species at final state (fully protonated state), and δ_{obs} indicates observed chemical shift upon titration.

By combining equations (5.7), (5.8), (5.9), and reported $pK_{aH}(\mathbf{HIn}^+)$ in acetonitrile (= 6.22)⁴⁰, $pK_{aH}(\mathbf{8}\cdot\mathbf{H}^+)$ was calculated based on the following equation:

$$pK_{aH}(\mathbf{8}\cdot\mathbf{H}^+) = 6.22 + \log \frac{(\delta_{\mathbf{8}} - \delta_{obs(\mathbf{8})})}{(\delta_{obs(\mathbf{8})} - \delta_{\mathbf{8}\cdot\mathbf{H}^+})} \frac{(\delta_{obs(\mathbf{In})} - \delta_{\mathbf{HIn}^+})}{(\delta_{\mathbf{In}} - \delta_{obs(\mathbf{In})})} \quad (5.10)$$

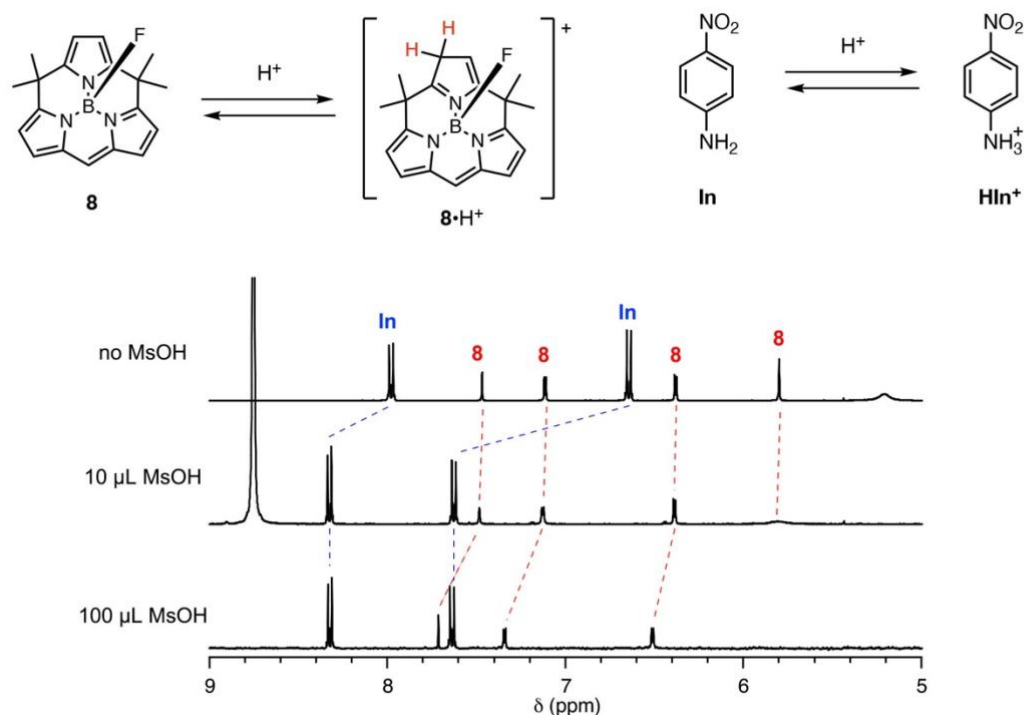


Figure 5-25. ^1H NMR spectra of **8** (6.0 mM) with 4-nitroaniline (1.0 mg) before addition of MSA, after addition of 10 μL of MsOH, and after addition of 100 μL of MsOH to reach at fully protonated state. (from top to bottom, acetonitrile- d_3 , 400 MHz, 298 K).

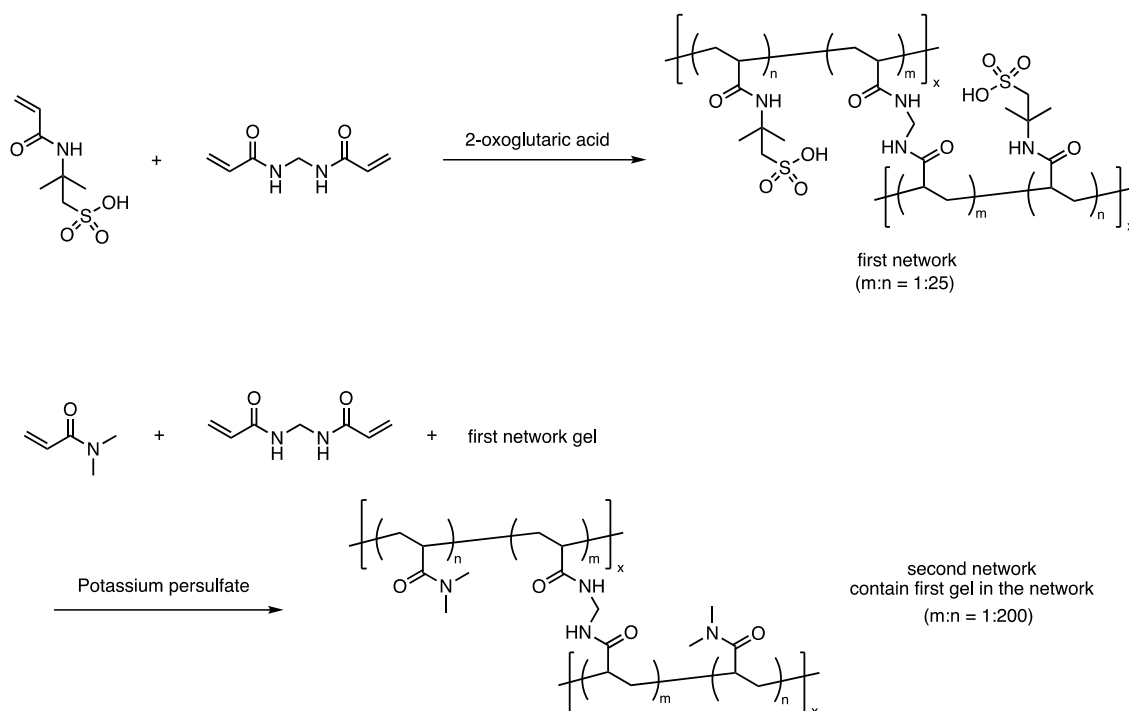
5.7.14. Staining NafionTM using BODIPY

Experimental procedure

NafionTM beads (ca. 50 mg for each 1 bead) were immersed in a 0.25 mM toluene solution of **8** or **12**. After kept at room temperature for 2 days, beads were taken out from the solution and rinsed with small amount of toluene and wiped. The beads were then analyzed its appearance under room light and fluorescence under UV light.

5.7.15. Preparation of acidic organogel and staining with BODIPY

Preparation



The organogel used here has double network structure and prepared by two step protocols. For the first network formation, aqueous solutions containing 2-acrylamide-2-methylpropanesulfonic acid (1 M), *N,N'*-methylenebis(acrylamide) (40 mM), and 2-oxoglutaric acid (1 mM) was prepared and solidified under irradiation of ultraviolet light (365 nm) for 8 hours. The resulting solid was crushed, dried, and used in the next step. For the second network formation, 30 mL of aqueous solution containing *N,N*-dimethylacrylamide (2 M), *N,N'*-methylene(bis)acrylamide (10 mM), and potassium persulfate (10 mM) was prepared. To this solution, the solid obtained in the first step (0.6 g) was added. The resulting suspension was stirred for a while and stand for 2 h until the solid swelled. Then the resulting slurry was added 300 μ L of *N,N,N',N'*-tetramethylethylenediamine and kept for 1 day to obtain double network hydrogel with sulfonic acid substituent.

Staining

Sulfonic acid gel was immersed in a 0.3 mM EtOH solution of **8**. After kept at room temperature for 12 h, gel was taken out from the solution and sunk in fresh EtOH for a while. The gel was then analyzed its appearance under room light and UV light.

Visualization of neutralization

The gel stained by **8** was immersed in a 0.1 M EtOH solution of triethylamine at room temperature. The neutralization was monitored by observation under 365 nm UV light.

5.8. References

1. Y. Inokuma, Z. S. Yoon, D. Kim, A. Osuka, *meso*-Aryl-Substituted Subporphyrins: Synthesis, Structures, and Large Substituent Effects on Their Electronic Properties, *J. Am. Chem. Soc.*, **2007**, *129*, 4747–4761.
2. N. Kobayashi, Y. Takeuchi, A. Matsuda, *meso*-Aryl Subporphyrins, *Angew. Chem. Int. Ed.*, **2007**, *46*, 758–760.
3. T. Tanaka, M. Kitano, S. Hayashi, N. Aratani, A. Osuka, Rational Synthesis of A₂B-type *meso*-Triarylsupporphyrins, *Org. Lett.*, **2012**, *14*, 2694–2697.
4. S. N. MacMillan, W. H. Harman, J. C. Peter, Facile Si–H bond activation and hydrosilylation catalysis mediated by a nickel–borane complex, *Chem. Sci.*, **2014**, *5*, 590–597.
5. A. Loudet, K. Burgess, BODIPY Dyes and Their Derivatives: Syntheses and Spectroscopic Properties, *Chem. Rev.*, **2007**, *107*, 4891–4932.
6. T. Kowada, H. Maeda, K. Kikuchi, Design, BODIPY-Based Probes for the Fluorescence Imaging of Biomolecules in Living Cells, *Chem. Soc. Rev.*, **2015**, *44*, 4953–4972.
7. N. Boens, V. Leen, W. Dehaen, Fluorescent indicators based on BODIPY, *Chem. Soc. Rev.*, **2012**, *41*, 1130–1172.
8. M. Wang, H. G. M. Vicente, D. Mason, P. Bobadova-Parvanova, Stability of a Series of BODIPYs in Acidic Conditions: An Experimental and Computational Study into the Role of the Substituents at Boron, *ACS Omega*, **2018**, *3*, 5502–5510.
9. L. Yang, R. Simionescu, A. Lough, H. Yan, Some Observations Relating to the Stability of the BODIPY Fluorophore under Acidic and Basic Conditions, *Dyes Pigm.*, **2011**, *91*, 264–267.
10. V. E. Rumyantsev, N. S. Alyoshin, S. Y. Marfin, Kinetic Study of Bodipy Resistance to Acids and Alkalis: Stability Ranges in Aqueous and Non-Aqueous Solutions, *Inorg. Chim. Acta*, **2013**, *408*, 181–185.
11. N. Boens, V. Leen, W. Dehaen, Fluorescent indicators based on BODIPY. *Chem. Soc. Rev.*, **2012**, *41*, 1130–1172.
12. T. Werner, C. Huber, S. Heintl, M. Kollmannsberger, J. Daub, O. S. Wolfbeis, Novel optical pH-sensor based on a boradiaza-indacene derivative. *Fresenius J. Anal. Chem.*, **1997**, *359*, 150–154.

13. S. Xia, M. Fang, J. Wang, J. Bi, W. Mazzi, Y. Zhang, R. L. Luck, H. Liu, Near-infrared fluorescent probes with BODIPY donors and rhodamine and merocyanine acceptors for ratiometric determination of lysosomal pH variance. *Sensors & Actuators: B. Chemical*, **2019**, *294*, 1–13.
14. M. Kollmannsberger, T. Gares, S. Heinl, J. Breu, J. Daub, Electrogenerated Chemiluminescence and Proton-Dependent Switching of Fluorescence: Functionalized Difluoroboradiaza-*s*-indacenes. *Angew. Chem. Int. Ed.*, **1997**, *36*, 1333–1335.
15. J. Peng, H. Chen, M. Sun, H. Yu, J. Hou, S. Wang, A benzooxazine-based ratiometric fluorescent probe for pH imaging in living cells and bacteria. *Sensors & Actuators: B. Chemical*, **2021**, *15*, 129711.
16. M. Krihak, M. T. Murtagh, M. R. Shahriari, A Spectroscopic Study of the Effects of Various Solvents and Sol-Gel Hosts on the Chemical and Photochemical Properties of Thionin and Nile Blue A. *J. Sol-Gel Sci. Tech.*, **1997**, *10*, 153–163
17. I. Yapici, K. S. S. Lee, T. Berbasova, M. Nosrati, X. Jia, C. Vasileiou, W. Wang, E. M. Santos, J. H. Geiger, B. Borhan, “Turn-On” Protein Fluorescence: In Situ Formation of Cyanine Dyes. *J. Am. Chem. Soc.*, **2015**, *137*, 1073–1080.
18. K. Miki, K. Kojima, K. Oride, H. Harada, A. Morinibu, K. Ohe, pH-Responsive near-infrared fluorescent cyanine dyes for molecular imaging based on pH sensing. *Chem. Commun.*, **2017**, *53*, 7792–7795.
19. P. Guo, L. Liu, Q. Shi, C. Yin, X. Shi, A rhodamine 6G derived Schiff base as a fluorescent and colorimetric probe for pH detection and its crystal structure. *J. Mol. Struct.*, **2017**, *1130*, 150–155.
20. Y. J. Kim, M. Jang, J. Roh, Y. J. Lee, H. J. Moon, J. Byun, J. Wi, S.-K. Ko, J. Tae, Rhodamine-Based Cyclic Hydroxamate as Fluorescent pH Probe for Imaging of Lysosomes. *Int. J. Mol. Sci.*, **2023**, *24*, 15073.
21. C. Bucher, R. S. Zimmerman, V. Lynch, V. Král, J. L. Sessler, Synthesis of Novel Expanded Calixphyrins: Anion Binding Properties of a Calix[6]phyrin with a Deep Cavity, *J. Am. Chem. Soc.*, **2001**, *123*, 2099–2100.
22. E. Palao, S. Moya, A. R. Agarrabeitia, I. Esnal, J. Bañuelos, Í. López-Arbeloa, M. J. Ortiz, Selective Lateral lithiation of Methyl BODIPYs: Synthesis, Photophysics, and Electrochemistry of New *Meso* Derivatives, *Org. Lett.*, **2014**, *16*, 4364–4367.
23. U. Gabe, Y. Urano, K. Kikuchi, H. Kojima, T. Nagano, Highly Sensitive Fluorescence Probes for Nitric Oxide Based on Boron Dipyrromethene Chromophore—Rational Design of Potentially Useful Bioimaging Fluorescence

- Probe, *J. Am. Chem. Soc.*, **2004**, *126*, 3357–3367.
24. F. G. Bordwell. Equilibrium Acidities in Dimethyl Sulfoxide Solution. *Acc. Chem. Res.*, **1988**, *21*, 456–463.
 25. I. V. Korendovych, M. Cho, O. V. Makhlynets, P. L. Butler, R. J. Staples, E. V. Rybak-Akimova. Anion and Carboxylic Acid Binding to Monotopic and Ditopic Amidopyridine Macrocycles, *J. Org. Chem.*, **2007**, *73*, 4771–4782
 26. P. Ayotte, M. Hébert, P. Marchand, Why is hydrofluoric acid a weak acid? *J. Phys. Chem.*, **2005**, *123*, 184501.
 27. R. A. Cox, K. Yates, Acidity functions: an update, *Can. J. Chem.*, **1983**, *61*, 2225–2243.
 28. N. Weder, N. S. Grudmann, B. Probst, O. Blacque, R. Ketkaew, F. Creazzo, S. Lubner, R. Alberto, Two Novel Dinuclear Cobalt Polypyridyl Complexes in Electro- and Photocatalysis for Hydrogen Production: Cooperativity Increases Performance. *ChemSusChem*, **2022**, *15*, e202201049.
 29. J. A. Therrien, M. O. Wolf, B. O. Patrick, Polyannulated Bis(N-heterocyclic carbene)palladium Pincer Complexes for Electrocatalytic CO₂ Reduction. *Inorg. Chem.*, **2015**, *54*, 11721–11732
 30. A. R. Watkins, Kinetics of Fluorescence Quenching by Inorganic Anions, *J. Phys. Chem.*, **1974**, *78*, 2555–2558.
 31. G. A. Olah, M. B. Comisarow, C. A. Cupas, C. U. Pittman Jr. Stable Carbonium Ions. XIII. Generation of Stable Alkyl, Alkylaryl, and Cycloalkyl Carbonium Ions from Alcohols in Fluorosulfonic Acid and Antimony Pentafluoride. *J. Am. Chem. Soc.*, **1965**, *87*, 2997–2998.
 32. K. A. Mauritz, R. B. Moore, State of Understanding of Nafion, *Chem. Rev.*, **2004**, *104*, 4535–4586.
 33. L. Liu, W. Chen, Y. Li, An overview of the proton conductivity of nafion membranes through a statistical analysis, *J. Membr. Sci.*, **2016**, *504*, 1–9.
 34. C. H.-Wirguin, Recent advances in perfluorinated ionomer membranes: structure, properties and applications, *J. Membr. Sci.*, **1996**, *120*, 1–33.
 35. M. A. Harmer, Q. Sun, Solid acid catalysis using ion-exchange resins, *Appl. Catal. A: Gen.*, **2001**, *221*, 45–62.
 36. G. M. Sheldrick, *SHELXT* – Integrated space-group and crystal-structure determination, *Acta Crystallogr. Sect. A*, **2015**, *71*, 3–8.
 37. G. M. Sheldrick, Crystal structure refinement with *SHELXL*, *Acta Crystallogr. Sect. C*, **2015**, *71*, 3–8.

38. Gaussian 16, Revision C.01, M. J. Frisch, G. W. Trucks, H. B. Schlegel, G. E. Scuseria, M. A. Robb, J. R. Cheeseman, G. Scalmani, V. Barone, G. A. Petersson, H. Nakatsuji, X. Li, M. Caricato, A. V. Marenich, J. Bloino, B. G. Janesko, R. Gomperts, B. Mennucci, H. P. Hratchian, J. V. Ortiz, A. F. Izmaylov, J. L. Sonnenberg, D. Williams-Young, F. Ding, F. Lipparini, F. Egidi, J. Goings, B. Peng, A. Petrone, T. Henderson, D. Ranasinghe, V. G. Zakrzewski, J. Gao, N. Rega, G. Zheng, W. Liang, M. Hada, M. Ehara, K. Toyota, R. Fukuda, J. Hasegawa, M. Ishida, T. Nakajima, Y. Honda, O. Kitao, H. Nakai, T. Vreven, K. Throssell, J. A. Montgomery, Jr., J. E. Peralta, F. Ogliaro, M. J. Bearpark, J. J. Heyd, E. N. Brothers, K. N. Kudin, V. N. Staroverov, T. A. Keith, R. Kobayashi, J. Normand, K. Raghavachari, A. P. Rendell, J. C. Burant, S. S. Iyengar, J. Tomasi, M. Cossi, J. M. Millam, M. Klene, C. Adamo, R. Cammi, J. W. Ochterski, R. L. Martin, K. Morokuma, O. Farkas, J. B. Foresman, and D. J. Fox, Gaussian, Inc., Wallingford CT, 2016.
39. K. Agnes, S. Sigrid, K. Ivari, T. Sofja, H. Agnes, D. Astrid, K. Karl, P. Mare, L. Ivo, pK_a values in organic chemistry – Maximum use of the available data, *Tetrahedron Lett.*, **2018**, *59*, 3738–3748.
40. T. Sofja, K. Agnes, L. Märt, K. Ivari, S. Jaan, H. Agnes, P. G. Paul, V. Robert, L. Ivo, On the Basicity of Organic Bases in Different Media, *Eur. J. Org. Chem.*, **2019**, *40*, 6733–6887.

Chapter 6

Conclusion and Future Outlook

6.1. Conclusion

In this thesis, the author has demonstrated the synthesis and properties of calix[3]pyrrole and its derivatives. The initial interest in synthesizing calix[3]pyrrole was to understand why tripyrrolic macrocycles were never found, and tetrapyrrolic macrocycles were selectively formed in acid-catalyzed condensation reactions of pyrrole and carbonyl compounds. However, as shown in Chapters 2-5, the strained small macrocyclic structure of calix[3]pyrrole led to the development of unique ring expansion reactions, new chiral motif, and the discovery of acid stability in the combination of tripyrrolic macrocycle and boron atom.

In Chapter 2, calix[3]pyrrole was synthesized, and its strained structure and unique ring expansion reaction were unveiled. The synthesis of calix[3]pyrrole was achieved by Paal-Knorr pyrrole formation reaction-based strategy. Single crystal structural analysis and theoretical calculations revealed that calix[3]pyrrole has a much strained structure compared with larger analogues. Induced by the strain, calix[3]pyrrole underwent a rapid ring expansion reaction under acidic conditions to give calix[6]pyrrole in 30 seconds, which was further transformed into calix[4]pyrrole over hours. Although the anion binding ability of calix[3]pyrrole was much less than larger analogues, this indicates that ring expansion reaction can drastically change its anion binding ability. These findings helped to explain the absence of tripyrrolic macrocycle and the selective formation of tetrapyrrolic macrocycle in traditional oligopyrrolic macrocycle synthesis. Furthermore, the ring expansion reaction was also expected to be a new tool to access large macrocyclic systems that were difficult to access by conventional synthetic methods.

In Chapter 3, the scope and mechanism of ring expansion reaction was investigated using furan embedded derivatives of calix[3]pyrrole with different degrees of strain. The strain of furan embedded derivatives, calix[n]furan[m]pyrroles ($n+m=3$), were found to decrease as the number of pyrrole decreased, determined from single crystal structural analyses and computational analyses. The reactivity of ring expansion reaction was also found to decrease as the strain decreased, declaring the relationship between strain and ring expansion reaction. Based on the successful isolation of the reaction intermediate, the reaction mechanism of ring expansion reaction was proposed to consist of ring cleavage driven by the release of strain after protonation of pyrrole and dimerization of resulting linear intermediate followed by intramolecular cyclization.

In Chapter 4, the construction of a chiral system based on the aromatic ring inversion of calix[3]pyrrole derivative. Calix[1]furan[1]pyrrole[1]thiophene was prepared as the asymmetric derivative of calix[3]pyrrole, and found to be separated into enantiomers due

to its relatively slower aromatic ring inversions. Although it underwent racemization at room temperature in solution, *N*-methylation of pyrrole successfully suppressed aromatic ring inversion to afford configurationally stable enantiomers. Given the different racemization behavior before and after *N*-methylation, dynamic kinetic resolution upon *N*-methylation was attempted, which resulted in asymmetric *N*-methylation with 10%*ee*, indicating the possibility of enantioselective molecular recognition. Calix[1]furan[1]pyrrole[1]thiophene underwent strain-induced ring expansion reaction to give two-, three-, and four-fold ring expanded product, not only emphasizing that the chirality is derived from suppressed aromatic ring inversion but also showing applicability of ring expansion reaction to access huge macrocycle systems.

In Chapter 5, the stability of boron-calix[3]pyrrole complex against acid was demonstrated. It was found that boron complex of calix[3]pyrrole can exist in acidic conditions by forming the adduct with acid through protonation of pyrrole and coordination of conjugate base on boron without deboronation. Cyclic BODIPY, which was designed as an application of the protonation gimmick, proved to have remarkable stability to acid compared with conventional BODIPY. The synthesized cyclic BODIPY was stable even in neat strong acid, in which conditions conventional BODIPY lose boron atom and fluorescence. Besides, cyclic BODIPY showed fluorescence switching upon protonation by acid. This highly acid-stable cyclic BODIPY was used to stain strongly acidic material, indicating the possibility to be used in the situations conventional BODIPYs cannot be used.

The current results provide access to novel large macrocycles that are difficult to synthesize by conventional methods, serve as a new motif for inherently chiral molecules, and expand the availability of BODIPY as a fluorescent probe. Further investigation of calix[3]pyrrole derivatives may lead to the development of various related chemistries.

6.2. Future Perspectives

Although the unique properties of calix[3]pyrrole and related compounds have been disclosed in this thesis, there should be more possibilities of calix[3]pyrrole derivatives that have not been found at this stage. For example, introduction of transition metal into calix[3]pyrrole-type ligand is expected to have unique features owing to flexible and non-planar structure of the ligand as calix[4]pyrrole has been explored its possibility as a ligand for metals¹. Boron complex of calix[3]pyrrole also has a space to be explored as a sterically hindered Lewis acidic substrate in frustrated Lewis pair chemistry as various boron Lewis acids have been investigated.² Furthermore, strain-induced ring expansion reaction would afford the synthesis of huge macrocycles that are expected to be used as host molecules for large guest molecules.

To realize these prospects, the improvement of synthetic methods and further exploration of properties are necessary, but the chemistry of calix[3]pyrrole-related compounds should attract more and more attention in the near future.

6.3. References

1. H. Ruppert, L. M. Sigmund, L. Greb, Calix[4]pyrroles as ligands: recent progress with a focus on the emerging p-block element chemistry, *Chem. Commun.*, **2021**, 57, 11751–11763.
2. D. W. Stephan, Frustrated Lewis Pairs, *J. Am. Chem. Soc.*, **2015**, 137, 10018–10032.

List of Publications

Chapter 2

Calix[3]pyrrole: A Missing Link in Porphyrin-Related Chemistry

Y. Inaba, Y. Nomata, Y. Ide, J. Pirillo, Y. Hijikata, T. Yoneda, A. Osuka, J. L. Sessler, Y. Inokuma,
J. Am. Chem. Soc., **2021**, *143*, 12355–12360.

Chapter 3

Strain-induced Ring Expansion Reactions of Calix[3]pyrrole-related Macrocycles

Y. Inaba, Y. Kakibayashi, Y. Ide, J. Pirillo, Y. Hijikata, T. Yoneda, Y. Inokuma,
Chem, Eur. J., **2022**, *28*, e202200056.

Chapter 4

Chiral Calix[3]pyrrole Derivatives: Synthesis, Racemization Kinetics, and Ring Expansion to Calix[9]- and Calix[12]pyrrole Analogues

Y. Inaba, J. Yang, Y. Kakibayashi, T. Yoneda, Y. Ide, Y. Hijikata, J. Pirillo, R. Saha, J. L. Sessler, Y. Inokuma,
Angew. Chem. Int. Ed., **2023**, *62*, e202301460.

Other Publications

Splitting and Reorientation of π -Conjugation by an Unprecedented Photo-Rearrangement Reaction

Y. Inaba, T. Yoneda, Y. Kitagawa, K. Miyata, Y. Hasegawa, Y. Inokuma,
Chem. Commun., **2020**, 56, 348–351.

Modular Synthesis of Oligoacetylacetones *via* Site-selective Silylation of Acetylacetone Derivatives

P. Sarkar, Y. Inaba, H. Shirakura, T. Yoneda, Y. Inokuma,
Org. Biomol. Chem., **2020**, 18, 3297–3302.

Spirosilicate Dimers of a Bowl-shaped Diol Generated by Intermolecular Cyclization of an Aliphatic Tetraketone Chains

Y. Inaba, Y. Inokuma,
Chem. Lett., **2020**, 49, 882–884.

Isopyrazole-Masked Tetraketone: Tautomerism and Functionalization for Fluorescent Metal Ligands

H. Shirakura, Y. Manabe, C. Kasai, Y. Inaba, M. Tsurui, Y. Kitagawa, Y. Hasegawa, T. Yoneda, Y. Ide, Y. Inokuma,
Eur. J. Org. Chem., **2021**, 4345–4349.

Alikali Metal Ion Binding Using Cyclic Polyketones

N. Ozawa, K. I. Shivakumar, M. Murugavel, Y. Inaba, T. Yoneda, Y. Ide, J. Pirillo, Y. Hijikata, Y. Inokuma,
Chem. Commun., **2022**, 58, 2971–2974.

Determination of the Critical Chain Length for Macromolecular Crystallization Using Structurally Flexible Polyketones

Y. Ide, Y. Manabe, Y. Inaba, Y. Kinoshita, J. Pirillo, Y. Hijikata, T. Yoneda, K. I. Shivakumar, S. Tanaka, H. Asakawa, Y. Inokuma,
Chem. Sci., **2022**, 13, 9848–9854.

Absorption Spectra of Calix[3]pyrrole Analogues as Probes for Contracted Macrocycles
K. Watanabe, R. Saha, Y. Inaba, Y. Manabe, T. Yoneda, Y. Ide, Y. Hijikata, Y. Inokuma,
J. Porphyrins Phthalocyanines, **2023**, *27*, 157–163.

Toward Calix[2]-Type Macrocycles: Synthesis and Structural Analysis of Cyclic
Tetraketone and Highly Strained Furanophane
T. Sano, Y. Sun, T. Mukai, Y. Inaba, T. Yoneda, Y. Ide, J. Pirillo, Y. Hijikata, Y. Inokuma,
J. Porphyrins Phthalocyanines, **2023**, *27*, 1067–1073

Machine Learning-Based Analysis of Molar and Enantiomeric Ratios and Reaction Yields
Using Images of Solid Mixtures
Y. Ide, H. Shirakura, T. Sano, M. Murugavel, Y. Inaba, S. Hu, I. Takigawa, Y. Inokuma,
Ind. Eng. Chem. Res., **2023**, *62*, 13790–13798.

Acknowledgements

The studies presented in this Ph.D. thesis were conducted under the supervision of Prof. Dr. Yasuhide Inokuma from April 2018 to March 2024 at the Graduate School of Chemical Science and Engineering, Hokkaido University.

First of all, I would like to express my gratitude to Prof. Yasuhide Inokuma for providing me with a research environment and for his advice during the entire period of my Ph.D. studies.

I would also like to appreciate Prof. Dr. Hajime Ito, Prof. Dr. Koichiro Ishimori, Prof. Dr. Yasuchika Hasegawa, and Assoc. Prof. Dr. Hisanori Senboku for dedicating their time as referees for my Ph.D. thesis with their helpful suggestions and comments.

I would also like to thank assistant professors, Dr. Tomoki Yoneda, Dr. Yuki Ide, and Dr. Yusuke Kinoshita for their helpful supports, discussions, and a lot of advice on both research works and daily life.

I am deeply grateful to the research collaborators, Assoc. Prof. Dr. Yuh Hijikata, Dr. Pirillo Jenny, Dr. Ranajit Saha, Prof. Dr. Jonathan L. Sessler, Mr. Jian Yang, and Assoc. Prof. Tasuku Nakajima for giving me the opportunity to participate in collaborative works.

My daily life in the lab was fully and warmly supported by my lab mates, not only in scientific discussions but also in daily life in the lab. My sincere appreciation goes to my lab mates Dr. Yumehiro Manabe, Mr. Mitsuharu Uesaka, Mr. Yuki Saito, Ms. Yoshiko Ashida, Ms. Chika Kasai, Ms. Mayu Takakuwa, Mr. Sugi Tei, Mr. Yosuke Katsuie, Mr. Jae Seob Shin, Mr. Hayato Shirakura, Ms. Mizuki Yagihashi, Mr. Narito Ozawa, Mr. Yu Nomata, Mr. Hidetoshi Matsuno, Mr. Yu Kakibayashi, Mr. Taichi Mukai, Mr. Ken Nagai, Ms. Mizuki Hayama, Mr. Taichi Sano, Mr. Keita Watanabe, Ms. Marimo Satoh, Mr. Yuhua Sun, Mr. Kotaro Shibata, Mr. Kyohei Yoshimura, Mr. Mizuki Matsui, Dr. Parantap Sarkar, Dr. Muthuchamy Murugavel, Dr. Kilingaru I. Shivakumar, Dr. Narendra Nath Pati, a technical assistant Ms. Mizuho Watanabe, and secretaries Ms. Kanako Ibaraki, Ms. Chiyuki Shiraki, Ms. Keiko Mori and Ms. Yuki Kawai.

My Ph.D. studies were also financially supported by JSPS Fellowship.

Finally, I would like to express my deepest gratitude to my family for their kind and warm support my life at the Hokkaido University.

March, 2024

Yuya Inaba